11-2023

Self-Assembling Peptide-Based High-Relaxivity Prostate-Cancer-Targeted MRI Contrast Agents

Andrew O'Brien
amo3668@rit.edu

Recommended Citation

O'Brien, Andrew, "Self-Assembling Peptide-Based High-Relaxivity Prostate-Cancer-Targeted MRI Contrast Agents" (2023). Thesis. Rochester Institute of Technology. Accessed from

Self-Assembling Peptide-Based High-Relaxivity Prostate-Cancer-Targeted MRI Contrast Agents

Andrew O'Brien

A thesis submitted in partial fulfillment of the requirements for the degree

Master of Science in Chemistry

Supervised by

Dr. Hans Schmitthenner

School of Chemistry and Materials Science

College of Science

Rochester Institute of Technology

November 2023

Signature of the Author ________________________________

Accepted by ____

Director, M.S. Degree Program Date

SCHOOL OF CHEMISTRY AND MATERIALS SCIENCE
COLLEGE OF SCIENCE

ROCHESTER INSTITUTE OF TECHNOLOGY
ROCHESTER, NEW YORK

CERTIFICATE OF APPROVAL

M.S. DEGREE THESIS

The M.S. Degree Thesis of Andrew O'Brien has
been examined and approved by the thesis
committee as satisfactory for the thesis required
for the M.S. Degree in Chemistry.

____
Dr. Hans Schmitthenner, Thesis Advisor

____
Dr. Emiliano Brini

____
Dr. Joseph Hornak

____
Dr. Scott Williams

____
Date

Abstract

Magnetic Resonance Imaging (MRI) is a widely used, highly effective imaging method for diagnosing cancer and guiding treatment. MRI contrast agents enhance image quality, with higher relaxivity (r_1) contrast agents providing the best utility. Attaching a cancer-specific-targeting group enhances the image further. Therefore, a high-relaxivity cancer-targeted contrast agent is a highly desirable tool for diagnosis and treatment.

Our group previously synthesized a peptide-based MRI contrast agent with the Ala(Gd-DO3A) chelator that targeted the prostate cancer biomarker PSMA using the small-molecule ligand DCL. While this agent displayed nominal relaxivity, it was serendipitously found that the relaxivity of a synthetic intermediate containing Fmoc-protected tryptophan (Trp) increased dramatically. This was hypothesized to occur due to intermolecular self-assembly above a critical aggregation concentration (CAC).

The first goal was to expand upon this finding by designing peptide-based MRI contrast agents using the simpler Lys(Gd-DOTA) chelator developed earlier in our lab. Di- and tripeptides were synthesized to test the effect of peptide length, net charge, and relative location and stereochemistry of Fmoc, Trp, and Lys(Gd-DOTA) on self-assembly through measuring r_1 at 1.0 Tesla. Self-assembly was found to increase r_1 from 3-7 to 13-17 $mM^{-1}s^{-1}$ in H_2O and PBS and 11-13 $mM^{-1}s^{-1}$ in FBS, with remarkably low CACs in FBS.

The second goal was to investigate self-assembly using other motifs, including Cbz-protected Trp, two adjacent Trp residues, and other Fmoc-protected aromatic amino acids.

The third goal was to apply these findings to synthesize high-relaxivity cancer-targeted MRI contrast agents. Two prostate-cancer-targeted self-assembling MRI contrast agents containing DCL and a breast-cancer-targeted MRI contrast agent containing the peptide 18-4 were synthesized. This work represents the first example of self-assembly in MRI contrast agents induced by Fmoc and aromatic amino acids, and in the broader scope, the synthetic approach is amenable to a wide variety of self-assembling cancer-targeted MRI contrast agents.

Acknowledgements

This thesis was made possible with the support of many others. First and foremost, I would like to thank my research advisor, Dr. Hans Schmitthenner, for his continuous support. Dr. Hans, thank you for seeing potential in me and letting me run wild with this project. I would also like to thank the fellow committee members, Dr. Emiliano Brini, Dr. Joseph Hornak, and Dr. Scott Williams, for supporting me during this work. I would also like to thank Dr. Michael Heagy and Dr. Dumindu Premachandra for additional assistance with fluorescence spectroscopy measurements.

I am thankful for all the other group members I have gotten to know over the years. I would like to thank Alex Deutsch and Griffin Pileski for being my personal “minions” on this project, as well as Matt Henry for the synthesis of DCL-DSS. I would also like to thank the past graduate students I have worked alongside, Sara Shaut, Dana Soika, and Chris DeNyse, for leading the way.

I would like to thank my family members for supporting me and always having my back during difficult times. I am especially grateful for my father, who was diagnosed with cancer himself during my time at RIT. I am also thankful for some of my high school teachers, in particular Brian Luca, August Eberling, and Dr. Paul Hesleitner for furthering my interest in chemistry and scientific research. I would also like to thank the School of Chemistry and Materials Science and the Academic Success Center for employment throughout my time at RIT.

I am especially appreciative of every person who has ever given me a second chance. Your gestures have not gone to waste.

Abbreviations:

ACN	Acetonitrile
Ala	Alanine
Boc	Tert-butoxycarbonyl
BODIPY	Boron-dipyrromethene
CAC	Critical Aggregation Concentration
Cbz	Carboxybenzyl
Dap	(S)-2,3-Diaminopropionic acid
DCL	N-[N-[(S)-1,3-dicarboxypropyl]-carbamoyl]-(S)-L-lysine
DCM	Dichloromethane
DEA	Diethylamine
D-	D-isomer of amino acid
DI	Deionized
DIPEA	Diisopropylethylamine
DMF	Dimethylformamide
DMSO	Dimethyl sulfoxide
DO3A	1,4,7,10-tetraazacyclododecane-1,4,7-tris(tert-butyl acetate)
DOTA	1,4,7,10-Tetraazacyclododecane-1,4,7,10-Tetraacetic acid
DTPA	2,2′,2″,2‴-{[(Carboxymethyl)azanediyl]bis(ethane-2,1-diylnitrilo)}tetraacetic acid
DSS	Disuccinimidyl suberate
EDC	1-Ethyl-3-(3-dimethylaminopropyl)carbodiimide
Et_2O	Diethyl ether
EtOAc	Ethyl acetate
Fmoc	Fluorenylmethoxycarbonyl
HATU	1-[Bis(dimethylamino)methylene]-1H-1,2,3-triazolo[4,5-b]pyridinium 3-oxide Hexafluorophosphate
HPLC	High Performance Liquid Chromatography
L-	L-isomer of amino acid
LC-MS	Liquid Chromatography – Mass Spectrometry
Lys	Lysine (L-Lysine when used in compound/peptide names, otherwise without regard to stereochemistry)
MS	Mass Spectrometry
Mtt	4-methyltrityl
MeOH	Methanol
MRI	Magnetic Resonance Imaging
NHS	N-hydroxysuccinimide
NIR	Near-infrared
OAt	Azabenzotriazole
PBS	Phosphate-buffered saline
PEG	Polyethylene glycol
Phe	Phenylalanine
PET	Positron Emission Tomography
PSMA	Prostate-Specific Membrane Antigen
SIC	Single Ion Chromatogram

SPE	Solid Phase Extraction
T	Tesla
TEA	Triethylamine
TFA	Trifluoroacetic acid
TMIA	Targeted Molecular Imaging Agent
Trp	Tryptophan (L-Tryptophan when used in compound/peptide names, otherwise without regard to stereochemistry)
Tyr	Tyrosine
TSTU	N,N,N’,N’-Tetramethyl-O-(N-succinimidyl)uronium tetrafluoroborate

Nomenclature of Peptides:

Peptide and peptide-derived structures in this document are described by standard peptide nomenclature which may not be familiar to all readers. In peptide nomenclature, the standard three-letter designations for amino acids are utilized. Peptides are conventionally drawn with the nitrogen of the first amino acid (N-terminus) on the left and the carbonyl of each amino acid on the right. The carbonyl on the last amino acid (C-terminus) on the right side is most often an acid (designated as -OH), or amide (-NH_2). Likewise, an H- prefix designates an unprotected amine at the peptide N-terminus.

For PEG linker compounds, H_2N- designates a primary amine, and -COOH instead designates a C-terminal carboxylic acid as -OH is used to designate a C-terminal primary alcohol.

Substituents on amino acids with terminal amines on the side chains (such as lysine) are written in parentheses after the amino acid designation. These are often protecting groups such as Boc or Cbz, but in these cases include metal chelates such as Gd-DOTA. This nomenclature is illustrated below for the following tripeptide with Fmoc attached to its N-terminus, Gd-DOTA attached to D-Lys, and Mtt attached to the side chain of Dap.

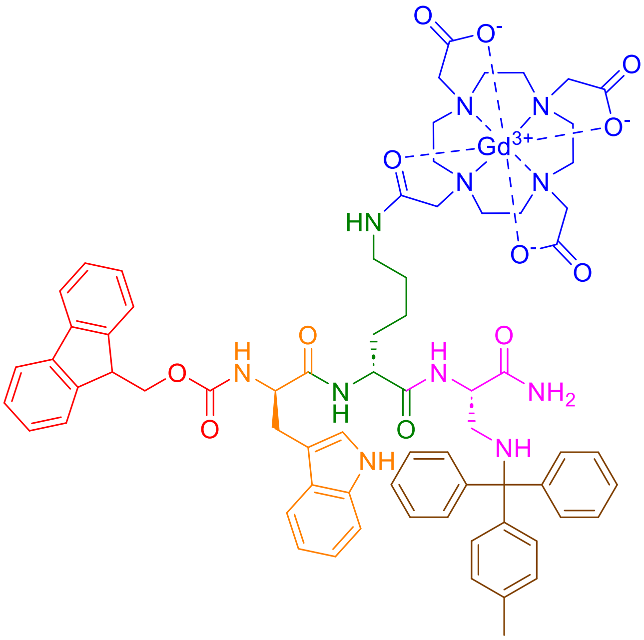

Compound: Fmoc-D-Trp-D-Lys(Gd-DOTA)-Dap(Mtt)-NH_2

Table of Contents

List of Figures

List of Schemes

List of Tables

1. Introduction:

1.1 Prostate Cancer Overview

Prostate cancer is the second most commonly diagnosed cancer in men worldwide. Prostate cancer makes up one out of every five new cancer cases in men, and around one in eight American men will be diagnosed with prostate cancer in their lifetime.[1,2] In 2020 alone, there were over 190,000 cases and 33,000 deaths estimated from prostate cancer. Although prostate cancer incidence has been steadily decreasing from a high of almost 250 annual cases per 100,000 men in the early 1990s, its incidence rate still remains high at around 100 annual cases per 100,000 men.[1] Aside from the high human cost, prostate cancer also imparts a high financial cost. The total estimated expenditure of prostate cancer diagnoses, treatments, and follow-up in the United States in 2006 was $9.862 billion.[3]

Prostate cancer cases have a unique set of demographics compared to other cancers, particularly in regard to age and race. Around 6 out of 10 men diagnosed with prostate cancer are 65 or older. The average age of prostate cancer diagnosis is 66, and it is seldom diagnosed in men under 40.[4] Prostate cancer is much more common in non-Hispanic men of African descent, who have incidence and mortality rates around two-thirds above average.[1]

1.2. Prostate Cancer Diagnosis and Imaging Methods

Prostate cancer diagnosis is reliant on the analysis of prostate-specific antigen (PSA) levels in the blood.[5] However, PSA tests evaluate a non-specific prostate cancer biomarker, lack a universally accepted PSA concentration for a positive result, and cannot determine the extent of tumor spread.[6] PSA tests also have a 70% false-positive rate and a 15% false-negative rate, frequently failing to discern cancerous and non-cancerous cases.[7] An elevated PSA level therefore often requires further verification through a prostate biopsy. During a prostate biopsy, tissue is extracted from the prostate with the assistance of transrectal ultrasound, as seen in Figure 1. Around one million prostate biopsies are performed annually in the United States. However, this technique can misclassify up to 50% of cases, including 30% of high-grade tumors.[6]

Short-term complications from prostate biopsies are also prevalent, with hospitalization occurring in almost 7% of patients.[8] This clearly portrays the need for more accurate screening methods that would ideally be based on imaging rather than invasive methods such as biopsies.

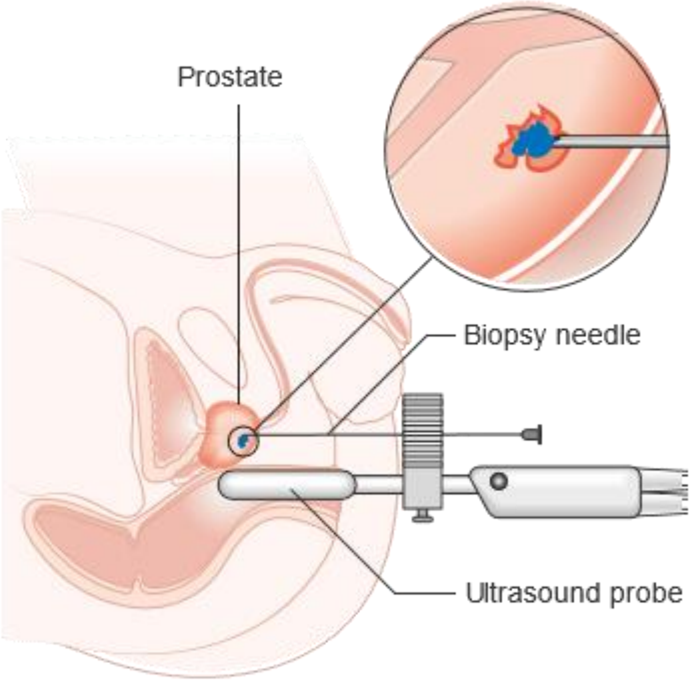

Figure 1: Illustration of a prostate biopsy, in which a probe and needle are inserted into the rectum in order to collect prostate tissue.[9]

In addition to screening methods, the determination of precise location and extent of prostate cancer is important for the design of treatment methods. There are several non-invasive methods available to image prostate cancer tumors, including positron emission tomography (PET), computed tomography (CT), ultrasound, and combination of these, as well as combined magnetic resonance imaging (MRI) and CT. However, these methods are exceedingly expensive, difficult to carry out, cannot accurately capture tumor size and location, and lack a functional screen to differentiate aggressive tumors from benign tumors.[10,11]

Furthermore, with these methods, the inability to detect metastasis (tumor growths at secondary sites within the body) is a major disadvantage because prostate cancer treatment is most effective if diagnosed while still within the prostate gland.[11] An ideal prostate cancer imaging-based diagnosis method should be highly accurate, location-specific, and noninvasive. More accurate and prostate cancer-specific diagnosis and imaging methods need to be developed in order to overcome these shortcomings.

1.3 Principles of Magnetic Resonance Imaging

One effective method used to image internal structures in the body is magnetic resonance imaging (MRI). MRI is particularly favored as an imaging method in clinical settings due to its high resolution and non-invasive procedure. Typical clinical MRI scanners operate at a magnetic field strength of 1.5 T or higher and have a spatial resolution of $1.5 \times 1.5 \times 4\ mm^3$.[12] MRI works by applying a strong magnetic field throughout the body. This field causes the magnetic moments of ^{1}H nuclei (referred to in MRI terminology as protons), found throughout the body in water molecules, to align. A brief pulse of electric current (“RF pulse”) is then pulsed in the span of nanoseconds, causing a temporary secondary magnetic field that disrupts the protons’ nuclei from their equilibrium. When this pulse is turned off, the protons’ magnetic moments return to their equilibrium positions in the span of milliseconds to seconds. These protons’ behavior while returning to equilibrium is described through their T_1 and T_2 relaxation times. T_1 relaxation time dictates the time for the protons’ longitudinal magnetic moments (parallel to the applied magnetic field) to return to equilibrium, whereas T_2 relaxation time dictates the time for the protons’ transverse magnetic moments (perpendicular to the applied magnetic field) to return to equilibrium.[13]

MRI contrast agents increase the contrast of internal structures within the body by shortening the T_1 relaxation time of nearby ^{1}H nuclei of water or fat molecules.[14] Regions in the body with more contrast agent uptake will produce a brighter MRI signal, leading to increased contrast in the final image. Bodily structures that can be imaged through contrast-agent-assisted MRI include regions with inflammation, blood vessels, and tumors.[15] An example MRI of the pelvis revealing inflammation of the right sacroiliac joint only after administration of a contrast agent is shown in Figure 2.

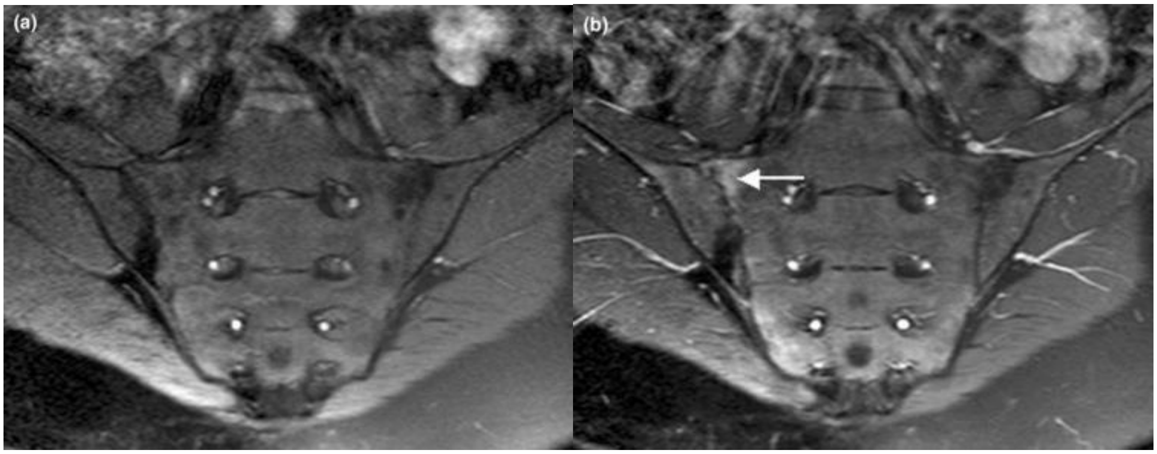

Figure 2: MRI of the pelvis administered without (left) and with (right) a contrast agent, revealing inflammation in the right sacroiliac joint (shown by the arrow).[16]

In T_1-weighted MRI, a more intense signal is produced from regions with low T_1 relaxation times. When an MRI contrast agent is present at the site of a tissue, the local T_1 relaxation time decreases, resulting in a brighter signal. This is demonstrated in Figure 3, which simulates the net magnetization (discussed further in Section 1.4) and subsequent image brightness in MRI following a 180° RF pulse for a given tissue with and without an MRI contrast agent present.

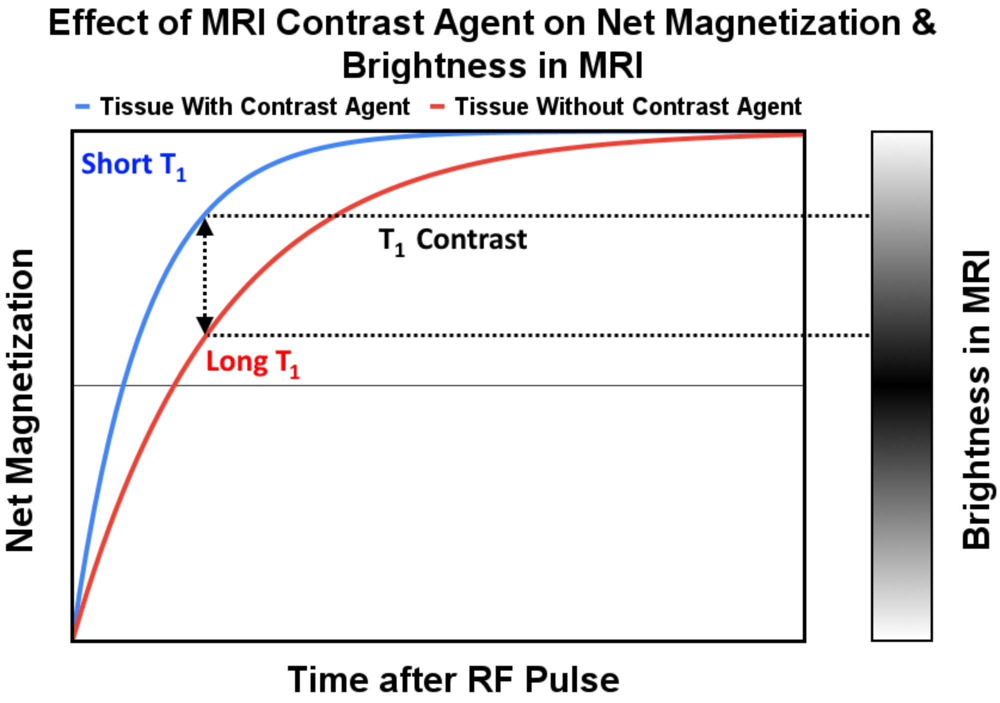

Figure 3: Net magnetization and image brightness for a tissue with and without an MRI contrast agent.

The relationship between T_1 and T_2 relaxation time and a contrast agent's concentration is described by its r_1 and r_2 relaxivities, as shown in Equation 1.[17]

$$\frac{1}{T_i} = \frac{1}{T_{i(0)}} + r_i[C] \tag{1}$$

In the above equation, T_i is the measured T_1 or T_2 relaxation time, $T_{i(0)}$ is the T_1 or T_2 relaxation time of a pure solvent in the absence of a contrast agent, r_i is the r_1 or r_2 relaxivity, and [C] is the concentration of a contrast agent in a solution. This equation shows that r_1 represents the change in $1/T_1$ of an MRI contrast agent with respect to its concentration. Increasing r_1, and therefore decreasing T_1, will result in a brighter signal produced by a contrast agent. A contrast agent with a higher r_1 value will produce a brighter signal than a contrast agent with a lower r_1 value at the same concentration. This also means that a lower concentration of a contrast agent with a higher r_1 value is required to produce the same intensity signal as a higher concentration of a contrast agent with a lower r_1 value.[18] As a result, contrast agents with higher r_1 values will be more effective at producing contrast in T_1-weighted MRI.

1.4 T_1 and r_1 Measurement

Nuclear magnetic resonance (NMR) can be used to determine a contrast agent's r_1 value. This classifies how effective a contrast agent is in T_1-weighted MRI. A discussion on atomic physics is important in order to understand the process of T_1 measurement. Spin is a property of atomic nuclei that causes them to carry an intrinsic angular momentum. In the presence of a magnetic field, atomic nuclei will align their spin either with or against the magnetic field, with alignment with the magnetic field energetically favored. This spin imbalance results in a magnetization vector, M. The distribution of these states with respect to temperature is given by Equation 2:

$$\frac{N^-}{N^+} = e^{\frac{-\Delta E}{k_B T}} \tag{2}$$

In the above equation, N^- and N^+ are the number of particles in the spin-down and spin-up states respectively, ΔE is the energy difference between the two states, k_B is the Boltzmann constant, and T is temperature.

When in a magnetic field, atomic nuclei will precess about the direction of the magnetic field, as shown by Equation 3:

$$\omega = \gamma B \tag{3}$$

In the above equation, ω is the precession frequency (commonly called the Larmor frequency), γ is the gyromagnetic ratio (42.58 MHz/T for ^{1}H nuclei), and B is the magnetic field strength. ω_H is the precession frequency for ^{1}H nuclei and is the frequency observed in ^{1}H NMR and MRI.

There are multiple steps required to measure the T_1 relaxation of a sample. A sample is first placed in an NMR spectrometer and exposed to a magnetic field B_0, causing an initial net magnetization M_0 along the z-axis. A 180° pulse induced by electric current at the Larmor frequency is applied to the sample, resulting in an inversion of M_0 about the z-axis. After an inversion time interval TI, in which the sample begins to return to its equilibrium magnetization along the z-axis, a 90° pulse is then applied, rotating the instantaneous net magnetization M entirely into the xy-plane. This results in a detectable signal proportional to M at TI. The signal intensity with respect to time can be fit using Equation 4:

$$S = S_0\left(1 - 2e^{\frac{-TI}{T_1}}\right) \tag{4}$$

In this equation, S is the instantaneous signal after an inversion time TI and S_0 is the initial signal before the 90° pulse. The T_1 value can be calculated from the curve's x-intercept, which occurs at $T_1\, ln(2)$, as shown in Figure4.

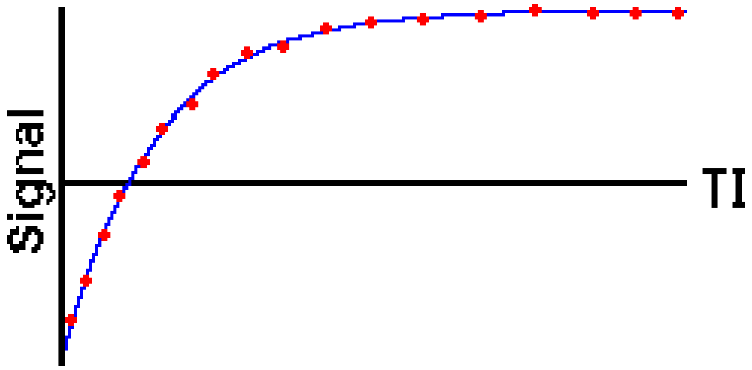

Figure 4: Example signal vs. inversion time graph for a T_1 relaxation measurement trial.[19]

The $1/T_1$ values of multiple samples of a contrast agent at varying concentrations can be fit to a calibration curve such as measurements in our lab of Gd-DOTA (Dotarem), shown in Figure 5 in order to determine r_1.[19] The resulting trendline follows Equation 1, in which r_1 is the slope. The contrast agent concentration required for these measurements is typically very small, on the order of 5 mM or less.

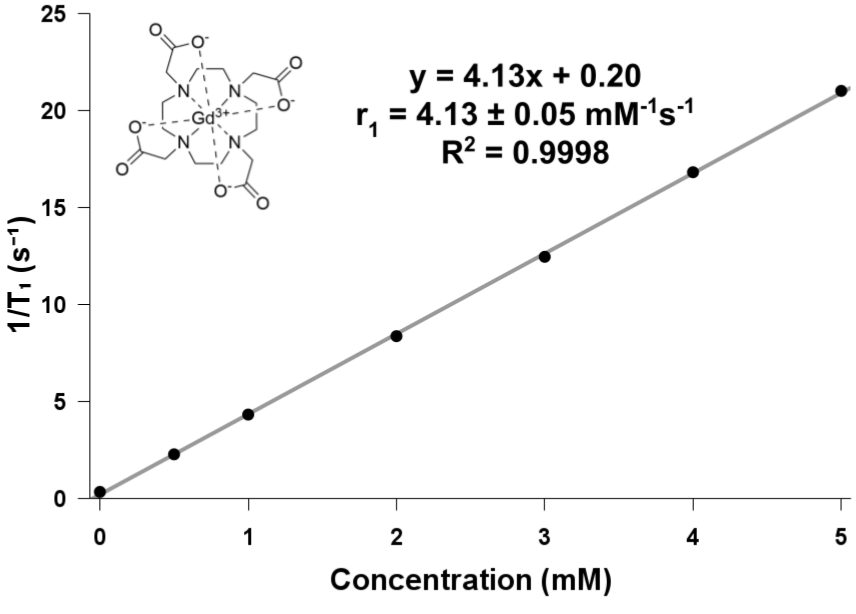

Figure 5: Example calibration curve to measure r_1 of a contrast agent, in this example the commercially used MRI contrast agent Gd-DOTA (Dotarem). The r_1 value is the slope of the trendline, which is 4.13 $mM^{-1}s^{-1}$.

1.5. Use of Gd(III) as an MRI Contrast Agent

Paramagnetic compounds have been demonstrated as effective T_1-weighted MRI contrast agents, with gadolinium in its +3 oxidation state (Gd(III)) being particularly effective. This is due to Gd(III) containing seven unpaired electrons, the highest out of any transition metal ion, resulting in a strong magnetic moment. Gd(III) also exhibits a relatively stable singlet state, leading to a slower relaxation rate and stronger interactions with protons in water molecules.[20] Gd(III) contrast agents are active in both T_1 and T_2 weighted MRI. However, the Gd(III) concentration required for T_2-weighted MRI is several mM, whereas T_1-weighted MRI requires a Gd(III) concentration below 1 mM.[21] Therefore, the majority of Gd(III) contrast agents are only used in T_1-weighted MRI.

Gd(III) based contrast agents have been in development since the 1980s. Gd-DTPA (Magnevist) was first reported in 1981 and approved by the Food and Drug Administration (FDA) in 1988. Eight other Gd-based contrast agents have since been FDA-approved. By the end of 2009, Gd(III) based contrast agents had been administered almost 90 million times, the majority being the original Gd-DTPA.[22] An estimated 30 metric tons of Gd(III) were administered to patients in the first decade since Magnevist's approval alone. By 1999, Gd(III) contrast agents were used in approximately 30% of MRI exams, a figure which has likely risen as new agents and applications have since been found.[23]

Free Gd(III) exists in aqueous solutions as a hydrated ion surrounded by water molecules, as the lone pairs on the adjacent water molecules' oxygen atoms coordinate with the positively-charged Gd(III) ion. Gd(III) interacts with eight to nine water molecules at a time. The $Gd(H_2O)_8^{3+}$ form is most commonly found, with each water molecule participating in coordination for only around 1 nanosecond. An additional water molecule can insert itself into the coordination complex, forming a 9-coordinate intermediate, followed by the dissociation of one water molecule to return to the $Gd(H_2O)_8^{3+}$ formation.[23] The rapid rate of this water exchange process is what enables Gd(III) to be such an effective MRI contrast agent, as a single molecule can magnetically relax millions of water molecules per second, causing the rapid return of net magnetization to equilibrium and the resulting increase in image brightness.

Despite Gd(III) being active in MRI, the metal itself cannot be administered into the body as a free ion due to its high toxicity. This is because it has a similar ionic radius as Ca(II) but a larger net charge, causing it to biologically compete in processes that normally require Ca(II).[23] For this reason, Gd(III) compounds must therefore be chelated with a ligand that forms multiple coordinate covalent bonds to the metal ion prior to use in the body. These chelators can protect the body against toxic effects of the metal, and as they are comprised of multiple acid and amine groups, can facilitate their rapid excretion from the body which further contributes to their safety.

There are four structures of Gd(III) chelates currently in clinical use: linear ionic, linear nonionic, macrocyclic ionic, and macrocyclic nonionic. Each of the nine FDA-approved Gd(III) contrast agents falls into one of these four categories. Gd-DTPA (Magnevist), Gd-BOPTA (MultiHance), Gd-EOB-DTPA (Primovist/Eovist), and MS-325 (Vasovist/Ablavar) are linear ionic, Gd-DTPA-BMA (Omniscan) and Gd-DTPA-BMEA (OptiMARK) are linear nonionic, Gd-DOTA (Dotarem) is macrocyclic ionic, and Gd-HP-DO3A (ProHance) and Gd-BT-DO3A (Gadovist/Gadavist) are macrocyclic nonionic.[21] Figure 6 displays the chemical structures of all nine FDA-approved Gd(III) chelates.

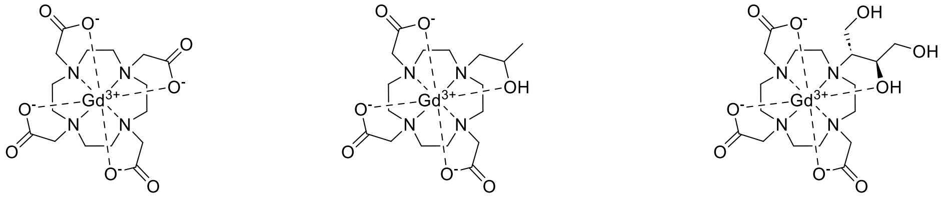

Gd-DOTA
Macrocyclic ionic
Extracellular

Gd-HP-DO3A
Macrocyclic nonionic
Extracellular

Gd-BT-DO3A
Macrocyclic nonionic
Extracellular

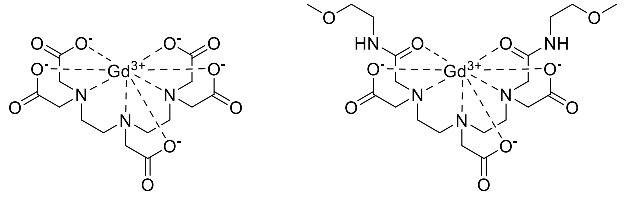

Gd-DTPA
Linear ionic
Extracellular

Gd-DTPA-BMEA
Linear nonionic
Extracellular

Gd-DTPA-BMA
Linear nonionic
Extracellular

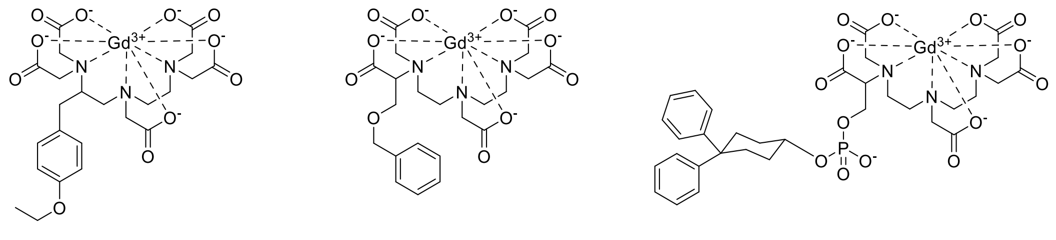

Gd-EOB-DTPA
Linear ionic
Hepatobiliary

Gd-BOPTA
Linear ionic
Hepatobiliary

MS-325
Linear ionic
Blood-pool

Figure 6: The nine FDA-approved Gd(III) chelates for use in MRI, categorized based on structure and active location in the body.

All Gd(III) ligands have multiple heteroatoms (usually nitrogen or oxygen) that surround a Gd(III) ion by forming covalent bonds. However, linear ligands have linear backbones that only partially wrap around the Gd(III) ion, whereas macrocyclic ligands have ring structures that fully encapsulate the Gd(III) ion. Nonionic chelates have a balanced net charge between the Gd(III) ion and ligand, while ionic chelates have a net negative charge. A typical Gd(III) chelate has eight coordination sites. Since Gd(III) can have eight to nine coordinate interactions at a time, free water molecules will go in and out of chelation at the ninth coordination site. This coordination site is the MRI active site in Gd(III)-based contrast agents because the interaction between Gd(III) and coordinated water molecules is responsible for the T_1 shortening effect.[21,24]

Gd(III) contrast agents fall into three categories based on where they are active in the body. Extracellular fluid (ECF) agents are distributed within the extracellular space. They are the longest used, most commonly used, and most well-documented contrast agents. Blood-pool contrast agents (BPCAs) remain in the blood vessels much longer than ECF agents. They are therefore used in angiography (the imaging of the blood vessels). BPCAs work through several mechanisms. These include binding to proteins such as human serum albumin (HSA), systems incorporating polymer macromolecules, or nanoparticles that have a different excretion route.

Targeted/organ-specific agents are designed to act on specific tissues. The only contrast agents in this category that are currently in use are hepatobiliary (acting within the liver). Gd-EOB-DTPA and Gd-BOPTA, the two hepatobiliary agents in use, both have lipophilic side groups that cause them to accumulate in the liver. This accumulation method is different from MS-325, which has a diphenyl cyclohexyl group that specifically binds to HSA.[21]

1.6. r_1 Relaxivity of MRI Contrast Agents

Small-molecule contrast agents typically have r_1 values of ~4-5 $mM^{-1}s^{-1}$ at magnetic field strengths used in MRI.[20] It is estimated that a change in $1/T_1$ of 0.5 s^{-1}, corresponding to an *in vivo* concentration of

0.125 mM for a contrast agent with an r_1 value of 4 $mM^{-1}s^{-1}$, is required to observe contrast between tissues in MRI.[25]

Different forms of interactions between MRI contrast agents and surrounding water molecules contribute to r_1 relaxivity. Inner-sphere relaxivity (r_1^{IS}) is caused by water molecules that directly coordinate with the Gd(III) ion, while outer-sphere relaxivity (r_1^{OS}) is caused by water molecules that are close to the Gd(III) ion but do not directly coordinate with it, such as those hydrogen-bonded to other heteroatoms on the chelate.[23] An MRI contrast agent's overall r_1 relaxivity equals the sum of r_1^{IS} and r_1^{OS}, as seen in Equation 5.[14] However, the r_1^{OS} term is often ignored due to difficulties in calculating the r_1 contribution from outer-sphere water molecules.[23]

$$r_1 = r_1^{IS} + r_1^{OS} \tag{5}$$

Contributions to inner-sphere relaxivity include the chelate hydration number q (the number of water molecules that can directly coordinate with the Gd(III) cation at a time), the proton Larmor frequency ω_H, the rotational correlation time τ_R, the Gd(III) electronic relaxation time T_{1e}, and the water residency time τ_M (the reciprocal of the water exchange rate k_{ex}). Several of these parameters that affect the r_1 relaxivity of a Gd(III) chelate are illustrated in Figure 7.

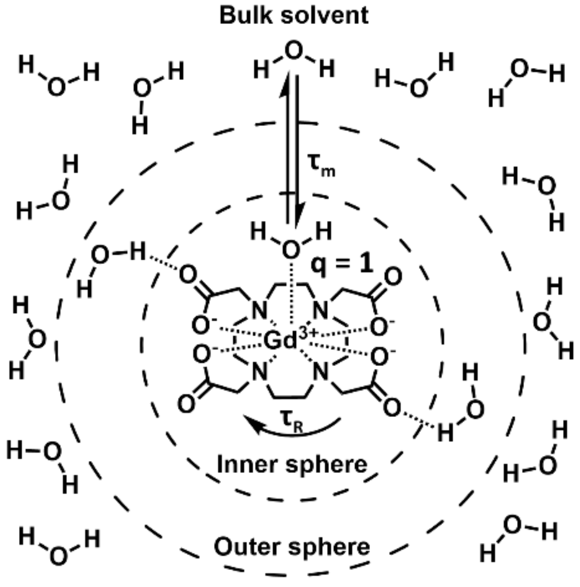

Figure 7: An illustration of relaxivity effects of Gd-DOTA (Dotarem) and parameters relevant to inner-sphere r_1: q, τ_M, and τ_R.[25]

The effect of these parameters on inner-sphere relaxivity is shown in Equations 6-8 and apply at magnetic field strengths of 0.1 T or greater. As outlined by Equation 8, τ_R, T_{1e}, and τ_M contribute to an overall correlation time τ_C, the reciprocal of which is the sum of the reciprocals of τ_R, T_{1e}, and τ_M. τ_c in turn contributes to the inner-sphere water relaxation time T_{1M}, which contributes to r_1.[25]

$$r_1^{IS} = \frac{q/[H_2O]}{T_{1M} + \tau_M} \tag{6}$$

$$\frac{1}{T_{1M}} \propto \frac{3\tau_C}{1+\omega_H^2\tau_C^2} \tag{7}$$

$$\frac{1}{\tau_c} = \frac{1}{\tau_R} + \frac{1}{T_{1e}} + \frac{1}{\tau_M} \tag{8}$$

As shown by these equations, r_1 increases with increasing τ_c. However, the value of τ_c is usually closest to τ_R, which is typically several orders of magnitude smaller than T_{1e} or τ_M. The small value of τ_R is caused by the fast rotation of MRI contrast agents, which limits their r_1 values. This is demonstrated in Table 1, where calculating τ_c based on previously reported physical parameters of Gd-DOTA in H_2O at room temperature yields a value that is much closer to τ_R than T_{1e} or τ_M.

Table 1: Physical Parameters of Gd-DOTA in H_2O at Room Temperature

q	τ_R (s)	T_{1e} (s)	τ_M (s)	τ_c (s) (from Equation 8)
1 [20]	$7.7 * 10^{-11}$ [20]	$(4.7 \pm 1.0) * 10^{-9}$ [26]	$2.44 * 10^{-7}$ (from reported k_{ex} value of $4.10 * 10^6$ s^{-1})[20]	$7.6 * 10^{-11}$

Equations 6-7 show that the optimal τ_c value to maximize r_1 is the reciprocal of ω_H. Calculating the optimal τ_c value at multiple field strengths in the range commonly used in MRI (0.5 T - 7.0 T) reveals that even the lowest optimal τ_c value at 7.0 T is roughly seven times higher than the calculated τ_c value in Table 2. In order to increase τ_c (and therefore r_1), τ_R must be raised by slowing down the rotation of MRI contrast agent molecules.

Table 2: Optimal τ_c Values at Different Magnetic Field Strengths Used in MRI

Magnetic Field Strength (T)	ω_H (s^{-1}) (from Equation 3)	Optimal τ_c value of $1/\omega_H$ (s)
0.5	$1.34*10^{7}$	$7.48*10^{-9}$
1.0	$2.68*10^{7}$	$3.74*10^{-9}$
1.5	$4.02*10^{7}$	$2.49*10^{-9}$
3.0	$8.03*10^{8}$	$1.24*10^{-9}$
7.0	$1.87*10^{9}$	$5.34*10^{-10}$

1.7 Molecular Self-Assembly

One method to increase τ_R of MRI contrast agent molecules is through self-assembly. Self-assembly is a process by which individual molecules interact with each other non-covalently to form larger, more ordered structures. A common example of self-assembling molecules are surfactants such soap molecules, as individual soap molecules spontaneously assemble into micelles above a critical concentration when dispersed in solution. Self-assembling MRI contrast agent molecules rotate much slower than non-self-assembling MRI contrast agent molecules as they exist in larger clusters and experience much stronger intermolecular forces. This results in a longer τ_R and higher r_1.

Peptide-based structures provide ideal properties for self-assembling MRI contrast agents. Low molecular weight peptides (<3,000 amu) can enhance bioavailability and they can be synthesized using well-established peptide coupling techniques. In addition, self-assembly properties can be modified by altering the presence and location of various aromatic amino acids and N-terminal substituents utilizing these peptide synthesis techniques. Moreover, peptides are amenable to the conjugation of disease biomarker-targeting agents through well-known coupling methods.

Many short peptides assemble freely into larger supramolecular configurations when in solution. Several non-covalent interactions such as electrostatic interactions, hydrophobic interactions, aromatic π-π interactions, and hydrogen bonding can drive peptide self-assembly. Peptide self-assembly is exhibited in biological processes such as cellular membrane formation and is even thought to contribute to neurodegenerative diseases like Alzheimer's disease.[27]

Mono- and dipeptides containing amino acids with aromatic protecting groups such 9-fluorenylmethoxycarbonyl (Fmoc) and N-carboxybenzyl (Cbz) have been reported to self-assemble in mixtures of water and methanol or acetone.[28,29] Peptides with aromatic groups have also been used in hydrogels, with the aromatic moieties of Fmoc-protected amino acids interacting non-covalently to induce gelation including in mono, di, and tripeptide-based hydrogels containing Fmoc-protected amino acids.[30–32] Hydrogels containing Fmoc-protected peptide chains have also been injected into mice and found to contribute to wound healing, suggesting Fmoc is biocompatible.[32]

Several peptide-based self-assembling MRI contrast agents have previously been reported. The synthesis of a peptide-based contrast agent that self-assembles upon reduction by furin and subsequent dimerization has been reported by Cao, as shown in Figure 8. These dimers feature a hydrophobic and macrocyclic benzothiazole core flanked by Gd-DOTA chelates attached to lysine residues, with self-assembly induced by π-π interactions between molecule cores. The r_1 value of this contrast agent at 1.5 T in phosphate buffer was 13.24 $mM^{-1}s^{-1}$ in its self-assembling form, compared to 6.00 $mM^{-1}s^{-1}$ in its non-reduced, non-self-assembling form.[33]

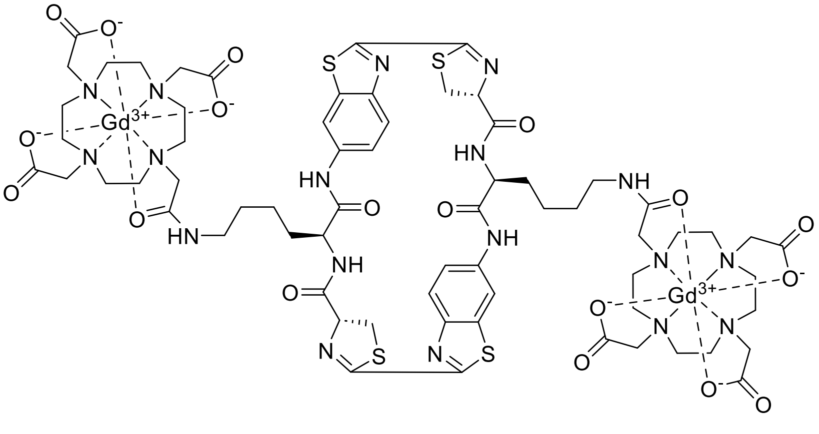

Figure 8: Self-assembling MRI contrast agent reported by Cao et al, featuring an aromatic benzothiazole core that induces self-assembly. [33]

In other related work, Gallo synthesized hydrogel contrast agents containing DOTA or DTPA-chelated Gd(III) attached to Phe-Tyr-Phe-Tyr-Phe-Tyr via PEG linkers, as shown in Figure 9. Like the self-assembling MRI contrast agents synthesized by Cao, these compounds self-assemble due to π-π interactions induced by the aromatic Phe and Tyr residues. The r_1 of these compounds at 0.5 T varied with concentration but were between 8 and 12 $mM^{-1}s^{-1}$ at concentrations between 0.5 and 20 mg/mL.[34] Both of these papers show that DOTA-based MRI contrast agents that self-assemble experience r_1 values higher than typical small-molecule contrast agents (~4-5 $mM^{-1}s^{-1}$) when in their self-assembled forms. However, neither of these papers identified a discrete critical aggregation concentration (CAC), representing the concentration above which their compounds primarily exist in self-assembled forms.

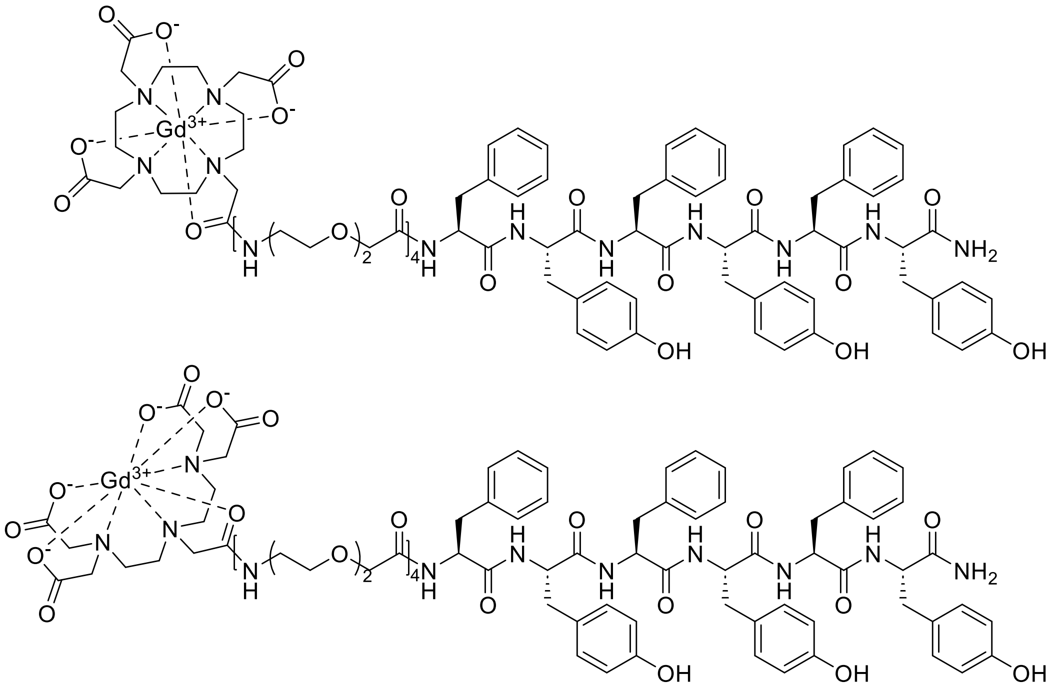

Figure 9: Self-assembling peptide-based MRI contrast agents reported by Gallo et al, consisting of DOTA or DTPA attached to an aromatic amino acid sequence via PEG linkers.[34]

One potential issue in the design of self-assembling peptide-based MRI contrast agents is poor water solubility stemming from the presence of multiple hydrophobic aromatic amino acids or N-terminal substituents. An ideal MRI contrast agent for clinical use should have a water solubility of at least 0.25 M, as commercially available MRI contrast agents are typically formulated at a concentration of 0.25 - 1.0 M.[35] Low water solubility also results in poor bioavailability and difficulty in creating calibration curves to measure r_1. The previously described self-assembling MRI contrast agents as featured zwitterionic Gd(III) chelates and hydrophilic linkers to overcome this problem.[33,34]

1.8 Molecular Targeting

The accuracy of a contrast agent can be improved by selective accumulation at the site of a tumor. This would also result in a lower required imaging agent concentration to produce the same signal, increasing the contrast agent's safety. Molecular targeting is a type of cancer treatment that uses drugs or other substances that selectively target cancer cells without affecting normal cells.[36] Molecular targeting groups interact with molecular biomarkers (molecules that indicate the presence of a biological process) that are unique to cancer cells. Cancer biomarkers have distinctive characteristics that enable specific therapeutic interventions. Many widespread anti-cancer drugs, such as tamoxifen for breast cancer, target specific receptors unique to a cancer cell in order to inhibit cellular processes.[37] Incorporating molecular targeting into Gd(III)-based contrast agents will result in higher imaging accuracy and safety due to selective tumor binding.

Most molecular targeting groups are monoclonal antibodies or small molecule drugs.[38,39] Monoclonal antibodies are artificially produced by cells, have molecular weights of around 150 kDa, and typically only bind to surface proteins. Monoclonal antibodies do not cause cell death directly, but rather trigger an immune response that results in cell death. Small-molecule drugs are typically chemically produced, have much lower molecular weights of around 500 Da, and are able to enter cells due to their small size. Small-molecule drugs are also usually less expensive and easier to administer than monoclonal antibodies.[38]

In the context of cancer imaging, molecular targeting can be used to increase the concentration of a contrast agent at the site of a tumor, even if not specifically used for therapeutic purposes. A contrast agent with a targeting group attached will accumulate at the site of a tumor. This will result in a lower effective dose required for tumor imaging, resulting in increased safety. Since the goal of this study is to create cancer imaging agents, rather than cancer treatment, the targeting group used will be a small molecule group.

1.9 PSMA and DCL for Targeting Prostate Cancer

Prostate-specific membrane antigen (PSMA), also known as glutamate carboxypeptidase, is a transmembrane peptidase protein found primarily on the surface of prostate cells. Since PSMA is expressed in cancerous prostate cells at a much higher rate than in noncancerous prostate cells, PSMA is an excellent biomarker for prostate cancer targeted therapies.[40–42] A tumor's PSMA expression level can also be used as an indicator for aggressiveness, allowing for a functional screen from PSMA-targeted imaging alone.[42]

Small-molecule PSMA targeting groups were first developed after the crystal structure of PSMA was determined through X-ray crystallography in the mid-2000s.[43,44] These small-molecule targeting groups can bind to the active site of PSMA, located within a cavity on the protein's surface. The active site of PSMA contains a binuclear zinc ion and two substrate-binding pockets, one pharmacophoric (enabling ligand binding) and another non-pharmacophoric. These targeting groups were designed to mimic the peptidyl neurotransmitter N-acetyl-L-aspartyl-L-glutamate (NAAG), which interacts with PSMA at its active site. Since these targeting groups bind to PSMA at the same site as NAAG but block PSMA from correctly functioning, they are also known as PSMA inhibitors. Small-molecule PSMA inhibitors feature L-glutamic acid and another amino acid substituent (usually lysine) coupled with a urea backbone. The carboxylate groups on the L-glutamic acid and amine groups on the urea are responsible for binding to the pharmacophoric pocket.[45]

N-[N-[(S)-1,3-dicarboxypropyl]-carbamoyl]-(S)-L-lysine (DCL), shown in Figure 10, is a PSMA inhibitor that has L-lysine coupled to L-glutamic acid via a urea linkage. The majority of PSMA inhibitors in clinical use and development utilize DCL as a targeting group. The presence of lysine in DCL has multiple benefits. One benefit is that lysine's flexible five-atom-long side chain enables it to maneuver into the PSMA active site cavity. Another benefit is that lysine's primary amine group on its side chain enables it to be coupled to form larger molecules. When a spacer moiety is coupled to this lysine, it enables the end of the molecule to clear the 20 Å long PSMA active site cavity.[46] This allows other groups to be attached to the molecule without worrying about spatial hindrance.

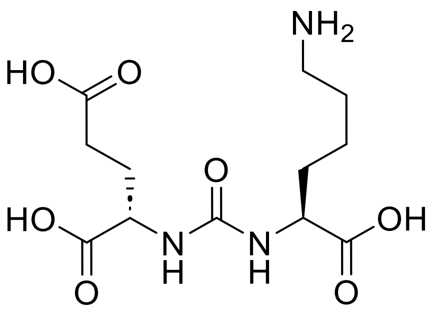

Figure 10: The structure of DCL, a commonly used PSMA inhibitor.

1.10 Targeted Molecular Imaging Agents (TMIAs)

A targeted molecular imaging agent (TMIA) is a compound that contains both a targeting group and a group active in a particular imaging modality. Our group has previously created TMIAs for a variety of imaging modalities, including MRI, PET, SPECT, confocal fluorescence microscopy (CFM), photoacoustic imaging (PAI), optical molecular imaging (OMI), and multispectral optoacoustic imaging (MSOT).[47]

TMIAs present an optimal solution to address the current problems with prostate cancer detection and imaging. TMIA-based imaging is highly accurate and location-specific due to the agents' selective accumulation at tumor sites. Due to this selectivity, PSMA-targeted MRI contrast agents would provide a nontoxic, non-invasive, and highly accurate method of prostate cancer detection.

There are several prior examples in literature of TMIAs that incorporate DCL in order to target PSMA. A 2016 study by Banerjee synthesized a variety of TMIAs featuring ^{68}Ga chelators and DCL. These TMIAs included DOTA, NOTA, and HBED-CC to chelate ^{68}Ga, which is active in PET imaging. The TMIAs also featured a linear disuccinimidyl suberate (DSS) spacer in between the DCL and chelating groups in order for the DCL to better reach the PSMA active site. It was demonstrated that these TMIAs could successfully be used for PSMA-targeted PET imaging in mice.[48] Another study by Banerjee from 2015 synthesized TMIAs, containing one to three Gd(III) chelators, DCL, and a linker group. It was found that these compounds could effectively target and differentiate human prostate cancer cells, both *in vitro* and *in vivo*.[49]

1.11 Self-Assembling Cancer-Targeted MRI Contrast Agents

There have been several previously reported MRI contrast agents that combine self-assembly and cancer targeting. Kim et al synthesized a variety of amphiphilic co-assemblies containing different arrangements of alternating hydrophobic amino acid sequences, PEG linkers, DOTA, and linear and cyclic octreotide as a targeting peptide for tumors, as shown in Figure 11. Self-assembly was induced by the hydrophobic amino acids, which formed intermolecular alternating β-sheets.

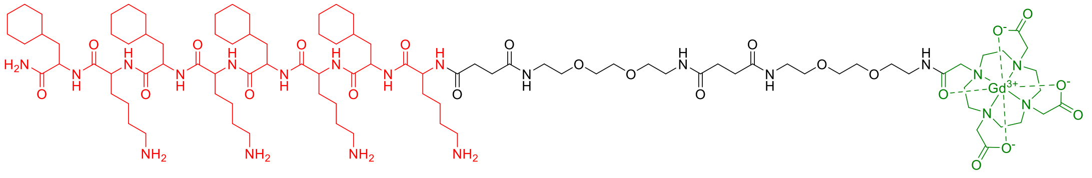

Cha-DOTA

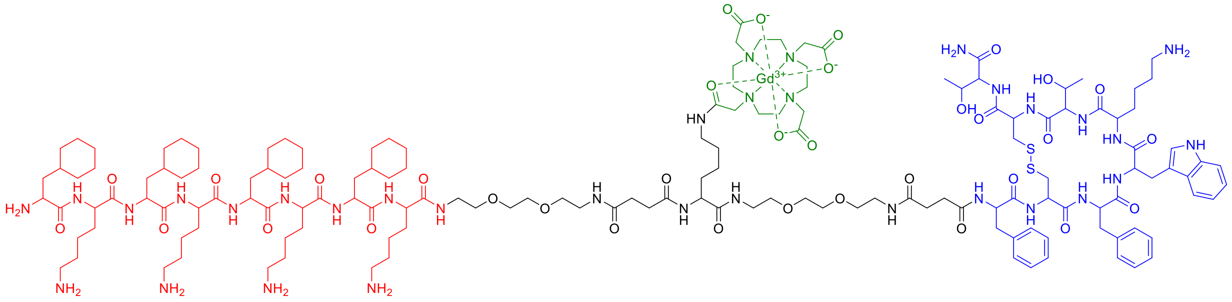

C-Cha-DOTA

Figure 11: Peptide amphiphiles synthesized by Kim et al containing hydrophobic amino acid sequences (red), PEG linkers (black), DOTA (green), and octreotide (blue).[50]

Although compound C-Cha-DOTA featured both octreotide and DOTA, the authors chose to investigate the co-assembly of C-Cha and Cha-DOTA (which feature only octreotide or DOTA respectively) due to the low synthetic yield of C-Cha-DOTA. The authors obtained r_1 values of 19.5, 17.1, and 17.2 $mM^{-1}s^{-1}$ at 4.7 T for 2:8, 5:5, and 8:2 ratios of Cha-DOTA:C-Cha respectively. In addition, the critical micellar concentration (CMC) for C-Cha was calculated to be 13 µM, far below the optimal concentration of 0.125 mM for *in vivo* imaging with typical MRI contrast agents.[25,50]

Li et al synthesized two PSMA-targeted MRI contrast agents that contained DCL separated by a disulfide linkage from a tetraphenylethylene core and the macrocyclic Gd(III) chelator Gd-DOTAGA, as shown in Figure 12. Once the contrast agents entered prostate cancer cells through endocytosis after binding with PSMA, the disulfide linkage was cleaved by glutathione (GSH), inducing self-assembly from the newly-exposed tetraphenylethylene groups. This had the effect of amplifying the contrast agent concentration inside the prostate cancer cells.

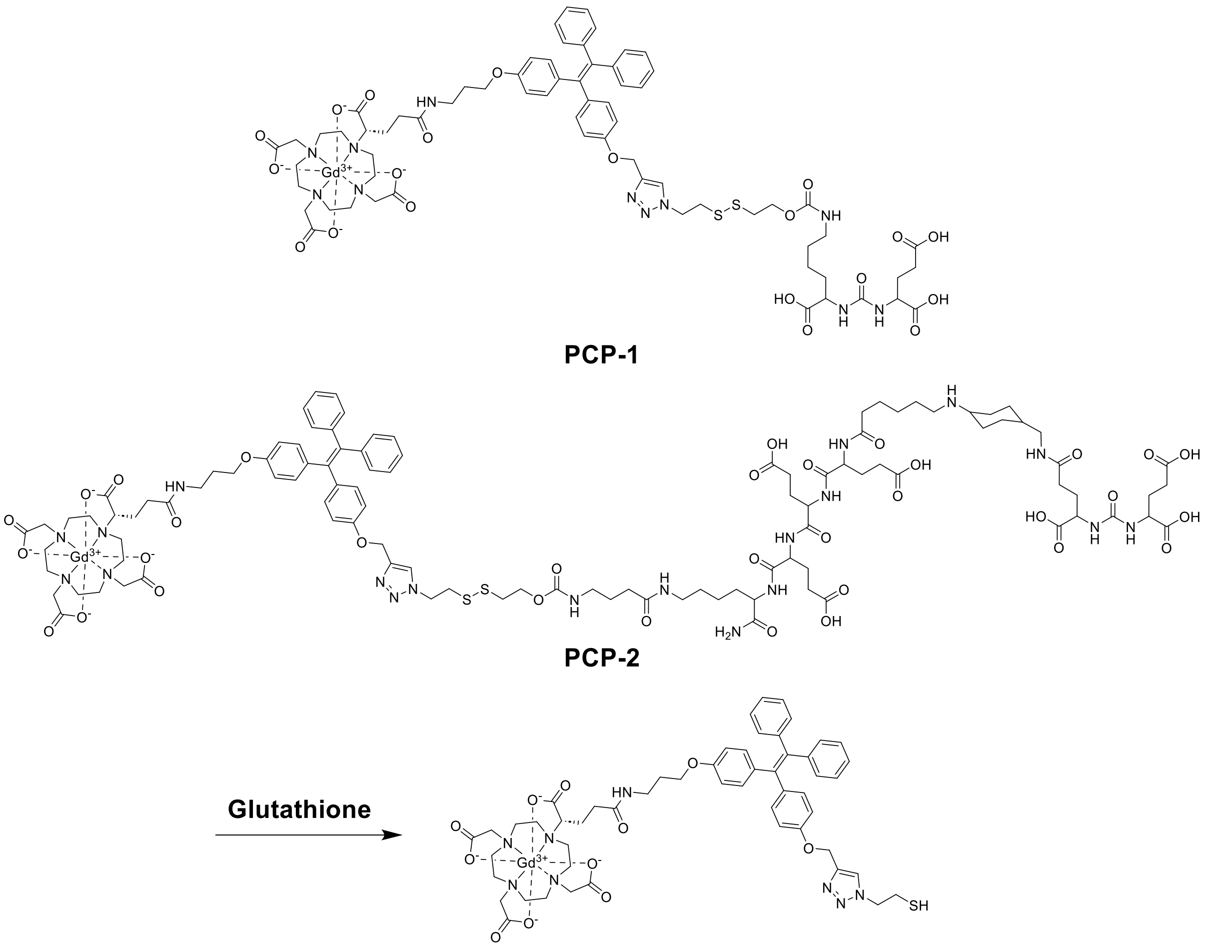

Figure 12: PSMA-targeted MRI contrast agents synthesized by Li et al that self-assemble upon cleavage by glutathione.[51]

The r_1 of PCP-1/ PCP-2 at 1.41 T were found to be 16.2 and 15.3 mM^{-1}s^{-1} respectively on their own and 21.1 and 23.4 mM^{-1}s^{-1} respectively following incubation with GSH overnight. The elevated r_1 values obtained compared to small-molecule contrast agents (~4-5 mM^{-1}s^{-1}) not only suggest that these r_1 values reflected the compounds' self-assembled states, but that the compounds could self-assemble without cleavage by GSH. Through fluorescence intensity experiments, the critical micelle concentrations (CMC) of PCP-1 and PCP-2 were measured to be 0.0953 and 0.1733 mM respectively.

However, PCP-1 was found to have poor *in vitro* selectivity for PSMA cells which was attributed to the low CMC, reflecting the diminished ability of DCL to bind to PSMA when in a self-assembling system. Although the IC_{50} of PCP-1 was measured to be 20.6 nM, several order of magnitudes below the CMC, the low value of the CAC implies that the compounds formed aggregates, even when dispersed in solution, prior to binding to PSMA.[51]

Taking these findings into consideration, an ideal self-assembling targeting MRI contrast agent for PSMA should have a CAC of at least 0.1 mM in order to prevent self-assembly from interfering with cell binding. As with the DCL compounds from Li et al that were found to enter cells through endocytosis, the contrast agent would accumulate inside the cell, raising the concentration enough to trigger self-assembly.[51] This would result in increased signal not only from the increase in concentration, but also the increase in r_1 above the critical concentration for self-assembly. However, the CAC should otherwise be as low as possible to ensure that the minimum contrast agent concentration is required to trigger the self-assembly that increases r_1. Ultimately, the optimal concentration to induce self-assembly would depend on the relative amount of compound taken up by cells compared to remaining in solution.

1.12 Puzzle Piece Synthetic Approach

Peptide-based chemistry can create convenient scaffolds for TMIAs. Utilizing amino acids allows for the straightforward coupling of different parts of a TMIA, including the active imaging agents, the targeting group, and any linkers. Small oligopeptides (< 10 amino acids) also have low molecular weights (< 3,000 Da), allowing them to serve as small-molecule imaging agents. Our group holds a patent for the synthesis of TMIAs using this peptide-based scaffold approach.[52] This method utilizes amino-acid-based "puzzle pieces" containing dyes or other groups active in imaging methods (such as Gd(III) chelates for MRI) attached at their side chains. These modules are referred to as "puzzle pieces" due to their ability to be coupled together, analogous to snapping together actual puzzle pieces.

TMIA synthesis involves three key steps, as shown in Figure 13: Fmoc deprotection, carboxylic acid activation, and coupling, In the first step, the Fmoc group is deprotected from a puzzle piece using the secondary amine diethylamine. In the second step, the carboxylic acid of a second puzzle piece is converted into an "active ester" using coupling reagents such as HATU or TSTU under basic conditions. In the third step, the Fmoc-deprotected amine of the first puzzle piece reacts with the active ester of the second puzzle piece to form a peptide bond. This cycle is then repeated to incorporate additional puzzle pieces, until the targeting group and linker are attached in the final step.

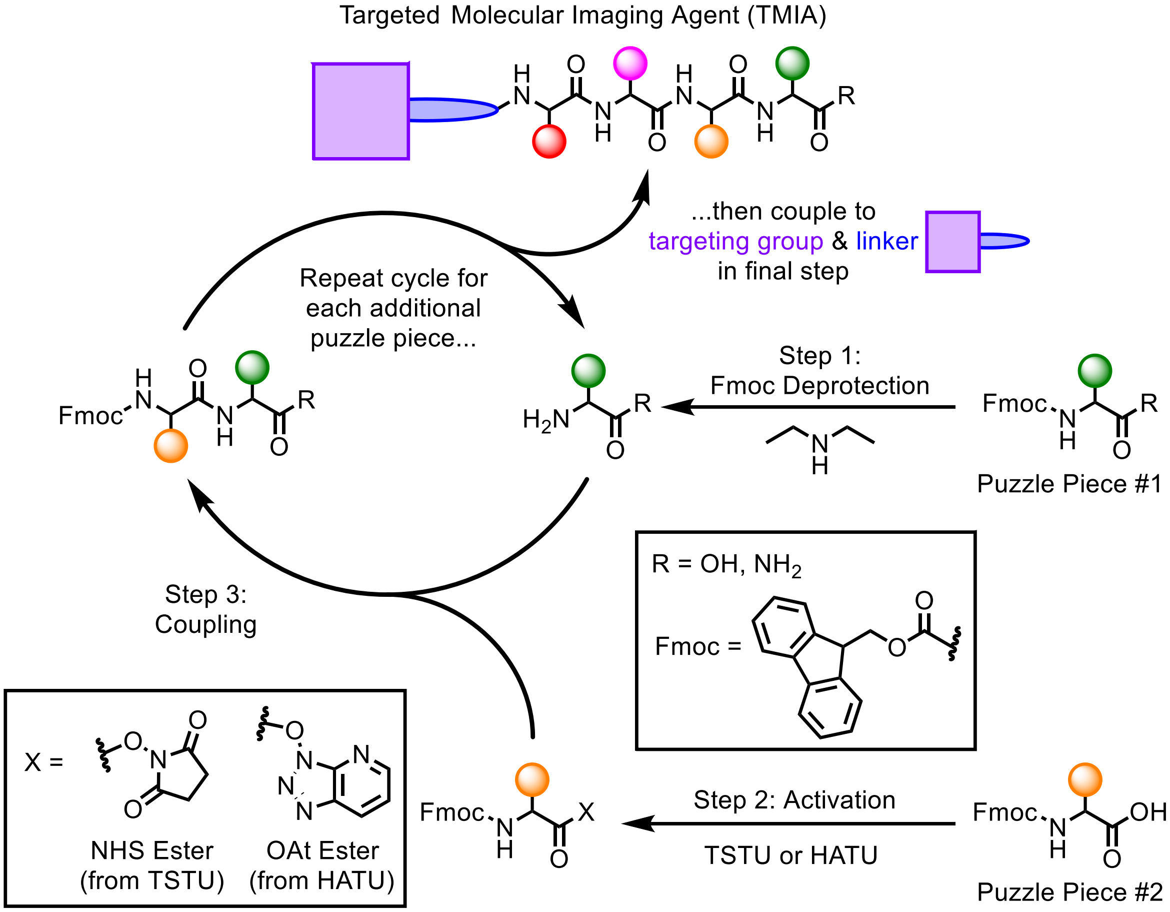

Figure 13: Synthetic cycle of the "puzzle piece" approach used for TMIAs.

This synthesis is linear, as amino acids are added onto the N-terminus of the existing peptide chain in a sequential manner. Since this method adds amino acids onto the N terminus of peptides, the carboxylic acid at the peptide C-terminus can be amidated to prevent side reactions. The purpose of the linker is to increase the separation between the amino acid puzzle pieces and the targeting agent. In addition, D-isomers of proteinogenic amino acids are used whenever they are not C-terminal carboxamides in order to ensure proteolytic stability.[52]

This synthesis design has the advantage of being fully modular, so a countless variety of TMIAs can be created. TMIAs can be “single-modal”, active in only one imaging method, or “dual-modal”, containing multiple puzzle pieces that are active in different imaging methods. This also allows for the easy tailoring of TMIAs towards specific types of cancers, since the targeting group is added in the final synthesis step. This modular puzzle-piece approach has been used by past group members to synthesize TMIAs and will be utilized in the TMIA syntheses presented in this study.

1.13 Past Students’ Work

Past students have created TMIAs that feature a variety of imaging agents and targeting groups. Imaging groups included near-infrared (NIR) dyes, DOTA-chelated radioligands for PET, and Gd-DOTA ligands; targeting groups have included DCL against prostate cancer receptors, cyclo(RGDyK) against lung and brain cancer receptors, and the 18-4 peptide against breast cancer receptors.[53–56] In these previously published studies, the MRI-active targeting module was a Gd-DOTA ligand coupled to the side chain of lysine, which is referred to as Lys(Gd-DOTA). The structures of this puzzle piece in C-terminal carboxamide form (with L-Lys) and C-terminal carboxylate form (with D-Lys) are shown in Figure 14. A key discovery enabling the synthesis of these Gd(III)-containing TMIAs was that Gd(III) acted as a protecting group for the carboxylate and amine ligands in DOTA by coordinating with them, preventing them from undergoing side reactions.[47]

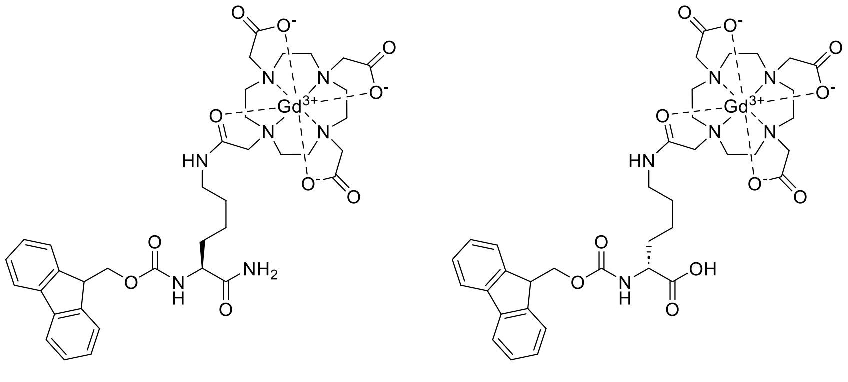

Fmoc-Lys(Gd-DOTA)-NH$_2$ Fmoc-D-Lys(Gd-DOTA)-OH

Figure 14: Lys(Gd-DOTA) puzzle pieces Fmoc-Lys(Gd-DOTA)-NH$_2$ and Fmoc-D-Lys(Gd-DOTA)-OH utilized in our group’s TMIAs.

Previous graduate students in the our research group have created TMIAs that contain both Lys(Gd-DOTA) and DCL in order to function in targeted MRI of prostate cancer. Kelsea Jones and Nicolas Schug synthesized single-modal and dual-modal TMIAs containing Lys(Gd-DOTA) puzzle pieces that contained DCL or cyclo(RGDyK) targeting groups, an example of which is shown in Figure 15.[53,55]

Schug's and earlier undergraduate research proved using CFM that the TMIAs were taken up by C42 prostate cancer cells through endocytosis.[53] Basant Kaur and Xinyu Xu demonstrated that conjugates of Lys(Gd-DOTA) and met-enkephalin or 18-4 could be entirely synthesized using solid-phase peptide synthesis, showing the synthetic versatility of the Lys(Gd-DOTA) puzzle piece.[54,56]

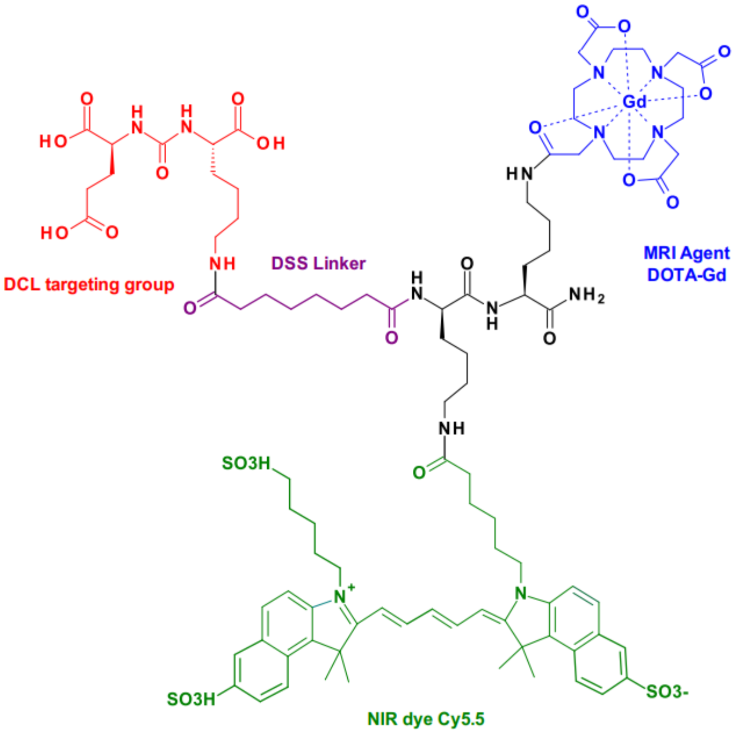

Figure 15: A dual-modal prostate cancer-targeted TMIA synthesized by Schug. The use of Lys(Gd-DOTA) and an NIR dye puzzle piece in the same molecule allows for a single molecule to participate in multiple imaging methods.[53]

1.14 Serendipitous Discovery of r_1 Increase from Fmoc & Tryptophan

In more recent work, graduate student Dana Soika utilized the Ala(Gd-DO3A) chelate first described by Boros et al (of the Peter Caravan group) in the synthesis of higher-relaxivity TMIAs. When used as part of larger peptides, as shown in Figure 16, a higher r_1 value (~8 $mM^{-1}s^{-1}$) than most commercially used MRI contrast agents (~4-5 $mM^{-1}s^{-1}$) at 1 T was achieved.[18] It was believed that by our group that this relaxivity increase was caused by Ala(Gd-DO3A) featuring a shortened side chain and chelation to the peptide backbone, raising τ_R as a result.

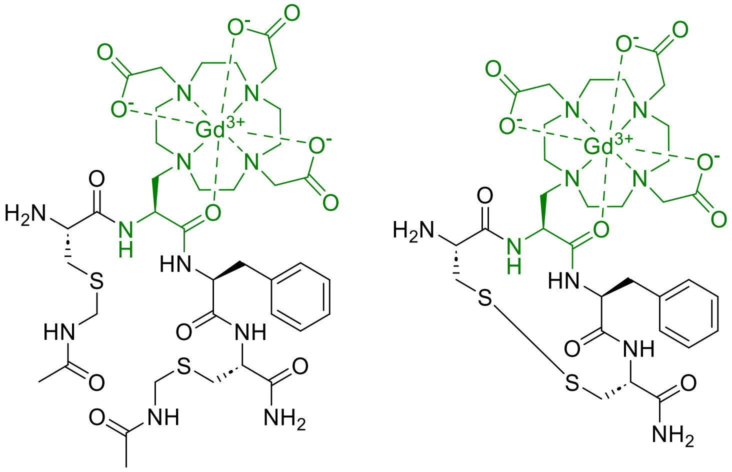

Figure 16: Peptides synthesized by Boros et al incorporating the Ala(Gd-DO3A) chelator (green) that demonstrated increased relaxivity at 1.0 T.[18]

In order to expedite synthesis, analysis, and purification, as well as to improve the design for better bioavailability, Soika's work also evaluated the effect of including tryptophan in the TMIAs, finding several benefits. By incorporating the D-isomer of tryptophan (D-Trp) as a spacer in-between the Ala(Gd-DO3A) and DCL-DSS modules as shown in Figure 17a, the overall size and mass of the TMIA was increased, which was expected to further raise both τ_R and r_1. In addition, the nonpolar side chain of tryptophan added lipophilicity, leading to easier couplings in the synthesis due to increased solubility in organic solvents. In another aspect, because the indole ring of tryptophan's side chain absorbs UV light, UV-Vis absorbance was also used in HPLC-MS to monitor the synthesis and purification of TMIAs and their intermediates.[57]

Moreover, as part of the fundamental design of these TMIAs, it was further hypothesized that the additional of tryptophan would also increase lipophilicity and thereby increase bioavailability by offering solubility in the body's hydrophobic tissues. In the prior reported TMIAs, the polarity as observed by HPLC retention time was exceptionally high, and the compounds were deemed too polar to be useful as imaging agents, as they would be excreted too rapidly.

Disappointingly, while the final DCL-DSS-conjugated targeted contrast agent was expected to have enhanced relaxivity from the Ala(Gd-DO3A) puzzle piece, the measurement of DCL-DSS-D-Trp-Ala(Gd-DO3A)-OH **(A)** yielded a nominal relaxivity of 6.0 ± 0.1 $mM^{-1}s^{-1}$, as shown in Figure 17b.

However, in an unpredicted and serendipitous observation, it was found that one synthetic intermediate, Fmoc-D-Trp-Ala(Gd-DO3A)-OH **(B)**, containing Fmoc-protected D-Trp attached to the N-terminus of Ala(Gd-DO3A), had a non-linear, bi-phasic increase in $1/T_1$ vs. concentration, as shown in Figure 17c. The relaxivity of **(B)** increased from 4.7 ± 0.2 $mM^{-1}s^{-1}$ at lower concentrations to 24.5 ± 1.2 $mM^{-1}s^{-1}$ at higher concentrations, above a threshold concentration of 1.79 mM.

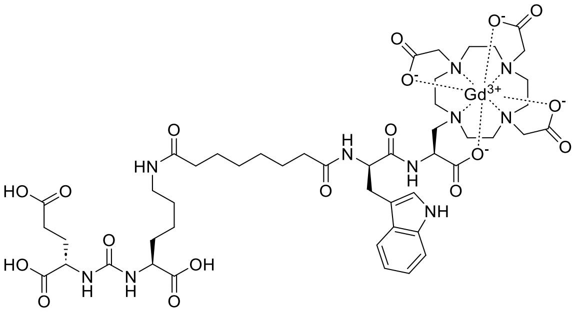
DCL-DSS-D-Trp-Ala(Gd-DO3A)-OH **(A)**

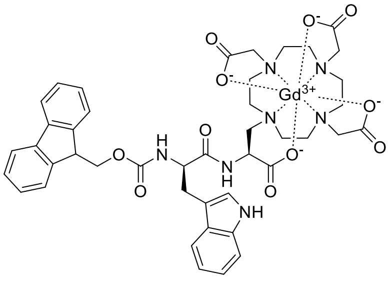
Fmoc-D-Trp-Ala(Gd-DO3A)-OH **(B)**

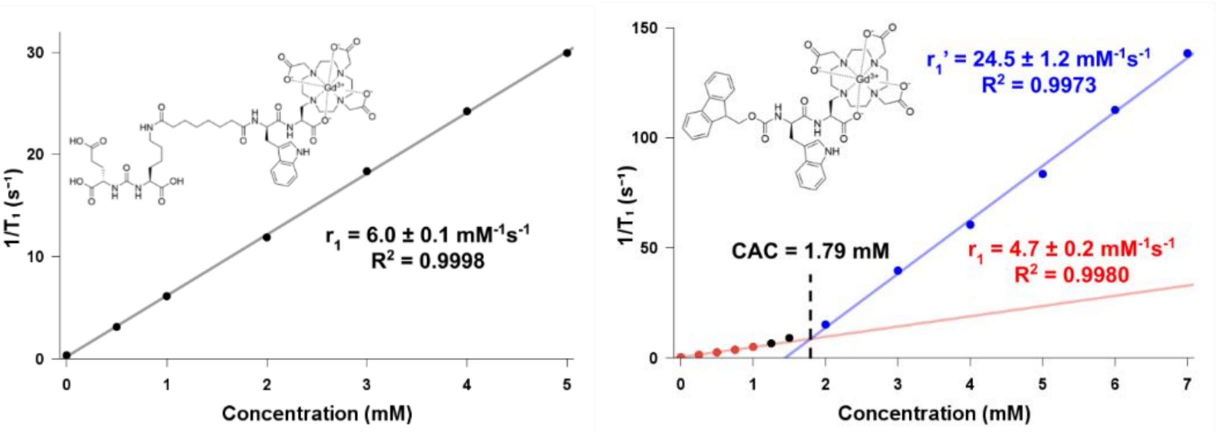

*Figures 17a-c: Structure of DCL-DSS-D-Trp-Ala(Gd-DO3A)-OH **(A)** and Fmoc-D-Trp-Ala(Gd-DO3A)-OH **(B)** (top) and 1/T1 vs. concentration graphs of **(A)** (bottom left) and serendipitous finding **(B)** (bottom right) in H_2O.*

The shape of this graph showed that Fmoc-D-Trp-Ala(Gd-DO3A)-OH **(B)** exhibited behavior that was not encountered in any of the previous compounds synthesized by our group. For this compound, the $1/T_1$ vs. concentration graph featured a linear region with a low slope at concentrations below 1 mM, a curved region with a gradually increasing slope between 1 and 2 mM, and another linear region with a much higher slope at concentrations above 2 mM. It is hypothesized that the likely cause of this relaxivity increase is intermolecular self-assembly driven by π-π interactions from the aromatic Fmoc and D-Trp groups, as the previously discussed MRI contrast agents featured aromatic substituents that induced self-assembly due to similar interactions.[33,34,51]

When describing such behavior of self-assembling compounds, r_1 indicates the slope of the linear trendline at low (non-self-assembling) concentrations, r_1' indicates the slope of the linear trendline at high (self-assembling) concentrations, and the CAC (critical aggregation concentration) indicates the concentration value at which these two trendlines intersect.

1.15 Synthetic Design of Self-Assembling High-Relaxivity TMIAs

Based on these unexpected findings, it was further hypothesized that the use of the shortened Ala(Gd-DO3A) was not the main cause of high-relaxivity in this case and that a relaxivity increase through self-assembly should be achievable using easier-to-synthesize lysine analogs. Therefore, despite the initial r_1 increase being originally reported for Fmoc-D-Trp-Ala(Gd-DO3A)-OH, Lys(Gd-DOTA) was chosen over Ala(Gd-DO3A) as the MRI-active puzzle piece for this project. Lys(Gd-DOTA) had an easier and newly optimized synthesis, requiring only one to three steps to synthesize instead of the six required for Ala(Gd-DO3A) (discussed more in detail in Section 2.1), as well as greater stability in acidic environments. Moreover, this enabled a wider range of molecular arrangements to be investigated, which would have been exceptionally difficult by the Ala(Gd-DO3A) method published earlier.

Three goals were established as part of this project. The first goal was to test the hypothesis that Fmoc and Trp could induce self-assembly in Lys(Gd-DOTA)-based compounds. As part of this goal, a variety of compounds were synthesized in order to test effects such as net charge and the relative stereochemistry and location of Fmoc, Trp, and Lys(Gd-DOTA) on self-assembly. The second goal was to investigate alternative motifs beyond Fmoc and Trp to induce self-assembly, including Cbz-protected Trp, two adjacent Trp residues, and other Fmoc-protected aromatic amino acids. The third goal was to utilize these findings to synthesize self-assembling TMIAs for both prostate cancer and breast cancer.

Table 3: Compounds and intermediates synthesized in this work.

Compound Number	**Compound Name**
1	Fmoc-Lys(Gd-DOTA)-OH
2	Fmoc-Lys(Gd-DOTA)-NH_2
3	H-Lys(Gd-DOTA)-NH_2
4*	Fmoc-D-Trp-Lys(Gd-DOTA)-NH_2
5*	H-D-Trp-Lys(Gd-DOTA)-NH_2
6*	Fmoc-Trp-Lys(Gd-DOTA)-NH_2
7	Fmoc-D-Lys(Gd-DOTA)-OH
8	H-D-Lys(Gd-DOTA)-OH
9*	Fmoc-D-Trp-D-Lys(Gd-DOTA)-OH
10	Fmoc-D-Lys(Gd-DOTA)-Lys(Gd-DOTA)-NH_2
11	H-D-Lys(Gd-DOTA)-Lys(Gd-DOTA)-NH_2
12*	Fmoc-D-Trp-D-Lys(Gd-DOTA)-Lys(Gd-DOTA)-NH_2
13*	Fmoc-D-Lys(Gd-DOTA)-D-Trp-Lys(Gd-DOTA)-NH_2
14	Fmoc-Dap(Mtt)-OH
15	Fmoc-Dap(Mtt)-D-Trp-Lys(Gd-DOTA)-NH_2
16*	Fmoc-Dap(H)-D-Trp-Lys(Gd-DOTA)-NH_2
17	Fmoc-Dap(Mtt)-Lys(Gd-DOTA)-NH_2
18	H-Dap(Mtt)-Lys(Gd-DOTA)-NH_2
19	Fmoc-D-Trp-Dap(Mtt)-Lys(Gd-DOTA)-NH_2
20*	Fmoc-D-Trp-Dap(H)-Lys(Gd-DOTA)-NH_2
21	Fmoc-Dap(Mtt)-NH_2
22	H-Dap(Mtt)-NH_2
23	Fmoc-D-Lys(Gd-DOTA)-Dap(Mtt)-NH_2

24	H-D-Lys(Gd-DOTA)-Dap(Mtt)-NH$_2$
25	Fmoc-D-Trp-D-Lys(Gd-DOTA)-Dap(Mtt)-NH$_2$
26*	Fmoc-D-Trp-D-Lys(Gd-DOTA)-Dap(H)-NH$_2$
27*	Cbz-D-Trp-Lys(Gd-DOTA)-NH$_2$
28*	Cbz-D-Trp-D-Lys(Gd-DOTA)-OH
29	Fmoc-D-Trp-D-Trp-Lys(Gd-DOTA)-NH$_2$
30	H-D-Trp-D-Trp-Lys(Gd-DOTA)-NH$_2$
31	DCL-DSS
32*	DCL-DSS-D-Trp-D-Trp-Lys(Gd-DOTA)-NH$_2$
33	Fmoc-D-Trp-NH$_2$
34	H-D-Trp-NH$_2$
35	Fmoc-D-Trp-D-Trp-NH$_2$
36	H-D-Trp-D-Trp-NH$_2$
37	Fmoc-D-Lys(Gd-DOTA)-D-Trp-D-Trp-NH$_2$
38	H-D-Lys(Gd-DOTA)-D-Trp-D-Trp-NH$_2$
39*	DCL-DSS-D-Lys(Gd-DOTA)-D-Trp-D-Trp-NH$_2$
40*	Fmoc-D-Phe-Lys(Gd-DOTA)-NH$_2$
41*	Fmoc-D-Tyr-Lys(Gd-DOTA)-NH$_2$
42*	Fmoc-D-Trp-D-Lys(Gd-DOTA)-Dap(DCL-DSS)-NH$_2$
43	H-PEG8-COOH
44*	Fmoc-D-Trp-D-Lys(Gd-DOTA)-PEG8-COOH
45	DCL
46*	Fmoc-D-Trp-D-Lys(Gd-DOTA)-PEG8-DCL
47	Fmoc-D-Trp-D-Lys(Gd-DOTA)-PEG8-18-4

*Relaxivity values measured in this work

2. Results and Discussion

2.1 Optimization of the One-Pot Puzzle Piece Synthesis

A major initial hurdle was the difficulty in the synthesis of the Lys(Gd-DOTA) puzzle pieces. The synthesis of Fmoc-Lys(Gd-DOTA)-NH_2 **(2)** and Fmoc-D-Lys(Gd-DOTA)-OH **(7)** was previously developed by prior group members via a one-pot coupling reaction between Fmoc-Lys-NH_2 or Fmoc-D-Lys-OH and DOTA using TSTU as a coupling agent. This reaction was carried out in DMF, with metalation using $Gd(OAc)_3$ in the final step. This was reported by our group to be an important advancement at the time versus prior literature methods which had required exceptionally expensive tri-tert-butyl-protected and mono-activated DOTA, and allowed the synthesis of useful 200 mg quantities. However, the approach still had disadvantages, including a large volume of solvent required (~50 mL per 500 mg DOTA) and a pre-heating step to 70°C to help suspend the DOTA due to the poor solubility of DOTA in DMF, the requirement of an inert atmosphere, and a slow addition of TSTU and Fmoc-Lys-NH_2 or Fmoc-D-Lys-OH via syringe pump. The large volume of solvent required also made workup difficult, as the DMF could only be removed via rotary evaporation with the aid of an external vacuum pump and heating. Further disadvantage came from the reaction's poor yield (28% for **(2)** and 24% for **(7)**), which bottlenecked the synthesis of further derivatives.[58]

To address these shortcomings, an improved one-pot procedure was developed. Fmoc-Lys(Gd-DOTA)-OH **(1)** and Fmoc-D-Lys(Gd-DOTA)-OH **(7)** were synthesized from DOTA, $Gd(OAc)_3$, and Fmoc-Lys-OH•HCl (for **(1)**) or Fmoc-D-Lys-OH•HCl (for **(7)**) as shown in Scheme 1. The coupling agent was changed to EDC/NHS and the solvent was changed to an aqueous-based H_2O/MeOH mixture, which DOTA was completely soluble in. One downside of this approach was incomplete activation of DOTA despite using an excess of EDC (1.5 eq.) and NHS (1.2 eq.) as shown in Figures 18a and 18b, which was seen via LCMS of a small aliquot of the crude reaction mixture quenched using 0.1% butylamine in acetonitrile. Despite this, the reaction still proceeded with improved yields (39% for **(1)** and 54% for **(7)**) without requiring an inert atmosphere, pre-heating, or slow addition.

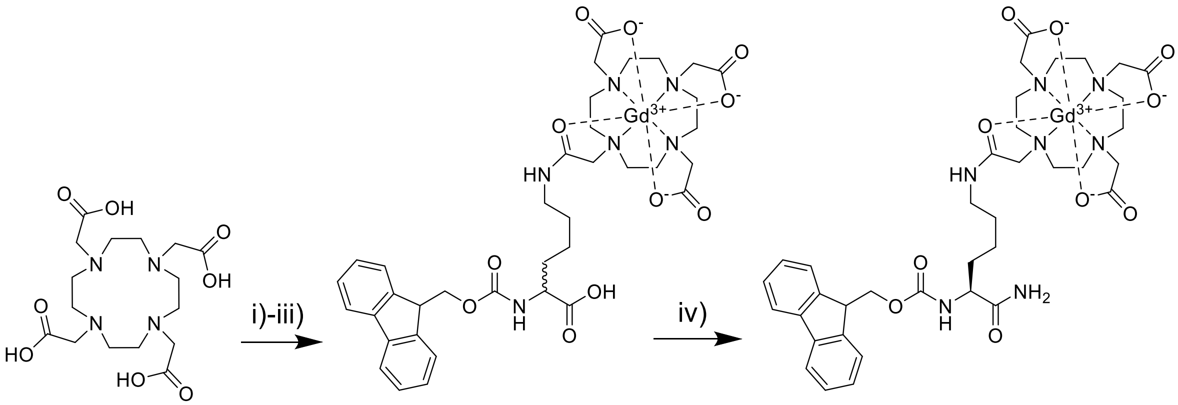

DOTA

Fmoc-Lys(Gd-DOTA)-OH **(1)**: 39%
Fmoc-D-Lys(Gd-DOTA)-OH **(7)**: 54%

Fmoc-Lys(Gd-DOTA)-NH$_2$ **(2)**
(from **(1)**)

Scheme 1: Improved one-pot synthesis of Fmoc-Lys(Gd-DOTA)-OH ***(1)*** *and Fmoc-D-Lys(Gd-DOTA)-OH* ***(7)*** *and amidation of* ***(1)*** *to form Fmoc-Lys(Gd-DOTA)-NH$_2$* ***(2)***. *i) EDC, NHS, TEA in H_2O; ii) Fmoc-L-Lys-OH•HCl (for* ***(1)****) or Fmoc-D-Lys-OH•HCl (for* ***(7)****), TEA, MeOH; iii) $Gd(OAc)_3$, MeOH; iv) NH_3 (aq), DIPEA, and HATU in DMF.*

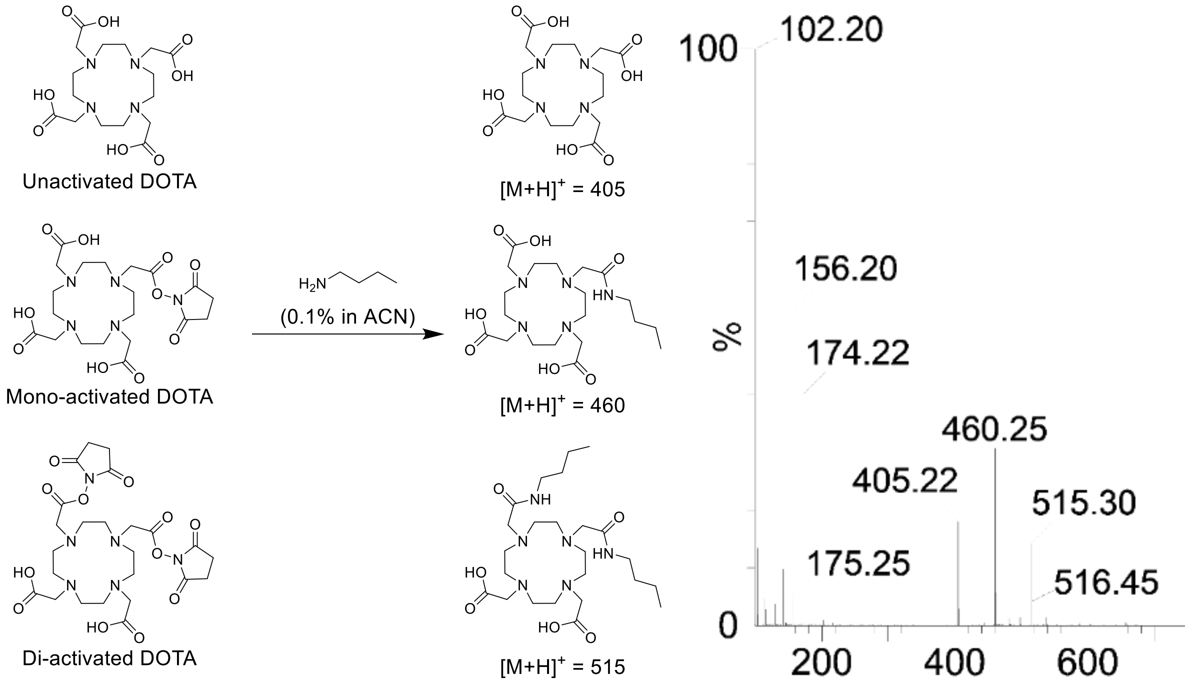

Figures 18a-b: Butyl-amidated derivatives of DOTA-NHS esters stable under MS conditions (left), and MS spectrum showing the 1:2:1 ratio of unactivated:mono-activated:di-activated DOTA using EDC/NHS after 60 minutes (right)

To form the C-terminal amide, **(1)** was then converted to Fmoc-Lys(Gd-DOTA)-NH$_2$ **(2)** by amidating the C-terminal carboxylate using HATU and aqueous ammonia. This new approach to synthesize **(2)** also required one fewer step than the previous synthesis, which began with the amidation of Fmoc-Lys(Boc)-OH, followed by Boc deprotection, prior to the one-pot coupling with DOTA.[58]

2.2 Dipeptide Compounds with Fmoc & Tryptophan

The first goal of this project was to confirm that the high-relaxivity of **(B)** applied to Lys(Gd-DOTA)-based analogues. This was tested by synthesizing dipeptides Fmoc-D-Trp-Lys(Gd-DOTA)-NH_2 **(4)**, Fmoc-Trp-Lys(Gd-DOTA)-NH_2 **(6)**, and Fmoc D-Trp-D-Lys(Gd-DOTA)-OH **(9)**. These compounds were synthesized using a standard solution-phase approach as shown in Scheme 2, in which Fmoc-Lys(Gd-DOTA)-NH_2 **(2)** and Fmoc-D-Lys(Gd-DOTA)-OH **(6)** were first deprotected followed by coupling to Fmoc-D-Trp-OH or Fmoc-L-Trp-OH using HATU. In order to induce self-assembly, the Fmoc groups were retained on the N-termini of the resulting compounds.

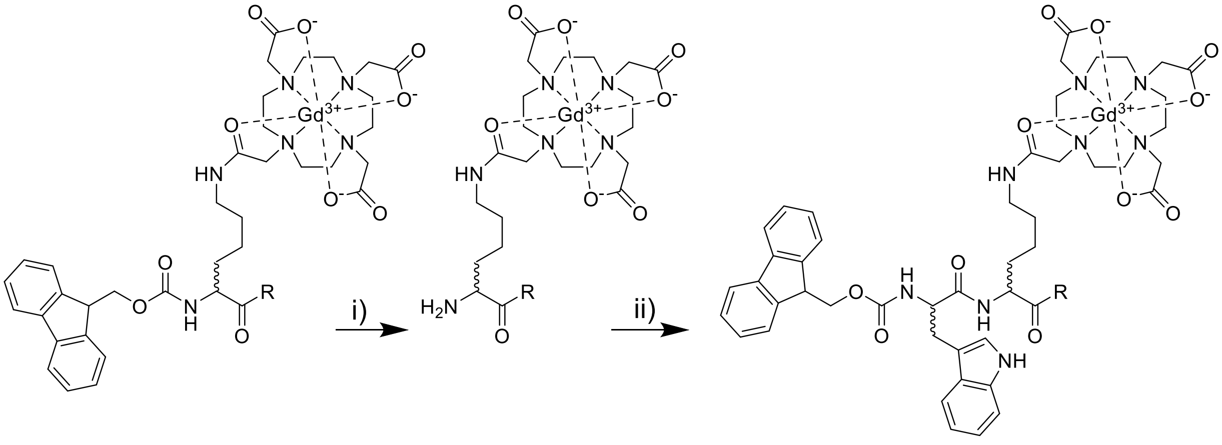

(2): R = NH_2
(7): R = OH

(3): R = NH_2
(8): R = OH

(4 and 6): R = NH_2
(9): R = OH

*Scheme 2: Synthesis of self-assembling MRI contrast agents Fmoc-D-Trp-Lys(Gd-DOTA)-NH_2 **(4)**, Fmoc-D-Trp-Lys(Gd-DOTA)-NH_2 **(6)**, and Fmoc-D-Trp-D-Lys(Gd-DOTA)-OH **(9)**. i) DEA, DMF; ii) Fmoc-D-Trp-OH or Fmoc-L-Trp-OH, HATU, DIPEA, DMF. Lysines are L-Lys when R = NH_2 **(2-4)** and **(6)** and D-Lys when R = OH **(7-9)**, and tryptophans are D-Trp for **(4)** and **(9)** and L-Trp for **(6)**.*

As seen in Table 4, the r_1 values measured for **(4)** and **(9)** (in their non-self-assembled states) in H_2O were 3.5 ± 0.4 and 5.0 ± 0.2 $mM^{-1}s^{-1}$ respectively. In comparison, the r_1' values for **(4)** and **(9)** (in their self-assembled state) in H_2O were markedly higher, measured to be 14.9 ± 1.0 and 14.1 ± 0.5 $mM^{-1}s^{-1}$ respectively. The measured CACs for **(4)** and **(9)** were 0.35 and 2.59 mM respectively indicating an important decrease for the C-terminal amide versus acid.

To confirm that both Fmoc and D-Trp are required to cause self-assembly, the r_1 of H-D-Trp-Lys(Gd-DOTA)-NH_2 **(5)**, which lacks Fmoc, was also measured in H_2O. In addition, Fmoc-Lys(Gd-DOTA)-NH_2 **(2)** and commercially sourced Gd-DOTA (Dotarem), were similarly found to not self-assemble in H_2O at concentrations up to 5 mM, as seen in Table 4 and Figure 19a.

The effect of using phosphate-buffered saline (PBS) in place of H_2O was then tested, due to the possible influence of various buffer systems on self-assembly. This change resulted in roughly halving the CAC of **(4)** and **(9)** without significantly affecting the r_1 or r_1' values. This is consistent with the behavior of self-assembling compounds, as increasing ionic strength has been shown to trigger peptide self-assembly.[59]

The effect of varying the stereochemistry of Trp was then tested by measuring the relaxivity of Fmoc-Trp-Lys(Gd-DOTA)-NH_2 **(6)**, which incorporates the L-isomer of Trp rather than the D-isomer of Trp found in **(4)**. This compound was also found to self-assemble in PBS, with a CAC of 0.35 mM. This finding shows that the relative stereochemistry of Trp and Lys(Gd-DOTA) does not affect self-assembly. This is important for the design of biologically-active probes, as site-specific substitutions of D-amino acids have been shown to increase proteolytic stability in short targeting peptides.[60]

Although PBS matches the pH and ion concentration of the human body (pH 7.4), a closer match to human blood is fetal bovine serum (FBS), as it is a biologically derived material. The r_1 relaxivity of Gd-DTPA at 0.94 T was previously reported to increase from 3.4 $mM^{-1}s^{-1}$ in water to 4.1 $mM^{-1}s^{-1}$ in FBS, which was attributed to the increased viscosity of FBS compared to water.[61,62] This r_1 increase in FBS is therefore due to an increase in τ_R as a result of higher viscosity, which slows molecular rotation. Similarly, τ_R values of a BODIPY derivative in methanol-glycerol mixtures were previously found to be higher with increased proportions of glycerol, which is more viscous than methanol.[63]

For compounds that did not self-assemble in H_2O, such as Gd-DOTA, relaxivity values in FBS were found to modestly increase compared to H_2O, as shown in Figures 19a and 19b. The relaxivity value of Gd-DOTA increased from 4.13 ± 0.05 $mM^{-1}s^{-1}$ in H_2O to 5.00 ± 0.07 $mM^{-1}s^{-1}$ in FBS, likely due to the increase in solvent viscosity in FBS compared to H_2O.

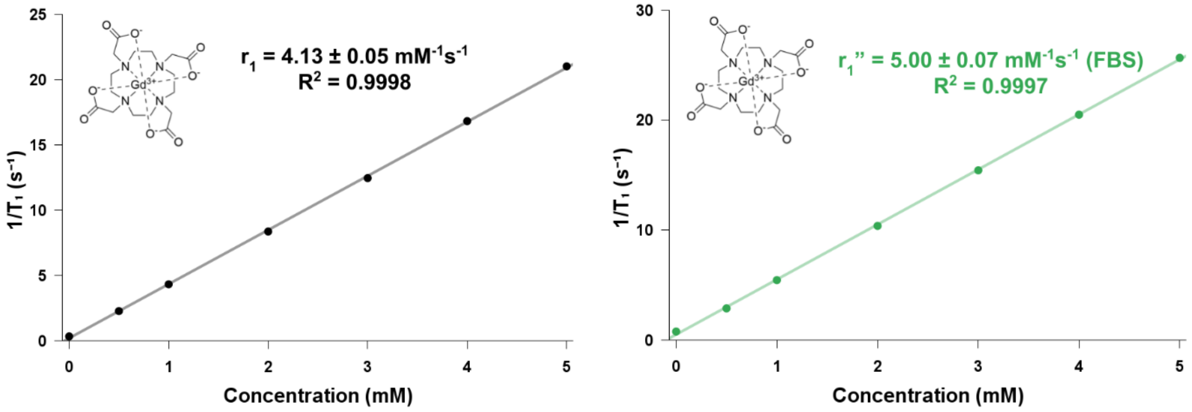

Figures 19a-b: $1/T_1$ vs. concentration graphs for Gd-DOTA in H_2O (left) and FBS (right)

Turning to the lysine-based compounds that were intentionally designed for self-assembly, the relaxivity values of Fmoc-D-Trp-Lys(Gd-DOTA)-NH_2 **(4)** were first measured in H_2O and PBS, (as shown in Figure 20a-b). In these two solvents, bi-phasic curves were observed just as in the original observation of Fmoc-D-Trp-Ala(Gd-DO3A)-OH **(B)** shown in Figure 17c. with a low relaxivity region (r_1 = ~3-7 $mM^{-1}s^{-1}$) and a high relaxivity region (r_1' = ~13-17 $mM^{-1}s^{-1}$).

It was later decided to test **(4)** in the more biologically relevant solvent, FBS, where the relaxivity was measured to be ~11-13 $mM^{-1}s^{-1}$. As shown in Figure 20c, These values were two to three times higher than the compounds' non-self-assembled r_1 values in H_2O and PBS (~3-7 $mM^{-1}s^{-1}$), but somewhat lower than the self-assembled r_1' values in H_2O and PBS (~13-17 $mM^{-1}s^{-1}$).

Surprisingly, as shown in Figure 20c, a remarkable lowering of the CAC occurred in FBS versus H_2O and PBS. The curve of $1/T_1$ with respect to concentration for all concentrations measured in FBS was also found to be linear, even at the smallest measured concentration of 0.025 mM. Since this relaxivity behavior did not match the findings of non-self-assembled or self-assembled compounds in H_2O or PBS, it was decided to refer to the measured relaxivity in FBS as r_1". While the modest increase in relaxivity has been reported in the literature as described above, this appears to be the first time a lowering of CAC by the use of FBS has been observed, while still maintaining close to the same higher relaxivity (two-to-three-fold) of the self-assembled MRI contrast agent.

In Figure 20c, it is worth noting that the concentration range measured in FBS is in the narrower range of 0.025 to 0.1 mM. This range was chosen as the biologically relevant range that would be utilized for a non-targeted contrast agent in the clinic, and because we wished to see if there would be a non-self assembling region (r). Such a region was not found. An attempt was made to study sub-0.025 mM concentrations, but the limit of quantitative solution preparation, combined with the very weak signal in this range, resulted in unreliable data at these low concentrations.

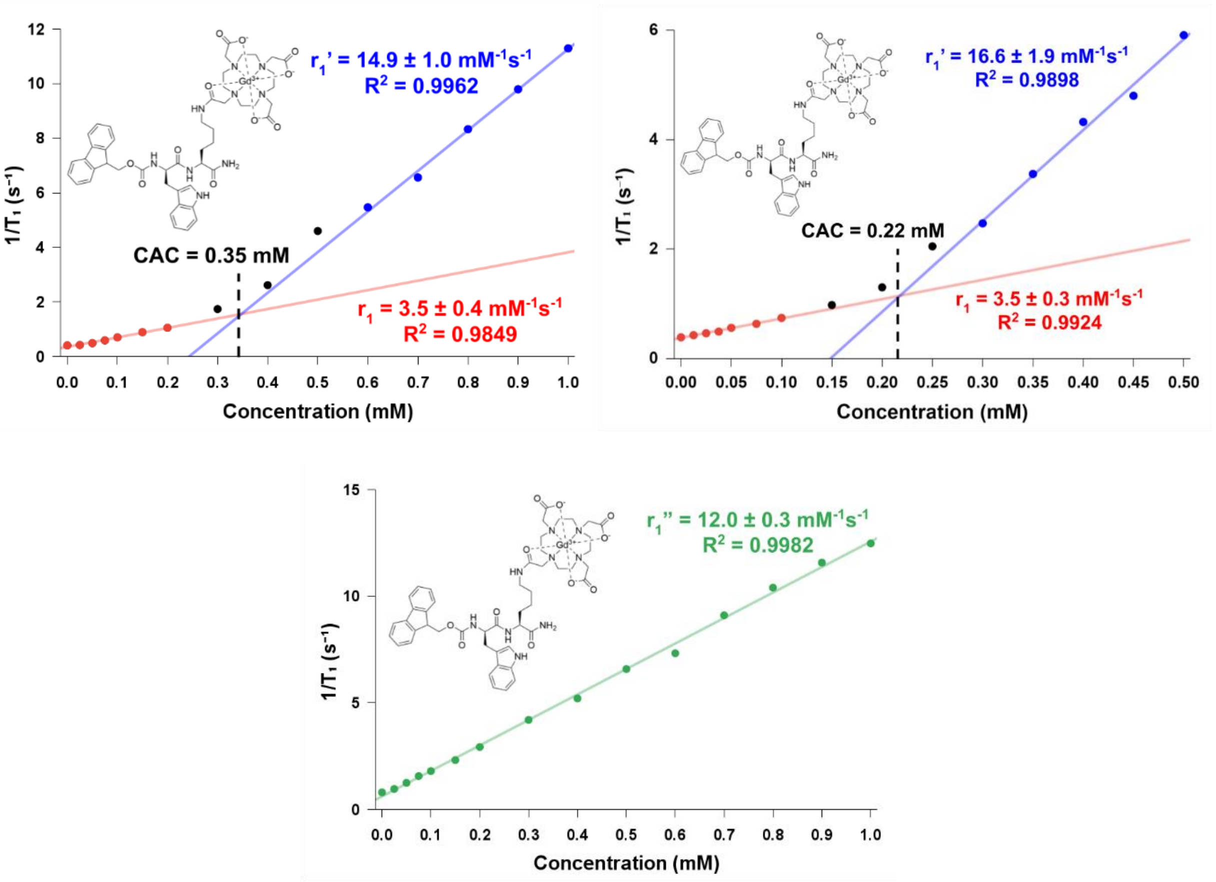

Figures 20a-c: 1/T_1 vs. concentration graphs for Fmoc-D-Trp-Lys(Gd-DOTA)-NH_2 in H_2O (top left), PBS (top right), and FBS (bottom)

Measurement of Fmoc-D-Trp-D-Lys(Gd-DOTA)-OH **(9)** yielded similar results, with r_1, r_1' of 5.0 ± 0.2/4.9 ± 0.2 $mM^{-1}s^{-1}$ and 14.1 ± 0.5/13.2 ± 0.2 $mM^{-1}s^{-1}$, in H_2O/PBS respectively with CAC values of 2.59/1.4 mM in H_2O/PBS respectively. The r_1" value in FBS was measured to be 13.0 ± 0.2 $mM^{-1}s^{-1}$ as shown in Figure 21c. A comparison of r_1, r_1', CAC, and r_1" values from these key intermediates in water, PBS, and FBS are shown in Table 4.

Based on these results, it is unclear if compounds that were found to self-assemble in H_2O and PBS also self-assemble in FBS. Based on the similar values in r' in water and PBS and r'' in FBS, it is most likely that the compounds also self-assemble in FBS, but that the FBS has a profound effect on the CAC. Although it is also possible that the increased relaxivity values could stem from the increase in solvent viscosity of FBS alone, the magnitude of increase would not be so large without self-assembly.

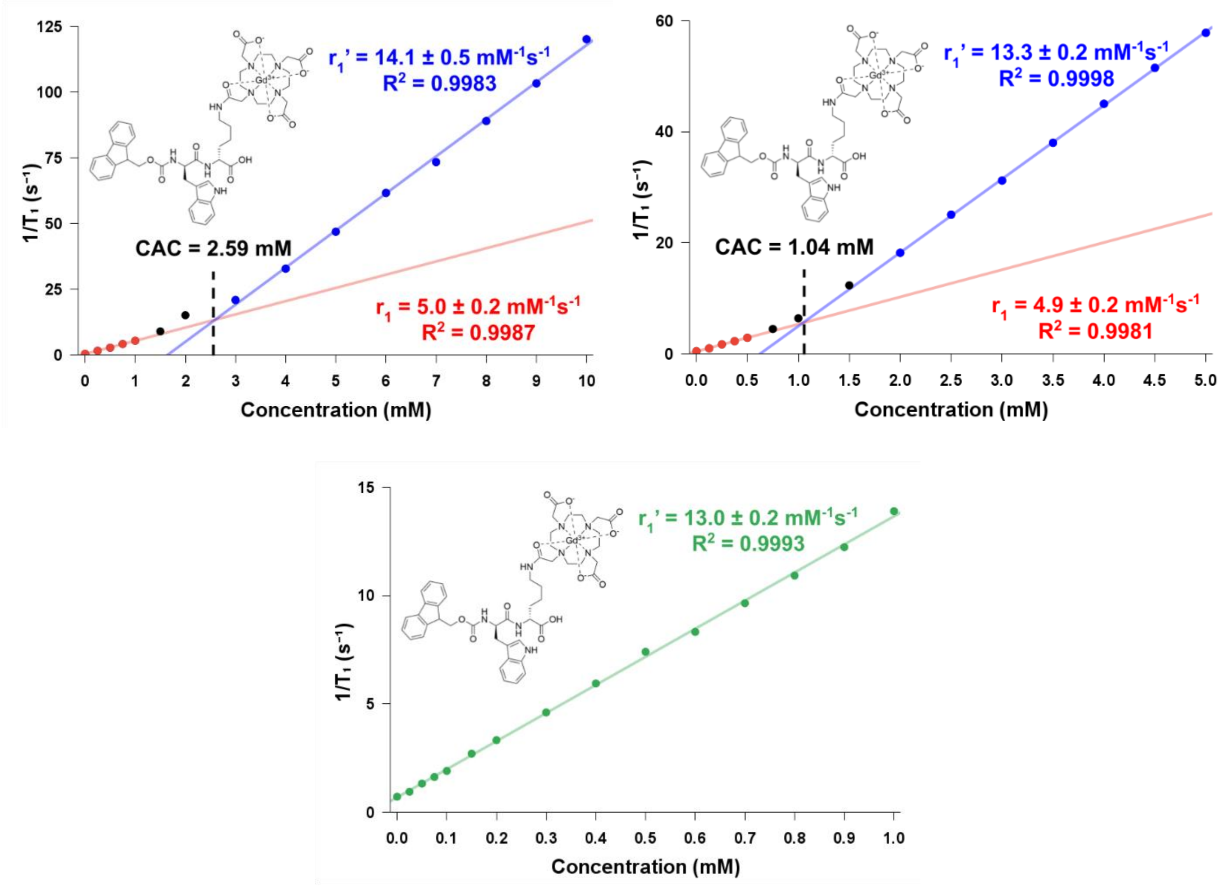

Figures 21a-c: 1/T_1 vs. concentration graphs for Fmoc-D-Trp-D-Lys(Gd-DOTA)-OH in H_2O (top left), PBS (top right), and FBS (bottom)

The comparisons between r_1, r_1', CAC, and r_1" values in water, PBS, and FBS are shown in Table 4. It is also important to understand that in the timeline of this work, the results in FBS were only discovered after all of the compounds in the following sections were synthesized, and after the relaxivity measurements of those compounds were completed. Thus, for the compounds in the remaining sections below that were synthesized to study the effect of structure on self-assembly, the comparisons were carried out in H_2O and PBS. However, all final targeted contrast agents (TMIAs) were measured in FBS.

Table 4:Comparison of r_1, r_1', CAC, and r_1" values in water, PBS, and FBS, of Fmoc-D-Trp-Lys(Gd-DOTA)-NH_2 ***(4)****, Fmoc-Trp-Lys(Gd-DOTA)-NH_2* ***(6)****, Fmoc-D-Trp-D-Lys(Gd-DOTA)-OH* ***(9)****, H-D-Trp-Lys(Gd-DOTA)-NH2* ***(5)****, Fmoc-Lys(Gd-DOTA)-NH2* ***(2)****, and Gd-DOTA (Dotarem)*

Compound	Solution	Non-self-assembled r_1 ($mM^{-1}s^{-1}$) (95% CI)	Self-assembled r_1' ($mM^{-1}s^{-1}$) (95% CI)	CAC (mM)	r_1" values in FBS ($mM^{-1}s^{-1}$) (95% CI)
Fmoc-D-Trp-Lys(Gd-DOTA)-NH_2 **(4)**	H_2O	3.5 ± 0.4	14.9 ± 1.0	0.35	-
	PBS	3.5 ± 0.3	16.6 ± 1.9	0.22	-
	FBS	-	-	-	12.0 ± 0.3
Fmoc-D-Trp-D-Lys(Gd-DOTA)-OH **(9)**	H_2O	5.0 ± 0.2	14.1 ± 0.5	2.59	-
	PBS	4.9 ± 0.2	13.2 ± 0.2	1.04	-
	FBS	-	-	-	13.0 ± 0.2
Fmoc-Trp-Lys(Gd-DOTA)-NH_2 **(6)**	PBS	4.5 ± 0.2	15.0 ± 0.7	0.35	-
H-D-Trp-Lys(Gd-DOTA)-NH_2 **(5)**	H_2O	4.8 ± 0.1	-	-	-
Fmoc-Lys(Gd-DOTA)-NH_2 **(2)**	H_2O	4.95[47]	-	-	-
	FBS	-	-	-	8.8 ± 0.2
Gd-DOTA (Dotarem)	H_2O	4.13 ± 0.05	-	-	-
	FBS	-	-	-	5.00 ± 0.07

2.3 Tripeptide Compounds with Fmoc & Tryptophan

The relative location of Fmoc and Trp on self-assembly was next evaluated, as the distance between Fmoc and Trp within a compound could affect the optimal orientation and overall favorability of self-assembly. In order to test this, two di-Gd(III) tripeptides, Fmoc-D-Trp-D-Lys(Gd-DOTA)-Lys(Gd-DOTA)-NH_2 **(12)** and Fmoc-D-Lys(Gd-DOTA)-D-Trp-Lys(Gd-DOTA)-NH_2 **(13)**, as shown in Figure 18, were synthesized. Like **(4)** and **(8)**, **(12)** features Fmoc and D-Trp adjacent to each other whereas **(13)** features Fmoc and D-Trp separated by a D-Lys residue.

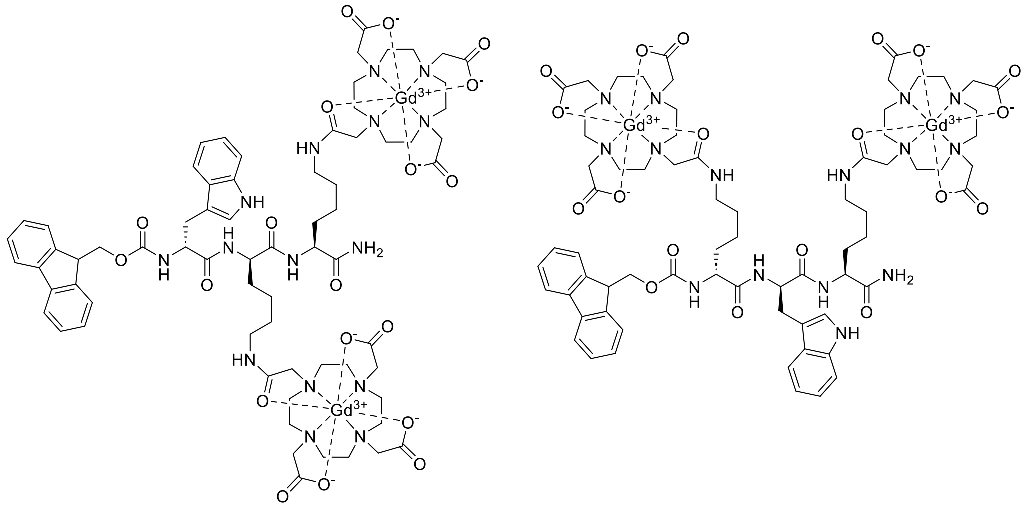

(12) **(13)**

Figure 22: Di-Gd(III) tripeptides Fmoc-D-Lys(Gd-DOTA)-D-Trp-Lys(Gd-DOTA)-NH_2 ***(12)*** *and Fmoc-D-Trp-D-Lys(Gd-DOTA)-Lys(Gd-DOTA)-NH_2* ***(13)****.*

As shown in Table 5 and Figures 23a and 23b, both compounds were found to self-assemble in PBS, with r_1 and r_1' values roughly twice that of the other mono-Gd(III) compounds. The r_1 values of **(12)** and **(13)** in PBS were comparable to the previously reported r_1 value for **(10)** in H_2O, which does not self-assemble in H_2O below 5 mM.

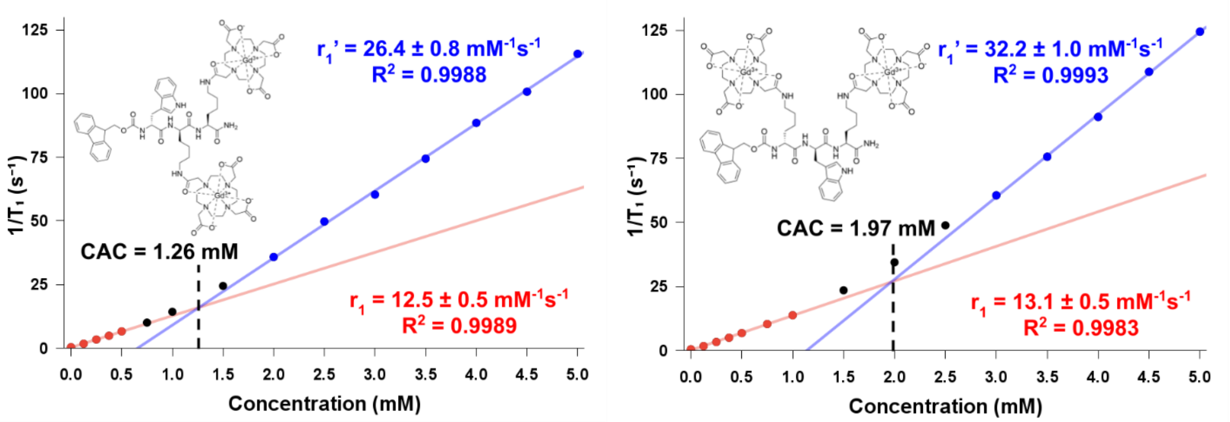

Figures 23a-b: 1/T_1 vs. concentration graphs of Fmoc-D-Lys(Gd-DOTA)-D-Trp-Lys(Gd-DOTA)-NH_2 ***(12)*** *(left) and Fmoc-D-Trp-D-Lys(Gd-DOTA)-Lys(Gd-DOTA)-NH_2* ***(13)*** *(right) in PBS.*

Table 5: r_1, r_1', and CAC values for Fmoc-D-Lys(Gd-DOTA)-D-Trp-Lys(Gd-DOTA)-NH_2 ***(12)****, Fmoc-D-Trp-D-Lys(Gd-DOTA)-Lys(Gd-DOTA)-NH_2* ***(13)****, and Fmoc-D-Lys(Gd-DOTA)-Lys(Gd-DOTA)-NH_2* ***(10)****, as measured in H_2O and PBS.*

Compound	Solution	Non-self-assembled r_1 ($mM^{-1}s^{-1}$) (95% CI)	Self-assembled r_1' ($mM^{-1}s^{-1}$) (95% CI)	CAC (mM)
Fmoc-D-Trp-D-Lys(Gd-DOTA)-Lys(Gd-DOTA)-NH_2 **(12)**	PBS	12.5 ± 0.5 (6.2 ± 0.2 per Gd(III))	26.4 ± 0.8 (13.2 ± 0.4 per Gd(III))	1.26
Fmoc-D-Lys(Gd-DOTA)-D-Trp-D-Lys(Gd-DOTA)-NH_2 **(13)**	PBS	13.1 ± 0.5 (6.8 ± 0.2 per Gd(III))	32.2 ± 1.0 (16.1 ± 0.5 per Gd(III))	1.97
Fmoc-D-Lys(Gd-DOTA)-Lys(Gd-DOTA)-NH_2 **(10)**	H_2O	11.33 (5.67 per Gd(III)[47]	-	-

Although **(12)** has a neutral charge and features Fmoc adjacent to D-Trp as in **(4)**, its CAC in PBS is still much higher than **(4)** (1.26 mM vs. 0.22 mM). This increase could be due to increased intramolecular electrostatic repulsion that hinders self-assembly due to the negatively charged pendant acetate groups on adjacent Lys(Gd-DOTA) residues. The CAC in PBS of **(13)** was also found to be higher than **(12)** (1.97 mM vs. 1.26 mM), as seen in Figures 23a and 23b, showing that Fmoc adjacent to D-Trp induces self-assembly at lower concentrations than Fmoc and D-Trp located one amino acid residue apart. Although **(12)** and **(13)** were found to self-assemble in PBS, they do not have an attachment point for DCL-DSS and therefore cannot be taken forward to make PSMA-targeted MRI contrast agents.

2.4 Mono-Gd(III) Dipeptides with Fmoc, Tryptophan, and Dap Linkers

With the discovery of relaxivity enhancement from Fmoc and Trp, a new problem presented itself. In the previously reported targeted imaging agent syntheses, the targeting group and/or linker were located at the peptide N-terminus.[47,52,58] Since the Fmoc group needed to be retained at the peptide N-terminus to induce self-assembly in **(4)**, **(6)**, **(9)**, **(12)**, and **(13)**, a new point of attachment was needed for DCL-DSS. A strategy was therefore designed in which an (S)-2,3-diaminopropionic acid (Dap) linker, shown in Figure 24, was used in the synthesis to allow DCL-DSS to be attached to the primary amine on its side chain. The Dap side chain amine was protected with the 4-methyltrityl (Mtt) protecting group prior to incorporation in the synthesis. Moreover, it was possible to remove Mtt using 1% TFA in DCM without resulting in Gd(III) demetallation.

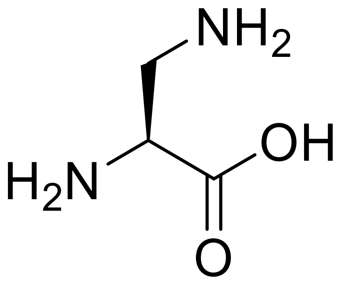

Figure 24: (S)-2,3-diaminopropionic acid (Dap), used as a linker for DCL-DSS.

Using a similar strategy, a series of three non-targeted mono-Gd(III) tripeptides, Fmoc-Dap(H)-D-Trp-Lys(Gd-DOTA)-NH_2 **(13)**, Fmoc-Dap(H)-D-Trp-Lys(Gd-DOTA)-NH_2 **(18)**, and Fmoc-D-Trp-D-Lys(Gd-DOTA)-Dap(H)-NH_2 **(26)**, whose structures are shown in Figure 25, were synthesized. In these compounds, the relative position of Dap relative to Fmoc, D-Trp, and Lys(Gd-DOTA) was varied in order to determine their effect on self-assembly.

To carry out the synthesis, the previously described modular synthetic approach was utilized, where the peptide chain was synthesized through repeated Fmoc deprotection and carboxylic acid activation and coupling of a second Fmoc-protected amino acid. The Mtt group was then deprotected after the entire peptide chain was formed, revealing a free amine to which DCL-DSS could be conjugated in order to create a PSMA-targeted MRI contrast agent.

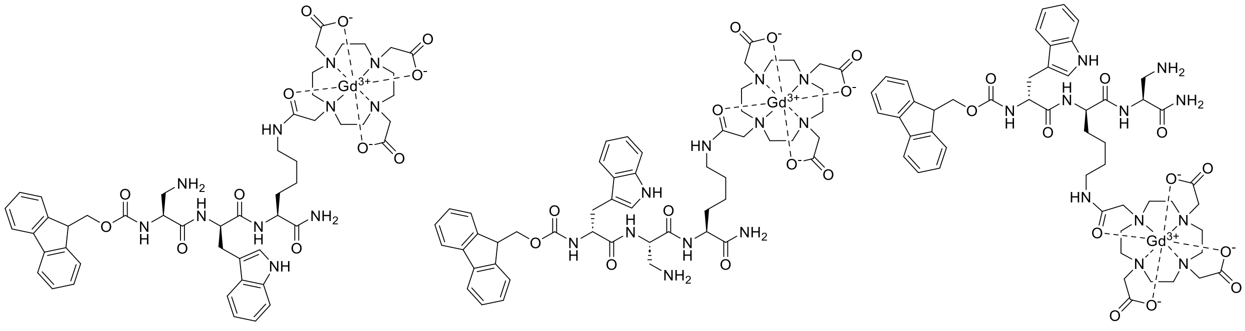

(16) **(20)** **(26)**

*Figure 25: Fmoc-Dap(H)-D-Trp-Lys(Gd-DOTA)-NH_2 **(16)**, Fmoc-Dap(H)-D-Trp-Lys(Gd-DOTA)-NH_2 **(20)**, and Fmoc-D-Trp-D-Lys(Gd-DOTA)-Dap(H)-NH_2 **(26)**.*

As portrayed in Figure 25, the tripeptides **(16)**, **(20)**, and **(26)**, were designed and synthesized to test the spatial impact of moving the amino acid spacer and linker Dap along the peptide chain. It was found that only **(20)** and **(26)** were found to self-assemble in H_2O, as shown in Table 6. These results are consistent with the results for **(12)** and **(13)** in PBS, showing that self-assembly is more effective when Fmoc is located on the N-terminus of D-Trp rather than separated by additional amino acids.

However, **(16)** was insoluble in PBS at a concentration of 5 mM, so its relaxivity and self-assembly behavior could not be determined. Despite this, compounds **(20)** and **(26)** were soluble in both H_2O and PBS at concentrations of 5 mM or higher and were found to self-assemble in both solvents with similar r_1, r_1', and CAC values, as shown in Figures 28a-c and Table 6.

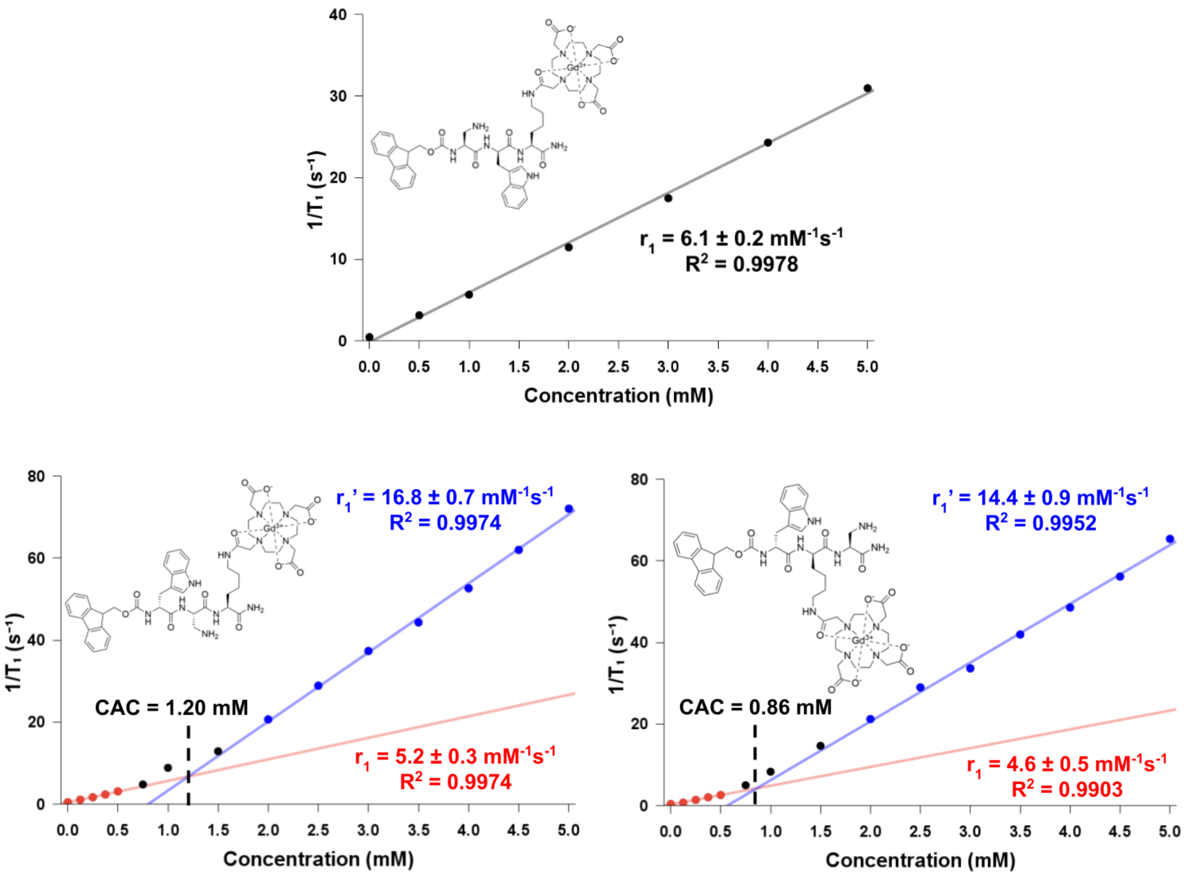

Figures 26a-c: 1/T_1 vs. concentration graphs of Fmoc-Dap(H)-D-Trp-Lys(Gd-DOTA)-NH_2 ***(16)*** *(top) in H_2O and Fmoc-Dap(H)-D-Trp-Lys(Gd-DOTA)-NH_2* ***(20)*** *(bottom left) and Fmoc-D-Trp-D-Lys(Gd-DOTA)-Dap(H)-NH_2* ***(26)*** *(bottom right) in PBS.*

Table 6: r_1, r_1', and CAC values of Fmoc-Dap(H)-D-Trp-D-Lys(Gd-DOTA)-NH_2 ***(16)****, Fmoc-D-Trp-Dap(H)-D-Lys(Gd-DOTA)-NH_2* ***(20)****, and Fmoc-D-Trp-Dap(H)-NH_2* ***(26)****, as measured in H_2O and PBS.*

Compound	Solution	Non-self-assembled r_1 ($mM^{-1}s^{-1}$) (95% CI)	Self-assembled r_1' ($mM^{-1}s^{-1}$) (95% CI)	CAC (mM)
Fmoc-Dap(H)-D-Trp-D-Lys(Gd-DOTA)-NH_2 **(16)**	H_2O	6.1 ± 0.2	-	-
Fmoc-D-Trp-Dap(H)-D-Lys(Gd-DOTA)-NH_2 **(20)**	H_2O	4.9 ± 0.3	13.8 ± 0.5	2.26
	PBS	5.2 ± 0.3	16.9 ± 0.7	1.20
Fmoc-D-Trp-D-Lys(Gd-DOTA)-Dap(H)-NH_2 **(26)**	H_2O	5.2 ± 0.3	13.2 ± 0.9	2.44
	PBS	4.6 ± 0.5	14.4 ± 0.9	0.86

In further observations, it was found that even though **(20)** and **(26)** also feature Fmoc adjacent to D-Trp like **(4)** and **(9)**, their CAC values were much closer to the higher value of carboxylate **(9)**, rather than the better-performing carboxamide **(4)**. Since **(20)** and **(26)** have a net charge of +1 at a pH of 7.4 due to the primary amine on the side chain of Dap, they may undergo electrostatic repulsion which hinders self-assembly. This points to the design of net-neutral compounds as preferred for high-relaxivity agents with low CACs.

2.5 Dipeptide Compounds with Cbz & Tryptophan

The second goal of this project was to investigate other motifs beyond Fmoc and Trp for self-assembly. Although the previously synthesized Fmoc compounds were found to self-assemble, there are likely to be perceived downsides to using Fmoc-protected compounds in biological systems. Fmoc cleavage typically occurs through deprotonation by secondary amines followed by β-elimination, so secondary amino acids such as proline that are naturally present in the bloodstream could remove Fmoc from these compounds. This would not only remove their ability to self-assemble, but also release the potentially toxic polycyclic aromatic hydrocarbon dibenzofulvene as a result, as shown in Figure 27.

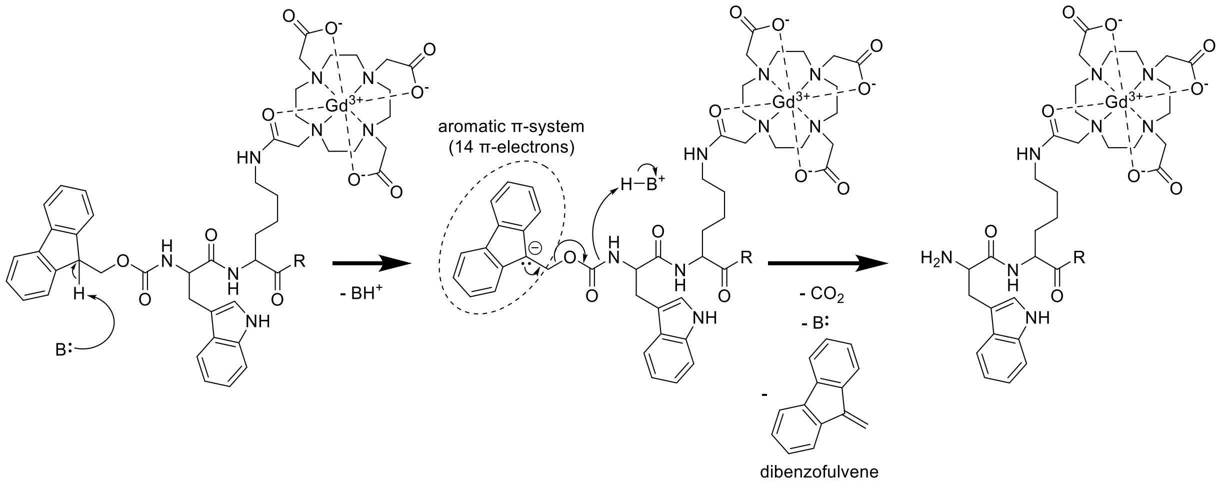

Figure 27: Base-catalyzed cleavage of Fmoc from a generic Fmoc-Trp-Lys(Gd-DOTA) dipeptide resulting in the liberation of dibenzofulvene.

To counteract this possible liability of Fmoc, the potential self-assembly of compounds containing Trp with the carboxybenzyl (Cbz) amine protecting group at its N-terminus was analyzed. Cbz and Fmoc have similar structures, as both are carbamates with planar aromatic substituents. However, Cbz is much more stable under basic conditions than Fmoc, with deprotection typically occuring via catalytic hydrogenolysis. Therefore, it was envisioned that the Cbz protecting group at the N-terminus of Trp would result in self-assembling compounds with increased biological stability.

With the assistance of fellow group member Griffin Pileski, Cbz-substituted analogues of **(4)** and **(9)**, Cbz-D-Trp-Lys(Gd-DOTA)-NH$_2$ **(27)** and Cbz-D-Trp-D-Lys(Gd-DOTA)-OH **(28)**, shown in Figure 28, were synthesized and their relaxivities were measured. These compounds were synthesized using the same method to synthesize compounds **(4)** and **(9)** as outlined in Section 2.2, except for using Cbz-D-Trp-OH in place of Fmoc-D-Trp-OH.

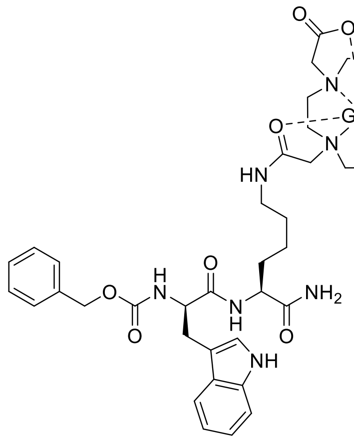

(27)

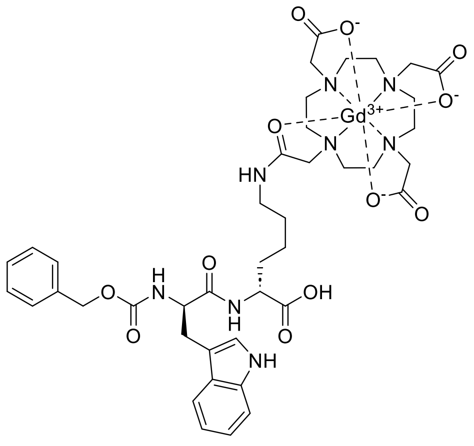

(28)

Figure 28: Cbz-D-Trp-Lys(Gd-DOTA)-NH_2 ***(27)*** *and Cbz-D-Trp-D-Lys(Gd-DOTA)-OH* ***(28)****.*

Disappointingly, an r_1 increase was not observed and neither Cbz analog produced self-assembly below 5 mM in either H_2O or PBS, as shown in Figures 29a and 29b and Table 7. This was surprising considering that both Fmoc and Cbz are carbamates with aromatic moieties, implying that the Fmoc group has unique π-stacking or other properties that is not offered by Cbz. This could be due to Fmoc being physically larger and having more π-electrons than Cbz, strengthening the intermolecular π-π interactions that induce self-assembly.

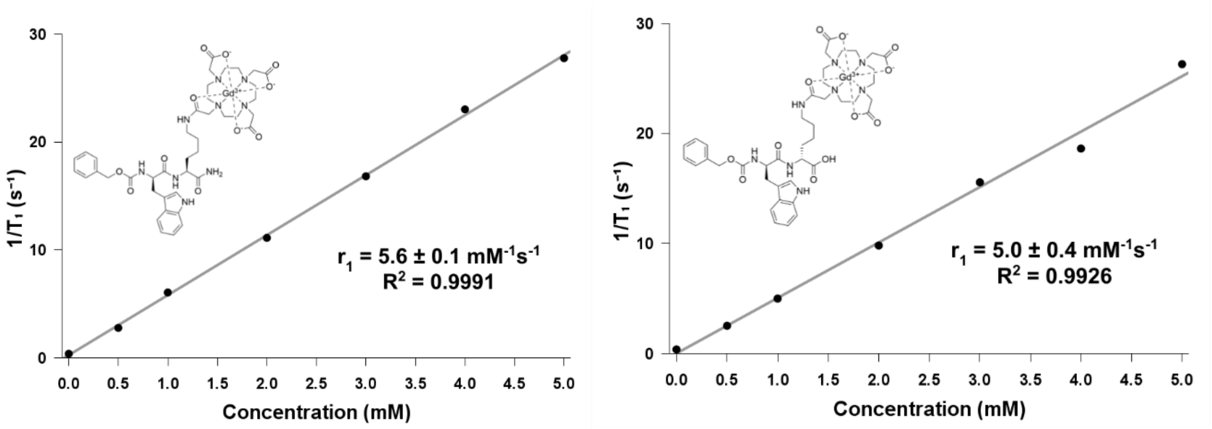

Figures 29a-b: 1/T_1 vs. concentration graphs of Cbz-D-Trp-Lys(Gd-DOTA)-NH_2 ***(27)*** *(left) and Cbz-D-Trp-D-Lys(Gd-DOTA)-OH* ***(28)*** *(right) in PBS.*

*Table 7: r_1 values of Cbz-D-Trp-D-Lys(Gd-DOTA)-NH_2 **(27)** and Cbz-D-Trp-Lys(Gd-DOTA)-OH **(28)** as measured in H2O and PBS.*

Compound	Solution	Non-self-assembled r_1 ($mM^{-1}s^{-1}$) (95% CI)
Cbz-D-Trp-Lys(Gd-DOTA)-NH_2 **(27)**	H_2O	5.2 ± 0.1
	PBS	5.6 ± 0.1
Cbz-D-Trp-D-Lys(Gd-DOTA)-OH **(28)**	H_2O	4.7 ± 0.2
	PBS	5.0 ± 0.4

2.6 Fluorescence Emission Measurements

To substantiate and further expand upon these findings, fluorescence spectroscopy was performed to confirm the self-assembling behavior of Fmoc-D-Trp compounds. Previously reported fluorenyl-capped Tyr-Leu dipeptides by Fleming et al found red-shifted fluorescence emission spectra for the compounds when measured as self-assembled hydrogels compared to free molecules in solution, as shown in Figure 30. This red-shifted emission was attributed to J-aggregate and excimer formation in the compounds' self-assembled states.[64]

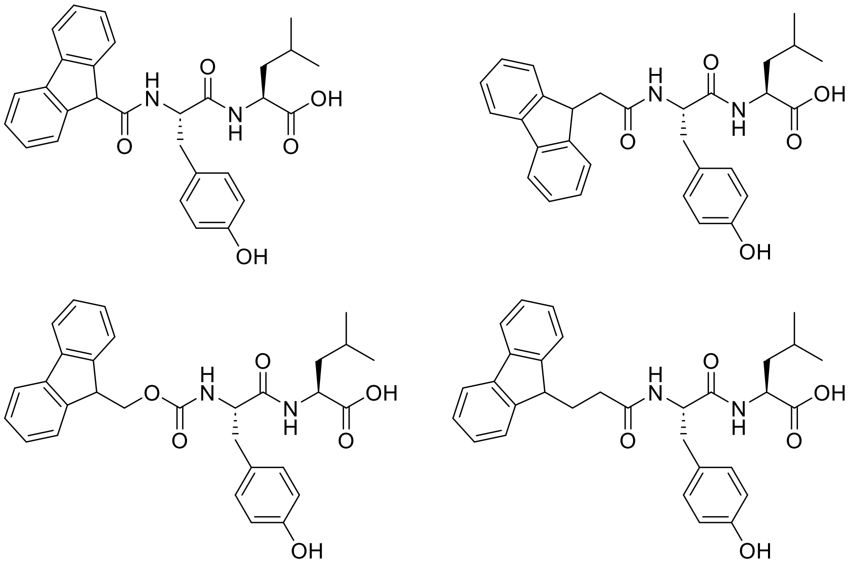

Figure 30: Fluorenyl-capped Tyr-Leu dipeptides reported by Fleming with red-shifted fluorescence emission in their self-assembled hydrogel forms compared to their non-self-assembled forms in solution.[64]

Fluorescence emission spectra of **(4)** and **(27)** were measured in H_2O at concentrations of 0.025 and 1 mM (corresponding to concentrations in the linear regions below and above the CAC for **(4)** in H_2O

respectively), as shown in Figures 31a-d. An excitation wavelength of 290 nm was used to selectively excite the indole moiety in D-Trp ($\lambda_{\text{max abs}}$ = 280 nm) rather than the fluorenyl fluorophore in Fmoc ($\lambda_{\text{max abs}}$ = 265 nm) or the carboxybenzyl fluorophore in Cbz ($\lambda_{\text{max abs}}$ = 272 nm). Fluorescence emission was collected between 330-550 nm in order to prevent interference from Raman scattering ($\lambda \approx 310$ nm) and Rayleigh scattering ($\lambda \approx 575$ nm)

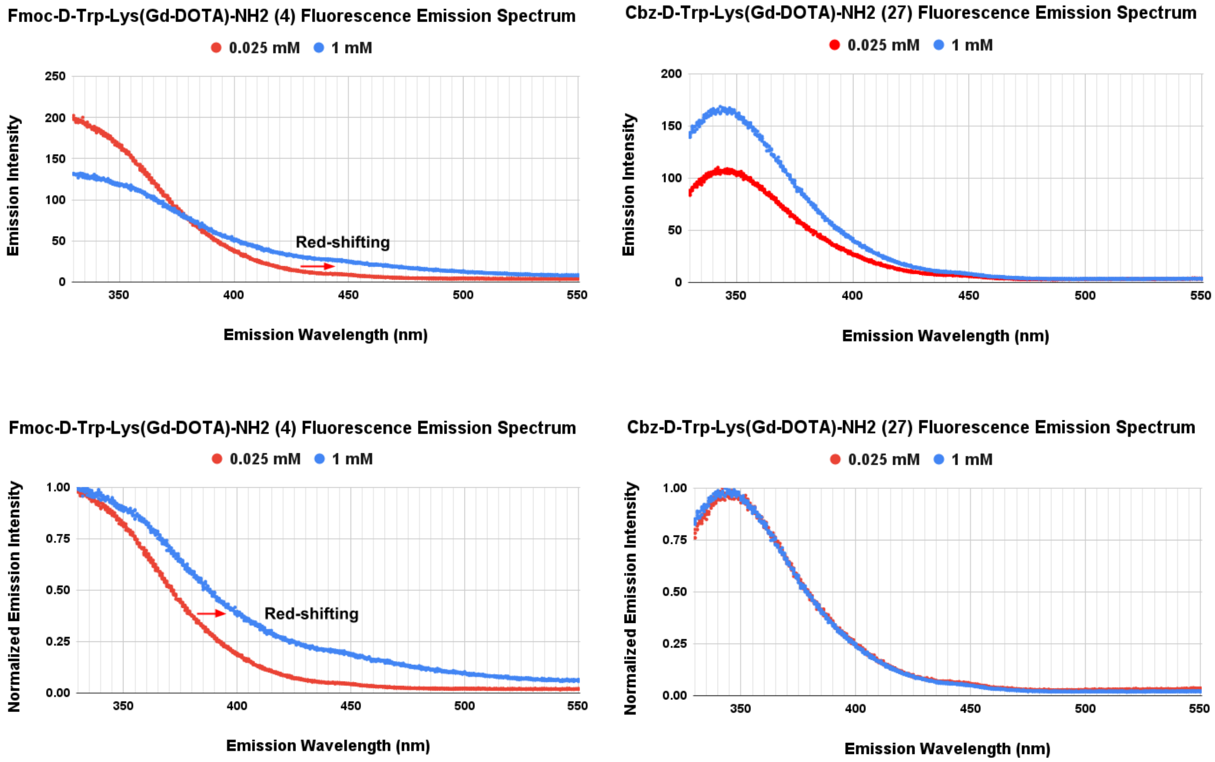

Figures 31a-d: Fluorescence emission spectra of Fmoc-D-Trp-Lys(Gd-DOTA)-NH$_2$ **(4)** *(top and bottom left) and Cbz-D-Trp-Lys(Gd-DOTA)-NH$_2$* **(27)** *(top and bottom right) at concentrations of 0.025 mM and 1 mM (λ_{ex} = 290 nm). The concentration-dependent red-shifted emission observed for* **(4)** *at 1 mM suggests* **(4)** *self-assembles at this concentration.*

It was observed that significant concentration-dependent red-shifting occurred for **(4)** at 1 mM whereas no concentration-dependent red-shifting was found for **(27)** at 1 mM. This agrees with the concentration-dependent r_1 increase for **(4)**, which further substantiates that the increased r_1 at high concentrations is indeed due to self-assembly.

Although the exact morphology of the self-assembled compounds was not determined in this study, these results can be used to further speculate on their structure. Fleming et al attributed the red-shifted fluorescence emission spectra of their compounds in their self-assembled states to J-aggregate formation, which occurs when fluorophores are vertically stacked while being horizontally offset to each other.[64,65] Previously reported X-ray crystal data from Rajbhandary et al of self-assembled Fmoc-Phe-OH hydrogel fibrils in DMSO found a similar orientation, as shown in Figures 32a and 32b.[66] This orientation featured the fluorene and phenylalanine fluorophores stacked vertically while the aromatic planes in the fluorene and phenyl fluorophores were laterally offset. The distances between repeating atoms in the fluorene and phenyl fluorophores were 5.015 ± 0.005 Å, while the angles between repeating atoms and the aromatic planes in each fluorene and phenyl fluorophore were 44.7 ± 0.5° and 65.3 ± 0.5° respectively.

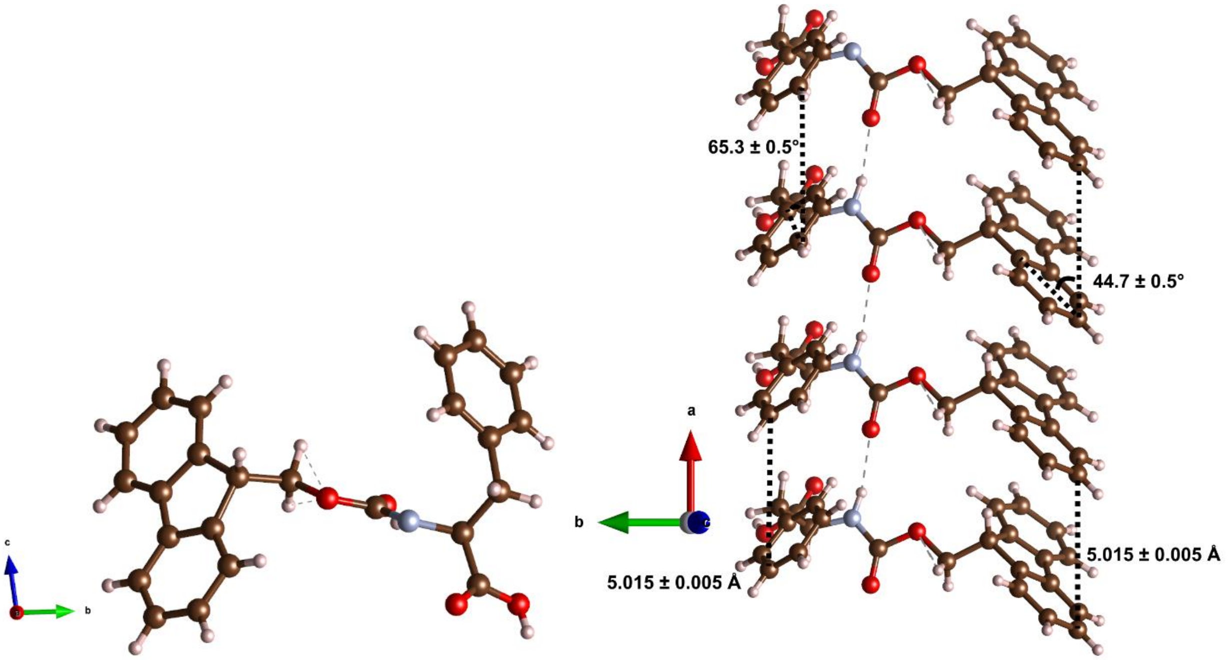

Figures 32a-b: Top view (left) and side view (right) of self-assembled Fmoc-Phe-OH molecules reported by Rajbhandary et al, with hydrogen-bonding represented by thin gray dashed lines and vectors for distance/angle measurements represented by thick black dotted lines.[66] Images were generated using VESTA software.[67]

Since **(4)**, **(6)**, **(9)**, **(12)**, **(20)**, and **(26)**, which were found to self-assemble in H_2O or PBS, have Fmoc-protected Trp at their N-termini, it is likely that they adopt a similar orientation in their self-assembled states. In addition, later results from Section 2.8 show that Fmoc-protected Phe at the N-terminus could also induce self-assembly in Lys(Gd-DOTA) compounds, further supporting this hypothesis.

2.7 Mono-Gd(III) Di-Tryptophan Compounds Without Fmoc

Another motif investigated to induce self-assembly was using two adjacent Trp residues. It was envisioned that two adjacent Trp residues could induce self-assembly in the same way as Fmoc attached to a single Trp residue, due to the resulting peptide still containing two aromatic groups.

Two di-Trp compounds were therefore synthesized: DCL-DSS-D-Trp-D-Trp-Lys(Gd-DOTA)-NH_2 **(32)** and DCL-DSS-D-Lys(Gd-DOTA)-D-Trp-D-Trp-NH_2 **(39)**, as shown in Figure 33. Both Trp residues were D-isomers in order to mimic the widely reported self-assembling peptide motif Fmoc-Phe-Phe, in which both Phe residues have the same stereochemistry.[68]

It was speculated that **(39)** would be more effective at self-assembling than **(32)** as it features highly polar DCL at one end and highly nonpolar D-Trp-D-Trp at the other end. This is similar to the layout of surfactant molecules, which commonly have hydrophilic and hydrophobic groups at opposite ends, with optimal orientation for self-assembly.

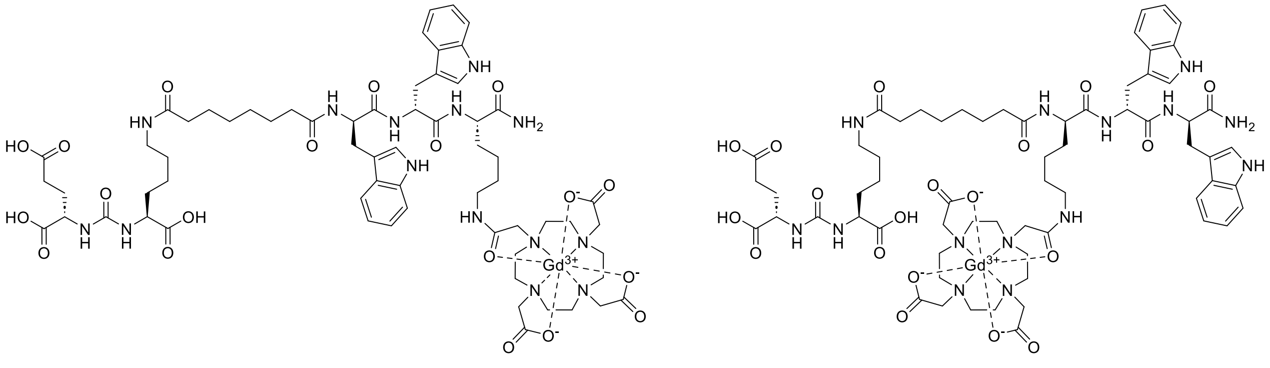

(32) **(39)**

*Figure 33: Di-Trp compounds DCL-DSS-D-Trp-D-Trp-Lys(Gd-DOTA)-NH_2 **(32)** and DCL-DSS-D-Lys(Gd-DOTA)-D-Trp-D-Trp-NH_2 **(39)**.*

However, it was observed that intermediates H-D-Trp-D-Trp-Lys(Gd-DOTA)-NH_2 **(31)** and H-D-Lys(Gd-DOTA)-D-Trp-D-Trp-NH_2 **(38)** were not completely soluble in either DI H_2O or PBS buffer at a concentration of 5 mM, whereas Fmoc-D-Trp-Lys(Gd-DOTA)-NH_2 was. This suggested that the hydrophobic or aromatic interactions between the two Trp residues were much stronger than the corresponding interactions between Fmoc and Trp. Although both **(32)** and **(39)** were soluble in PBS at concentrations of 5 mM, neither were found to self-assemble, as seen in Figures 34a and 34b and Table 8. This implies that only Fmoc can effectively induce the π-π interactions with a neighboring Trp residue that result in self-assembly. However, the effect of varying the relative stereochemistry of adjacent Trp residues on self-assembly remains unexplored and could be investigated by a future student.

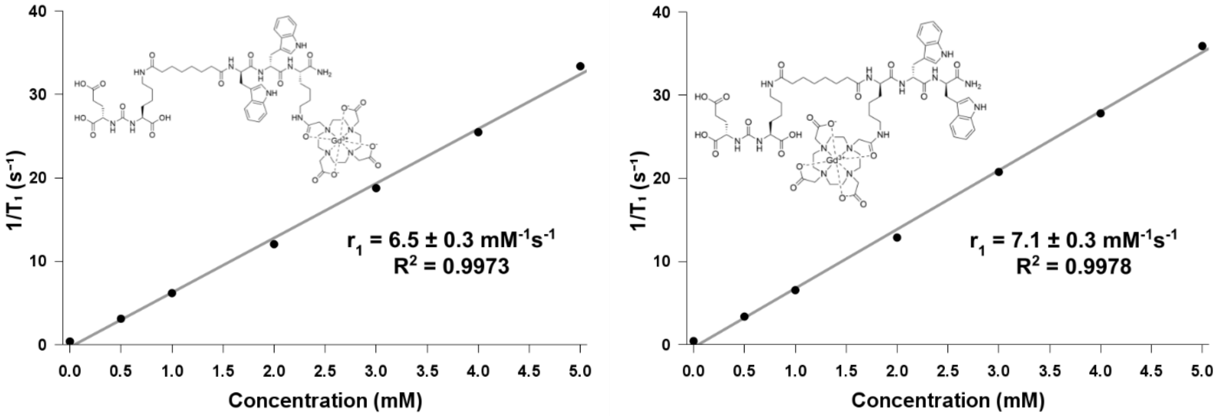

Figures 34a-b: 1/T_1 vs. concentration graphs of DCL-DSS-D-Trp-D-Trp-Lys(Gd-DOTA)-NH_2 ***(32)*** *(left) and DCL-DSS-D-Lys(Gd-DOTA)-D-Trp-D-Trp-NH_2* ***(39)*** *(right) in PBS.*

Table 8: r_1 values of di-Trp compounds DCL-DSS-D-Trp-D-Trp-Lys(Gd-DOTA)-NH_2 ***(32)*** *and DCL-DSS-D-Lys(Gd-DOTA)-D-Trp-D-Trp-NH2* ***(39)****, as measured in PBS.*

Compound	Solution	Non-self-assembled r_1 (mM^{-}1s^{-1}) (95% CI)
DCL-DSS-D-Trp-D-Trp-Lys(Gd-DOTA)-NH_2 **(32)**	PBS	6.5 ± 0.2
DCL-DSS-D-Lys(Gd-DOTA)-D-Trp-D-Trp-NH_2 **(39)**	PBS	7.1 ± 0.3

2.8 Mono-Gd(III) Dipeptides with Fmoc & Other Aromatic Amino Acids

In addition, the use of other Fmoc-protected aromatic amino acids to induce self-assembly was also investigated. With further help from Griffin Pileski, two analogues of **(4)** with phenylalanine (Phe) and tyrosine (Tyr) in place of tryptophan, Fmoc-D-Phe-Lys(Gd-DOTA)-NH_2 **(40)** and Fmoc-D-Tyr-Lys(Gd-DOTA)-NH_2 **(41)**, shown in Figure 35, were synthesized and their relaxivities were measured in PBS.

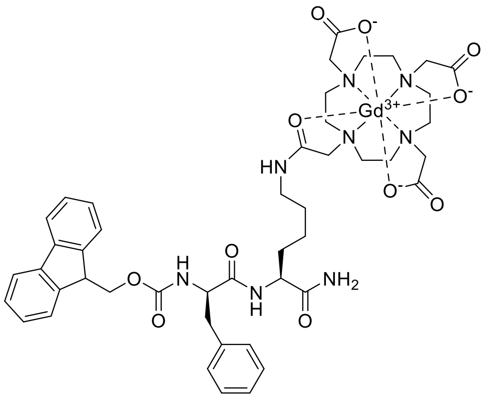

(40)

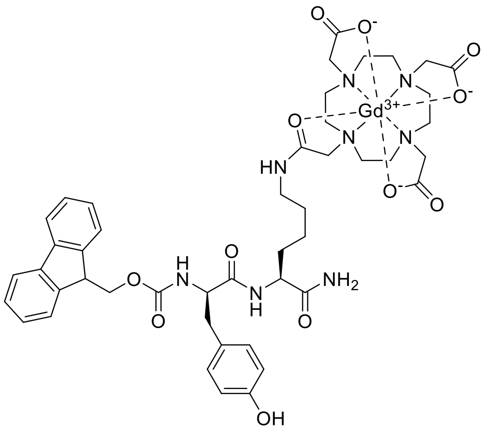

(41)

*Figure 35: Fmoc-D-Phe-Lys(Gd-DOTA)-NH$_2$ **(40)** and Fmoc-D-Tyr-Lys(Gd-DOTA)-NH$_2$ **(41)**.*

As shown in Figures 36a and 36b and Table 9, it was found that **(40)** and **(41)** could self-assemble in PBS, with r$_1$, r$_1$', and CAC values of 4.9 ± 0.5/4.8 ± 0.3 mM^{-1}s^{-1}, 15.2 ± 0.5/15.8 ± 0.7 mM^{-1}s^{-1}, and 1.19/1.09 mM respectively. However, their CAC values were roughly five times that of **(4)** in PBS (0.22 mM). Based on these findings, it can be concluded that Fmoc with D-Phe and D-Tyr induces self-assembly but not as effectively as with D-Trp. As with the discussion of Fmoc vs. Cbz in Section 2.4, the indole side chain of Trp is physically larger and has more π-electrons than the phenyl and phenol side chains of Phe and Tyr, which could result in stronger intermolecular π-π interactions.

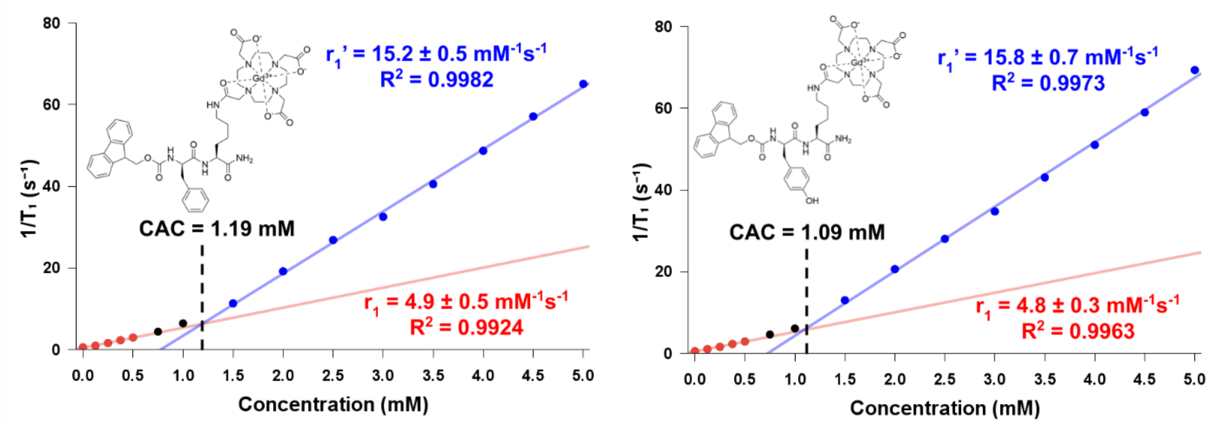

*Figures 36a-b: 1/T$_1$ vs. concentration graphs of Fmoc-D-Phe-Lys(Gd-DOTA)-NH$_2$ **(40)** (left) and Fmoc-D-Tyr-Lys(Gd-DOTA)-NH$_2$ **(41)** (right) in PBS.*

Table 9: r_1, r_1', and CAC values of Fmoc-D-Phe-Lys(Gd-DOTA)-NH_2 ***(40)*** *and Fmoc-D-Tyr-Lys(Gd-DOTA)-NH2* ***(41)*** *as measured in PBS*

Compound	Solution	Non-self-assembled r_1 ($mM^{-1}s^{-1}$) (95% CI)	Self-assembled r_1' ($mM^{-1}s^{-1}$) (95% CI)	CAC (mM)
Fmoc-D-Phe-Lys(Gd-DOTA)-NH_2 **(40)**	PBS	4.9 ± 0.5	15.2 ± 0.5	1.19
Fmoc-D-Tyr-Lys(Gd-DOTA)-NH_2 **(41)**	PBS	4.8 ± 0.3	15.8 ± 0.7	1.09

2.9 PSMA-Targeted Self-Assembling Compound with Fmoc, Tryptophan, and a Dap Linker

The third goal of this project was to use the previous findings to synthesize self-assembling MRI contrast agents targeted to prostate and breast cancer. It was decided to use the utilize Fmoc and Trp motif for self-assembly, as it was found to produce self-assembling compounds with the lowest CAC values in H_2O or PBS. This was chosen in the hopes that the self-assembly would remain unaffected in biological settings.

Using the results from Section 2.5, Fmoc-D-Trp-D-Lys(Gd-DOTA)-Dap(H)-NH_2 **(26),** was chosen to take forward to form a PSMA-targeted self-assembling MRI contrast agent. This compound features Fmoc directly attached to D-Trp, which was found to result in compounds with lower CACs than those with Fmoc and D-Trp separated by additional amino acids (indicated by the lower CAC values of **(12)** vs. **(13)**, and **(20)** and **(26)** vs. **(16)**).

In addition, despite similar r_1, r_1', and CAC values, **(26)** was chosen over Fmoc-D-Trp-Dap(H)-Lys(Gd-DOTA)-NH_2 **(20)** because it provides the greatest physical separation between the Fmoc-D-Trp group that induces self-assembly and the DCL that binds to PSMA, in order to minimize any potential interference of self-assembly with cell binding.

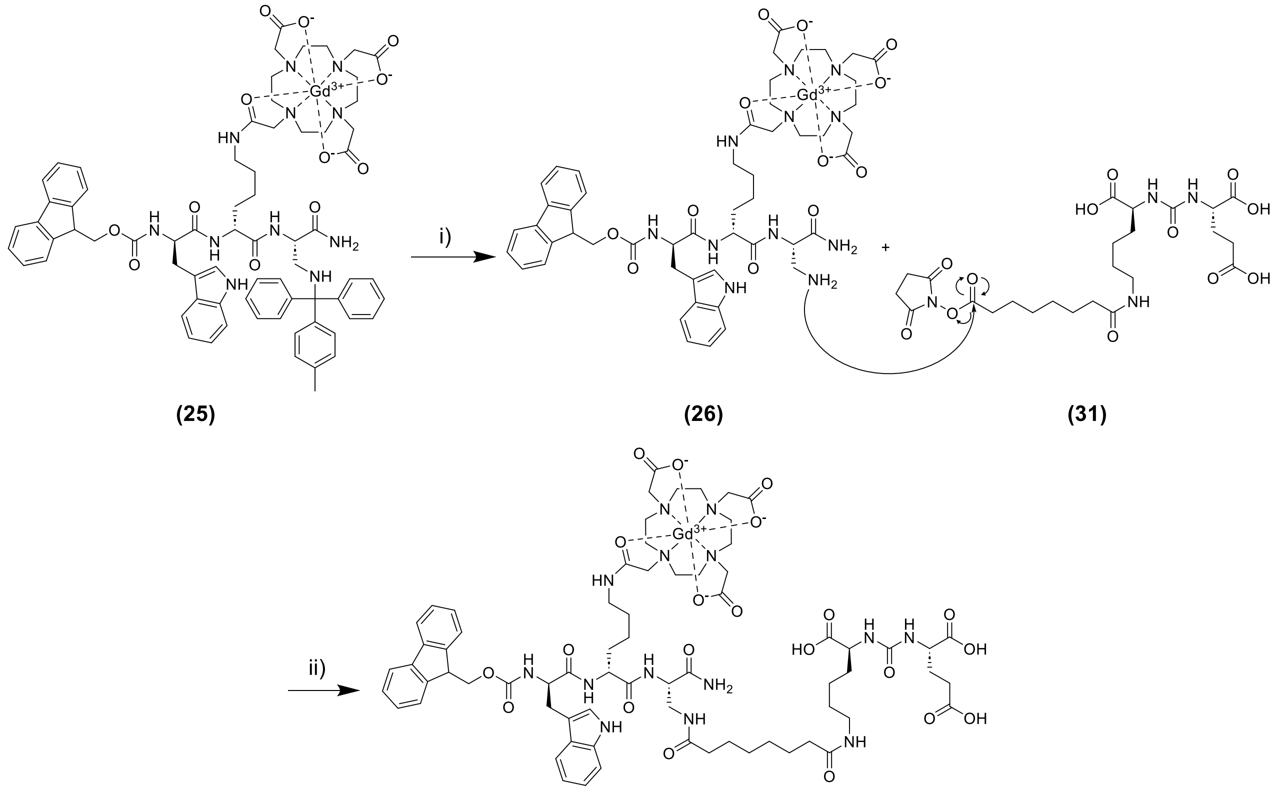

(25) **(26)** **(31)**

(42)

Scheme 3: Synthesis of Fmoc-D-Trp-D-Lys(Gd-DOTA)-Dap(DCL-DSS)-NH$_2$ ***(42)*** *from Fmoc-D-Trp-D-Lys(Gd-DOTA)-Dap(Mtt)-NH2* ***(25)****. i) 1% TFA in DCM; ii) TEA, DMF*

Fmoc-D-Trp-D-Lys(Gd-DOTA)-Dap(H)-NH$_2$ **(26)** was coupled with DCL-DSS **(31)** to form the ultimate targeted contrast agent, Fmoc-D-Trp-D-Lys(Gd-DOTA)-Dap(DCL-DSS)-NH$_2$ **(42)**, as shown in Scheme 3. As seen in Figures 37a and 37b and Table 10, this compound was found to self-assemble in both H_2O and PBS. In addition, its r_1" value in FBS was tested and found to be 11.9 ± 0.2 $mM^{-1}s^{-1}$, as shown in Figure 34c, consistent with the values of **(4)** and **(9)**.

The measured CAC values for **(42)** in H_2O and PBS were unexpectedly higher than precursor Dap compound **(26)** (2.70 mM in H_2O and 2.47 mM in PBS for **(42)** vs. 2.44 mM in H_2O and 0.86 mM in PBS for **(26)**), as shown in Figures 34a and 34b. This could be due to DCL containing three carboxylic acids, increasing intermolecular repulsion and decreasing the propensity to self-assemble.

However, when measured in FBS, just as in the prior observations for the intermediates, the final targeted agent **(42)** displayed a single-phase curve with an r'' value of 11.9 ± 0.2 $mM^{-1}s^{-1}$, as shown in

Figure 37c. While this is modestly less than the measured value for the compound in H_2O and PBS, the CAC was once again driven below 0.025 mM in FBS.

It is noteworthy that enhanced relaxivity is achieved at concentrations below 0.1 mM, as shown in Figure 37c. Since a change in $1/T_1$ relaxation of 0.5 s^{-1} is typically required to achieve robust tissue contrast in MRI, compared with a required *in vivo* concentration of 0.125 mM for a typical MRI contrast agent with an r_1 of 4 $mM^{-1}s^{-1}$, **(42)** would only require an *in vivo* concentration of only around 0.042 mM to achieve an identical change in T_1 relaxation based on its r_1'' value of 11.9 ± 0.2 $mM^{-1}s^{-1}$ in FBS.[25] On the other hand, if **(42)** is administered at the same *in vivo* concentration of 0.125 mM, the image contrast would be even brighter than if a typical MRI contrast agent were used.

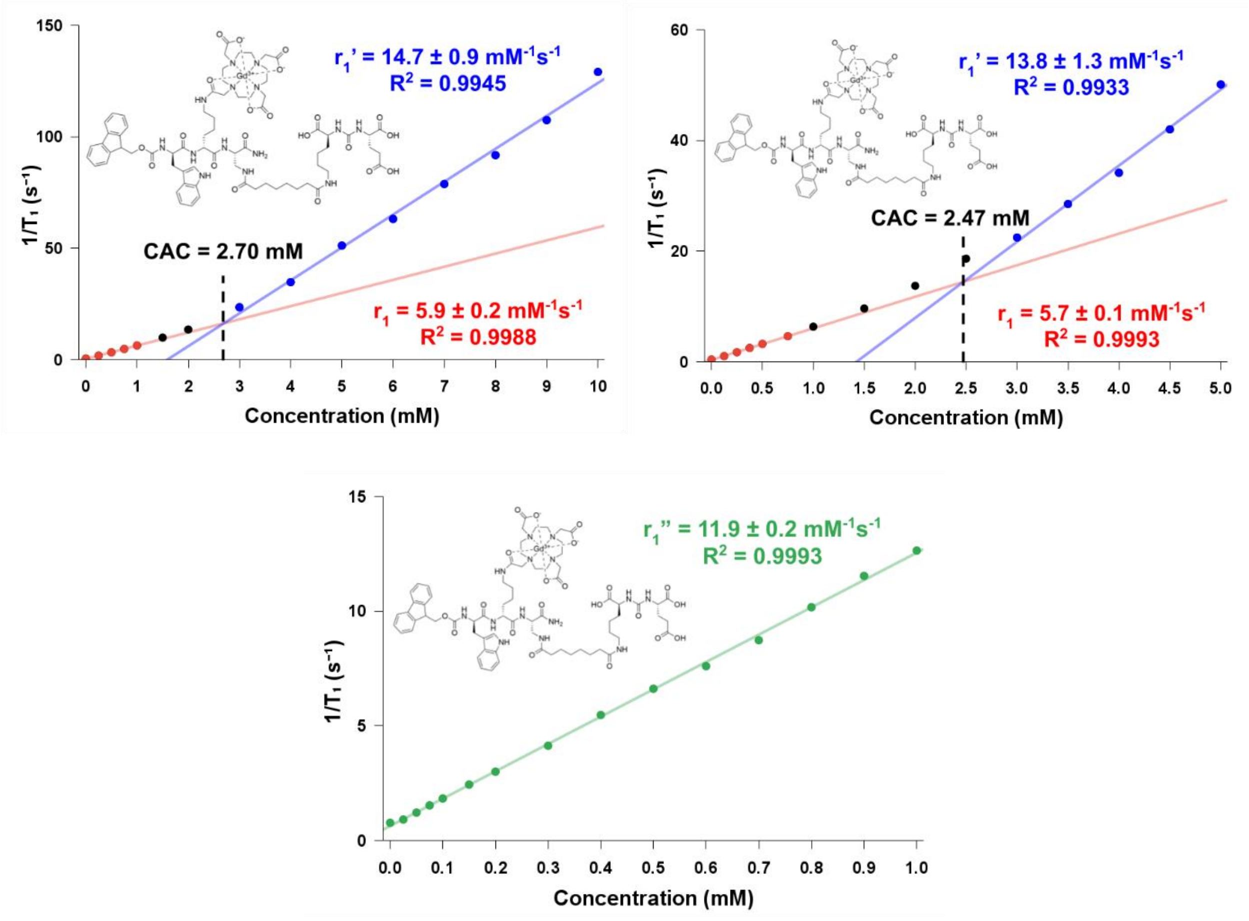

Figures 37a-c: $1/T_1$ vs. concentration graphs of Fmoc-D-Trp-D-Lys(Gd-DOTA)-Dap(DCL-DSS)-NH_2 ***(42)*** *in H_2O (top left), PBS (top right), and FBS (bottom)*

*Table 10: r1, r1', CAC, and r_1" values of Fmoc-D-Trp-D-Lys(Gd-DOTA)-Dap(DCL-DSS)-NH_2 **(42)** as measured in H_2O, PBS, and FBS.*

Compound	Solution	Non-self-assembled r_1 ($mM^{-1}s^{-1}$) (95% CI)	Self-assembled r_1' ($mM^{-1}s^{-1}$) (95% CI)	CAC (mM)	r_1" values in FBS ($mM^{-1}s^{-1}$) (95% CI)
Fmoc-D-Trp-D-Lys(Gd-DOTA)-Dap(DCL-DSS)-NH_2 **(42)**	H_2O	5.9 ± 0.2	14.8 ± 0.9	2.70	-
	PBS	5.7 ± 0.1	13.8 ± 0.9	2.47	-
	FBS	-	-	-	11.9 ± 0.2

2.10 PSMA-Targeted Self-Assembling Compound with a Fmoc, Tryptophan, and a PEG Linker

Although Fmoc-D-Trp-D-Lys(Gd-DOTA)-Dap(DCL-DSS)-NH_2 **(42)** was successfully synthesized and found to self-assemble, its synthesis was cumbersome, requiring eight steps when starting from the synthesis of Fmoc-Dap(Mtt)-OH. One issue with the design of this compound is that it features both a Dap and DSS linker to ultimately link the carboxyl group in Fmoc-D-Trp-D-Lys(Gd-DOTA)-OH **(9)** with the primary amine on DCL. Instead of using two linkers—one with two amines (Dap) and another with two carboxyl groups (DSS) —a single linker with one amine and one carboxyl group could be used.

Fmoc-NH-PEG8-COOH, a bifunctional PEG linker with eight PEG units, an Fmoc-protected primary amine on one end, and a carboxylic acid on the other end, as shown in Figure 38, was chosen as an alternative linker. Since this linker is an Fmoc-protected amino acid itself (albeit not an alpha-amino acid like the proteogenic amino acids), it could be incorporated into the synthesis of these compounds using the same reactions (Fmoc deprotection, carboxylic acid activation, and peptide coupling). PEG linkers are known to increase water solubility, allowing for more nonpolar peptide residues or targeting groups to be conjugated with the hope of achieving sufficiently high water solubility for biological utility.

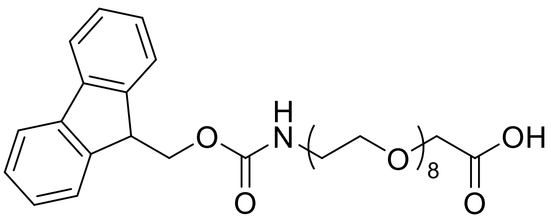

Fmoc-NH-PEG8-COOH

Figure 38: PEG linker Fmoc-NH-PEG8-COOH

A new targeted contrast agent was therefore designed which utilized the Fmoc-D-Trp-Lys(Gd-DOTA) motif, that was found to induce self-assembly in **(4)**, **(9)**, **(12)**, **(20)**, (**26)**, and **(42)**, and DCL **(45)** conjugated to the C-terminus of the PEG linker. The resulting compound, Fmoc-D-Trp-D-Lys(Gd-DOTA)-PEG8-DCL **(46)**, was synthesized as shown in Scheme 4.

In this synthesis, Fmoc-NH-PEG8-COOH was first Fmoc-deprotected to form H_2N-PEG8-COOH **(43)** and then coupled to Fmoc-D-Trp-D-Lys(Gd-DOTA)-OH **(9)** to form Fmoc-D-Trp-D-Lys(Gd-DOTA)-PEG8-COOH **(44)**. **(46)** was synthesized by coupling DCL **(45)** to **(44)**. This was achieved by preparing and isolating the NHS ester of **(44)** using TSTU, which was then coupled to **(45)**. Unlike with a typical one-pot approach where the amine, carboxylic acid, and coupling agent are present simultaneously, this step-wise approach ensured selectivity for the amidation of the carboxylic acid only on **(44)** rather than any of the three carboxylic acids present on the on DCL targeting moiety.

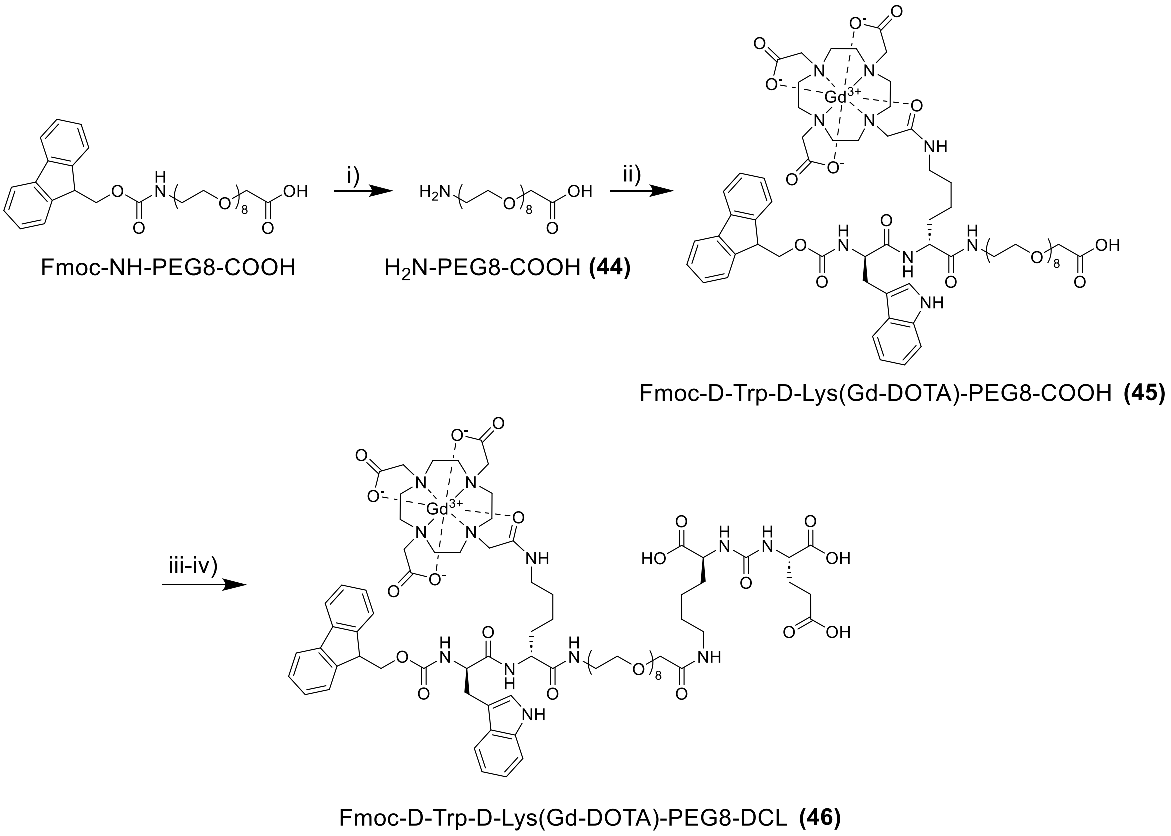

Scheme 4: Synthesis of Fmoc-D-Trp-D-Lys(Gd-DOTA)-PEG8-DCL ***(46)*** *from Fmoc-NH-PEG8-COOH* ***(44)****. i) DEA,DCM; ii) Fmoc-D-Trp-D-Lys(Gd-DOTA)-OH* ***(9)****, HATU, DIPEA, DMF; iii) TSTU, DIPEA, DMF, iv) DCL* ***(45)****, DIPEA, DMF*

As was hoped, both **(46)** and its precursor compound **(44)** were found to self-assemble in PBS as shown in Figures 39a and 39b and Table 11, with r_1, r_1', and CAC values of 7.4 ± 0.2/6.9 ± 0.3 $mM^{-1}s^{-1}$, 13.5 ± 0.4/14.2 ± 1.1 $mM^{-1}s^{-1}$, and 1.65/1.80 mM respectively. Similar to the DSS version (**42**), the PEG version, **(46)** also had a measured r_1" value in FBS of 11.2 ± 0.2 $mM^{-1}s^{-1}$, as shown in Figure 39c. In addition, when measured in PBS, **(46)** was found to have a lower CAC value than PSMA-targeted compound **(42)** (1.65 mM vs. 2.47 mM).

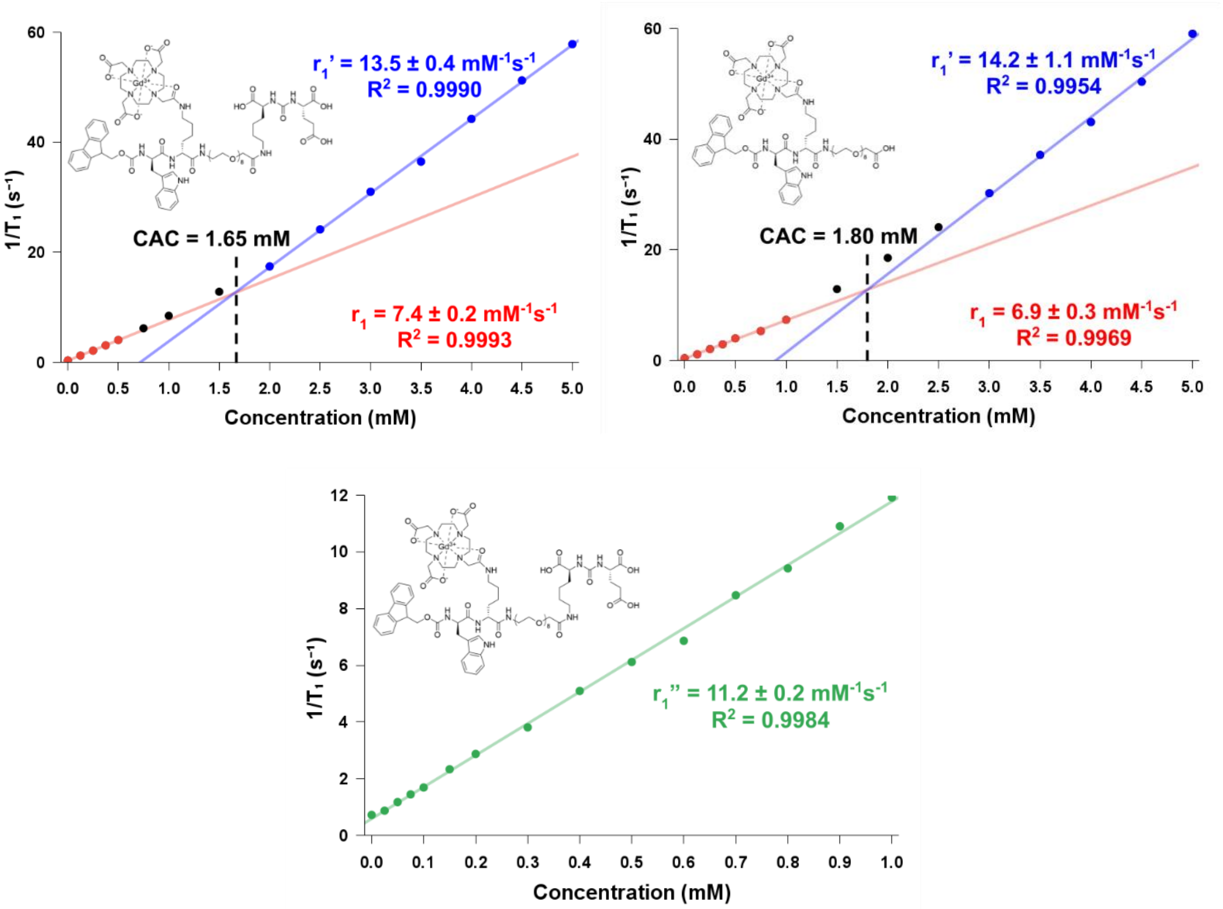

Figures 39a-c: 1/T_1 vs. concentration graphs of Fmoc-D-Trp-D-Lys(Gd-DOTA)-PEG8-DCL ***(46)*** *in PBS (top left) and FBS (top right) and Fmoc-D-Trp-D-Lys(Gd-DOTA)-PEG8-COOH* ***(44)*** *(bottom) in PBS*

*Table 11: r_1, r_1', CAC, and r_1" values of Fmoc-D-Trp-D-Lys(Gd-DOTA)-PEG8-DCL **(46)** and Fmoc-D-Trp-D-Lys(Gd-DOTA)-PEG8-COOH **(44)** as measured in PBS and FBS*

Compound	Solution	Non-self-assembled r_1 ($mM^{-1}s^{-1}$) (95% CI)	Self-assembled r_1' ($mM^{-1}s^{-1}$) (95% CI)	CAC (mM)	r_1" in FBS ($mM^{-1}s^{-1}$) (95% CI)
Fmoc-D-Trp-D-Lys(Gd-DOTA)-PEG8-DCL **(46)**	PBS	7.4 ± 0.2	13.5 ± 0.4	1.65	-
	FBS	-	-	-	11.2 ± 0.2
Fmoc-D-Trp-D-Lys(Gd-DOTA)-PEG8-COOH **(44)**	PBS	6.9 ± 0.3	14.2 ± 1.1	1.80	-

In the broader scope, the self-assembly of **(44)** set an important precedent for the design of future TMIAs in that other targeting groups could be conjugated to **(44)** without affecting the self-assembly induced by Fmoc and D-Trp at the N-terminus.

2.11 Breast-Cancer-Targeted Compound with a PEG Linker

The approach used to synthesize **(46)** was also used to synthesize a second cancer-targeting compound that is of interest to our research group: Fmoc-D-Trp-D-Lys(Gd-DOTA)-PEG8-18-4 **(47)**. This compound featured the decapeptide 18-4 (shown in Figure 40a), which was identified by our collaborator Dr. Kamaljit Kaur at Chapman University to bind to the keratin 1 receptor overexpressed in breast cancer (BrCa) cells.[69–71] Although previous graduate students Basant Kaur and Xinyu Xu had previously synthesized MRI-active single- and dual-modal conjugates of 18-4 featuring Lys(Gd-DOTA) with and without the NIR dye Cy5.5, relaxivity studies were not performed.[54,56]

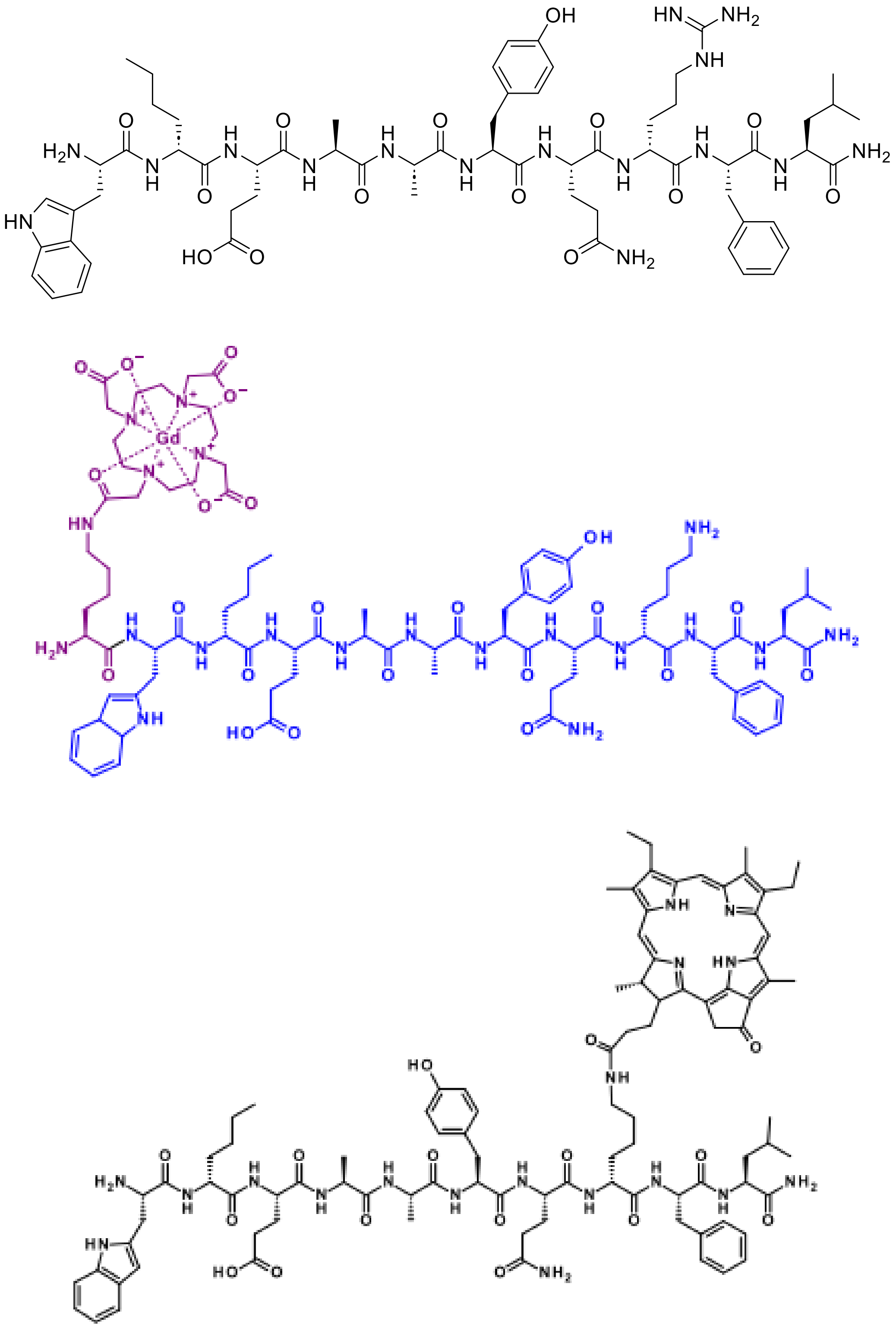

Figures 40a-c: Originally reported form of 18-4 by Dr. Kaur with D-Arg as the third residue (top), MRI-active 18-4 conjugate featuring Lys(Gd-DOTA) at the eleventh residue synthesized by Basant Kaur (middle), and photosensitizer-18-4 conjugate featuring meso pyropheophorbide-a attached to D-Lys at the third residue synthesized by Sara Shaut (bottom)[56,72]

The design of **(47)**, as shown in Figure 41, intended to address several issues with 18-4 conjugates synthesized by prior students. Although the originally reported form of peptide 18-4 contained D-Arg as the third residue, earlier 18-4 conjugates made by past graduate students Basant Kaur, Sara Shaut, and Xinyu Xu (such as the MRI-active conjugate in Figure 40b) substituted D-Arg with D-Lys in order to create an alternate attachment point for imaging modalities such as NIR dyes or porphyrin-based photosensitizers.[54,56,71,72] However, this method of attachment imaging modalities (as shown in Figure 40c) was found to disrupt cell binding, as reported by past graduate student Chris DeNyse. Subsequent 18-4 conjugates have exclusively utilized imaging agents substituted to the side chain or N-terminal amine of a lysine residue that is then attached to the Trp residue of 18-4 (in its original form with D-Arg).[73]

The poor water solubility of 18-4 was also identified as an issue with previously synthesized conjugates.[72,73] Water solubility is crucial for MRI contrast agents, as not only is relaxivity measured by using a calibration curve in water or aqueous buffer (like PBS), but T_1 relaxation enhancement by MRI contrast agents occurs through their direct and indirect interactions with water molecules, as outlined in Section 1.6. Therefore, the PEG linker in **(47)** was important to enhance the water solubility of the final conjugate.

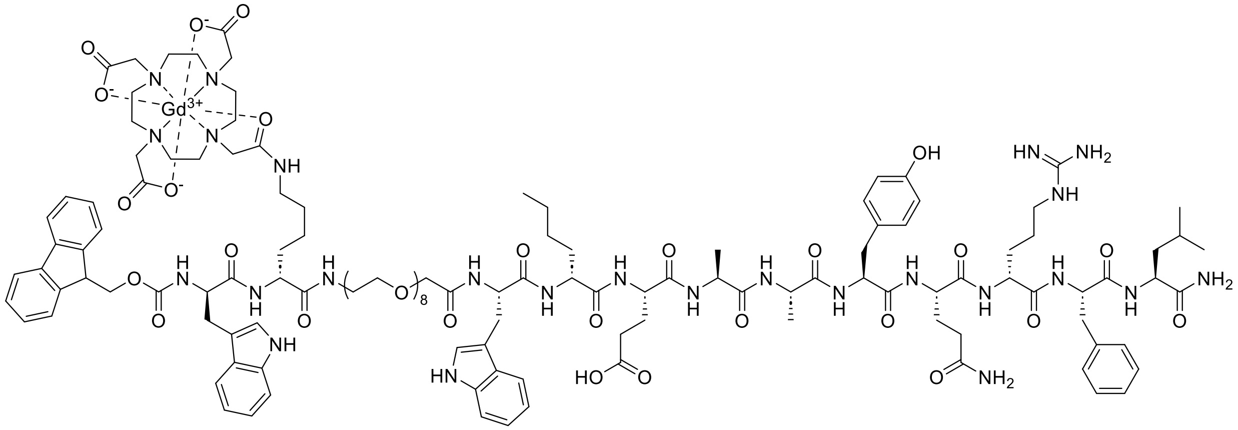

(47)

Figure 41: Fmoc-D-Trp-D-Lys(Gd-DOTA)-PEG8-18-4 ***(47)***

(47) was synthesized from **(45)** using the same approach as the synthesis of **(46)**, except that side-chain-unprotected 18-4 was used in place of DCL. The pH of this reaction during the coupling step was also carefully monitored to be no higher than 9 in order to prevent potential side reactions from deprotonated Tyr or Arg residues. Although **(47)** was successfully synthesized, it unfortunately proved too water-insoluble for its relaxivity to be measured. Despite this, the synthesis of **(46)** and **(47)** from common intermediate **(45)** represents a truly modular method to synthesize self-assembling MRI contrast agents with any cancer-targeting group that contains a primary amine (whether on a peptide N-terminus or Lys side chain). However, the poor water solubility of **(47)** shows that the targeting group must be sufficiently water-soluble to ensure the water solubility of the whole conjugate. **(46)** likely has a much greater water solubility than **(47)** because **(46)** a net charge of -3 due to the 3 carboxylates on DCL whereas **(47)** has a net charge of 0 at a pH of 7.4.

3. Conclusion

Peptide-based MRI contrast agents containing Fmoc and Trp were found to have concentration-dependent increases in relaxivity due to self-assembly. Compounds in their non-self-assembled forms were found to have r_1 values between 3.6 and 7.4 $mM^{-1}s^{-1}$ per Gd(III) whereas their r_1' values in their self-assembled forms values increased dramatically from 13.2 to 16.9 $mM^{-1}s^{-1}$ per Gd(III) when measured in H2O or PBS.

It was further determined that the CAC of these compounds ranged from 0.35 mM to 2.70 mM in H_2O and 0.22 mM to 2.47 mM in PBS for **(4)** and **(42)** respectively. Compounds whose relaxivity values were measured in H_2O and PBS and were found to self-assemble had a markedly lower CAC in PBS than H_2O. This is consistent with an increase in ionic strength that disfavors interactions between the hydrophobic aromatic rings and solvent and favors the intermolecular π-π interactions that cause self-assembly.

In addition, it was discovered that FBS has a remarkable effect in reducing the CAC in self-assembled, high relaxivity compounds. Using FBS thus resulted in a linear curve at all measured concentrations with r_1" values of 5-9 $mM^{-1}s^{-1}$ for compounds that did not self-assemble in H_2O and 11-13 $mM^{-1}s^{-1}$ for compounds that self-assembled in H_2O or PBS. The increase of r_1" in nominal relaxivity compounds is likely due to the increased viscosity of FBS compared to H_2O or PBS. However, in compounds that self-assembled to yield high relaxivity in H_2O or PBS, rather than to increase the r_1’ value further, the effect was to decrease the CAC below 0.025 mM. This is an important aspect as the enhanced relaxivity in FBS occurs at the *in vivo* contrast agent concentrations used in MRI, as discussed in Sections 1.6 and 2.10.

The regional placement of Fmoc relative to D-Trp was found to impact self-assembly. Fmoc directly adjacent to D-Trp, as found in **(4)**, **(9)**, **(12)**, **(20)**, and (**26)**, produced lower CAC values than compounds with Fmoc and D-Trp separated by one amino acid, as found in **(13)** and **(16)**. This is likely due to stronger π-π interactions between Fmoc and Trp occurring when they are closer together in space.

Net charge was also found to affect the CAC of self-assembling compounds. Uncharged compounds displayed lower CACs than their analogues with a net charge, as seen by the roughly fivefold decrease of CAC in PBS for **(4)** compared to **(9)** (0.22 vs. 1.04 mM). **(20)**, and **(26)**, which featured a positively charged primary amine on the side chain of their Dap residues, had CACs of 2.26 and 2.44 mM in H_2O and 1.20 and 0.86 mM in PBS respectively, which were similarly higher than the CACs in H_2O and PBS for **(4)** (0.35 and 0.22 mM).

However, the relative stereochemistry of Trp and Lys was not found to affect self-assembly. Both **(4)** and **(6)**, which differ only by the stereoisomer of Trp used, were found to self-assemble in PBS with little change in CAC (0.22 and 0.35 mM).

Self-assembly was not found to occur when Fmoc-D-Trp was replaced with Cbz-D-Trp, as observed in **(27)** and **(28)**, or with two adjacent D-Trp residues, as observed in **(32)** and **(39)**. However, self-assembly was found to occur when Fmoc-D-Trp was replaced with Fmoc-D-Phe or Fmoc-D-Tyr, as observed in **(40)** and **(41)**. Self-assembly was most effective when D-Trp was used over D-Phe or D-Tyr, as indicated by the low CAC value in PBS for **(4)** compared to **(40)** or **(41)** (0.22 mM vs. 1.19 mM and 1.09 mM respectively). This could be due to the indole side chain of Trp being physically larger and containing more π-electrons than the phenyl and phenol side chains of Phe and Tyr, resulting in stronger π-π interactions with Fmoc.

These results suggest that Fmoc uniquely induces self-assembly in conjunction with aromatic amino acids. Fmoc-Phe-Phe, a motif commonly found in self-assembling peptides, has been previously reported to have an optimal combination of π-π interactions and hydrogen-bonding for self-assembly,[68] pointing to further directions of study, likely guided better by computational modeling studies.

Utilizing these findings, PSMA-targeted MRI-active TMIAs containing both Fmoc-D-Trp and DCL **(42)** and **(46)** were designed and synthesized, followed by measurement of their relaxivities. The synthesis of **(42)** utilized the Dap linker approach found in tripeptides **(16)**, **(20)**, and **(26)**, while **(46)** utilized a more synthetically straightforward PEG linker approach. Both **(42)** and **(46)** were found to self-assemble in H_2O and PBS, but the CAC values of **(42)** in H_2O and PBS were the highest out of all self-assembling compounds (2.70 and 2.47 mM). This is likely due to DCL containing three carboxylates, resulting in a net charge of -3. In addition, **(46)** was also found to also self-assemble in PBS, with a somewhat lower CAC of 1.65 mM.

In addition to the TMIA for prostate cancer, the approach utilized to synthesize **(46)** was employed to synthesize a breast-cancer-targeted TMIA **(47)**. However, **(47)** proved to be too water-insoluble for its relaxivity to be measured. Despite this, the synthesis of **(46)** and **(47)** from common intermediate **(45)** represents the application of a truly modular method to synthesize self-assembling MRI contrast agents with a targeting group for additional types of cancer, provided that the targeting group imparts sufficient water solubility to the conjugate.

Clearly, more research is needed to determine how self-assembly of targeted MRI contrast agents affects their distribution in biological systems and cell-binding activity. However, the results reported here appear to be unprecedented, and will spark further development. Current research in our group involves investigating more stable structural analogues of Fmoc as well as using new strategies to enhance the water solubility of Lys(Gd-DOTA)-18-4 conjugates. We are hopeful that the targeted compounds that were synthesized can be tested in both *in vitro* and *in vivo* experiments with a collaborator in the near future.

4. Experimental

Materials and Methods

Synthesis/Purification:

A Waters 2695 Alliance HPLC with a Waters 2998 Diode Array Detector and a Waters 3100 SQ Mass Spectrometer was used for HPLC-MS. The columns used in HPLC were: an Agilent XDB C18 column, with dimensions of 3 mm x 100 mm, or a Waters XBridge C18 column ,with dimensions of 50 mm x 3 mm and 3µ particle size. Mass spectra from this instrument were recorded at unit resolution with positive and negative switching mode at 35 or 50 V cone voltages. The flow rate for HPLC-MS was 0.5 mL/min. All aqueous mobile phases for HPLC are 0.01M ammonium acetate. Preparative HPLC was carried out with a Waters 600E system controller and Waters 600 multi-solvent delivery system using a 30 mL/min flow rate.

For SPE purifications, Varian Bond Elut (C18, 12CC/2GRM) SPE cartridges were used. Aqueous mobile phases for SPE are not buffered. The SPE cartridges were conditioned with their respective organic solvent, then equilibrated with the initial gradient concentration. Gradients were performed in 10% increments with 3-10 mL fractions collected in 16 x 100 mm glass test tubes unless otherwise noted.

Flash chromatography was performed using a Biotage Selekt flash chromatography instrument. Biotage Sfär C18 Duo columns were used with a flow rate of 50 mL/min.

Chromatography gradients for HPLC, preparative HPLC, flash chromatography, and SPE are noted as (method X: Y, t) where X is the organic mobile phase, Y is the starting percentage or overall range of the organic mobile phase, and t is the overall time in minutes of the gradient except for SPE where this is not applicable. For example, method (ACN:H_2O, 10%-100%, 20 min) is a gradient that is initially 10% ACN and 90% H2O, but linearly transitions to 100% ACN and 0% H2O in 20 minutes.

High resolution mass spectra (HRMS) were obtained on a Waters Synapt G2Si (School of Chemical Sciences, University of Illinois at Urbana-Champaign) using the following parameters: Flow injection at flow rate of 0.1 mL/min, H2O/ACN/0.1% Formic Acid, positive and negative mode ESI, Cone voltage =

25, capillary voltage = 3.0, ion source temperature = -100°C, desolation temperature = 180°C, nebulizing gas (N_2) flow = 200 L/h, cone gas (N_2) flow = 5L/h.

Relaxivity Measurements:

Relaxivity values were measured at 1.0 T and 20°C using a Magritek 43 MHz Spinsolve Benchtop NMR Spectrometer. r_1 values were measured using solutions in either 18 MΩ-cm deionized water, 1X PBS buffer, or fetal bovine serum (FBS). 1X PBS buffer (pH of 7.4) was prepared using the Cold Spring Harbor protocol.[74] For each relaxivity measurement, the most concentrated solution measured served as a mother solution which was diluted to create the other solutions. This mother solution was sonicated for five minutes prior to dilution to ensure complete solubility of the compound. All solutions appeared transparent with no indication of compound suspension.

20 µL of each solution was transferred into ~ 0.9 mm ID × 90 mm length borosilicate glass capillary tubes (Kimble Chase). The capillary tube was loaded into a standard 5 mm OD glass NMR tube (Wilmad-LabGlass) with a Teflon® capillary tube adapter. An inversion recovery (IR) sequence was used to measure the spin-lattice relaxation time (T_1) of each solution. 11 inversion time (TI) values were used for each sample. The maximum TI ranged from 4 to 15 s, depending on the sample concentration. Plots of the integrated ^{1}H water signal versus TI were fit using Equation 4 to determine T_1 for a sample.

r_1 and r_1' values for each compound were calculated by plotting $1/T_1$ vs. contrast agent concentration ([CA]). r_1 values were found by performing linear regression on all points (for non-self-assembling compounds) or points within the linear region below the CAC (for self-assembling compounds). r_1' values of self-assembling compounds were found by performing linear regression on all points (for self-assembling compounds) in the linear region above the CAC. Linear regressions were performed using the LINEST function in Microsoft Excel. r_1 and r_1' values are reported as the respective slope(s) of the best-fit trendline(s) for the linear regression(s), and the CAC values for self-assembling compounds are reported as the concentration value at the intersection of the two best-fit trendlines. All r_1 and r_1' values are reported as 95% confidence intervals.

Fluorescence Emission Spectroscopy:

Fluorescence emission spectroscopy measurements were performed using a Shimadzu RF-6000 spectrofluorometer. The scans were performed with an excitation wavelength of 290 nm, an emission wavelength range of 300-550 nm, a data interval of 1 nm, an excitation bandwidth of 2 nm, emission bandwidth of 3 nm, and a scan speed of 200 nm/min.

Experimental Procedures:

Fmoc-Lys(Gd-DOTA)-OH (1)

DOTA (999.2 mg, 1.950 mmol) and 1.2 equivalents of NHS (272.9 mg, 2.371 mmol) were dissolved in 15 mL H2O and added to a round bottom flask under an ambient atmosphere. The flask was cooled to 4°C via ice bath, and the pH was raised to 5 by adding TEA. 1.5 equivalents of EDC (561.1 mg, 2.926 mmol) was dissolved in 5 mL H_2O, added to the reaction, and allowed to react for 1 hour. 1.2 equivalents of Fmoc-Lys-OH•HCl (946.4 mg, 2.337 mmol) were dissolved in 10 mL MeOH and added to the reaction. The flask was removed from the ice bath as the pH was raised to 8 by adding TEA and allowed to react for 30 minutes. 1.1 equivalents of $Gd(OAc)_3$ (720.2 mg, 2.145 mmol) was suspended in 10 mL MeOH, added to the reaction, and allowed to react for 15 minutes. The excess solvent was rotary evaporated and the urea byproduct from the EDC was removed *in vacuo*. The crude material was purified using flash chromatography (ACN:H_2O, 10%-100%, 20 min). Yield: 696.0 mg (39%) with respect to DOTA. LC-MS (LR, ESI) = Calcd. for $C_{37}H_{47}GdN_6O_{11}$: 909.25 (m/z), found: 910.00 $[M+H]^+$

Fmoc-Lys(Gd-DOTA)-NH_2 (2)

Fmoc-Lys(Gd-DOTA)-OH **(1)** (696.0 mg, 0.766 mmol) was dissolved in 5 mL DMF and 5 mL DMSO. Added in quick succession were 30 equivalents of DIPEA (4.00 mL, 22.97 mmol) and 1.2 equivalents of HATU (352.1 mg, 0.926 mmol). After 10 minutes, 3.3 equivalents of 30% aqueous ammonia (126.3 µL, 2.528 mmol) was added to the solution. The reaction was run for 1h. The product was precipitated using Et_2O and dried under Ar (g). Purification was done by flash chromatography (ACN:H_2O, 10%-100%, 20 min). Yield: 375.0 mg (54%). LC-MS (LR, ESI) = Calcd. for $C_{37}H_{48}GdN_7O_{10}$: 908.27 (m/z), found: 909.07 $[M+H]^+$

H-Lys(Gd-DOTA)-NH_2 (3)

H-Lys(Gd-DOTA)-NH_2 **(3)** was prepared from Fmoc-Lys(Gd-DOTA)-NH_2 **(2)** according to our previous literature method.[2] LC-MS (LR, ESI) = Calcd. for $C_{22}H_{38}GdN_7O_8$: 686.20 (m/z), found: 686.98 $[M+H]^+$

Fmoc-D-Trp-Lys(Gd-DOTA)-NH_2 (4)

Fmoc-D-Trp-OH (168.1 mg, 0.394 mmol) was dissolved in DMF (3.5 mL) and to this solution was added 10 equivalents of DIPEA (679.9 uL, 3.942 mmol) and 1.1 equivalents of HATU (163.6 mg, 0.430 mmol). H-Lys(Gd-DOTA)-NH_2 **(3)** (267.7 mg, 0.390 mmol) was dissolved in DMSO (5 mL) and added to the reaction. To this solution was added additional DIPEA (679.9 uL, 3.942 mmol). The reaction ran for 1 hrs. Crude product was precipitated by the addition of Et_2O, and the organic layer was decanted after centrifugation. Pure product was obtained by SPE (ACN:H_2O, 10%-100%). Fractions containing pure product were collected, concentrated by rotary evaporation, and freeze dried. Yield: 188.8 mg (44%). MS (HR,ESI) = Calcd. for $C_{48}H_{58}GdN_9O_{11}$: 1094.34969 (m/z), found: 1093.3463 $[M-H]^-$

H-D-Trp-D-Lys(Gd-DOTA)-NH_2 (5)

To a solution of Fmoc-D-Trp-Lys(Gd-DOTA)-NH_2 **(4)** (188.8 mg, 0.173 mmol) in DMF (2 mL) was added 20 equivalents of DEA (356.7 uL, 3.45 mmol). After stirring under ambient conditions for 0.5 hr, crude product was precipitated by the addition of Et_2O to the reaction flask, centrifuging the mixture, and decanting the organic solvent. This product was dried under Ar(g). Yield: 148.2 mg (98%). LC-MS (LR, ESI) = Calcd. for $C_{33}H_{48}GdN_9O_9$: 872.28 (m/z), found: 873.12 $[M+H]^+$, 437.08 $([M+2H]/2)^{2+}$

Fmoc-Trp-Lys(Gd-DOTA)-NH_2 (6)

Fmoc-Trp-OH (13.2 mg, 0.031 mmol) was dissolved in DMF (0.5 mL) and to this solution was added 10 equivalents of DIPEA (50.8 uL, 0.292 mmol) and HATU (12.9 mg, 0.034 mmol). This reaction stirred under argon for 5 min and was monitored by HPLC-MS after treating a sample with 0.1% aqueous butylamine. H-Lys(Gd-DOTA)-NH_2 **(1)** (20.2 mg, 0.029 mmol) was dissolved in DMSO (1 mL) and added to the reaction. To this solution was added 10 equivalents of DIPEA (50.8 uL, 0.292 mmol. The reaction ran for 2 hrs. Crude product was precipitated by the addition of Et_2O, and the organic layer was decanted after centrifugation. Pure product was obtained by flash chromatography (ACN:H_2O, 10%-100%, 20 min). Fractions containing pure product were collected, concentrated by rotary evaporation, and freeze dried. Yield: 15.4 mg (48%). MS (LR,ESI) = Calcd. for $C_{48}H_{58}GdN_9O_{11}$: 1094.35 (m/z), found: 1095.34 $[M+H]^+$

Fmoc-D-Lys(Gd-DOTA)-OH (7)

1 equivalent of DOTA (498.8 mg, 0.973 mmol) and 1.2 equivalents of NHS (135.1 mg, 1.174 mmol) were dissolved in 7.5 mL H2O and added to a round bottom flask under an ambient atmosphere. The flask was brought to 4°C via ice bath, and the pH was raised to 5 using TEA. 1.5 equivalents of EDC (283.6 mg, 1.47 mmol) was dissolved in 2.5 mL H2O, added to the reaction, and allowed to react for 1 hour. 1.2 equivalents of Fmoc-D-Lys-OH•HCl (475.6 mg, 1.175 mmol) was dissolved in 5 mL MeOH and added to the reaction. The flask was removed from the ice bath as the pH was raised to 8 using TEA and allowed to react for 30 minutes. 1.1 equivalents of $Gd(OAc)_3$ (358.2 mg, 1.071 mmol) was suspended in 5 mL MeOH, added to the reaction, and allowed to react for 15 minutes. The excess solvent was rotary evaporated and the urea byproduct from the EDC was removed *in vacuo*. The crude material was purified using flash chromatography (ACN:H_2O, 10%-100%, 20 min). Yield: 478.5 mg (54%). LC-MS (LR, ESI) = Calcd. for $C_{37}H_{47}GdN_6O_{11}$: 909.25 (m/z), found: 910.11 $[M+H]^+$. This product was identical to that published previously by a non-aqueous method carried out in DMF.[58]

H-D-Lys(Gd-DOTA)-OH (8)

To a solution of Fmoc-D-Lys(Gd-DOTA)-OH **(7)** (200.0 mg, 0.220 mmol) in DMF (2 mL) was added 20 equivalents of DEA (455.0 uL, 4.400 mmol). After stirring under ambient conditions for 30 minutes, crude product was precipitated by the addition of Et_2O to the reaction flask, centrifuging the mixture, and decanting the organic solvent. This product was dried under Ar(g). Yield: 143.6 mg (95%). LC-MS (LR, ESI) = Calcd. for $C_{22}H_{37}GdN_6O_9$: 687.19 (m/z), found: 688.11 $[M+H]^+$

Fmoc-D-Trp-D-Lys(Gd-DOTA)-OH (9)

Fmoc-D-Trp-OH (94.7 mg, 0.222 mmol) was dissolved in DMF (2.5 mL) and to this solution was added 10 equivalents of DIPEA (376.9 uL, 2.221 mmol) and 1.1 equivalents of HATU (90.7 mg, 0.239 mmol). This reaction was stirred under argon for 5 minutes. H-D-Lys(Gd-DOTA)-OH **(8)** (148.6 mg, 0.216 mmol) was dissolved in DMSO (2.5 mL) and added to the reaction. To this reaction was added an additional 10 equivalents of DIPEA (376.9 uL, 2.221 mmol). The reaction ran for 2 hrs. Crude product was precipitated by the addition of Et_2O, and the organic layer was decanted after centrifugation. Pure product was obtained by SPE (ACN:H_2O, 10%-100%). Fractions containing pure product were collected, concentrated by rotary evaporation, and freeze dried. Yield: 58.9 mg (24%). LC-MS (LR, ESI): Calcd. for $C_{48}H_{57}GdN_8O_{12}$: 1095.33 (m/z), found: 1096.30 $[M+H]^+$. MS (HR,ESI) = Calcd. for $C_{48}H_{57}GdN_8O_{12}$: 1095.33371 (m/z), found: 1094.3280 $[M-H]^-$

Fmoc-D-Lys(Gd-DOTA)-Lys(Gd-DOTA)-NH$_2$ (10)

Fmoc-D-Lys(Gd-DOTA)-Lys(Gd-DOTA)-NH$_2$ **(10)** was synthesized from Fmoc-D-Lys(Gd-DOTA)-OH **(7)** and H-Lys(Gd-DOTA)-NH$_2$ **(3)** following previous literature procedure.[47] LC-MS (LR,ESI) = Calcd. for $C_{59}H_{83}Gd_2N_{13}O_{18}$: 1577.45 (m/z), found: 789.22 $([M+2H]/2)^{2+}$.

H-D-Lys(Gd-DOTA)-Lys(Gd-DOTA)-NH$_2$ (11)

H-D-Lys(Gd-DOTA)-Lys(Gd-DOTA)-NH$_2$ **(11)** was synthesized from Fmoc-D-Lys(Gd-DOTA)-Lys(Gd-DOTA)-NH$_2$ **(10)** following previous literature procedure.[47] LC-MS (LR,ESI) = Calcd. for $C_{44}H_{73}Gd_2N_{13}O_{16}$: 1355.38 (m/z), found: 1356.31 $[M+H]^+$, 678.30 $([M+2H]/2)^{2+}$.

Fmoc-D-Trp-D-Lys(Gd-DOTA)-Lys(Gd-DOTA)-NH$_2$ (12)

Fmoc-D-Trp-OH (8.1 mg, 0.019 mmol) was dissolved in DMSO (0.5 mL) and to this solution was added 10 equivalents of DIPEA (31.7 uL, 0.182 mmol) and HATU (7.8 mg, 0.021 mmol). This reaction stirred under argon for 5 min. H-D-Lys(Gd-DOTA)-Lys(Gd-DOTA)-NH_2 **(11)** (24.6 mg, 0.018 mmol) was dissolved in DMSO (1 mL) and added to the reaction. To this solution was added 10 equivalents of DIPEA (31.7 uL, 0.182 mmol). The reaction ran for 3 hrs. Crude product was precipitated by the addition of EtOAc, and the organic layer was decanted after centrifugation. Pure product was obtained by flash chromatography (ACN:H_2O, 10%-100%, 20 min). Fractions containing pure product were collected, concentrated by rotary evaporation, and freeze dried. Yield: 4.7 mg (15%). MS (LR,ESI) = Calcd. for $C_{70}H_{93}Gd_2N_{15}O_{19}$: 1763.53, found: 1764.16 $[M+H]^+$, 881.66 $([M+2H]/2)^{2+}$

Fmoc-D-Lys(Gd-DOTA)-D-Trp-Lys(Gd-DOTA)-NH_2 (13)

Fmoc-D-Lys(Gd-DOTA)-OH **(6)** (158.9 mg, 0.175 mmol) was dissolved in DMSO (2 mL) and to this solution was added 10 equivalents of DIPEA (296.4 uL, 1.702 mmol) and 1.1 equivalents of HATU (72.4 mg, 0.190 mmol). This reaction was stirred under argon for 5 minutes. H-D-Trp-Lys(Gd-DOTA)-NH_2 **(5)** (148.4 mg, 0.170 mmol) was dissolved in DMSO (3 mL) and added to the reaction. To this solution was added an additional 10 equivalents of DIPEA (296.4 uL, 1.702 mmol). The reaction ran for 2 hrs. Crude product was precipitated by the addition of EtOAc and the organic layer was decanted after centrifugation. Pure product was obtained by flash chromatography (ACN:H_2O, 10%-100%, 20 min). Fractions containing pure product were collected, concentrated by rotary evaporation, and freeze dried. Yield: 70.7 mg (24%). MS (HR,ESI) = Calcd. for $C_{70}H_{93}Gd_2N_{15}O_{19}$: 1763.52544, found: 882.7718 $([M+2H]/2)^{2+}$

Fmoc-Dap(Mtt)-OH (14)

A solution of Fmoc-Dap(Boc)-OH (499.7 mg, 1.172 mmol) in DCM (5 mL) was cooled to 0°C in an ice bath. TFA (5 mL) was added to the cooled solution then the reaction vessel was removed from the ice bath. The mixture was stirred for 0.5 hr and monitored via HPLC. 10 mL of dry Et_2O was added twice as the solution was rotary evaporated. The product was redissolved in 5 mL of DCM. 4-methyltritylchloride (Mtt-Cl) (343.1 mg, 1.172 mmol) and DIPEA (3.14 mL, 18.03 mmol) were added and the mixture was stirred for 3 hr and monitored via HPLC. The solution was washed with 5 mL of half-saturated aqueous NaCl solution. 5 mL of fresh DCM was used to back-extract the aqueous layer. The DCM layers were combined and removed in vacuo and the remaining solid was dried over vacuum. The crude material was purified using normal-phase column chromatography with a 50%-100% EtOAc:Hxs solvent gradient followed by a 0%-50% MeOH:EtOAc gradient. Rf = 0.50 in EtOAc. Yield: 279.8 mg (41%). LC-MS (LR,ESI) = Calcd. for $C_{38}H_{34}GdN_2O_4$: 582.25 (m/z), found: 583.49 $[M+H]^+$. MS (HR,ESI) = Calcd. for $C_{38}H_{34}GdN_2O_4$: 582.25186 (m/z), found: 581.2443 $[M-H]^-$

Fmoc-Dap(Mtt)-D-Trp-Lys(Gd-DOTA)-NH$_2$ (15)

Fmoc-Dap(Mtt)-OH **(14)** (20.1 mg, 0.034 mmol) was dissolved in DMF (1 mL) and to this solution was added 10 equivalents of DIPEA (59.9 uL, 0.344 mmol) and 1.1 equivalents of HATU (14.5 mg, 0.038 mmol). This reaction was stirred under argon for 5 min. H-D-Trp-Lys(Gd-DOTA)-NH2 (5) (29.7 mg, 0.034 mmol) was dissolved in DMSO (3 mL) and added to the reaction. To this solution was added an additional 10 equivalents of DIPEA (59.9 uL, 0.344 mmol). The reaction ran for 6 hrs. Crude product was precipitated by the addition of $E_{t2}O$, and the organic layer was decanted after centrifugation. The product was taken without further purification. LC-MS (LR, ESI) = Calcd. for $C_{71}H_{80}GdN_{11}O_{12}$: 1436.52 (m/z), found: 1435.41 $[M+H]^+$

Fmoc-Dap(H)-D-Trp-Lys(Gd-DOTA)-NH$_2$ (16)

The crude Fmoc-Dap(Mtt)-D-Trp-Lys(Gd-DOTA)-NH2 **(15)** from the previous procedure was dissolved in DCM (1 mL). The flask was placed in an ice bath and pure TFA (10 uL) was added via syringe. The flask was removed from the ice bath and the reaction was stirred under ambient conditions for 1.5 hrs. Crude product was precipitated by the addition of Et_2O, and the organic layer was decanted after centrifugation. The product was purified using Waters 600 preparative HPLC (ACN:H_2O, 5%-100%, 40 min). Yield: 29.8 mg (30%, 2 steps). LC-MS (LR, ESI) = Calcd. for $C_{51}H_{64}GdN_{11}O_{12}$: 1180.40 (m/z), found: 1180.19 $[M+H]^+$

Fmoc-Dap(Mtt)-Lys(Gd-DOTA)-NH$_2$ (17)

Fmoc-Dap(Mtt)-OH **(14)** (31.0 mg, 0.053 mmol) was dissolved in DMF (2 mL) and to this solution were added 1.1 equivalents of HATU (22.6 mg, 0.059 mmol) and 10 equivalents of DIPEA (89.7 uL, 0.515 mmol). This reaction was stirred under argon for 5 min. H-Lys(Gd-DOTA)-NH_2 (37.6 mg) was dissolved in DMSO (2 mL) and added to the reaction. To this solution was added an additional 10 equivalents of DIPEA (89.7 uL, 0.515 mmol) and stirred for 1 hour. The product was precipitated using Et_2O. The product was taken forward without purification.

H-Dap(Mtt)-Lys(Gd-DOTA)-NH_2 (18)

The crude Fmoc-Dap(Mtt)-Lys(Gd-DOTA)-NH_2 **(17)** from the previous procedure was dissolved in DMF (1 mL) and DEA (110.0 uL, 1.063 mmol) was added. After stirring under ambient conditions for 30 minutes, crude product was precipitated by the addition of Et_2O to the reaction flask, centrifuging the mixture, and decanting the organic solvent. This product was dried under Ar(g). The product was purified using SPE ($ACN:H_2O$, 10%-100%). Yield: 22.6 mg (41%, 2 steps). LC-MS (LR, ESI) = Calcd. for $C_{45}H_{60}GdN_9O_9$: 1028.38 (m/z), found: 1029.16 $[M+H]^+$

Fmoc-D-Trp-Dap(Mtt)-Lys(Gd-DOTA)-NH_2 (19)

Fmoc-D-Trp-OH (16.6 mg, 0.039 mmol) was dissolved in DMF (2 mL) and to this solution were added 1.1 equivalents of HATU (16.4 mg, 0.043 mmol) and 10 equivalents of DIPEA (65.0 uL, 0.373 mmol). This reaction was stirred under argon for 5 min. H-Dap(Mtt)-Lys(Gd-DOTA)-NH_2 **(18)** (38.4 mg, 0.037 mmol) and an additional 10 equivalents of DIPEA (65.0 uL, 0.373 mmol) were added to the flask and stirred for 2 hours. The reaction was monitored using HPLC-MS. The product was purified using SPE ($ACN:H_2O$, 10%-100%). Yield: 17.2 mg (32%). LC-MS (LR, ESI) = Calcd. for $C_{71}H_{80}GdN_{11}O_{12}$: 1436.52 (m/z), found: 1437.21 $[M+H]^+$

Fmoc-D-Trp-Dap(H)-Lys(Gd-DOTA)-NH_2 (20)

Fmoc-D-Trp-Dap(Mtt)-Lys(Gd-DOTA)-Dap(Mtt)-NH_2 **(19)** (32.5 mg, 0.023 mmol) was dissolved in DCM (2 mL). The flask was placed in an ice bath and pure TFA (20 uL) was added via syringe. The flask was removed from the ice bath and the reaction stirred under ambient conditions for 45 minutes and was monitored by HPLC-MS. Crude product was precipitated by the addition of Et_2O, and the organic layer was decanted after centrifugation. The reaction was purified using SPE (ACN:H_2O, 10%-100%) with 13 x 100 mL size test tube fractions. Yield: 19.0 mg (71%). LC-MS (LR,ESI) = Calcd. for $C_{51}H_{64}GdN_{11}O_{12}$: 1180.40 (m/z), found: 1181.07 $[M+H]^+$, 591.10 $([M+2H]/2)^{2+}$. MS (HR,ESI) = Calcd. for $C_{51}H_{64}GdN_{11}O_{12}$: 1180.3977 (m/z), found: 1179.3945 $[M-H]^-$

Fmoc-Dap(Mtt)-NH_2 (21)

Fmoc-Dap(Mtt)-OH **(14)** (172.9 mg, 0.297 mmol) was dissolved in DCM (5 mL) under Ar(g). Added in quick succession were 30 equivalents of DIPEA (1.56 mL, 8.956 mmol) and 2 equivalents of TSTU (179.4 mg, 0.595 mmol). After 30 minutes, 30% aqueous ammonia (53.9 uL, 1.069 mmol) was added to the solution. The reaction was run for 2 h. The solution was rotary evaporated and dried under high vacuum. The solution was washed with 5 mL of half-saturated aqueous NaCl solution. 5 mL of fresh DCM was used to back-extract the aqueous layer. The product was taken forward without any further purification. MS (HR,ESI) = Calcd. for $C_{38}H_{35}N_3O_3$: 581.26784 (m/z), found: 582.2781 $[M+H]^+$

H-Dap(Mtt)-NH_2 (22)

The crude Fmoc-Dap(Mtt)-NH_2 **(21)** from the previous procedure was dissolved in DCM (5 mL) and DEA (735.1 uL, 7.106 mmol) was added. After stirring under ambient conditions for 4 hours, crude product was precipitated by the addition of hexanes, then washed with 1 mL of Et_2O. The product was rotary evaporated, then dried under high vacuum. Yield: 86.8 mg (68%, 2 steps). LC-MS (LR, ESI) = Calcd. for $C_{23}H_{25}N_3O$: 359.20 (m/z), found: 359.20 $[M+H]^+$

Fmoc-D-Lys(Gd-DOTA)-Dap(Mtt)-NH_2 (23)

Fmoc-D-Lys(Gd-DOTA)-OH **(7)** (217.5 mg, 0.239 mmol) was dissolved in DMF and to this solution were added 1.1 equivalents of HATU (99.7 mg, 0.262 mmol) and 10 equivalents of DIPEA (420.2 uL, 2.412

mmol). This reaction was stirred under argon for 5 min. H-Dap(Mtt)-NH2 (86.8 mg, 0.242 mmol) and an additional 10 equivalents of DIPEA (420.2 uL, 2.412 mmol) were added to the flask and stirred for 1.5 hours. The product was purified using SPE (ACN:H_2O, 10%-100%). Yield: 75.0 mg (25%). LC-MS (LR, ESI) = Calcd. for $C_{60}H_{70}GdN_9O_{11}$: 1250.44 (m/z), found: 1251.27 $[M+H]^+$. MS (HR,ESI) = Calcd. for $C_{60}H_{70}GdN_9O_{11}$: 1250.44359 (m/z), found: 1249.4395 $[M-H]^-$

H-D-Lys(Gd-DOTA)-Dap(Mtt)-NH_2 (24)

To a solution of Fmoc-D-Lys(Gd-DOTA)-Dap(Mtt)-NH_2 **(23)** (75.0 mg, 0.060 mmol) in DMF (2 mL) was added 20 equivalents of DEA (124.0 uL, 1.20 mmol). After stirring under ambient conditions for one hour, crude product was precipitated by the addition of Et_2O to the reaction flask, centrifuging the mixture, and decanting the organic solvent. This product was dried under high vacuum. Yield: 70.7 mg (98%). LC-MS (LR, ESI) = Calcd. for $C_{45}H_{60}GdN_9O_9$: 1028.38 (m/z), found: 1029.22 $[M+H]^+$

Fmoc-D-Trp-D-Lys(Gd-DOTA)-Dap(Mtt)-NH_2 (25)

Fmoc-D-Trp-OH (24.7 mg, 0.058 mmol) was dissolved in DMF (1 mL) and to this solution were added 1.1 equivalents of HATU (22.0 mg, 0.058 mmol) and 10 equivalents of DIPEA (98.5 uL, 0.688 mmol). This reaction was stirred under argon for 5 min. H-D-Lys(Gd-DOTA)-Dap(Mtt)-NH_2 **(24)** (70.7 mg, 0.056 mol) and an additional 10 equivalents of DIPEA (98.5 uL, 0.688 mmol) were added to the flask and stirred for 1.5 hours under argon. Crude product was precipitated by the addition of Et_2O, and the organic layer was decanted after centrifugation. The product was purified using SPE (ACN:H_2O, 10%-100%) Yield: 56.9 mg (70%).

Fmoc-D-Trp-D-Lys(Gd-DOTA)-Dap(H)-NH_2 (26)

Fmoc-D-Trp-D-Lys(Gd-DOTA)-Dap(Mtt)-NH_2 **(25)** (56.9 mg, 0.040 mmol) was dissolved in DCM (3 mL). The flask was placed in an ice bath and pure TFA (30 uL) was added via syringe. The flask was removed from the ice bath and the reaction stirred under ambient conditions for 1.5 hours and was monitored by HPLC-MS. Crude product was precipitated by the addition of Et_2O, and the organic layer was decanted after centrifugation. The reaction was purified using SPE (ACN:H_2O, 10%-100%) with 13 x 100 mL size test tube fractions. Yield: 39.3 mg (84%). LC-MS (LR, ESI) = Calcd. for $C_{51}H_{64}GdN_{11}O_{12}$: 1180.40 (m/z), found: 1181.13 $[M+H]^+$.MS (HR,ESI) = Calcd. for $C_{51}H_{64}GdN_{11}O_{12}$: 1180.3977 (m/z), found: 1179.3926 $[M-H]^-$.

Cbz-D-Trp-Lys(Gd-DOTA)-NH$_2$ (27)

Cbz-D-Trp-OH (49.3 mg, 0.146 mmol) was dissolved in DMF (2 mL) and to this solution was added 10 equivalents of DIPEA (254.0 uL, 1.458 mmol) and 1.1 equivalents of HATU (61.0 mg, 0.147 mmol). This reaction was stirred under argon for 5 min. H-Lys(Gd-DOTA)-NH$_2$ **(3)** (101.0 mg was dissolved in DMSO (3 mL) and added to the reaction. To this solution was added an additional 10 equivalents of DIPEA (254.0 uL, 1.458 mmol). The reaction ran for 2 hrs. Crude product was precipitated by the addition of EtOAc, and the organic layer was decanted after centrifugation. Pure product was obtained by SPE (5%-50% ACN:H_2O). Fractions containing pure product were collected, concentrated by rotary evaporation, and freeze dried. Yield: 89.6 mg (61%). LC-MS (LR,ESI) = Calcd. for $C_{41}H_{54}GdN_9O_{11}$: 1006.32 (m/z), found: 1007.17 $[M+H]^+$. MS (HR,ESI) = Calcd. for $C_{41}H_{54}GdN_9O_{11}$: 1006.31839 (m/z), found: 1007.3290 $[M+H]^+$, 504.1678 $([M+2H]/2)^{2+}$

Cbz-D-Trp-D-Lys(Gd-DOTA)-OH (28)

Cbz-D-Trp-OH (12.8 mg, 0.038 mmol) was dissolved in DMF (1 mL) and to this solution was added 10 equivalents of DIPEA (63.4 uL, 0.364 mmol) and 1.1 equivalents of HATU (16.0 mg, 0.042 mmol). This reaction was stirred under argon for 5 min. H-D-Lys(Gd-DOTA)-OH **(8)** (27.3 mg, 0.040 mmol) was dissolved in DMSO (1 mL) and added to the reaction. To this solution was added an additional 10 equivalents of DIPEA (63.4 uL, 0.364 mmol). The reaction ran for 2 hrs. Crude product was precipitated by the addition of EtOAc, and the organic layer was decanted after centrifugation. Pure product was obtained by SPE (ACN:H_2O, 10%-100%). Fractions containing pure product were collected, concentrated by rotary evaporation, and freeze dried. Yield: 14.7 mg (41%). LC-MS (LR,ESI) = Calcd. for $C_{41}H_{53}GdN_8O_{12}$:1007.30 (m/z), found: 1008.24 $[M+H]^+$. MS (HR,ESI) = Calcd. for $C_{41}H_{53}GdN_8O_{12}$:1007.30241 (m/z), found: 1008.3143 $[M+H]^+$, 504.6606 ([M+2H]/2)

Fmoc-D-Trp-D-Trp-Lys(Gd-DOTA)-NH_2 (29)

Fmoc-D-Trp-OH (27.9 mg, 0.065 mmol) was dissolved in DMF (2 mL) and to this solution was added 10 equivalents of DIPEA (113.9 uL, 0.655 mmol) and 1.1 equivalents of HATU (27.5 mg, 0.072 mmol). This reaction stirred under argon for 5 min. H-D-Trp-Lys(Gd-DOTA)-NH2 (31.0 mg, 0.035 mmol) was dissolved in DMSO (1 mL) and added to the reaction. To this solution was added an additional 10 equivalents of DIPEA (113.9 uL, 0.655 mmol). The reaction ran for 2 hrs. Crude product was precipitated by the addition of Et_2O, and the organic layer was decanted after centrifugation. Pure product was obtained by SPE (ACN:H_2O, 10%-100%) Fractions containing pure product were collected, concentrated by rotary evaporation, and freeze dried. Yield: 49.7 mg (59%). LC-MS (LR,ESI) = Calcd. for $C_{59}H_{68}GdN_{11}O_{12}$:1280.49 (m/z), found: 1281.27 $[M+H]^+$.

H-D-Trp-D-Trp-Lys(Gd-DOTA)-NH_2 (30)

To a solution of Fmoc-D-Trp-D-Trp-Lys(Gd-DOTA)-NH_2 **(29)** (0.0497 mg, 0.039 mmol) in DMF (5 mL) was added 20 equivalents of DEA (80.3 uL, 0.78 mmol). After stirring under ambient conditions for 0.5 hr, crude product was precipitated by the addition of Et_2O to the reaction flask, centrifuging the mixture, and decanting the organic solvent.This product was dried under high vacuum. Yield: 39.7 mg (96%) LC-MS (LR,ESI) = Calcd. for $C_{44}H_{58}GdN_{11}O_{10}$: 1058.36 (m/z), found: 1058.66 $[M+H]^+$.

DCL-DSS (31)

DCL-DSS **(31)** was synthesized according to previous literature procedure.[58]

DCL-DSS-D-Trp-D-Trp-Lys(Gd-DOTA)-NH_2 (32)

H-D-Trp-D-Trp-Lys(Gd-DOTA)-NH_2 **(30)** (10.0 mg, 0.009 mmol) was dissolved in DMF (1.5 mL) under argon. 10 equivalents of TEA (46.9 uL, 0.094 mmol) was added to the flask. DCL-DSS **(21)** (7.0 mg, 0.013 mmol) was dissolved in DMF (1 mL) under argon and added to the flask. The reaction was stirred for 5 hours. Crude product was precipitated by the addition of Et_2O, and the organic layer was decanted after centrifugation. The reaction was purified using SPE (ACN:H_2O, 10%-100%), with 13 x 100 mL size test tube fractions. Yield: 3.1 mg (22%). LC-MS (LR,ESI) = Calcd. for $C_{64}H_{89}GdN_{14}O_{19}$: 1515.73 (m/z), found: 1515.67 $[M+H]^+$, 758.80 $([M+2H]/2)^{2+}$

Fmoc-D-Trp-NH_2 (33)

The solid Fmoc-D-Trp-OH (2.14 g, 5.02 mmol) was dissolved in 100 mL of DCM. Added in quick succession were 3 equivalents of DIPEA (2.62 mL, 15.09 mmol), and 1.2 equivalents HATU (2.30 g, 6.04 mmol). After 5 minutes, 30% aqueous ammonia (1.14 mL, 54.19 mmol) was added to the solution. The reaction was monitored every 0.5h by TLC (50:50 mixture of EtOAc:hexanes). The reaction was run for 1h. The solution was rotary evaporated and dried under high vacuum. Purification was done by extraction using DCM versus potassium sulfate, sodium carbonate, and sodium chloride with a sequential back extraction of aqueous layers with a single DCM layer. The product in organic phase was rotary evaporated and dried under high vacuum. Yield: 1.860 g (87%). LC-MS (LR,ESI) = Calcd. for $C_{26}H_{23}N_3O_3$: 425.17 (m/z), found: 426.24 $[M+H]^+$

H-D-Trp-NH_2 (34)

To a solution of Fmoc-D-Trp-NH_2 **(33)** (497.9 mg, 1.17 mmol) in DCM (10 mL) was added 20 equivalents of DEA (2.43 mL, 23.5 mmol). After stirring under ambient conditions for one hour, crude product was precipitated by the addition of Et_2O to the reaction flask, centrifuging the mixture, and decanting the organic solvent. This product was dried under high vacuum. Yield: 213.6 mg (90%). LC-MS (LR,ESI) = Calcd. for $C_{11}H_{13}N_3O$: 203.11 (m/z), found: 204.19 $[M+H]^+$

Fmoc-D-Trp-D-Trp-NH_2 (35)

Fmoc-D-Trp-OH (99.1 mg, 0.232 mmol) was dissolved in DMF (1 mL) and to this solution was added 10 equivalents of DIPEA (408.5 uL, 2.34 mmol) and HATU (96.7 mg, 0.254 mmol). This reaction stirred under argon for 5 minutes. H-D-Trp-NH_2 **(34)** (47.0 mg, 0.231 mmol) was dissolved in DMF (2 mL). To this solution was added 15 equivalents of DIPEA (601.0 uL, 3.45 mmol). The reaction ran for 2 hrs. The reaction was quenched by diluting to a volume of 25 mL with H2O and then extracted with 25 mL EtOAc. Pure product was obtained by normal-phase column chromatography (50%-100% EtOAC:hexanes). Fractions containing pure product were collected, concentrated by rotary evaporation, and freeze dried. Yield: 44.2 mg (31%). LC-MS (LR,ESI) = Calcd. for $C_{37}H_{33}N_5O_4$: 611.25 (m/z), found: 612.56 $[M+H]^+$

H-D-Trp-D-Trp-NH_2 (36)

To a solution of Fmoc-D-Trp-D-Trp-NH_2 **(35)** (44.2 mg, 0.072 mmol) in DMF (1 mL) was added 20 equivalents of DEA (149.5 uL, 1.45 mmol). After stirring under ambient conditions for one hour, crude product was precipitated by the addition of hexanes to the reaction flask, centrifuging the mixture, and decanting the organic solvent. This product was dried under high vacuum. Yield: 24.1 mg (86%). Yield: 44.2 mg (31%). LC-MS (LR,ESI) = Calcd. for $C_{22}H_{23}N_5O_2$: 389.18 (m/z), found: 390.47 $[M+H]^+$

Fmoc-D-Lys(Gd-DOTA)-D-Trp-D-Trp-NH_2 (37)

Fmoc-D-Lys(Gd-DOTA)-OH **(7)** (205.4 mg, 0.225 mmol) was dissolved in DMF (3 mL) and to this solution was added 10 equivalents of DIPEA (392.7 uL, 2.25 mmol) and HATU (95.9 mg, 0.252 mmol). This reaction stirred under argon for 5 minutes. H-D-Trp-D-Trp-NH_2 **(36)** (87.8 mg, 0.225 mmol) was dissolved in DMF (2 mL). To this solution was added 10 equivalents of DIPEA (392.7 uL, 2.25 mmol). The reaction ran for 2 hrs. Crude product was precipitated by the addition of Et_2O, and the organic layer was decanted after centrifugation. Pure product was obtained by SPE. Fractions containing pure product were collected, concentrated by rotary evaporation, and freeze dried. Yield: 58.1 mg (15%). LC-MS (LR,ESI) = Calcd. for $C_{59}H_{68}GdN_{11}O_{12}$: 1280.49 (m/z), found: 1281.60 $[M+H]^+$.

H-D-Lys(Gd-DOTA)-D-Trp-D-Trp-NH_2 (38)

To a solution of Fmoc-D-Lys(Gd-DOTA)-D-Trp-D-Trp-NH_2 **(37)** (58.1 mg, 0.045 mmol) in DMF (1 mL) was added DEA (93.9 uL, 0.907 mmol). After stirring under ambient conditions for 1 hour, crude product was precipitated by the addition of Et_2O to the reaction flask, centrifuging the mixture, and decanting the organic solvent. This product was dried under high vacuum. Yield: 45.3 mg (94%). LC-MS (LR,ESI) = Calcd. for $C_{44}H_{58}GdN_{11}O_{10}$: 1058.36 (m/z), found: 1058.68 $[M+H]^+$.

DCL-DSS-D-Lys(Gd-DOTA)-D-Trp-D-Trp-NH_2 (39)

H-D-Lys(Gd-DOTA)-D-Trp-D-Trp-NH2 **(26)** (8.5 mg, 0.008 mmol) was dissolved in DMF (1.5 mL) under argon. 10 equivalents of TEA (8.8 uL, 0.080 mmol) was added to the flask. DCL-DSS **(27)** (10.1 mg, 0.018 mmol) was dissolved in DMF (1 mL) under argon and added to the flask. The reaction was stirred for 5 hours. Crude product was precipitated by the addition of Et_2O, and the organic layer was decanted after centrifugation. The reaction was purified using SPE (ACN:H_2O, 10%-100%), with 13 x 100 mL size test tube fractions. Yield: 2.2 mg (22%). LC-MS (LR,ESI) = Calcd. for $C_{64}H_{89}GdN_{14}O_{19}$: 1516.52 (m/z), found: 1516.52 $[M+H]^+$, 758.79 $([M+2H]/2)^{2+}$

Fmoc-D-Phe-Lys(Gd-DOTA)-NH_2 (40)

Fmoc-D-Phe-OH (11.3 mg, 0.029 mmol) was dissolved in DMF (0.5 mL) and to this solution was added 10 equivalents of DIPEA (50.8 uL, 0.292 mmol) and 1.1 equivalents of HATU (0.292 mg, 0.032 mmol). This reaction stirred under argon for 5 minutes. H-Lys(Gd-DOTA)-NH_2 **(3)** (19.9 mg, 0.029 mmol) was dissolved in DMSO (1 mL) and added to the reaction. To this solution was added 10 equivalents of DIPEA (50.9 uL, 0.292 mmol). The reaction ran for 2 hrs. Crude product was precipitated by the addition of Et_2O, and the organic layer was decanted after centrifugation. Pure product was obtained by flash chromatography. Purification was done by flash chromatography (ACN:H_2O, 10%-100%, 20 min). Fractions containing pure product were collected, concentrated by rotary evaporation, and freeze dried.

Yield: 11.2 mg (35%). LC-MS (LR,ESI) = Calcd. for $C_{46}H_{57}GdN_8O_{11}$: 1055.34 (m/z), found: 1056.37 $[M+H]^+$

Fmoc-D-Tyr-Lys(Gd-DOTA)-NH$_2$ (41)

Fmoc-D-Tyr-OH (12.2 mg, 0.030 mmol) was dissolved in DMF (0.5 mL) and to this solution was added 10 equivalents of DIPEA (25.4 uL, 0.146 mmol) and 1.1 equivalents of HATU (11.6 mg, 0.031 mmol). This reaction stirred under argon for 5 minutes. H-Lys(Gd-DOTA)-NH$_2$ **(3)** (20.2 mg, 0.029 mmol) was dissolved in DMSO (1 mL) and added to the reaction. The reaction ran for 2 hrs with careful monitoring of pH to ensure it remained between 9 and 10. Crude product was precipitated by the addition of Et_2O, and the organic layer was decanted after centrifugation. Purification was done by flash chromatography (ACN:H_2O, 10%-100%, 20 min). Fractions containing pure product were collected, concentrated by rotary evaporation, and freeze dried. Yield: 12.8 mg (41%). LC-MS (LR,ESI) = Calcd. for $C_{46}H_{57}GdN_8O_{12}$: 1071.33 (m/z), found: 1072.29 $[M+H]^+$

Fmoc-D-Trp-D-Lys(Gd-DOTA)-Dap(DCL-DSS)-NH2 (42)

Fmoc-D-Trp-D-Lys(Gd-DOTA)-Dap(H)-NH$_2$ **(26)** (10.2 mg, 0.0086 mmol) was dissolved in DMF (1.5 mL) under argon. 40 equivalents of TEA (46.9 uL, 0.336 mmol) was added to the flask. DCL-DSS **(31)** (7.4 mg, 0.0129 mmol) was dissolved in DMF (1 mL) under argon and added to the flask. The reaction was stirred for 5 hours. Crude product was precipitated by the addition of Et_2O, and the organic layer was decanted after centrifugation. The reaction was purified using SPE (ACN:H_2O, 5%-50%), with 13 x 100 mL size test tube fractions. Yield: 8.5 mg (60%). LC-MS (LR, ESI) = Calcd. for $C_{71}H_{95}GdN_{14}O_{21}$: 1637.60 (m/z), found: 1638.31 $[M+H]^+$, 820.09 $([M+2H]/2)^{2+}$. MS (HR,ESI) = Calcd. for $C_{71}H_{95}GdN_{14}O_{21}$: 1637.60373 (m/z), found: 1636.6024 $[M-H]^-$, 817.7964 $([M-2H]/2)^{2-}$, 819.8121 $([M+2H]/2)^{2+}$.

H-PEG8-COOH (43)

To a solution of Fmoc-NH-PEG8-COOH (25.1 mg, 0.039 mmol) in DCM (1 mL) was added 20 equivalents of DEA (79.6 uL, 0.770 mmol). After stirring under ambient conditions for three hours, crude product was precipitated by the addition of hexanes to the reaction flask, centrifuging the mixture, and decanting the organic solvent. This product was dried under high vacuum. Yield: 15.3 mg (93%). (41%). LC-MS (LR,ESI) = Calcd. for $C_{18}H_{37}NO_{10}$: 427.24 (m/z), found: 428.50 $[M+H]^+$

Fmoc-D-Trp-D-Lys(Gd-DOTA)-PEG8-COOH (44)

Fmoc-D-Trp-D-Lys(Gd-DOTA)-OH **(9)** (59.6 mg, 0.054 mmol) was dissolved in DMF (1 mL) and to this solution was added 10 equivalents of DIPEA (92.1 uL, 0.529 mmol) and HATU (23.5 mg,). This reaction stirred under argon for 5 minutes. H-PEG8-COOH **(43)** (22.6 mg, 0.053 mmol) was dissolved in DMF (0.5 mL). To this solution was added an additional 10 equivalents of DIPEA (92.1 uL, 0.529 mmol). The reaction ran for 2 hrs. Crude product was precipitated by the addition of Et_2O, and the organic layer was decanted after centrifugation. Pure product was obtained by flash chromatography (ACN:H_2O, 10%-100%, 20 min). Fractions containing pure product were collected, concentrated by rotary evaporation, and freeze dried. Yield: 55.0 mg (69%). LC-MS (LR,ESI) = Calcd. for $C_{66}H_{92}GdN_9O_{21}$: 1504.74 (m/z), found: 1505.63 $[M+H]^+$, 752.37 $([M+2H]/2)^{2+}$

DCL (45)

DCL **(45)** was synthesized according to previous literature procedure.[58]

Fmoc-D-Trp-D-Lys(Gd-DOTA)-PEG8-DCL (46)

Fmoc-D-Trp-D-Lys(Gd-DOTA)-PEG8-COOH (10.7 mg, 0.007 mmol) was dissolved in DMF (0.5 mL) and to this solution was added 10 equivalents of DIPEA (12.6 uL, 0.072 mmol) and 1.2 equivalents of TSTU (2.9 mg, 0.010 mmol). This reaction stirred under argon for 30 minutes and was monitored by HPLC-MS after treating a sample with 0.1% aqueous butylamine. The crude product was then isolated through precipitation with warm EtOAc followed by drying under argon. The crude product was redissolved in DMF (1 mL) and 2 equivalents of DCL **(45)** (3.5 mg, 0.011 mmol) and 10 equivalents of

DIPEA (12.6 uL, 0.072 mmol) were added. The reaction ran for 3 hrs. Crude product was precipitated by the addition of Et_2O, and the organic layer was decanted after centrifugation. Pure product was obtained by flash chromatography (ACN:H_2O, 10%-100%, 20 min). Fractions containing pure product were collected, concentrated by rotary evaporation, and freeze dried. LC-MS (LR,ESI) = Calcd. for $C_{78}H_{111}GdN_{12}O_{27}$: 1805.69 (m/z), found: 1807.24 $[M+H]^+$, 903.44 $([M+2H]/2)^{2+}$. MS (HR,ESI) = Calcd. for $C_{78}H_{111}GdN_{12}O_{27}$: 1805.69227 (m/z), found: 1806.6989 $[M+H]^+$, 903.8563 $([M+2H]/2)^{2+}$, 602.9069 $([M+3H]/3)^{3+}$

Fmoc-D-Trp-D-Lys(Gd-DOTA)-PEG8-18-4 (47)

Fmoc-D-Trp-D-Lys(Gd-DOTA)-PEG8-COOH **(46)** (11.5 mg, 0.008 mmol) was dissolved in DMF (0.5 mL) and to this solution was added 10 equivalents of DIPEA (13.5 uL, 0.078 mmol) and 1.2 equivalents of TSTU (3.1 mg, 0.010 mmol). This reaction stirred under argon for 30 minutes and was monitored by HPLC-MS after treating a sample with 0.1% aqueous butylamine. The crude product was then isolated through precipitation with warm EtOAc followed by drying under argon. The crude product was redissolved in DMF (1 mL) and 2 equivalents of 18-4 (14.7 mg, 0.015 mmol) and 10 equivalents of DIPEA (13.5 uL, 0.078 mmol) were added. The reaction ran for 3 hrs. Crude product was precipitated by the addition of Et_2O, and the organic layer was decanted after centrifugation. Pure product was obtained by flash chromatography (ACN:H_2O, 10%-100%, 20 min). Fractions containing pure product were collected, concentrated by rotary evaporation, and freeze dried. Yield: 2.2 mg (10%). LC-MS (LR,ESI) = Calcd. for $C_{129}H_{180}GdN_{25}O_{34}$: 2781.24 (m/z), found: 1391.87 $([M+2H]/2)^{2+}$, 927.95 $([M+3H]/3)^{3+}$. MS (HR, ESI) = Calcd. for $C_{129}H_{180}GdN_{25}O_{34}$: 2781.2366 (m/z), found: 1391.6276 $([M+2H]/2)^{2+}$, 928.0878 $([M+3H]/3)^{3+}$

References:

(1) Siegel, R. L.; Miller, K. D.; Jemal, A. Cancer Statistics, 2020. *CA. Cancer J. Clin.* **2020**, *70* (1), 7–30. https://doi.org/10.3322/caac.21590.

(2) CDCBreastCancer. *Who Is at Risk for Prostate Cancer?*. Centers for Disease Control and Prevention. https://www.cdc.gov/cancer/prostate/basic_info/risk_factors.htm (accessed 2021-10-26).

(3) Roehrbom, C. G.; Black, L. K. The Economic Burden of Prostate Cancer. *BJU Int.* **2011**, *108* (6), 806–813. https://doi.org/10.1111/j.1464-410X.2011.10365.x.

(4) *Key Statistics for Prostate Cancer | Prostate Cancer Facts*. https://www.cancer.org/cancer/prostate-cancer/about/key-statistics.html (accessed 2021-11-09).

(5) *PSA test - Mayo Clinic*. https://www.mayoclinic.org/tests-procedures/psa-test/about/pac-20384731 (accessed 2021-10-25).

(6) Jones, T. A.; Radtke, J. P.; Hadaschik, B.; Marks, L. S. Optimizing Safety and Accuracy of Prostate Biopsy. *Curr. Opin. Urol.* **2016**, *26* (5), 472–480. https://doi.org/10.1097/MOU.0000000000000310.

(7) Ilic, D.; Djulbegovic, M.; Jung, J. H.; Hwang, E. C.; Zhou, Q.; Cleves, A.; Agoritsas, T.; Dahm, P. Prostate Cancer Screening with Prostate-Specific Antigen (PSA) Test: A Systematic Review and Meta-Analysis. *BMJ* **2018**, *362*, k3519. https://doi.org/10.1136/bmj.k3519.

(8) *Johns Hopkins Study Reveals Significant Rise in Prostate Biopsy Complications and High Post-Procedure Hospitalization Rate - 09/22/2011*. https://www.hopkinsmedicine.org/news/media/releases/johns_hopkins_study_reveals_significant_rise_in_prostate_biopsy_complications_and_high_post_procedure_hospitalization_rate (accessed 2021-10-26).

(9) uploader, C. R. U. *English: Diagram Showing a Transperineal Prostate Biopsy*; 2016. https://commons.wikimedia.org/w/index.php?curid=46505428 (accessed 2023-11-12).

(10) Sonn, G. A.; Margolis, D. J.; Marks, L. S. Target Detection: Magnetic Resonance Imaging-Ultrasound Fusion-Guided Prostate Biopsy. *Urol. Oncol.* **2014**, *32* (6), 903–911. https://doi.org/10.1016/j.urolonc.2013.08.006.

(11) Ukimura, O.; Hung, A. J.; Gill, I. S. Innovations in Prostate Biopsy Strategies for Active Surveillance and Focal Therapy. *Curr. Opin. Urol.* **2011**, *21* (2), 115–120. https://doi.org/10.1097/MOU.0b013e3283435118.

(12) Super-resolution in Magnetic Resonance Imaging: A Review. https://doi.org/10.1002/cmr.a.21249.

(13) Berger, A. Magnetic Resonance Imaging. *BMJ* **2002**, *324* (7328), 35.

(14) Caravan, P.; Amedio Jr., J. C.; Dunham, S. U.; Greenfield, M. T.; Cloutier, N. J.; McDermid, S. A.; Spiller, M.; Zech, S. G.; Looby, R. J.; Raitsimring, A. M.; McMurry, T. J.; Lauffer, R. B. When Are Two Waters Worse Than One? Doubling the Hydration Number of a Gd–DTPA Derivative Decreases Relaxivity. *Chem. – Eur. J.* **2005**, *11* (20), 5866–5874. https://doi.org/10.1002/chem.200500338.

(15) | *GE Healthcare (United States)*. https://www.gehealthcare.com/article/overview-of-mri-contrast (accessed 2021-11-23).

(16) Østergaard, F. M., Marissa Lassere and Mikkel. *English: Magnetic Resonance Images of Sacroiliac Joints: Psoriatic Arthritis. Shown Are T1-Weighted Semi-Coronal Magnetic Resonance Images through the Sacroiliac Joints (a) before and (b) after Intravenous Contrast Injection. Enhancement Is Seen at the Right Sacroiliac Joint (Arrow), Indicating Active Sacroiliitis.*; 2006. https://commons.wikimedia.org/w/index.php?curid=5881581 (accessed 2023-11-22).

(17) Rohrer, M.; Bauer, H.; Mintorovitch, J.; Requardt, M.; Weinmann, H.-J. Comparison of Magnetic Properties of MRI Contrast Media Solutions at Different Magnetic Field Strengths. *Invest. Radiol.* **2005**, *40* (11), 715–724. https://doi.org/10.1097/01.rli.0000184756.66360.d3.

(18) Boros, E.; Polasek, M.; Zhang, Z.; Caravan, P. Gd(DOTAla): A Single Amino Acid Gd-Complex as a Modular Tool for High Relaxivity MR Contrast Agent Development. *J. Am. Chem. Soc.* **2012**, *134* (48), 19858–19868. https://doi.org/10.1021/ja309187m.

(19) Hornak, J. P. *The Basics of NMR*; Interactive Learning Software, 1996.

(20) Caravan, P.; Ellison, J. J.; McMurry, T. J.; Lauffer, R. B. Gadolinium(III) Chelates as MRI Contrast Agents: Structure, Dynamics, and Applications. *Chem. Rev.* **1999**, *99* (9), 2293–2352. https://doi.org/10.1021/cr980440x.

(21) Hao, D.; Ai, T.; Goerner, F.; Hu, X.; Runge, V. M.; Tweedle, M. MRI Contrast Agents: Basic Chemistry and Safety. *J. Magn. Reson. Imaging* **2012**, *36* (5), 1060–1071. https://doi.org/10.1002/jmri.23725.

(22) Pierre, V. C.; Allen, M. J.; Caravan, P. Contrast Agents for MRI: 30+ Years and Where Are We Going? *J. Biol. Inorg. Chem. JBIC Publ. Soc. Biol. Inorg. Chem.* **2014**, *19* (2), 127–131. https://doi.org/10.1007/s00775-013-1074-5.

(23) Sherry, A. D.; Caravan, P.; Lenkinski, R. E. A Primer on Gadolinium Chemistry. *J. Magn. Reson. Imaging JMRI* **2009**, *30* (6), 1240–1248. https://doi.org/10.1002/jmri.21966.

(24) Clough, T. J.; Jiang, L.; Wong, K.-L.; Long, N. J. Ligand Design Strategies to Increase Stability of Gadolinium-Based Magnetic Resonance Imaging Contrast Agents. *Nat. Commun.* **2019**, *10* (1), 1420. https://doi.org/10.1038/s41467-019-09342-3.

(25) Wahsner, J.; Gale, E. M.; Rodríguez-Rodríguez, A.; Caravan, P. Chemistry of MRI Contrast Agents: Current Challenges and New Frontiers. *Chem. Rev.* **2019**, *119* (2), 957–1057. https://doi.org/10.1021/acs.chemrev.8b00363.

(26) Borel, A.; Helm, L.; Merbach, A. E.; Atsarkin, V. A.; Demidov, V. V.; Odintsov, B. M.; Belford, R. L.; Clarkson, R. B. T_{1e} in Four Gd^{3+} Chelates: LODEPR Measurements and Models for Electron Spin Relaxation. *J. Phys. Chem. A* **2002**, *106* (26), 6229–6231. https://doi.org/10.1021/jp0203752.

(27) La Manna, S.; Di Natale, C.; Onesto, V.; Marasco, D. Self-Assembling Peptides: From Design to Biomedical Applications. *Int. J. Mol. Sci.* **2021**, *22* (23), 12662. https://doi.org/10.3390/ijms222312662.

(28) Koshti, B.; Kshtriya, V.; Naskar, S.; Narode, H.; Gour, N. Controlled Aggregation Properties of Single Amino Acids Modified with Protecting Groups. *New J. Chem.* **2022**, *46* (10), 4746–4755. https://doi.org/10.1039/D1NJ05172E.

(29) Singh, P.; Manhas, P.; Sharma, R.; Pandey, S. K.; Sharma, R. K.; Katare, O. P.; Wangoo, N. Self-Assembled Dipeptide Nanospheres as Single Component Based Delivery Vehicle for Ampicillin and Doxorubicin. *J. Mol. Liq.* **2020**, *312*, 113420. https://doi.org/10.1016/j.molliq.2020.113420.

(30) Halder, M.; Bhatia, Y.; Singh, Y. Self-Assembled Di- and Tripeptide Gels for the Passive Entrapment and pH-Responsive, Sustained Release of an Antidiabetic Drug, Glimepiride. *Biomater. Sci.* **2022**, *10* (9), 2248–2262. https://doi.org/10.1039/D2BM00344A.

(31) Croitoriu, A.; Nita, L. E.; Chiriac, A. P.; Rusu, A. G.; Bercea, M. New Physical Hydrogels Based on Co-Assembling of FMOC–Amino Acids. *Gels* **2021**, *7* (4), 208. https://doi.org/10.3390/gels7040208.

(32) Sharma, R.; Tomar, S.; Puri, S.; Wangoo, N. Self-Assembled Peptide Hydrogel for Accelerated Wound Healing: Impact of N-Terminal and C-Terminal Modifications. *ChemBioChem* **2022**, *23* (22), e202200499. https://doi.org/10.1002/cbic.202200499.

(33) Cao, C.-Y.; Shen, Y.-Y.; Wang, J.-D.; Li, L.; Liang, G.-L. Controlled Intracellular Self-Assembly of Gadolinium Nanoparticles as Smart Molecular MR Contrast Agents. *Sci. Rep.* **2013**, *3* (1), 1024. https://doi.org/10.1038/srep01024.

(34) Gallo, E.; Diaferia, C.; Di Gregorio, E.; Morelli, G.; Gianolio, E.; Accardo, A. Peptide-Based Soft Hydrogels Modified with Gadolinium Complexes as MRI Contrast Agents. *Pharmaceuticals* **2020**, *13* (2), 19. https://doi.org/10.3390/ph13020019.

(35) *Department of Radiology - UW-Madison | contrast corner*. https://radiology.wisc.edu/a/gad-calc/ (accessed 2022-12-25).

(36) *How Targeted Therapies Are Used to Treat Cancer*. https://www.cancer.org/treatment/treatments-and-side-effects/treatment-types/targeted-therapy/what-is.html (accessed 2021-10-29).

(37) *Biomarkers as Molecular Targets of Drug Interventions | Elsevier Enhanced Reader*. https://doi.org/10.1016/j.soncn.2012.03.004.

(38) Imai, K.; Takaoka, A. Comparing Antibody and Small-Molecule Therapies for Cancer. *Nat. Rev. Cancer* **2006**, *6* (9), 714–727. https://doi.org/10.1038/nrc1913.

(39) *Targeted Therapy for Cancer - National Cancer Institute*. https://www.cancer.gov/about-cancer/treatment/types/targeted-therapies (accessed 2021-10-30).

(40) Kratochwil, C.; Giesel, F. L.; Stefanova, M.; Benešová, M.; Bronzel, M.; Afshar-Oromieh, A.; Mier, W.; Eder, M.; Kopka, K.; Haberkom, U. PSMA-Targeted Radionuclide Therapy of Metastatic Castration-Resistant Prostate Cancer with ^{177} Lu-Labeled PSMA-617. *J. Nucl. Med.* **2016**, *57* (8), 1170–1176. https://doi.org/10.2967/jnumed.115.171397.

(41) Lapidus, R. G.; Tiffany, C. W.; Isaacs, J. T.; Slusher, B. S. Prostate-Specific Membrane Antigen (PSMA) Enzyme Activity Is Elevated in Prostate Cancer Cells. *The Prostate* **2000**, *45* (4), 350–354. https://doi.org/10.1002/1097-0045(20001201)45:4<350::aid-pros10>3.0.co;2-u.

(42) Hyväkkä, A.; Virtanen, V.; Kemppainen, J.; Grönroos, T. J.; Minn, H.; Sundvall, M. More Than Meets the Eye: Scientific Rationale behind Molecular Imaging and Therapeutic Targeting of Prostate-Specific Membrane Antigen (PSMA) in Metastatic Prostate Cancer and Beyond. *Cancers* **2021**, *13* (9), 2244. https://doi.org/10.3390/cancers13092244.

(43) Davis, M. I.; Bennett, M. J.; Thomas, L. M.; Bjorkman, P. J. Crystal Structure of Prostate-Specific Membrane Antigen, a Tumor Marker and Peptidase. *Proc. Natl. Acad. Sci. U. S. A.* **2005**, *102* (17), 5981–5986. https://doi.org/10.1073/pnas.0502101102.

(44) Mesters, J. R.; Barinka, C.; Li, W.; Tsukamoto, T.; Majer, P.; Slusher, B. S.; Konvalinka, J.; Hilgenfeld, R. Structure of Glutamate Carboxypeptidase II, a Drug Target in Neuronal Damage and Prostate Cancer. *EMBO J.* **2006**, *25* (6), 1375–1384. https://doi.org/10.1038/sj.emboj.7600969.

(45) Banerjee, S. R.; Foss, C. A.; Castanares, M.; Mease, R. C.; Byun, Y.; Fox, J. J.; Hilton, J.; Lupold, S. E.; Kozikowski, A. P.; Pomper, M. G. Synthesis and Evaluation of Technetium-99m- and Rhenium-Labeled Inhibitors of the Prostate-Specific Membrane Antigen (PSMA). *J. Med. Chem.* **2008**, *51* (15), 4504–4517. https://doi.org/10.1021/jm800111u.

(46) Kopka, K.; Benešová, M.; Bařinka, C.; Haberkorn, U.; Babich, J. Glu-Ureido–Based Inhibitors of Prostate-Specific Membrane Antigen: Lessons Learned During the Development of a Novel Class of Low-Molecular-Weight Theranostic Radiotracers. *J. Nucl. Med.* **2017**, *58* (Supplement 2), 17S-26S. https://doi.org/10.2967/jnumed.116.186775.

(47) Schmitthenner, H. F.; Barrett, T. M.; Beach, S. A.; Heese, L. E.; Weidman, C.; Dobson, D. E.; Mahoney, E. R.; Schug, N. C.; Jones, K. G.; Durmaz, C.; Otasowie, O.; Aronow, S.; Lee, Y. P.; Ophardt, H. D.; Becker, A. E.; Hornak, J. P.; Evans, I. M.; Ferran, M. C. Modular Synthesis of Peptide-Based Single- and Multimodal Targeted Molecular Imaging Agents. *ACS Appl. Bio Mater.* **2021**, *4* (7), 5435–5448. https://doi.org/10.1021/acsabm.1c00157.

(48) Ray Banerjee, S.; Chen, Z.; Pullambhatla, M.; Lisok, A.; Chen, J.; Mease, R. C.; Pomper, M. G. Preclinical Comparative Study of ^{68} Ga-Labeled DOTA, NOTA, and HBED-CC Chelated Radiotracers for Targeting PSMA. *Bioconjug. Chem.* **2016**, *27* (6), 1447–1455. https://doi.org/10.1021/acs.bioconjchem.5b00679.

(49) Banerjee, S. R.; Ngen, E. J.; Rotz, M. W.; Kakkad, S.; Lisok, A.; Pracitto, R.; Pullambhatla, M.; Chen, Z.; Shah, T.; Artemov, D.; Meade, T. J.; Bhujwalla, Z. M.; Pomper, M. G. Synthesis and Evaluation of Gd(III) -Based Magnetic Resonance Contrast Agents for Molecular Imaging of Prostate-Specific Membrane Antigen. *Angew. Chem. Int. Ed Engl.* **2015**, *54* (37), 10778–10782. https://doi.org/10.1002/anie.201503417.

(50) Kim, I.; Han, E. H.; Ryu, J.; Min, J.-Y.; Ahn, H.; Chung, Y.-H.; Lee, E. One-Dimensional Supramolecular Nanoplatforms for Theranostics Based on Co-Assembly of Peptide Amphiphiles. *Biomacromolecules* **2016**, *17* (10), 3234–3243. https://doi.org/10.1021/acs.biomac.6b00966.

(51) Li, H.; Luo, D.; Yuan, C.; Wang, X.; Wang, J.; Basilion, J. P.; Meade, T. J. Magnetic Resonance Imaging of PSMA-Positive Prostate Cancer by a Targeted and Activatable Gd(III) MR Contrast Agent. *J. Am. Chem. Soc.* **2021**, *143* (41), 17097–17108. https://doi.org/10.1021/jacs.1c07377.

(52) Schmitthenner, H. F.; Beach, S.; Weidman, C.; Barrett, T. Modular Imaging Agents Containing Amino Acids and Peptides. US20150038672A1, February 5, 2015. https://patents.google.com/patent/US20150038672A1/en (accessed 2021-12-06).

(53) Schug, N. C. Modular Synthesis of Dual- and Tri-Modal Targeted Molecular Imaging Agents. 114.

(54) Xu, X. Solid Phase Synthesis of Modular Peptide-Based Targeted Molecular Imaging Agents. https://scholarworks.rit.edu/theses/10120/.

(55) Jones, K. Modular Synthesis of Targeted Molecular Imaging Agents for MRI, PET, and PET-MRI of Cancer. 109.

(56) Kaur, B. Synthesis of Single-Modal and Dual-Modal Targeted Molecular Imaging Agents for MRI-NIR Imaging of Breast Cancer. https://scholarworks.rit.edu/theses/10880/.

(57) Soika, D. Synthesis of Modular DO3A-Based High-Relaxivity Contrast Agents for MRI of Prostate Cancer, 2022. https://scholarworks.rit.edu/theses/11300.

(58) Schmitthenner, H. F.; Dobson, D. E.; Jones, K. G.; Akporji, N.; Soika, D. Q. M.; Nastiuk, K. L.; Hornak, J. P. Modular Synthesis of DOTA-Metal-Based PSMA-Targeted Imaging Agents for MRI and PET of Prostate Cancer. *Chem. Weinh. Bergstr. Ger.* **2019**, *25* (61), 13848–13854. https://doi.org/10.1002/chem.201903390.

(59) Ozbas, B.; Kretsinger, J.; Rajagopal, K.; Schneider, J. P.; Pochan, D. J. Salt-Triggered Peptide Folding and Consequent Self-Assembly into Hydrogels with Tunable Modulus. *Macromolecules* **2004**, *37* (19), 7331–7337. https://doi.org/10.1021/ma0491762.

(60) Tugyi, R.; Uray, K.; Iván, D.; Fellinger, E.; Perkins, A.; Hudecz, F. Partial D-Amino Acid Substitution: Improved Enzymatic Stability and Preserved Ab Recognition of a MUC2 Epitope Peptide. *Proc. Natl. Acad. Sci.* **2005**, *102* (2), 413–418. https://doi.org/10.1073/pnas.0407677102.

(61) Boehm-Sturm, P.; Haeckel, A.; Hauptmann, R.; Mueller, S.; Kuhl, C. K.; Schellenberger, E. A. Low-Molecular-Weight Iron Chelates May Be an Alternative to Gadolinium-Based Contrast Agents for T1-Weighted Contrast-Enhanced MR Imaging. *Radiology* **2018**, *286* (2), 537–546. https://doi.org/10.1148/radiol.2017170116.

(62) Barnes, S. L.; Whisenant, J. G.; Loveless, M. E.; Ayers, G. D.; Yankeelov, T. E. Assessing the Reproducibility of Dynamic Contrast Enhanced Magnetic Resonance Imaging in a Murine Model of Breast Cancer. *Magn. Reson. Med.* **2013**, *69* (6), 1721–1734. https://doi.org/10.1002/mrm.24422.

(63) Steinmark, I. E.; Chung, P.-H.; Ziolek, R. M.; Cornell, B.; Smith, P.; Levitt, J. A.; Tregidgo, C.; Molteni, C.; Yahioglu, G.; Lorenz, C. D.; Suhling, K. Time-Resolved Fluorescence Anisotropy of a Molecular Rotor Resolves Microscopic Viscosity Parameters in Complex Environments. *Small* **2020**, *16* (22), 1907139. https://doi.org/10.1002/smll.201907139.

(64) Fleming, S.; Debnath, S.; M. Frederix, P. W. J.; Tuttle, T.; V. Ulijn, R. Aromatic Peptide Amphiphiles: Significance of the Fmoc Moiety. *Chem. Commun.* **2013**, *49* (90), 10587–10589. https://doi.org/10.1039/C3CC45822A.

(65) Würthner, F.; Kaiser, T. E.; Saha-Möller, C. R. J-Aggregates: From Serendipitous Discovery to Supramolecular Engineering of Functional Dye Materials. *Angew. Chem. Int. Ed.* **2011**, *50* (15), 3376–3410. https://doi.org/10.1002/anie.201002307.

(66) Rajbhandary, A.; Brennessel, W. W.; Nilsson, B. L. Comparison of the Self-Assembly Behavior of Fmoc-Phenylalanine and Corresponding Peptoid Derivatives. *Cryst. Growth Des.* **2018**, *18* (2), 623–632. https://doi.org/10.1021/acs.cgd.7b00709.

(67) Momma, K.; Izumi, F. VESTA 3 for Three-Dimensional Visualization of Crystal, Volumetric and Morphology Data. *J. Appl. Crystallogr.* **2011**, *44* (6), 1272–1276. https://doi.org/10.1107/S0021889811038970.

(68) Wang, Y.; Geng, Q.; Zhang, Y.; Adler-Abramovich, L.; Fan, X.; Mei, D.; Gazit, E.; Tao, K. Fmoc-Diphenylalanine Gelating Nanoarchitectonics: A Simplistic Peptide Self-Assembly to Meet

Complex Applications. *J. Colloid Interface Sci.* **2023**, *636*, 113–133. https://doi.org/10.1016/j.jcis.2022.12.166.

(69) Ogunnigbagbe, O.; Bunick, C. G.; Kaur, K. Keratin 1 as a Cell-Surface Receptor in Cancer. *Biochim. Biophys. Acta BBA - Rev. Cancer* **2022**, *1877* (1), 188664. https://doi.org/10.1016/j.bbcan.2021.188664.

(70) Soudy, R.; Etayash, H.; Bahadorani, K.; Lavasanifar, A.; Kaur, K. Breast Cancer Targeting Peptide Binds Keratin 1: A New Molecular Marker for Targeted Drug Delivery to Breast Cancer. *Mol. Pharm.* **2017**, *14* (3), 593–604. https://doi.org/10.1021/acs.molpharmaceut.6b00652.

(71) Soudy, R.; Gill, A.; Sprules, T.; Lavasanifar, A.; Kaur, K. Proteolytically Stable Cancer Targeting Peptides with High Affinity for Breast Cancer Cells. *J. Med. Chem.* **2011**, *54* (21), 7523–7534. https://doi.org/10.1021/jm200750x.

(72) Shaut, S. Light Directed Targeted Photodynamic Therapy of Breast Cancer. *Theses* **2022**.

(73) DeNyse, C. Dual Function Molecular Imaging Probes for Breast Cancer. *Theses* **2023**.

(74) Phosphate-Buffered Saline (PBS). *Cold Spring Harb. Protoc.* **2006**, *2006* (1), pdb.rec8247. https://doi.org/10.1101/pdb.rec8247.

Appendix

LRMS/HRMS Spectra

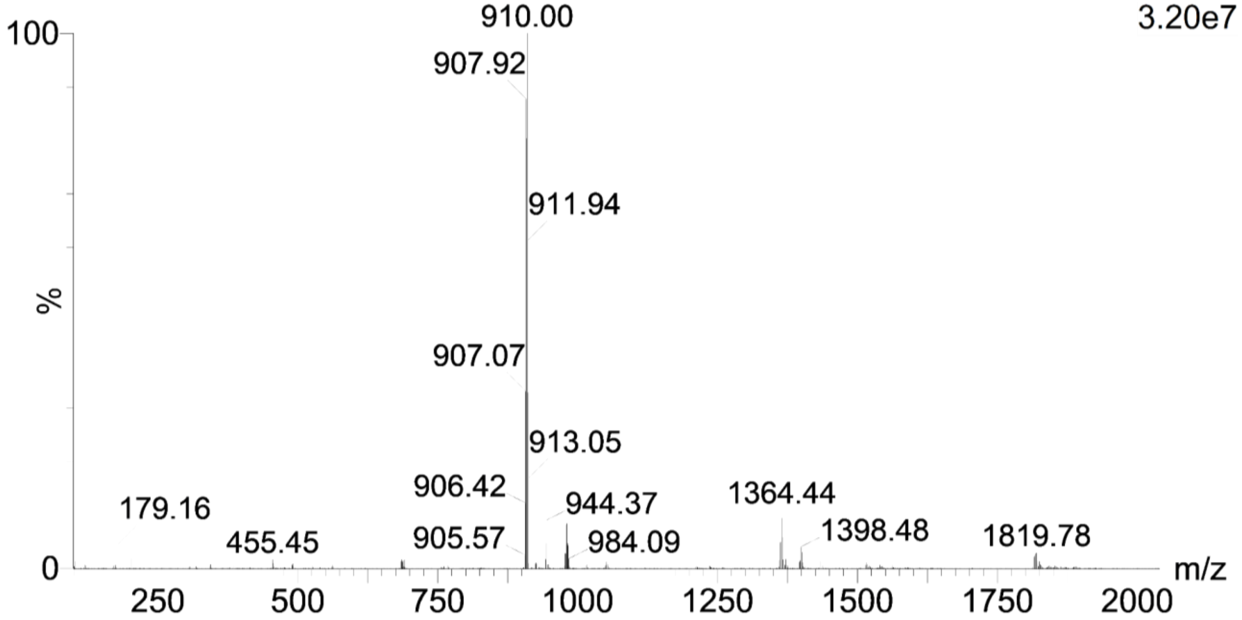

Figure S1: Positive-ion LRMS of Fmoc-Lys(Gd-DOTA)-OH **(1)**, 910.00 $[M+H]^+$

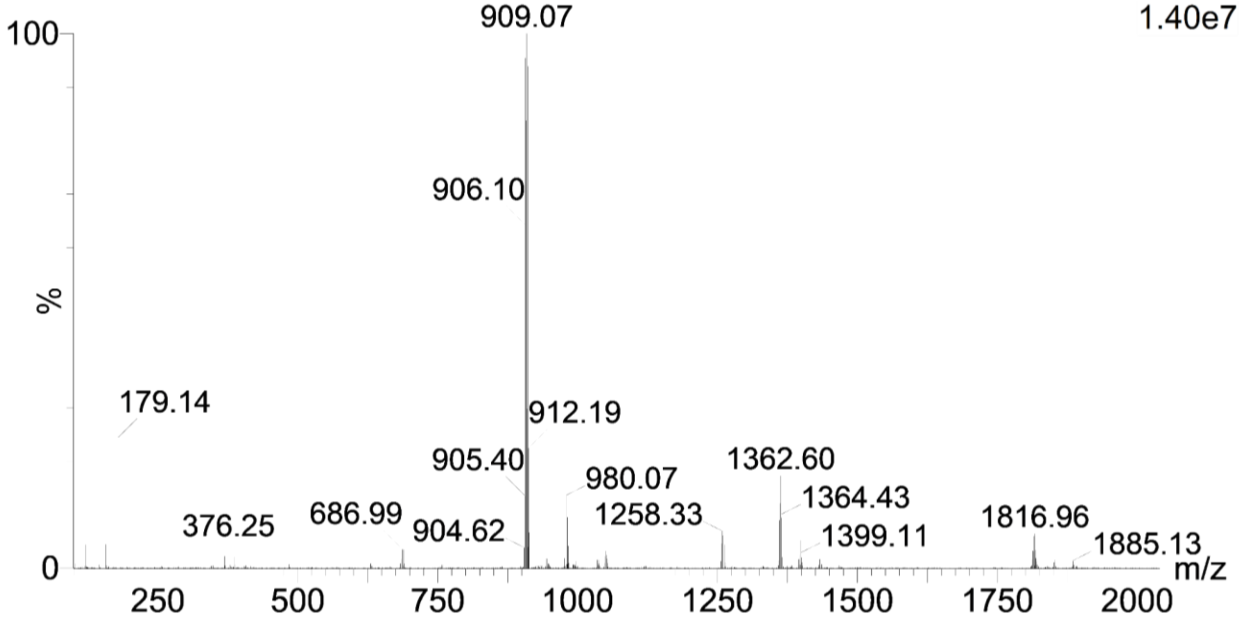

Figure S2: Positive-ion LRMS of Fmoc-Lys(Gd-DOTA)-NH_2 **(2)**, 909.07 $[M+H]^+$

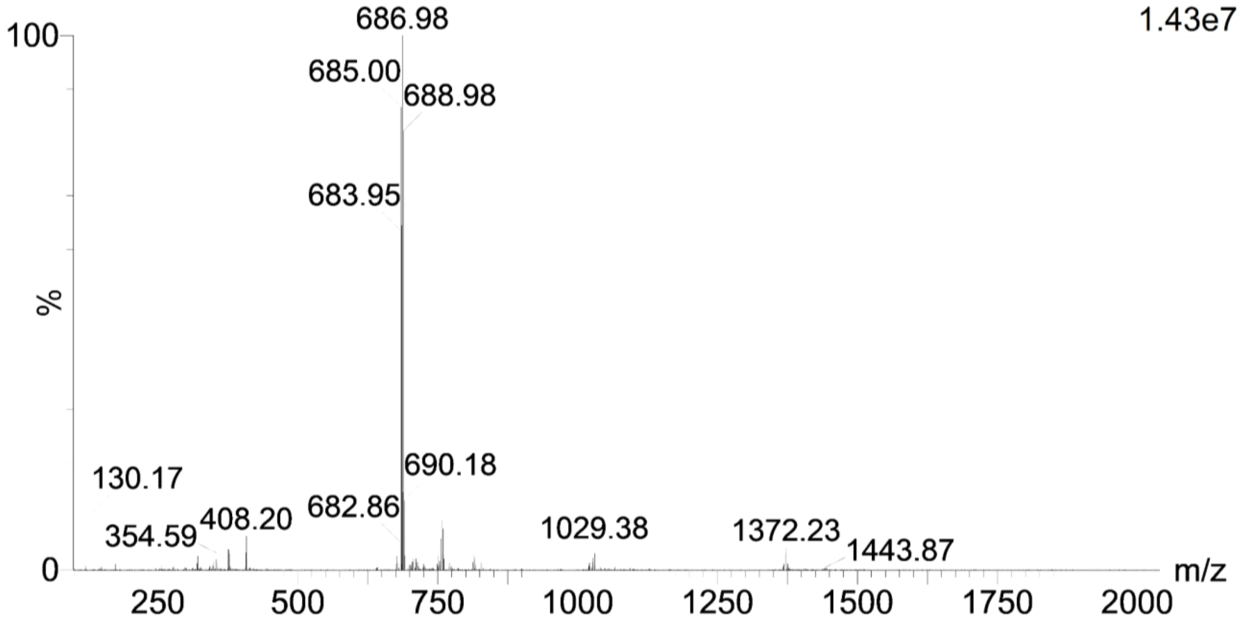

Figure S3: Positive-ion LRMS of H-Lys(Gd-DOTA)-NH_2 **(3)**, 686.98 $[M+H]^+$

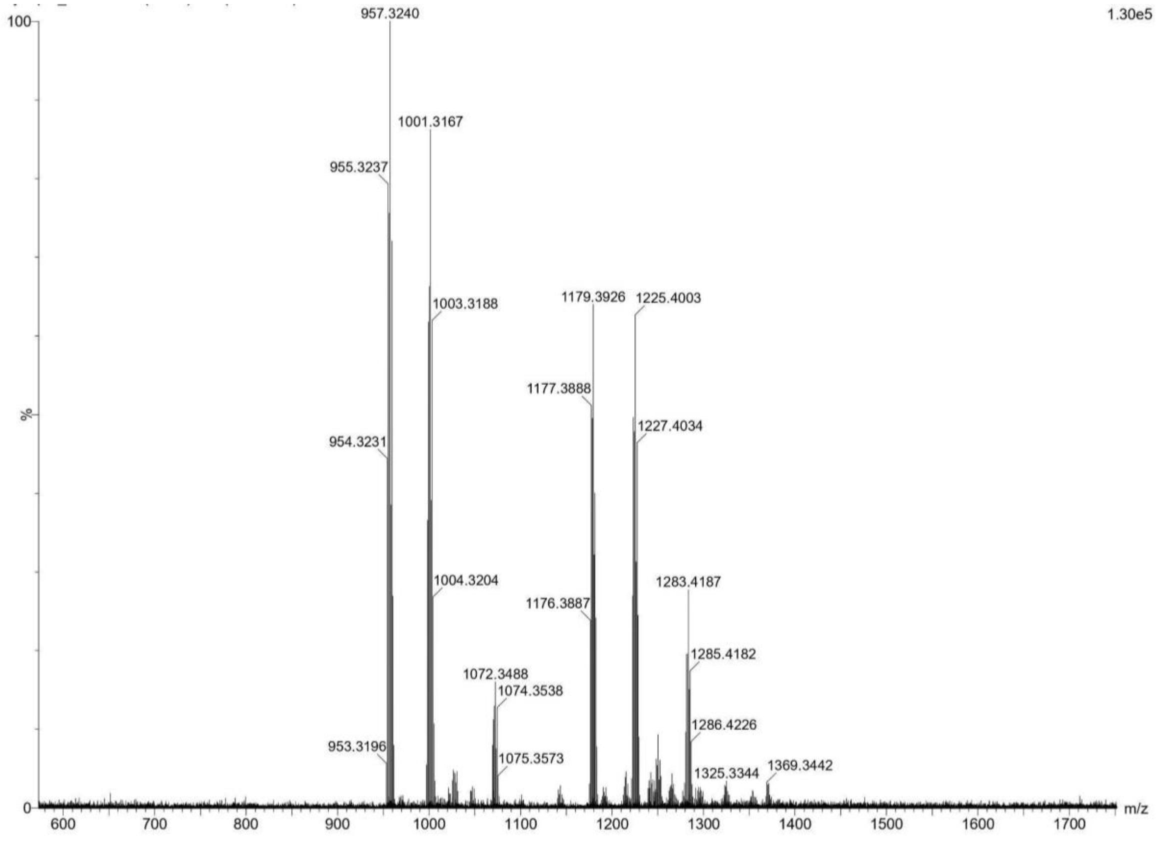

Figure S4: Negative-ion HRMS of Fmoc-D-Trp-Lys(Gd-DOTA)-NH_2 **(4)**, 1179.3926 $[M-H]^-$

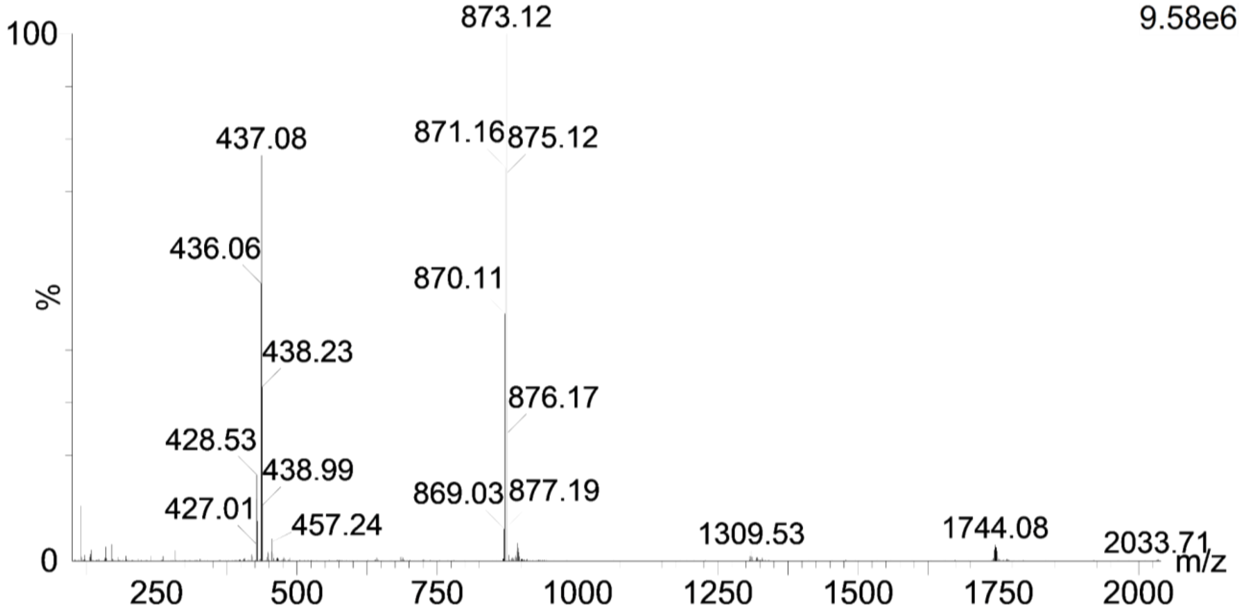

Figure S5: Positive-ion LRMS of H-D-Trp-Lys(Gd-DOTA)-NH_2 **(5)**, 873.12 $[M+H]^+$, 437.08 $([M+2H]/2)^{2+}$

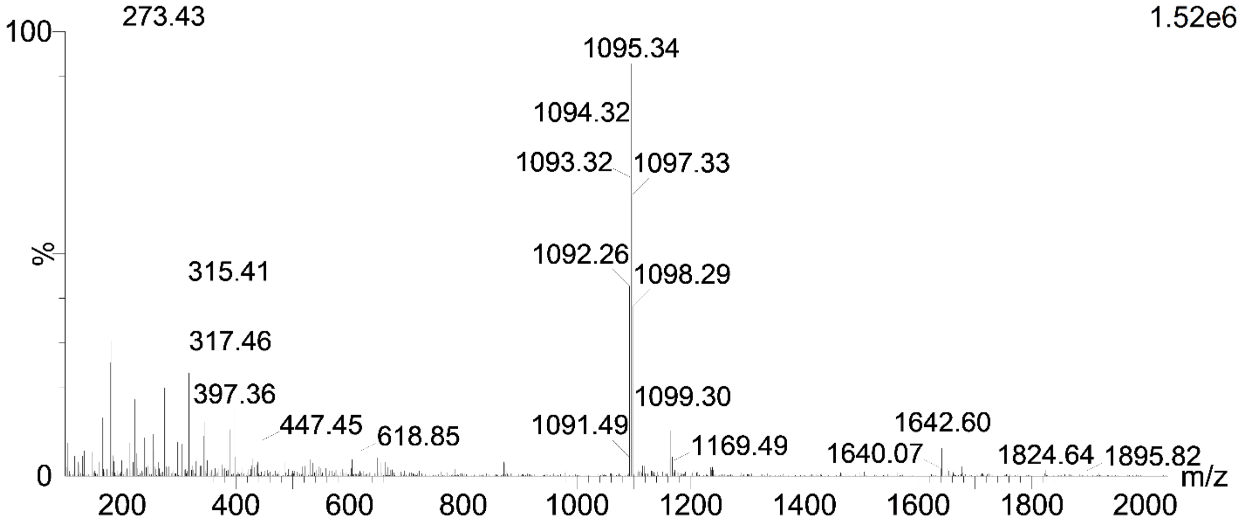

Figure S6: Positive-ion LRMS of Fmoc-Trp-Lys(Gd-DOTA)-NH_2 **(6)**, 1095.34 $[M+H]^+$

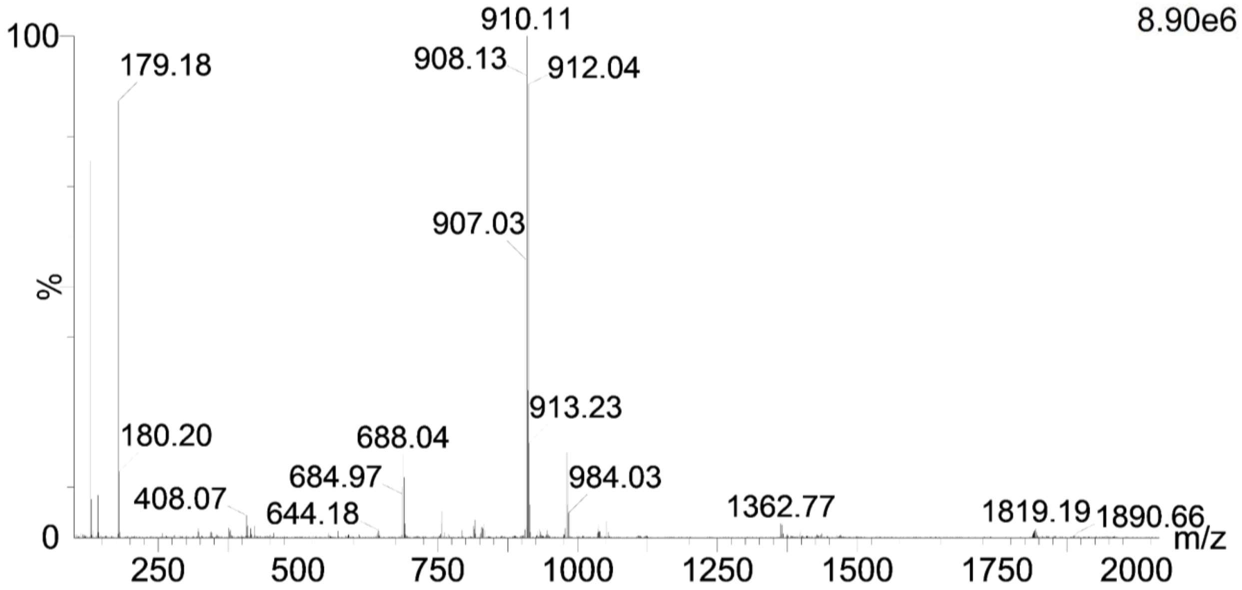

Figure S7: Positive-ion LRMS of Fmoc-D-Lys(Gd-DOTA)-OH **(7)**, 910.11 [M+H]$^+$

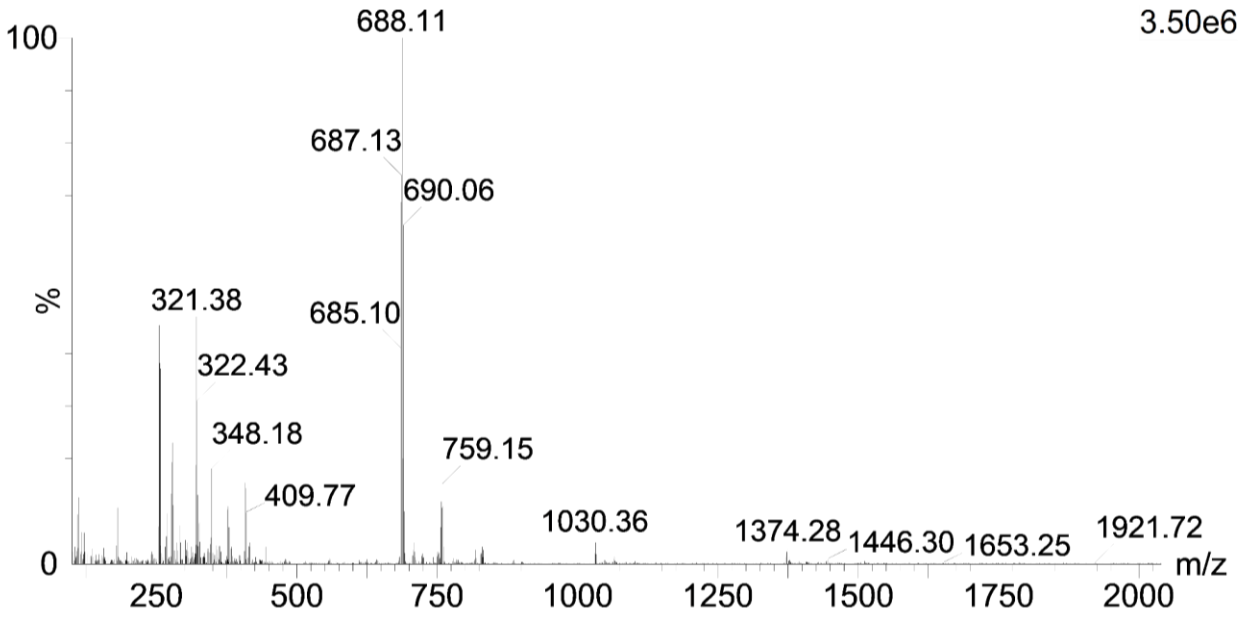

Figure S8: Positive-ion LRMS of H-D-Lys(Gd-DOTA)-OH **(8)**, 688.11 [M+H]$^+$

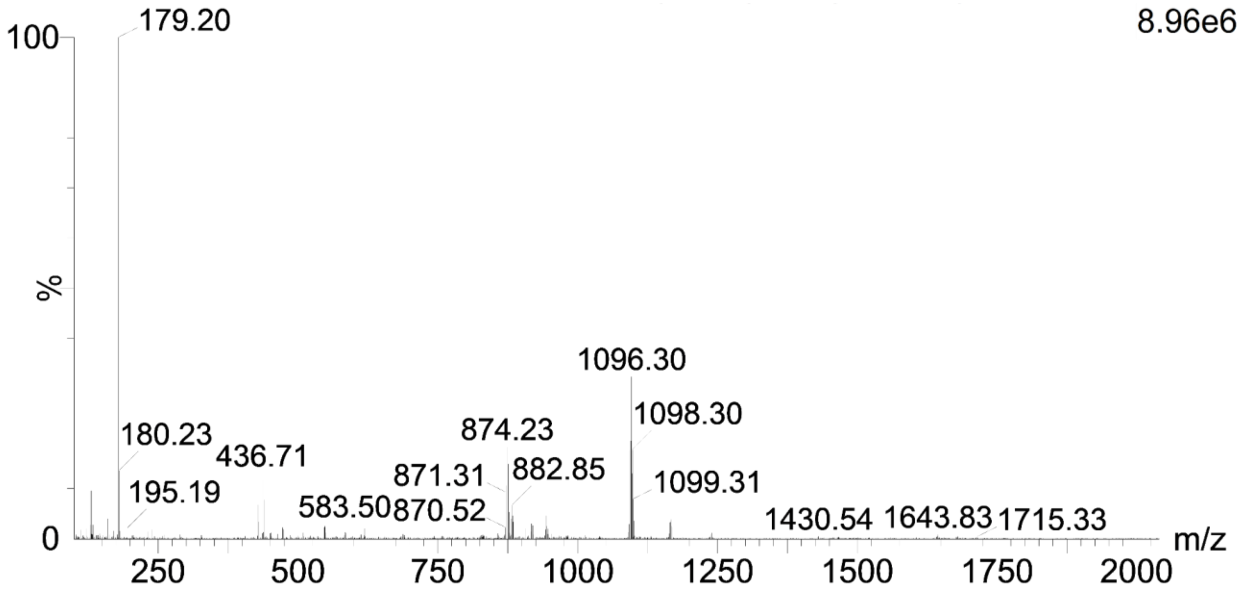

Figure S9a: Positive-ion LRMS of Fmoc-D-Trp-D-Lys(Gd-DOTA)-OH **(9)**, 1096.30 $[M+H]^+$

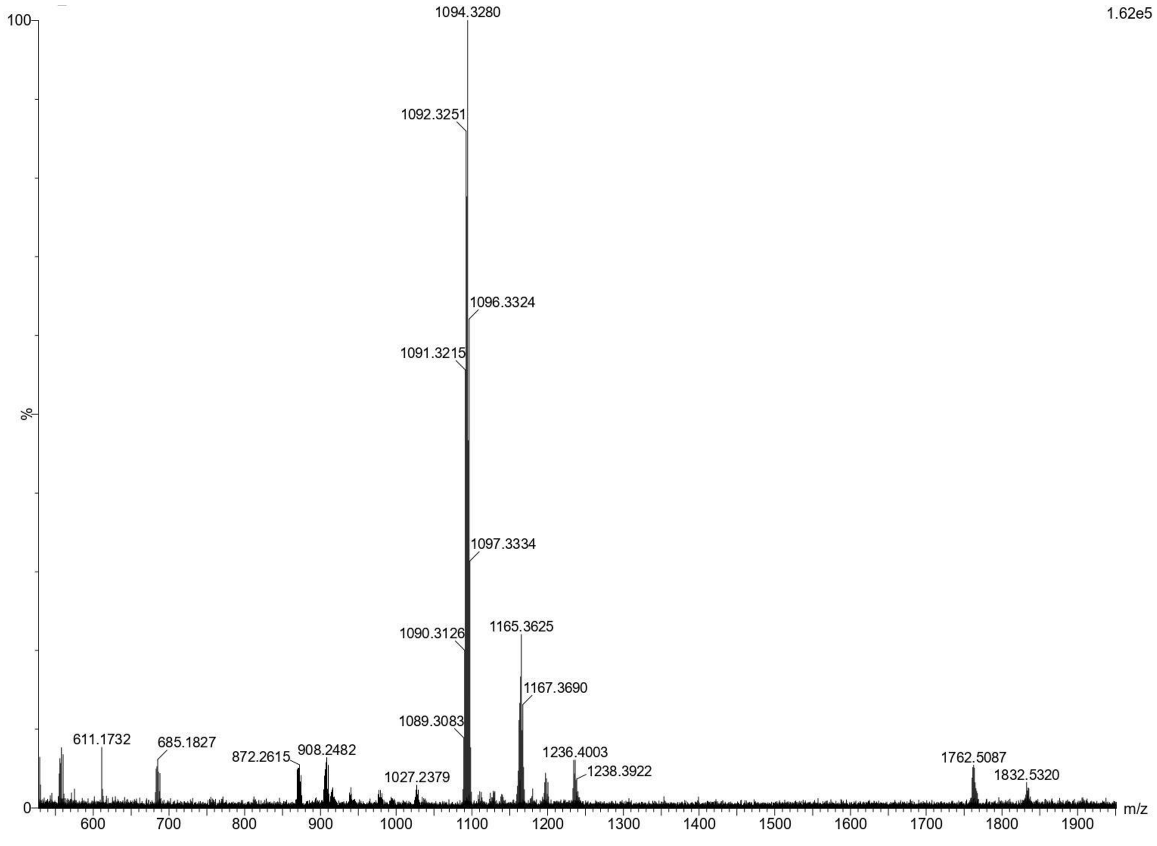

Figure S9b: Negative-ion HRMS of Fmoc-D-Trp-D-Lys(Gd-DOTA)-OH **(9)**, 1094.3280 $[M-H]^-$

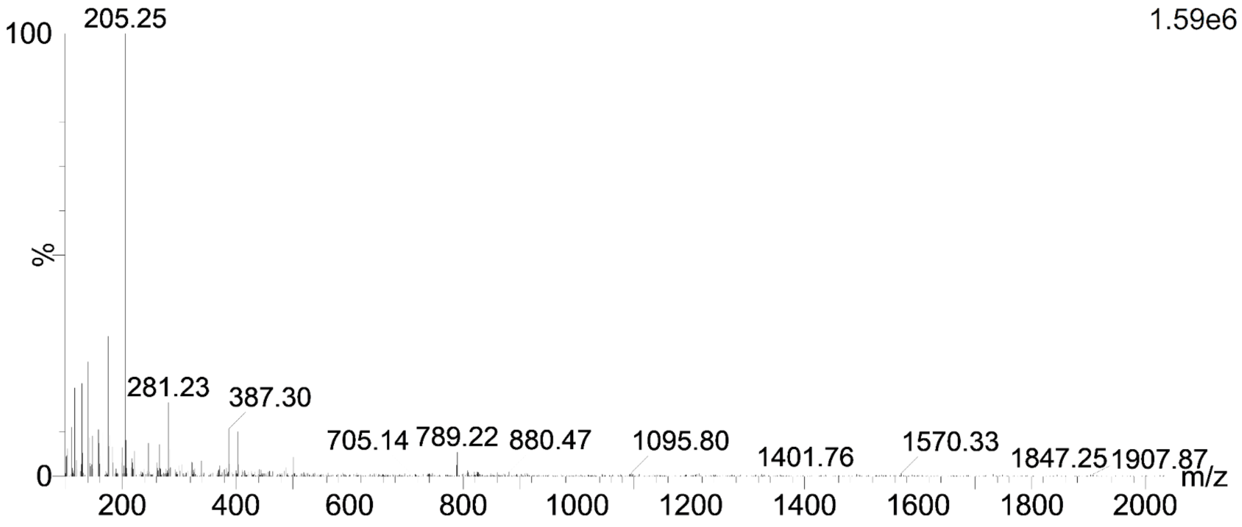

Figure S10: Positive-ion LRMS of Fmoc-D-Lys(Gd-DOTA)-Lys(Gd-DOTA)-NH$_2$ **(10)**, 789.22 ([M+2H]/2)$^{2+}$

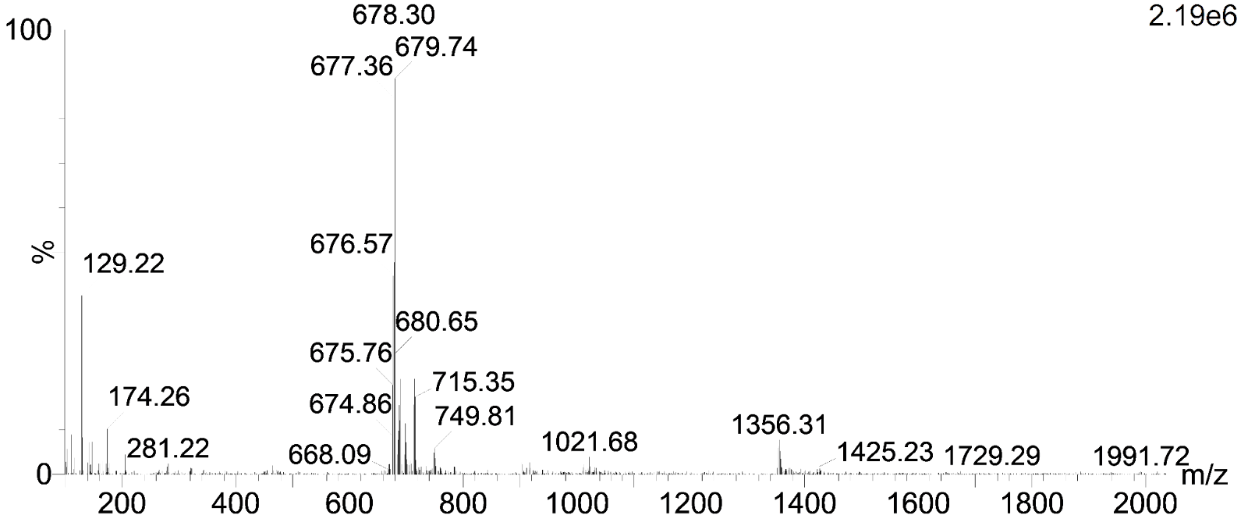

Figure S11: Positive-ion LRMS of H-D-Lys(Gd-DOTA)-Lys(Gd-DOTA)-NH$_2$ **(11)**, 1356.31 [M+H]$^+$, 678.30 ([M+2H]/2)$^{2+}$

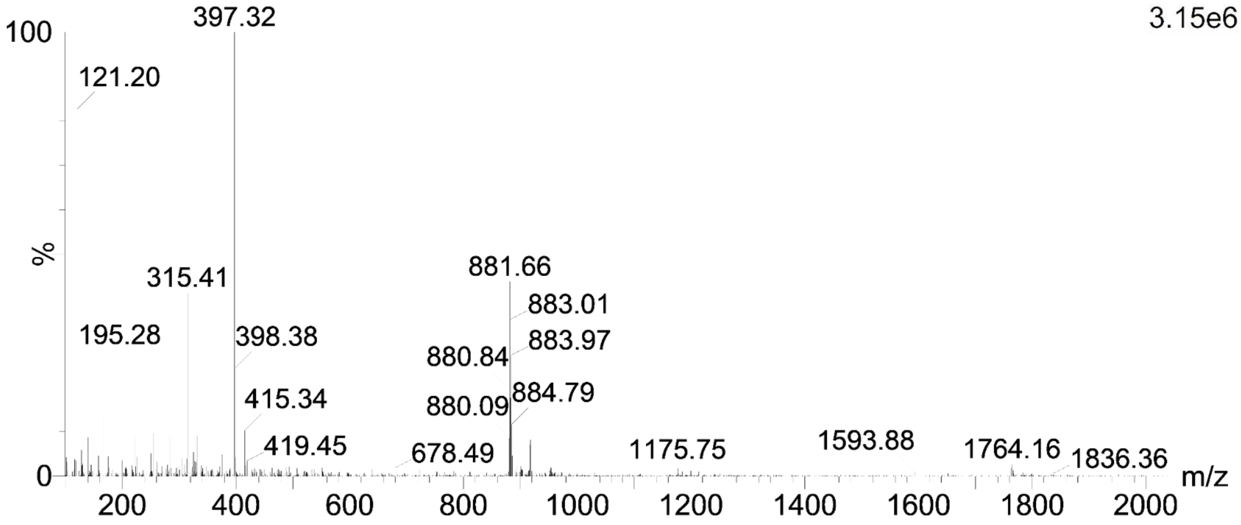

Figure S12: Positive-ion LRMS of Fmoc-D-Trp-D-Lys(Gd-DOTA)-Lys(Gd-DOTA)-NH_2 **(12)**, 1764.16 $[M+H]^+$, 881.66 $([M+2H]/2)^{2+}$

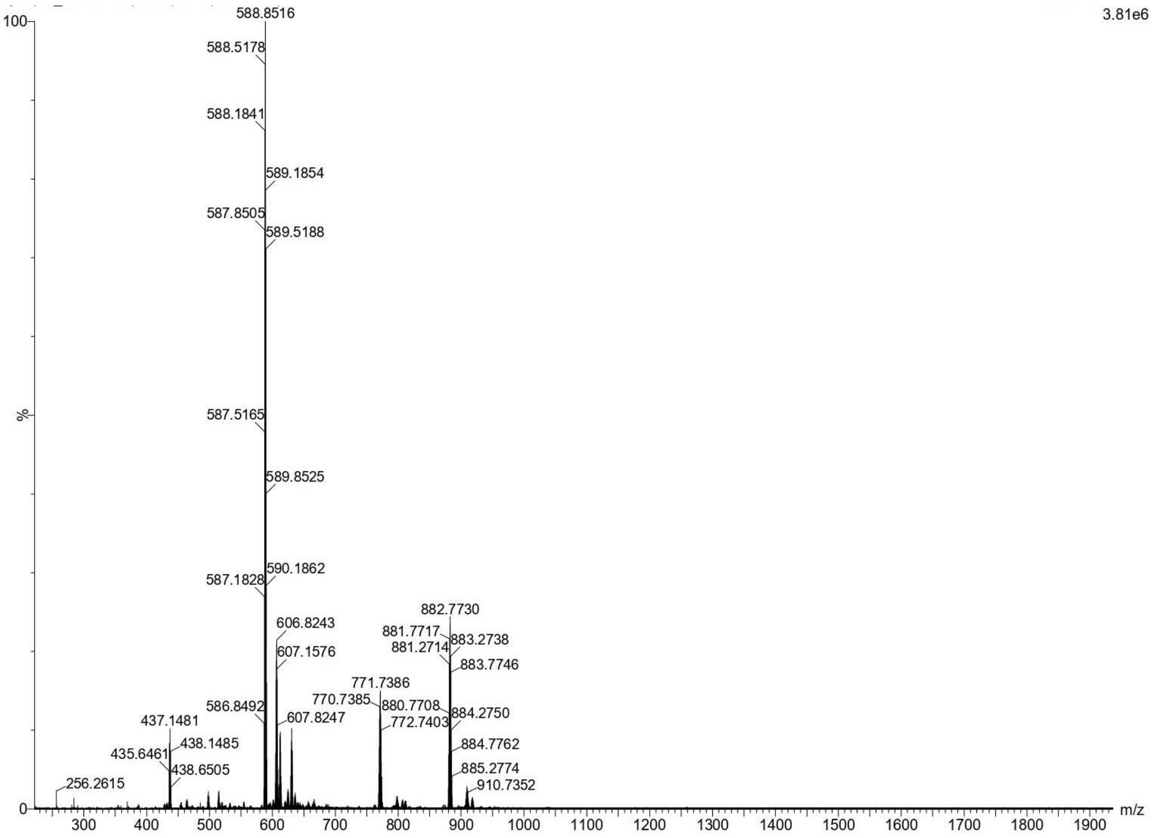

Figure S13: Positive-ion HRMS of Fmoc-D-Lys(Gd-DOTA)-D-Trp-Lys(Gd-DOTA)-NH_2 **(13)**, 882.7730 $([M+2H]/2)^{2+}$

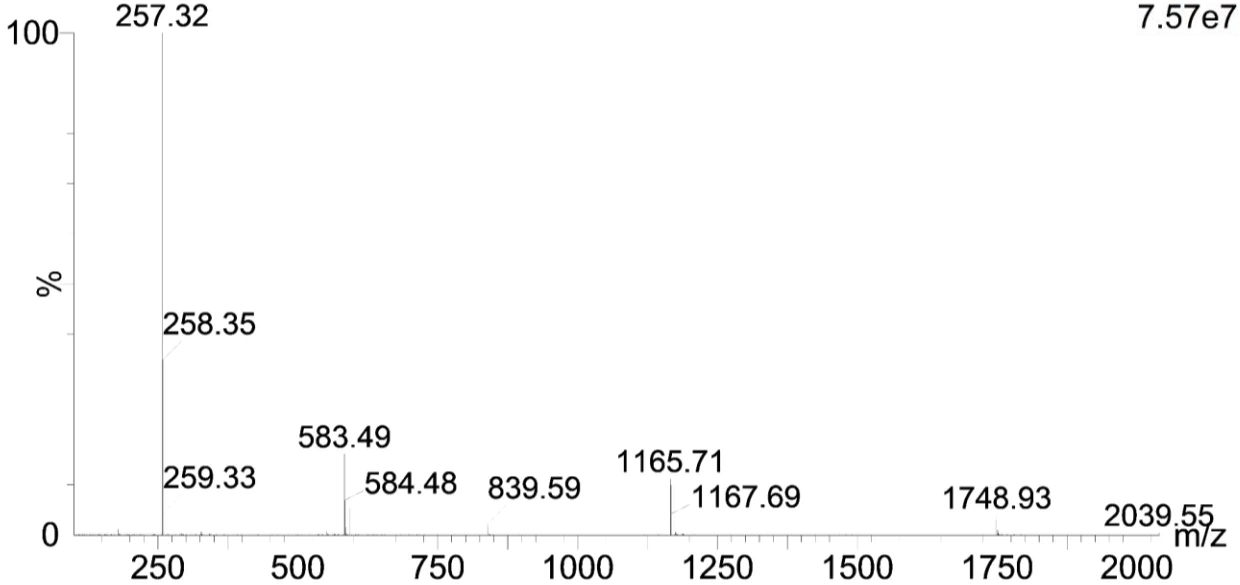

Figure S14a: Positive-ion LRMS of Fmoc-Dap(Mtt)-OH **(14)**, 583.49 $[M+H]^+$

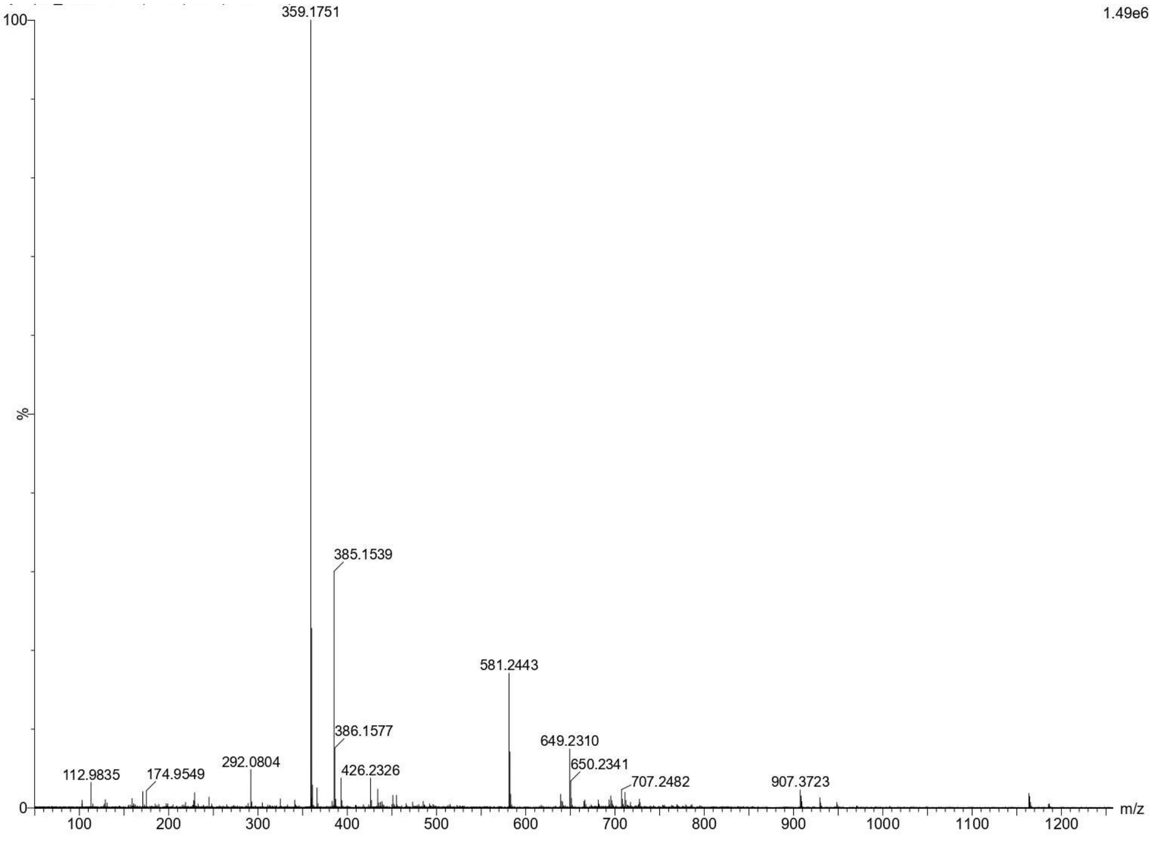

Figure S14b: Negative-ion HRMS of Fmoc-Dap(Mtt)-OH **(14)**, 581.2443 $[M-H]^-$

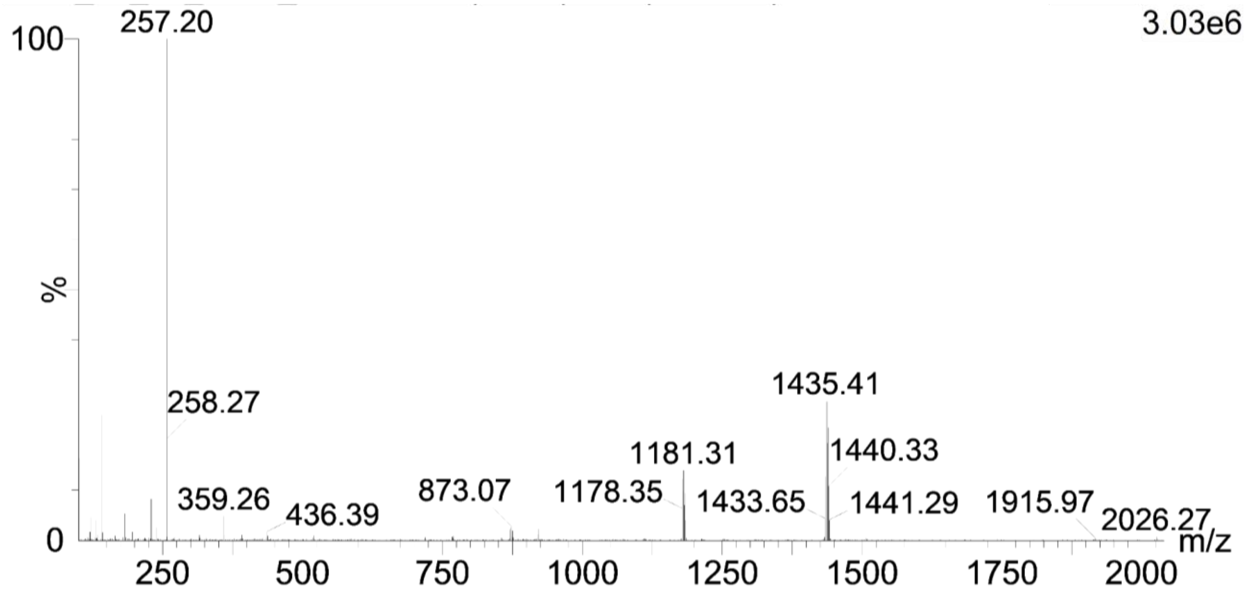

Figure S15: Positive-ion LRMS of Fmoc-Dap(Mtt)-D-Trp-Lys(Gd-DOTA)-OH **(15)**, 1435.41 $[M+H]^+$

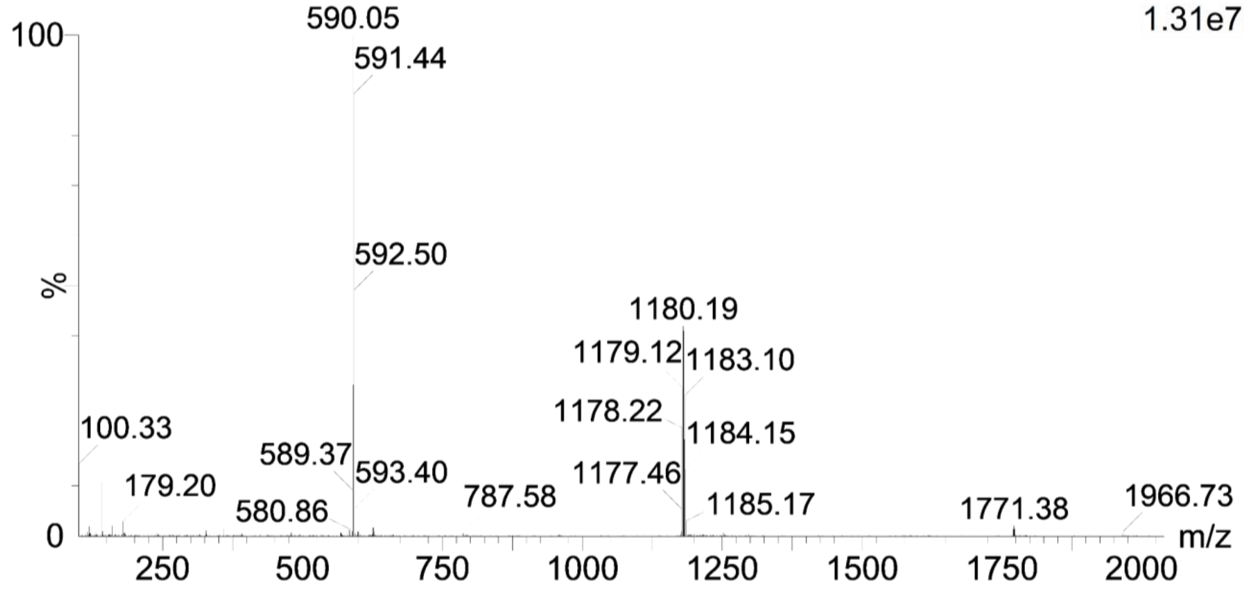

Figure S16: Positive-ion LRMS of Fmoc-Dap(H)-D-Trp-Lys(Gd-DOTA)-OH **(16)**, 1180.19 $[M+H]^+$, 590.05 $([M+2H]/2)^{2+}$

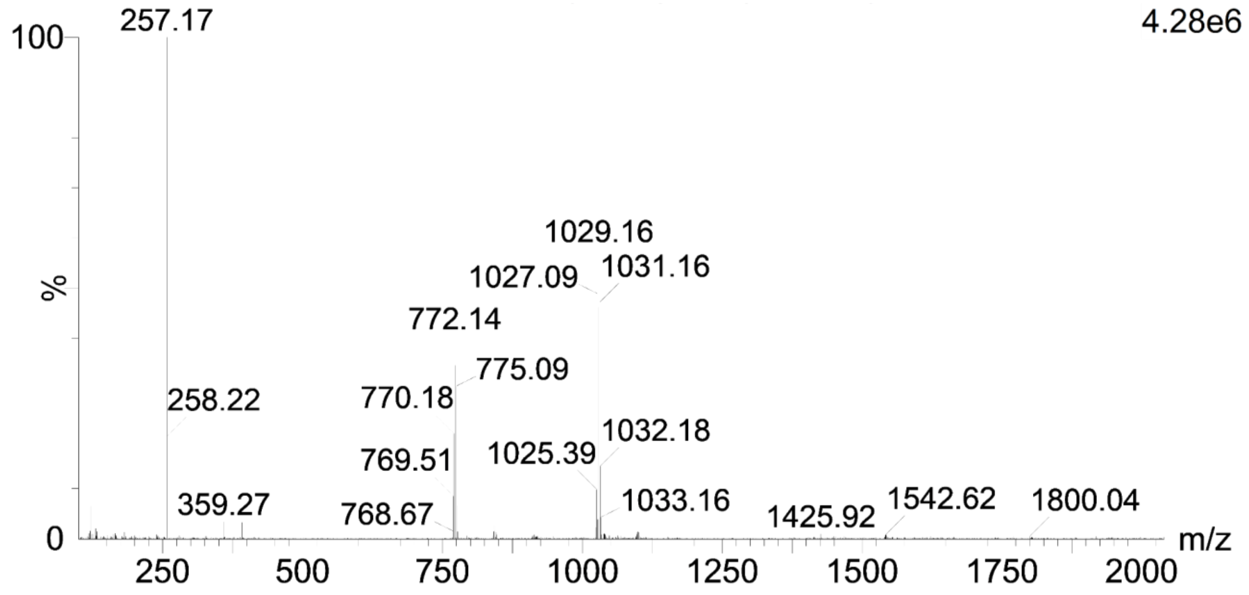

Figure S17: Positive-ion LRMS of H-Dap(Mtt)-Lys(Gd-DOTA)-NH$_2$ **(18)**, 1029.16 [M+H]$^+$

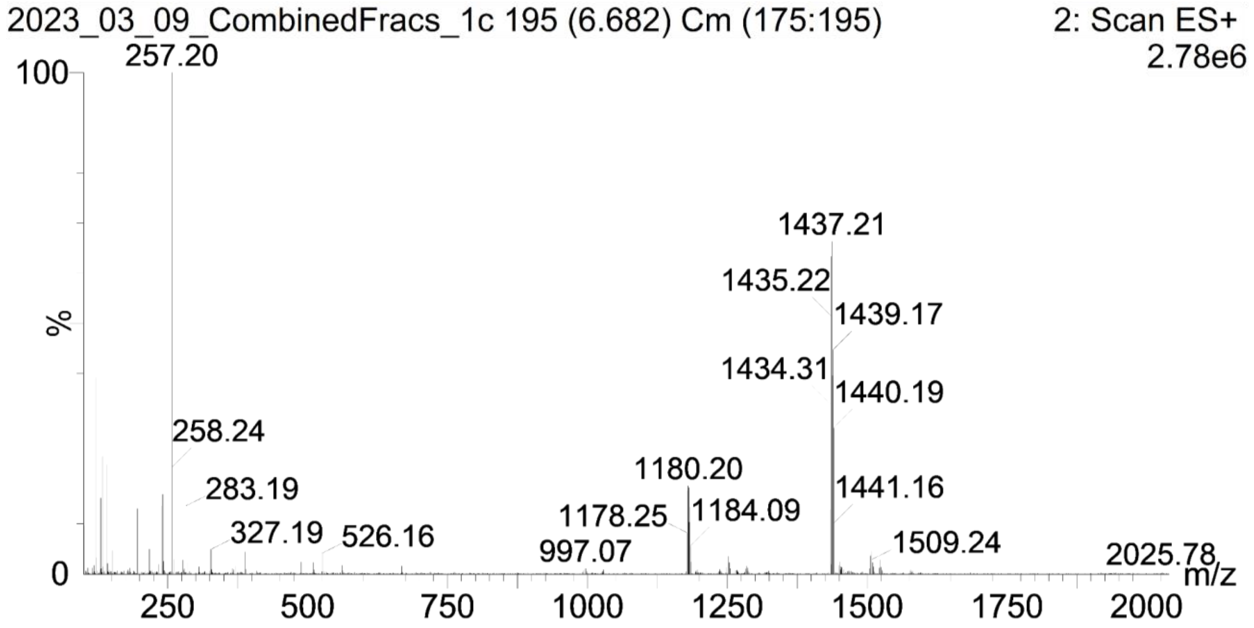

Figure S18: Positive-ion LRMS of Fmoc-D-Trp-Dap(Mtt)-Lys(Gd-DOTA)-NH$_2$ **(19)**, 1437.21 [M+H]$^+$

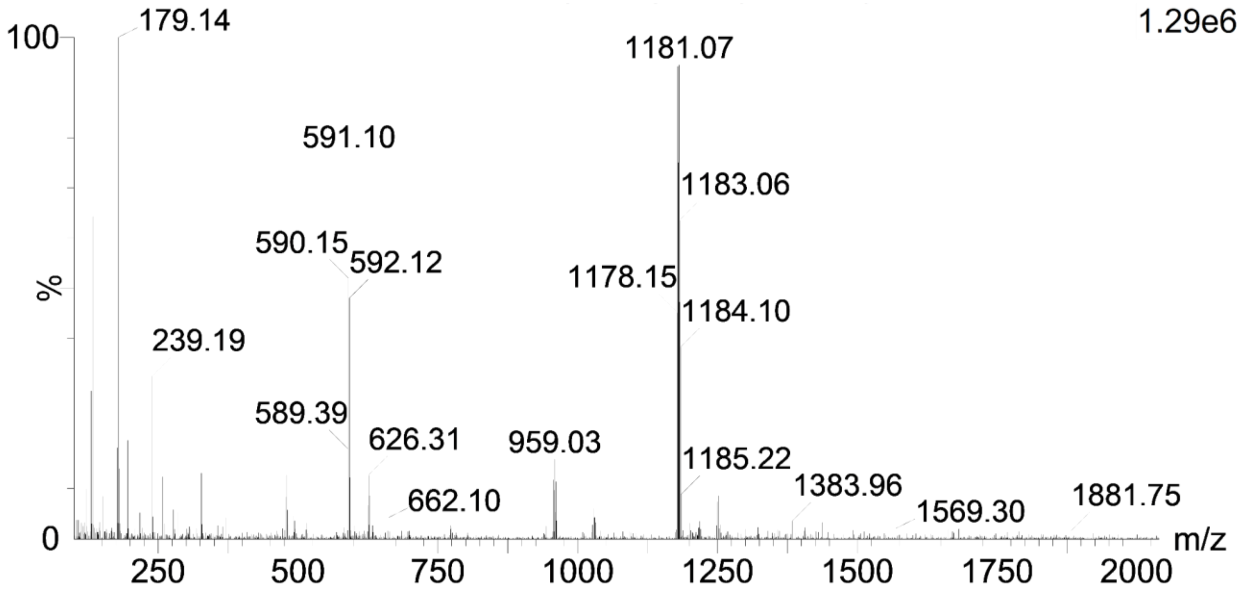

Figure S19a: Positive-ion LRMS of Fmoc-D-Trp-Dap(H)-Lys(Gd-DOTA)-NH_2 **(20)**, 1181.07 $[M+H]^+$, 591.10 $([M+2H]/2)^{2+}$

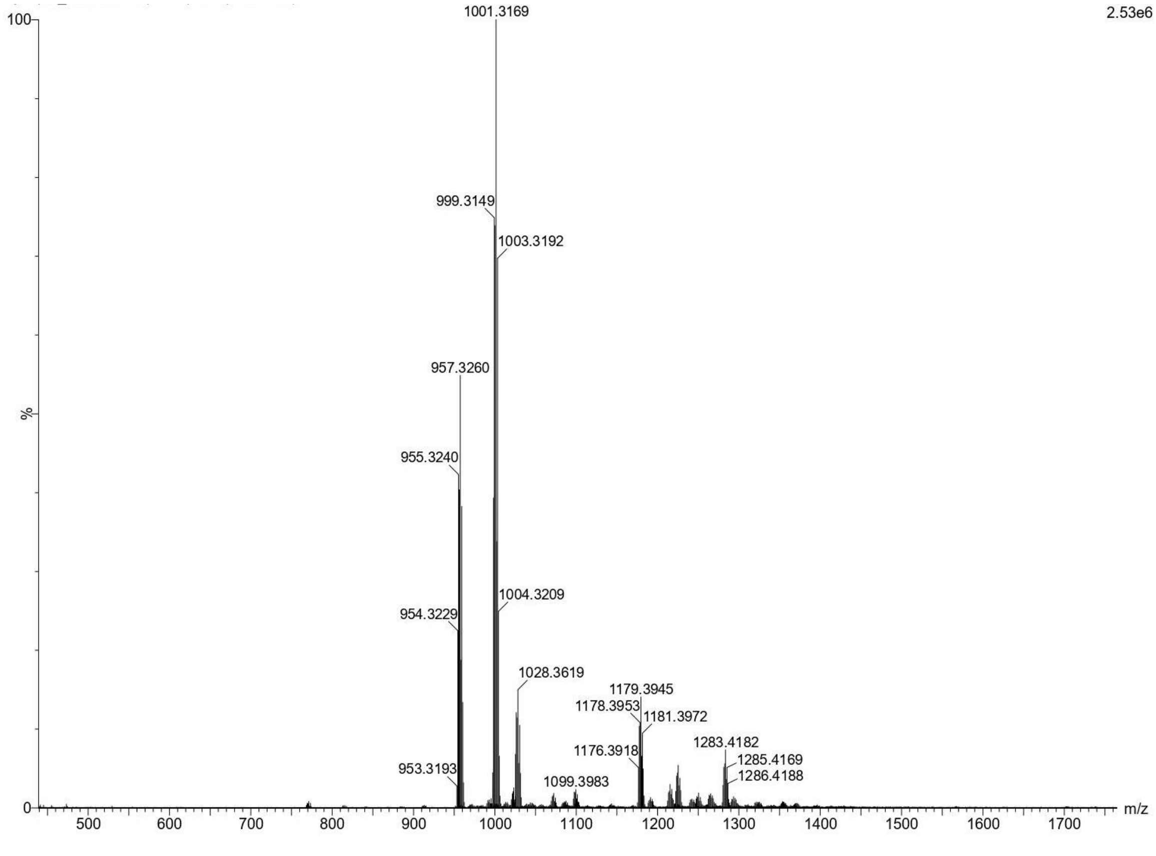

Figure S19b: Negative-ion HRMS of Fmoc-D-Trp-Dap(H)-Lys(Gd-DOTA)-NH_2 **(20)**, 1179.3945 $[M-H]^-$

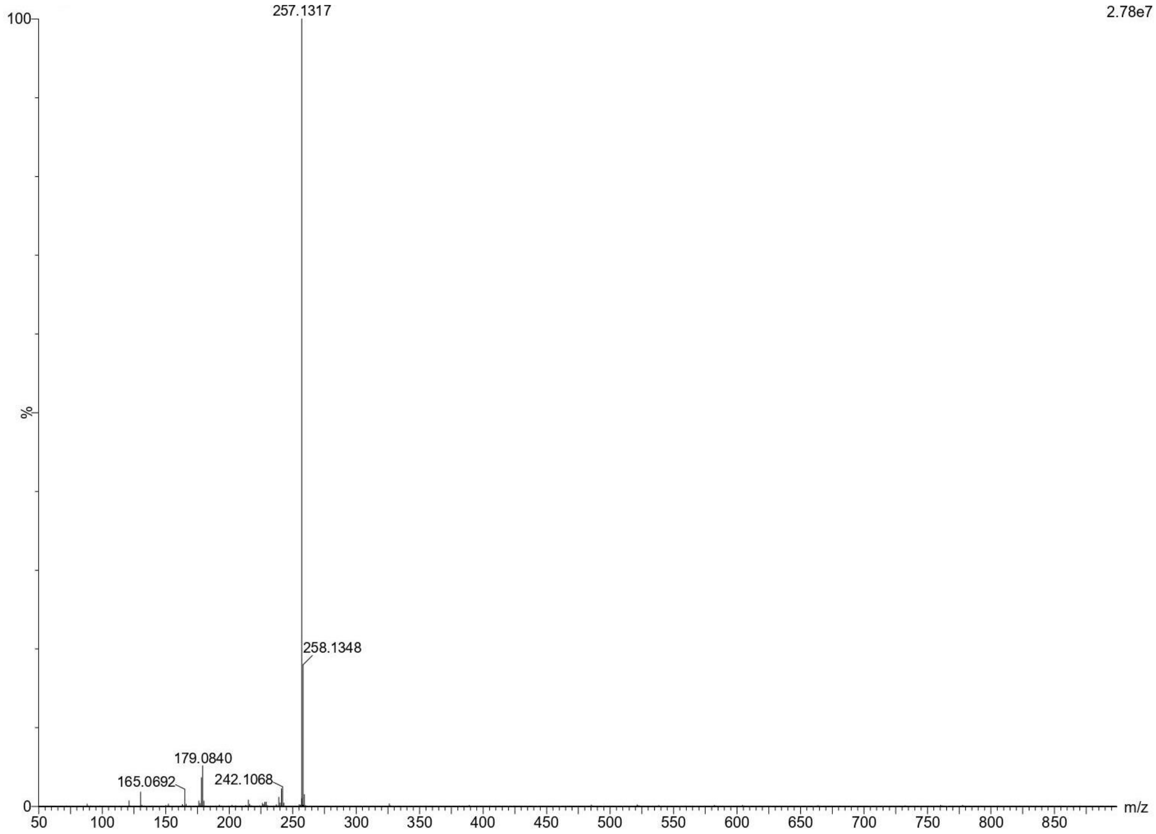

Figure S20a: Positive-ion HRMS of Fmoc-Dap(Mtt)-NH_2 **(21)** showing Mtt fragment at 257 (m/z)

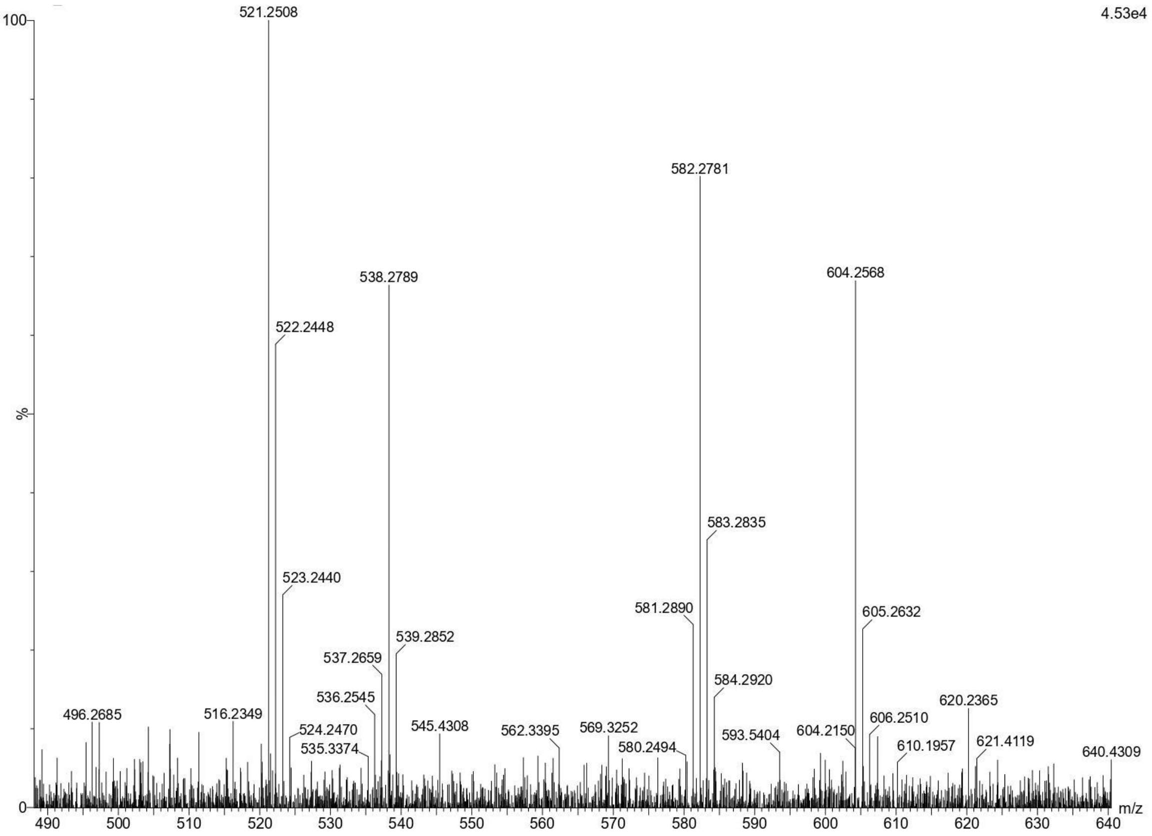

Figure S20b: Positive-ion HRMS of Fmoc-Dap(Mtt)-NH_2 **(21)** zoomed-in to show the parent ion fragment, 538.2789 $[M+H]^+$

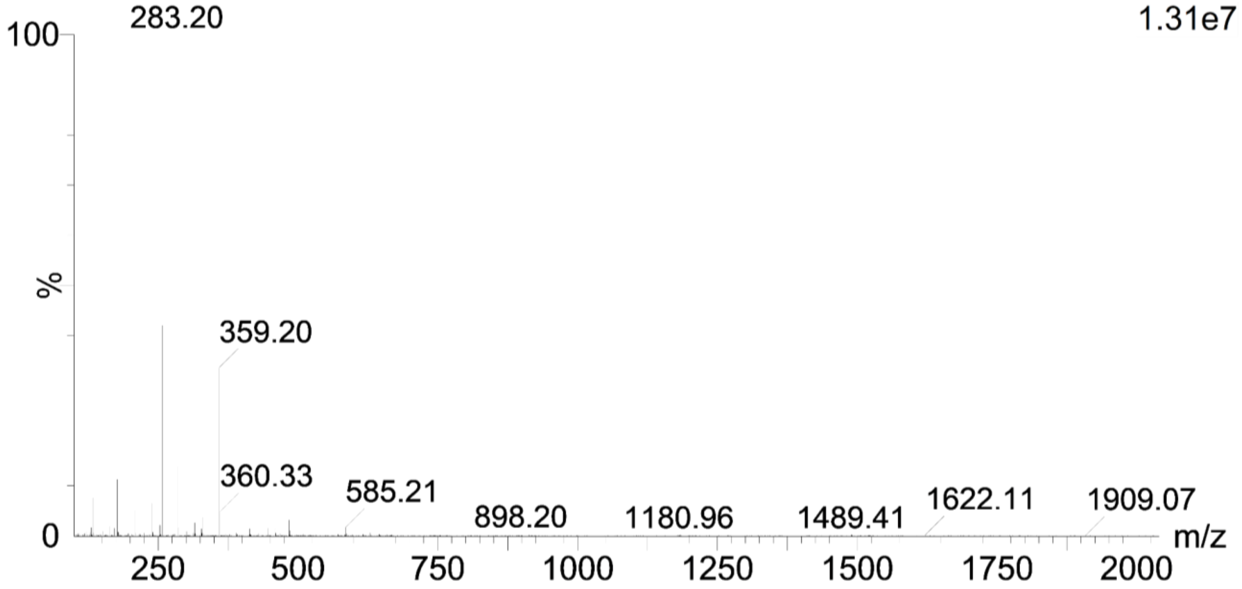

Figure S21: Positive-ion LRMS of H-Dap(Mtt)-NH_2 **(22)**, 359.20 $[M+H]^+$

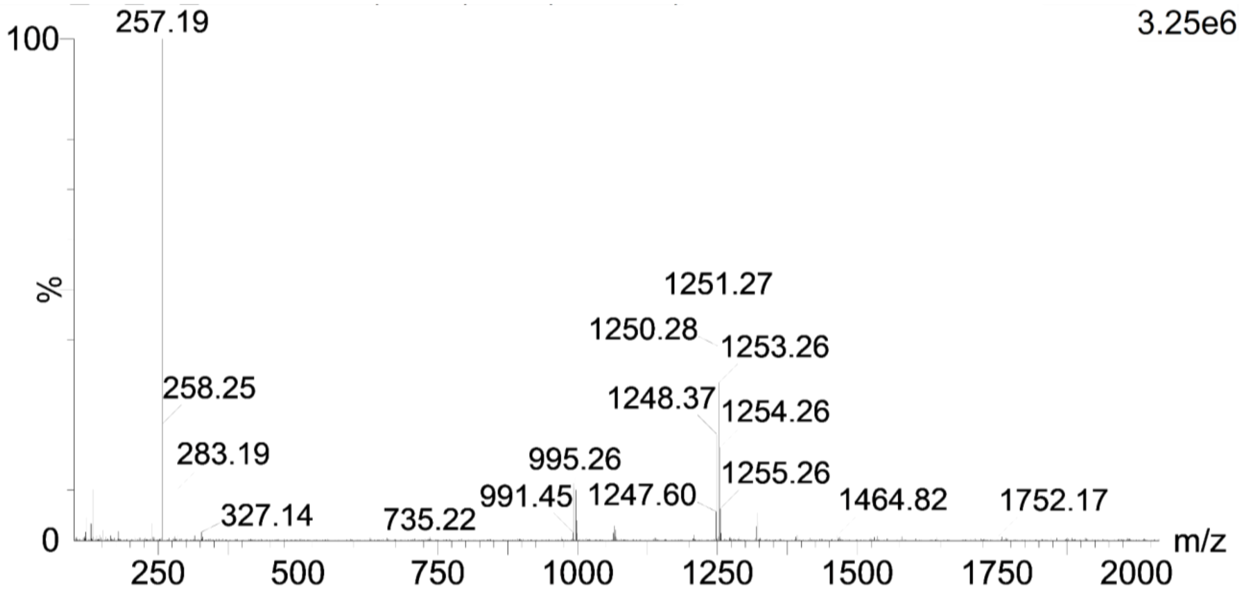

Figure S22a: Positive-ion LRMS of Fmoc-D-Lys(Gd-DOTA)-Dap(Mtt)-NH_2 **(23)**, 1251.27 $[M+H]^+$

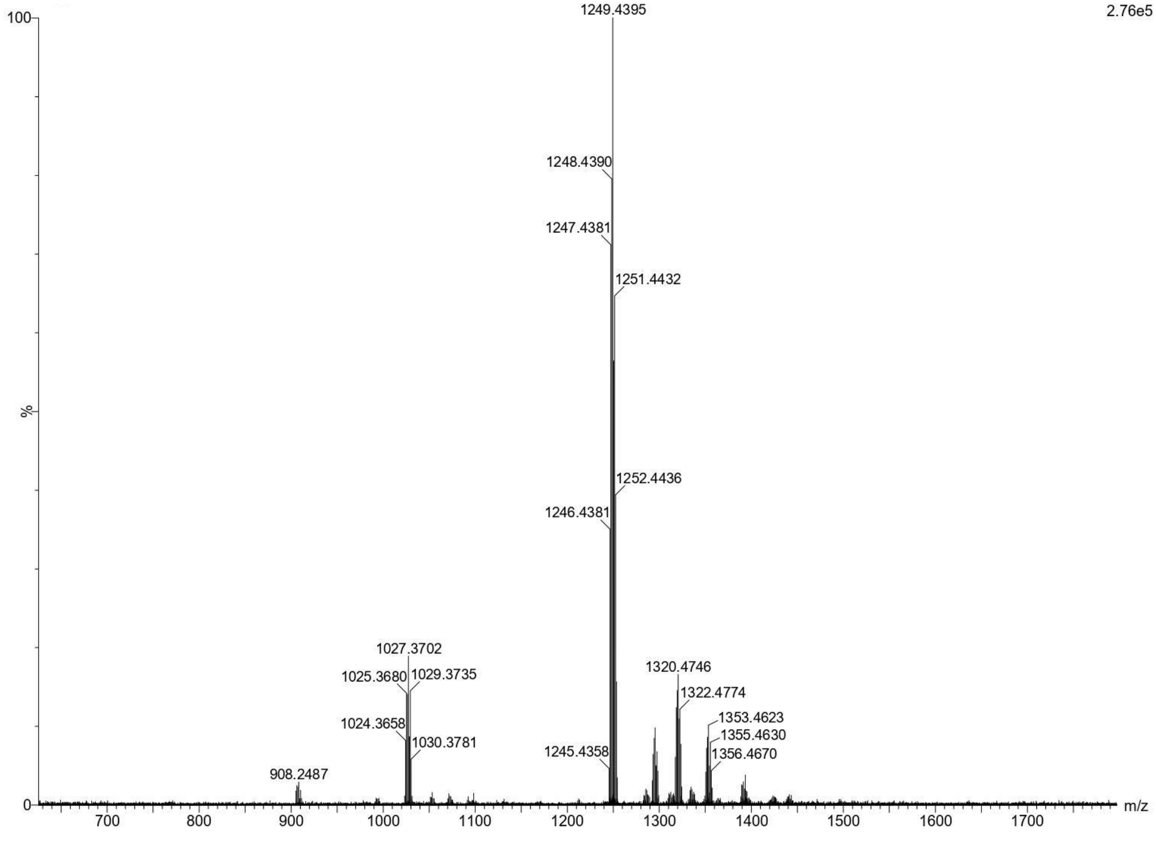

Figure S22b: Negative-ion HRMS of Fmoc-D-Lys(Gd-DOTA)-Dap(Mtt)-NH_2 **(23)**, 1249.4395 $[M-H]^-$

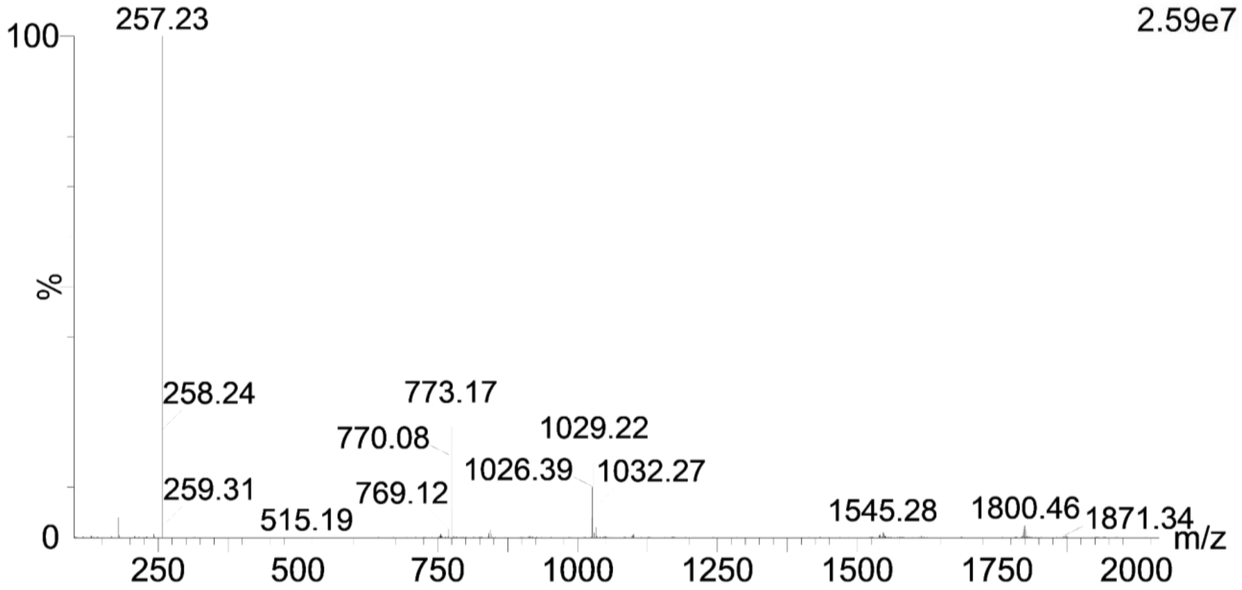

Figure S23: Positive-ion LRMS of H-D-Lys(Gd-DOTA)-Dap(Mtt)-NH_2 **(24)**, 1029.22 $[M+H]^+$

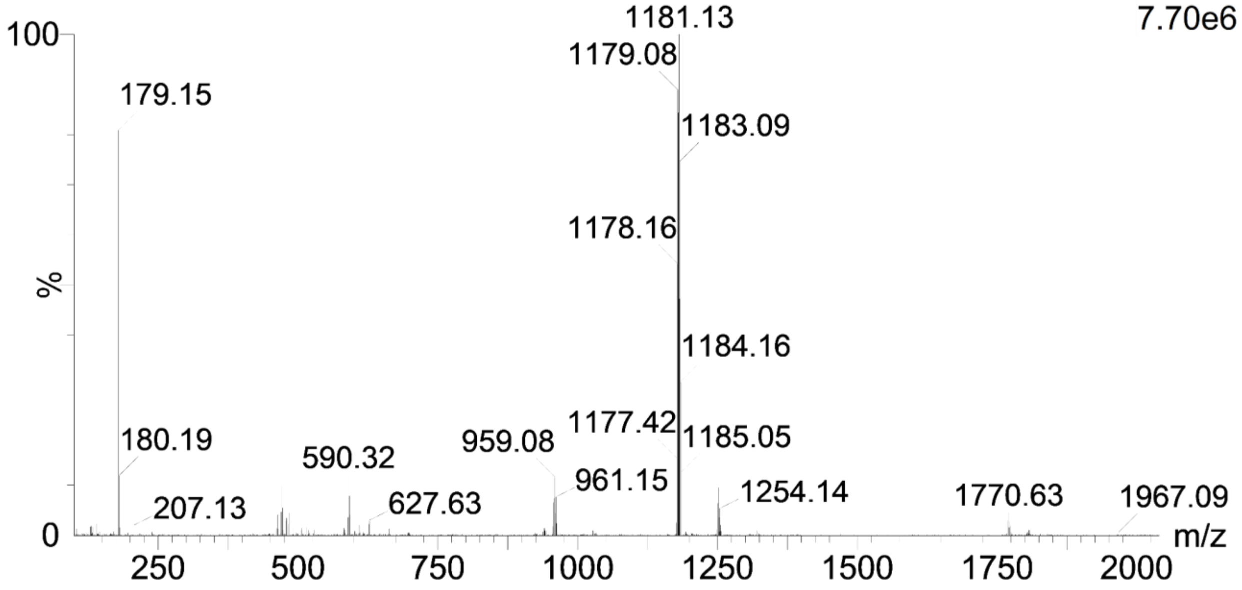

Figure S24a: Positive-ion LRMS of Fmoc-D-Trp-Lys(Gd-DOTA)-Dap(H)-NH_2 **(26)**, 1181.13 $[M+H]^+$

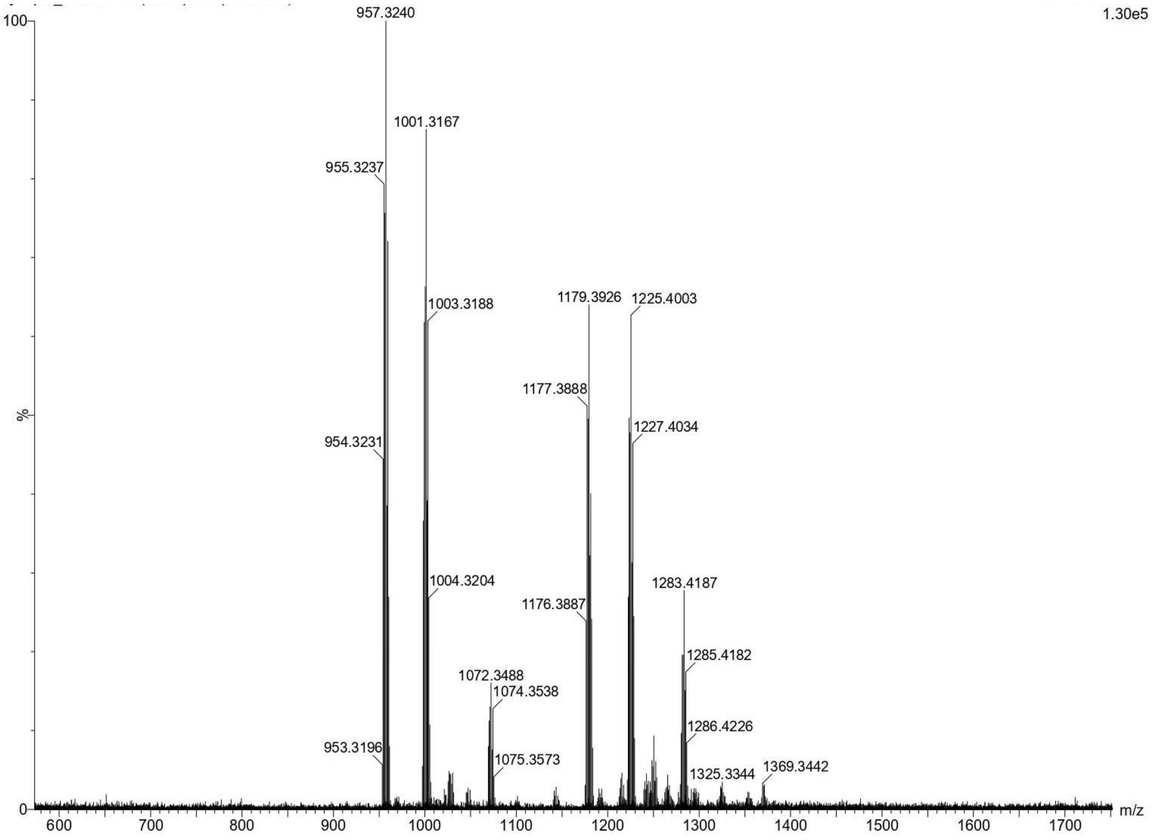

Figure S24b: Negative-ion HRMS of Fmoc-D-Trp-Lys(Gd-DOTA)-Dap(H)-NH_2 **(26)**, 1179.3926 $[M-H]^-$

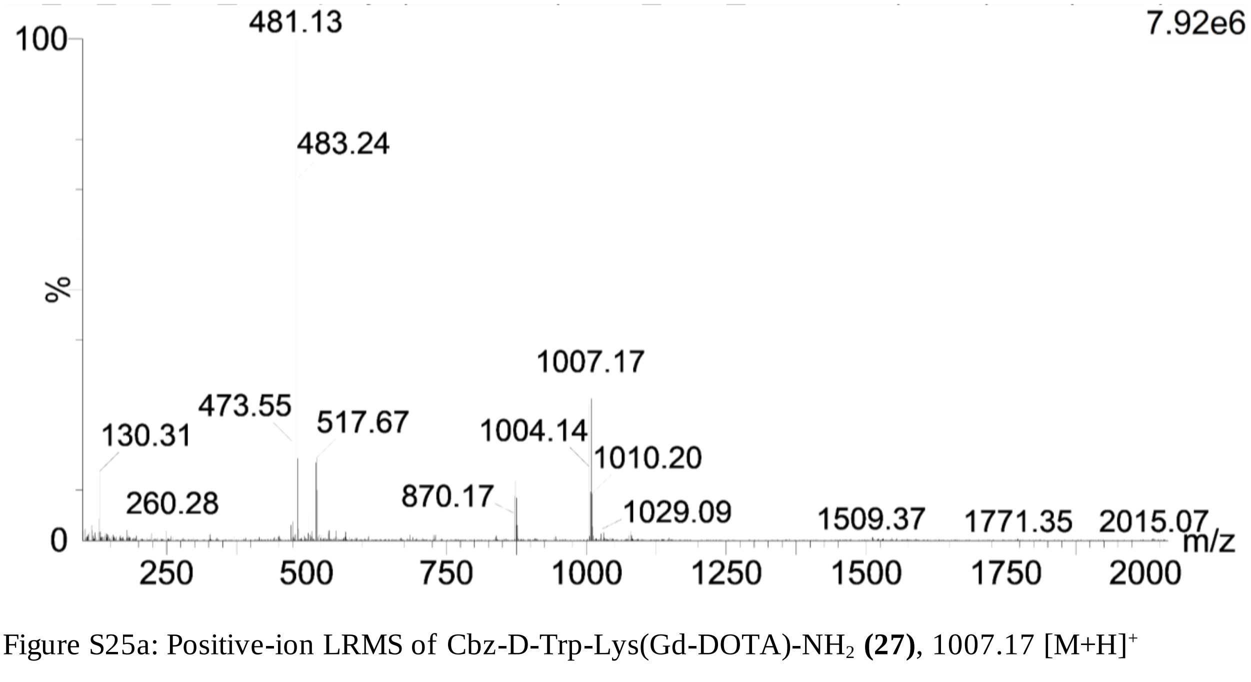

Figure S25a: Positive-ion LRMS of Cbz-D-Trp-Lys(Gd-DOTA)-NH_2 **(27)**, 1007.17 $[M+H]^+$

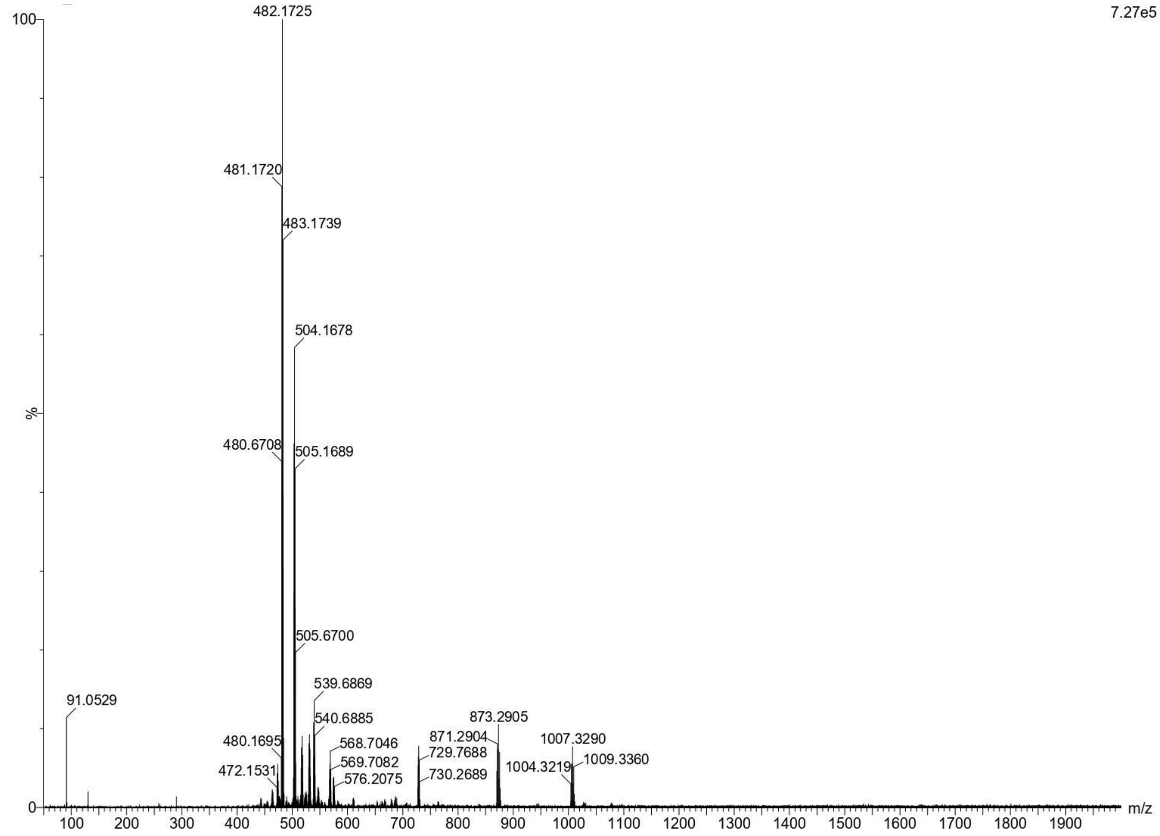

Figure S25b: Positive-ion HRMS of Cbz-D-Trp-Lys(Gd-DOTA)-NH_2 **(27)**, 1007.3290 $[M+H]^+$, 504.1678 $([M+2H]/2)^{2+}$

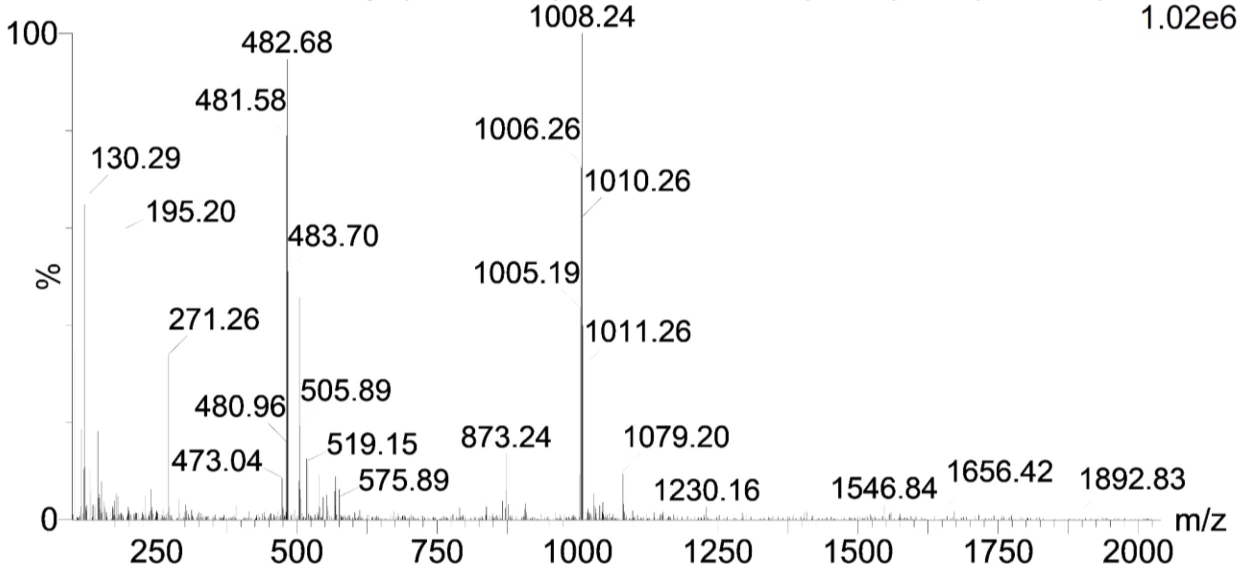

Figure S26a: Positive-ion LRMS of Cbz-D-Trp-D-Lys(Gd-DOTA)-OH **(28)**, 1008.24 $[M+H]^+$

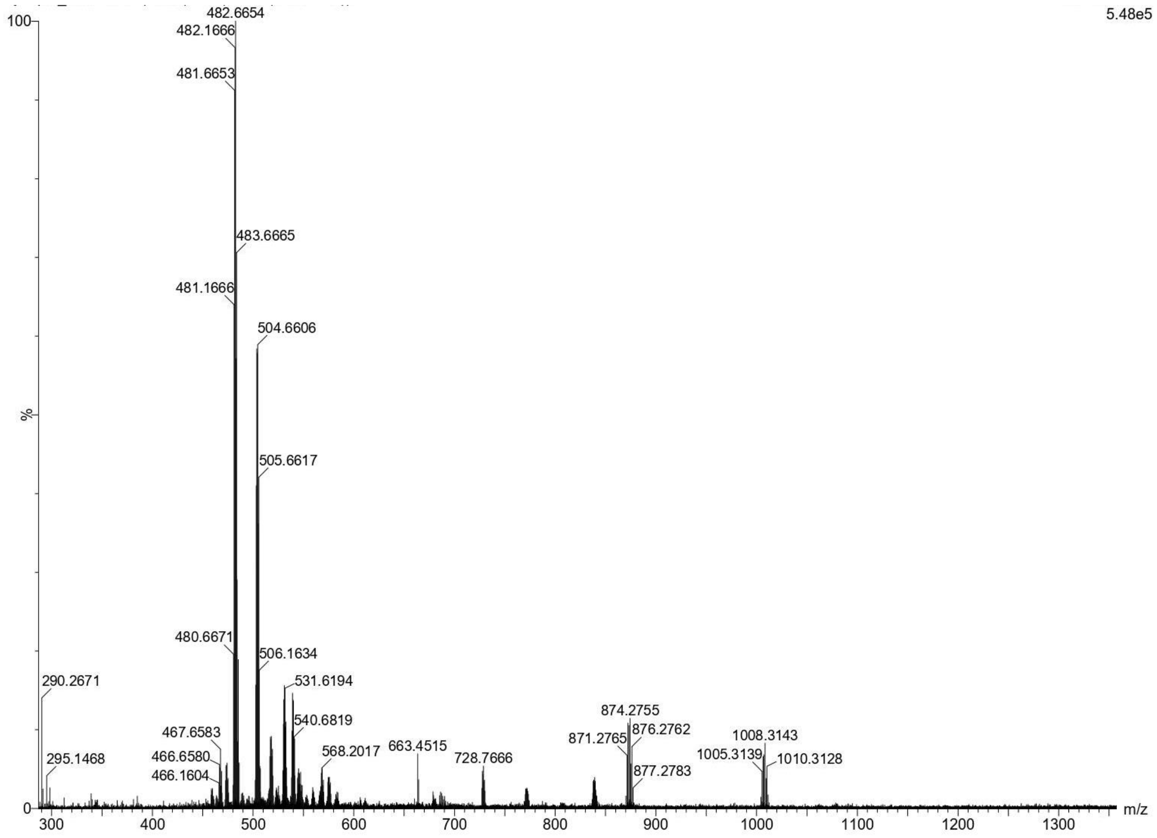

Figure S26b: Positive-ion HRMS of Cbz-D-Trp-D-Lys(Gd-DOTA)-OH **(28)**, 1008.3143 $[M+H]^+$, 504.6606 $([M+2H]/2)^{2+}$

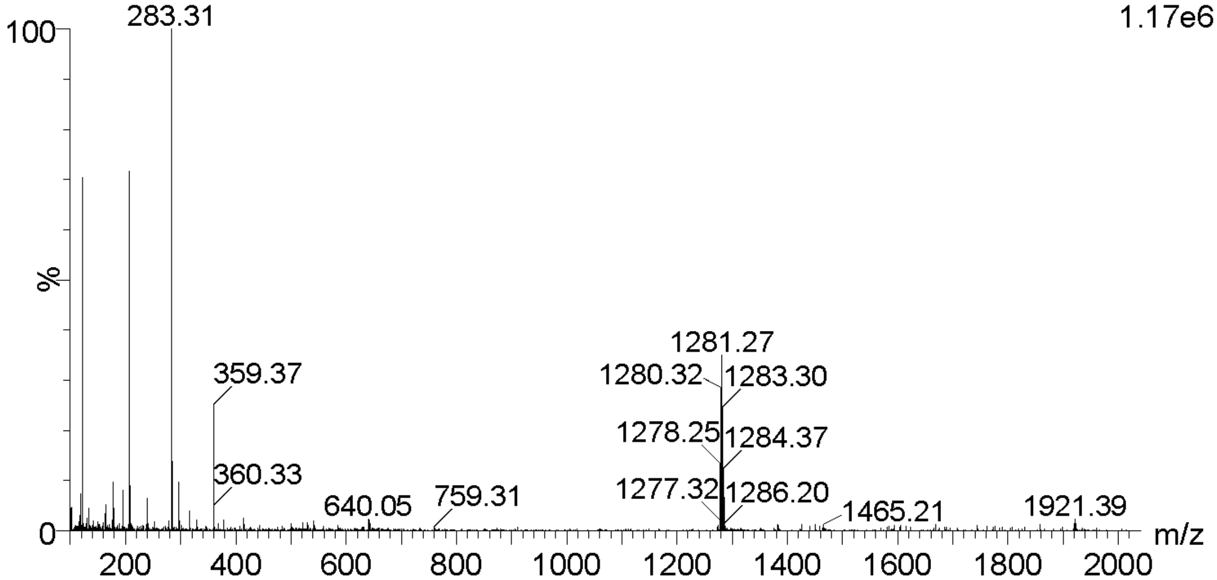

Figure S27: Positive-ion LRMS of Fmoc-D-Trp-D-Trp-Lys(Gd-DOTA)-NH_2 **(29)**, 1281.27 $[M+H]^+$

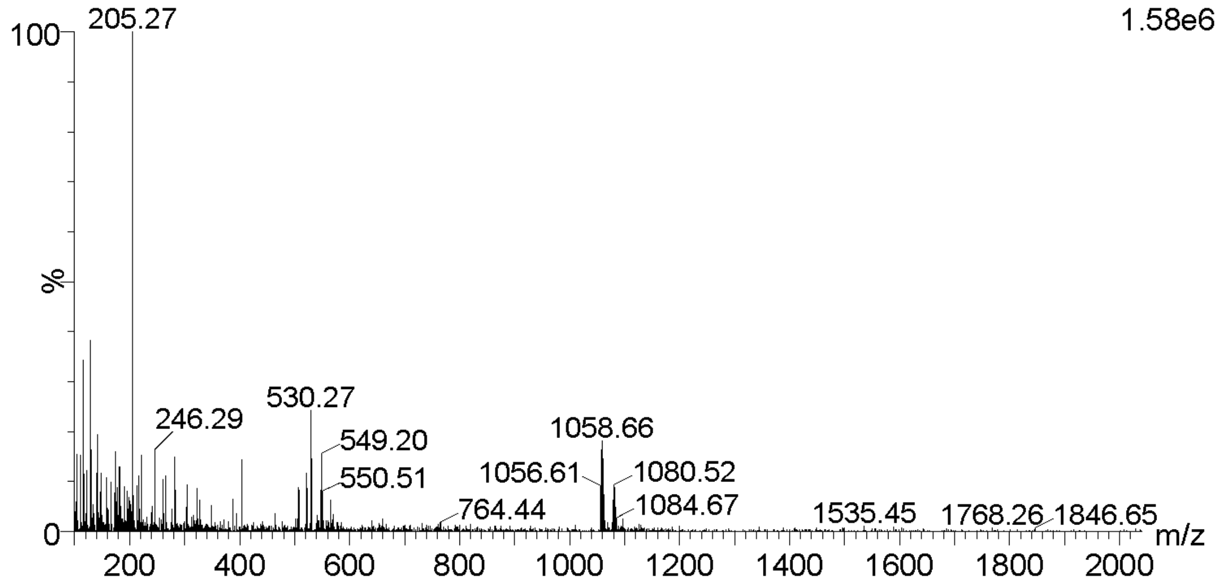

Figure S28: Positive-ion LRMS of H-D-Trp-D-Trp-Lys(Gd-DOTA)-NH$_2$ **(30)**, 1058.66 [M+H]$^+$, 530.27 ([M+2H]/2)$^{2+}$

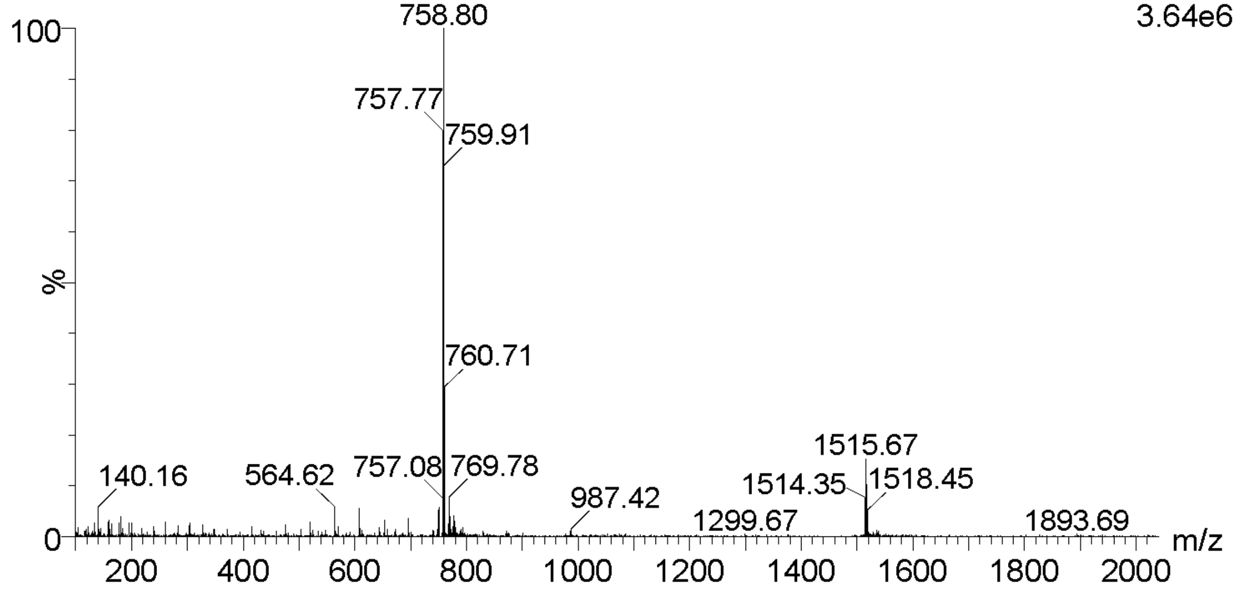

Figure S29a: Positive-ion LRMS of DCL-DSS-D-Trp-D-Trp-Lys(Gd-DOTA)-NH$_2$ **(31)**, 1515.67 [M+H]$^+$, 758.80 ([M+2H]/2)$^{2+}$

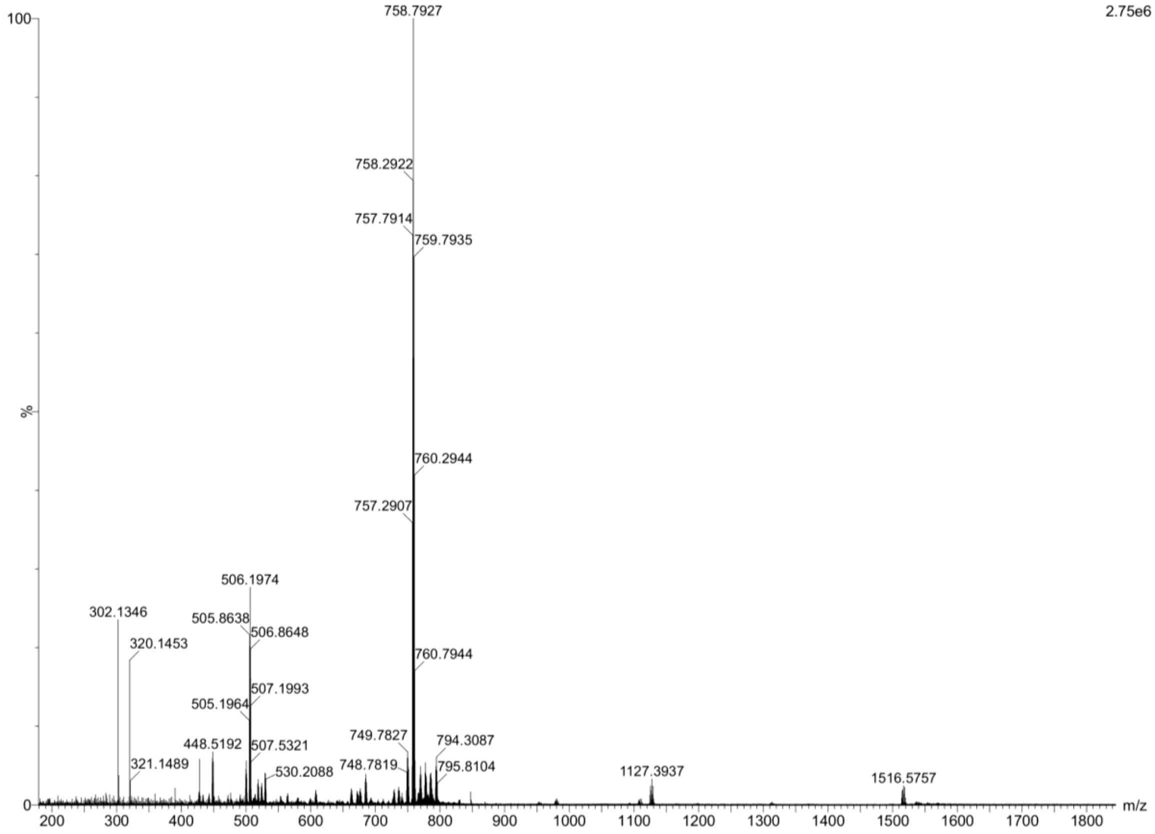

Figure S29b: Positive-ion HRMS of DCL-DSS-D-Trp-D-Trp-Lys(Gd-DOTA)-NH_2 **(31)**, 1516.7567 $[M+H]^+$, 758.7927 ($([M+2H]/2)^{2+}$), 506.1974 ($([M+3H]/3)^{3+}$)

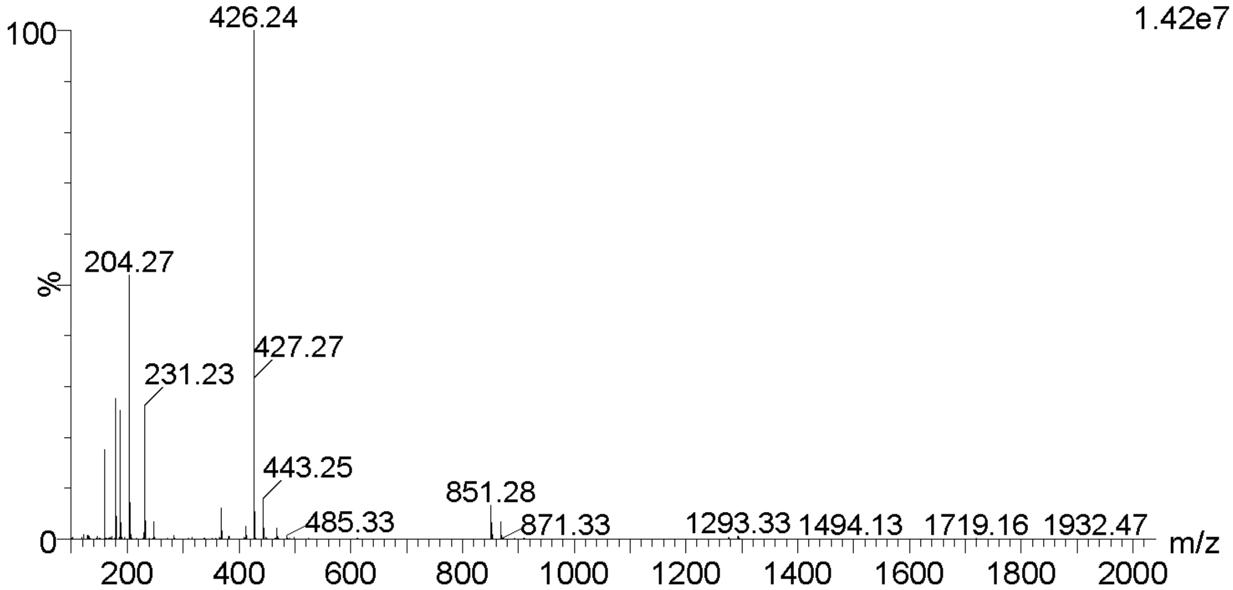

Figure S30: Positive-ion LRMS of Fmoc-D-Trp-NH_2 **(33)**, 426.24 $[M+H]^+$

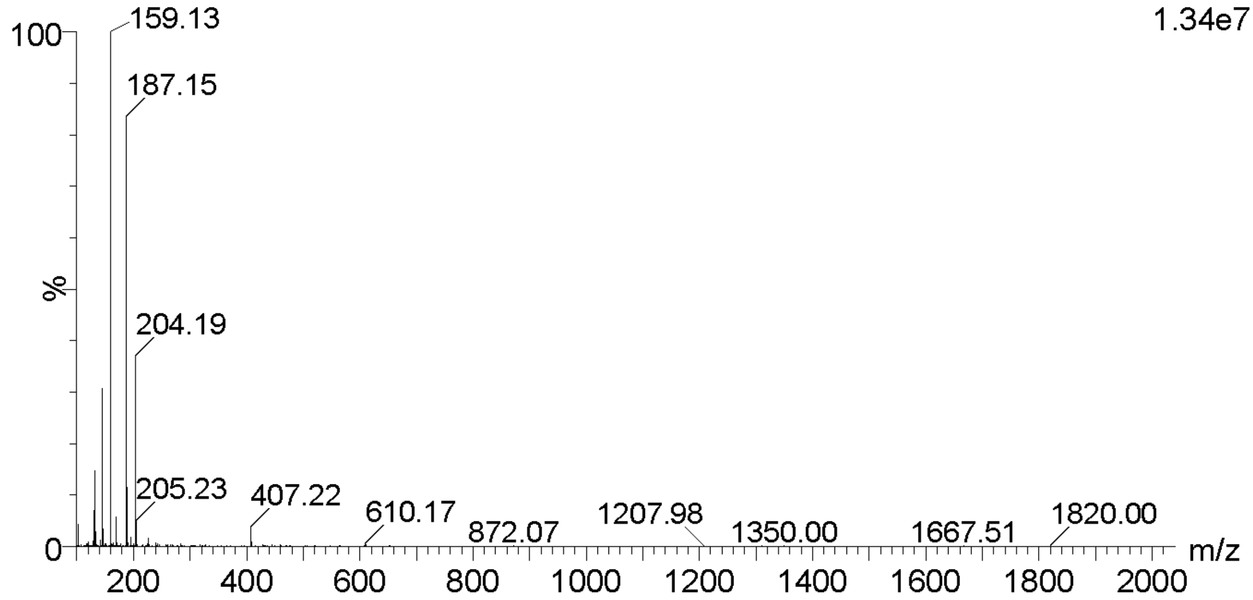

Figure S31: Positive-ion LRMS of H-D-Trp-NH_2 **(34)**, 204.19 $[M+H]^+$

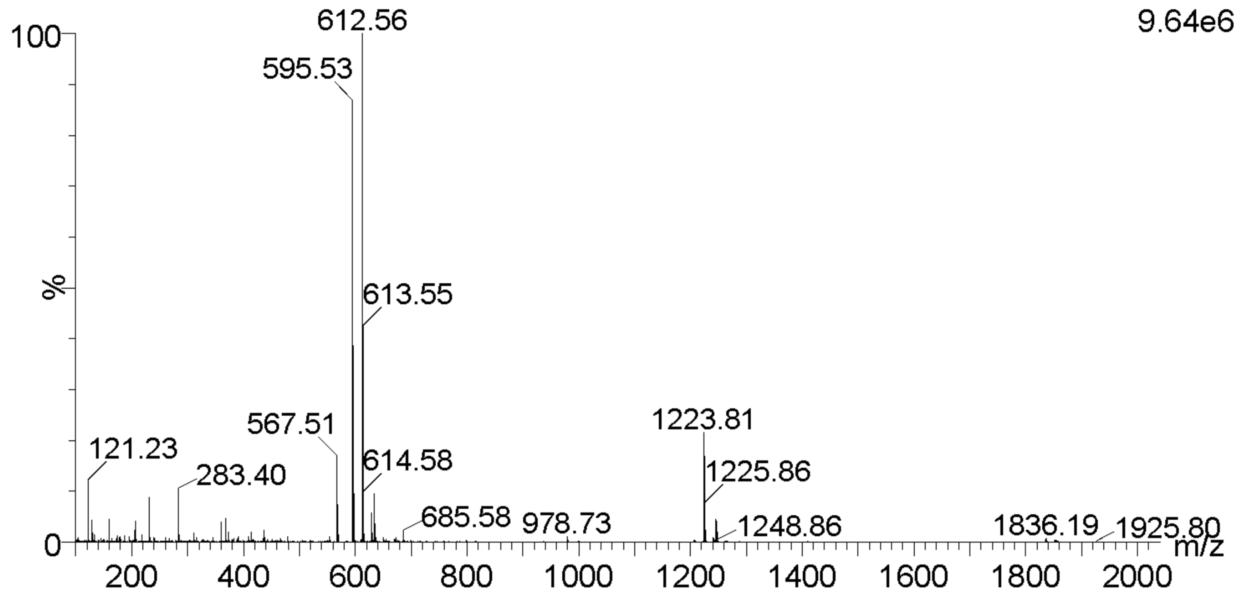

Figure S32: Positive-ion LRMS of Fmoc-D-Trp-D-Trp-NH_2 **(35)**, 612.56 $[M+H]^+$

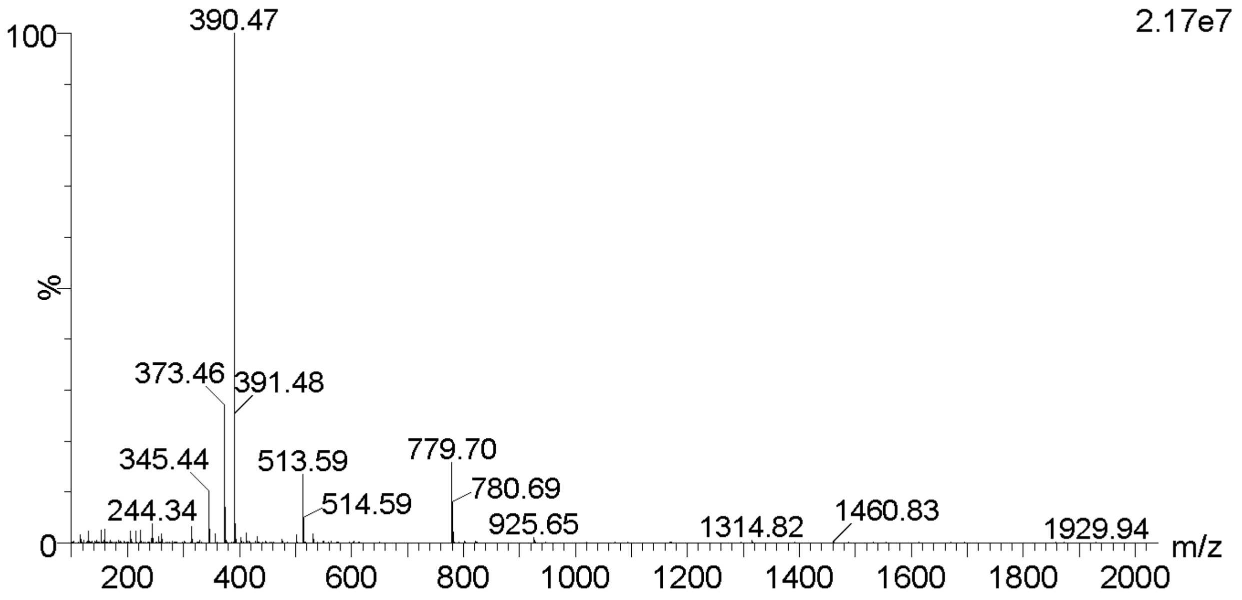

Figure S33: Positive-ion LRMS of H-D-Trp-D-Trp-NH_2 **(36)**, 390.47 $[M+H]^+$

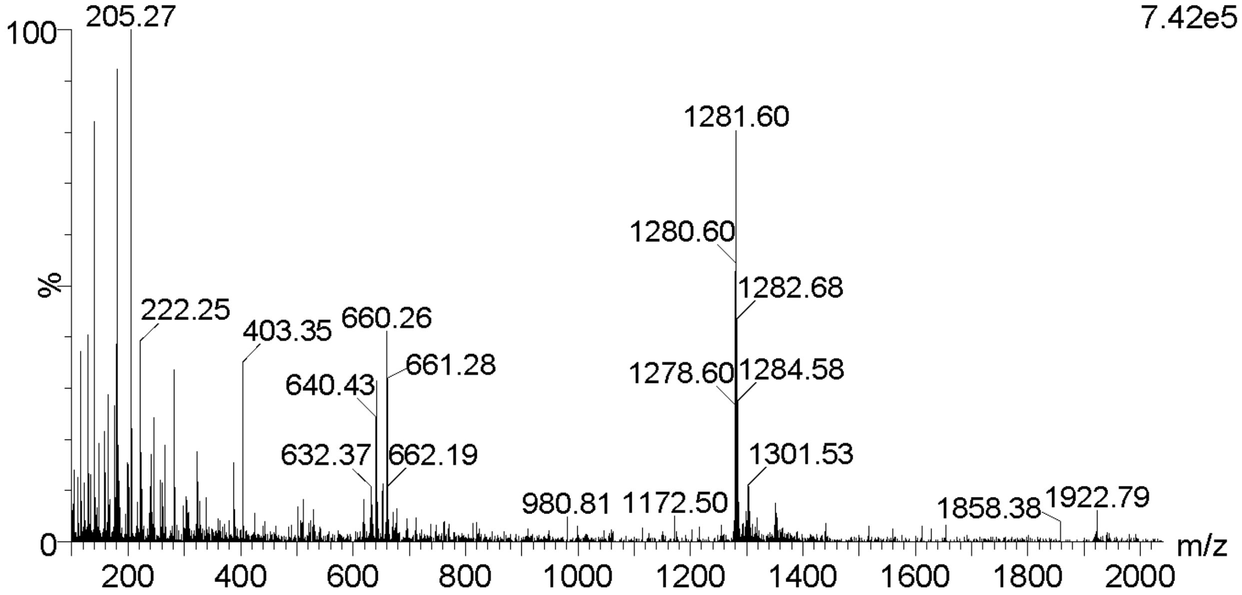

Figure S34: Positive-ion LRMS of Fmoc-D-Lys(Gd-DOTA)-D-Trp-D-Trp-NH_2 **(37)**, 1281.60 $[M+H]^+$

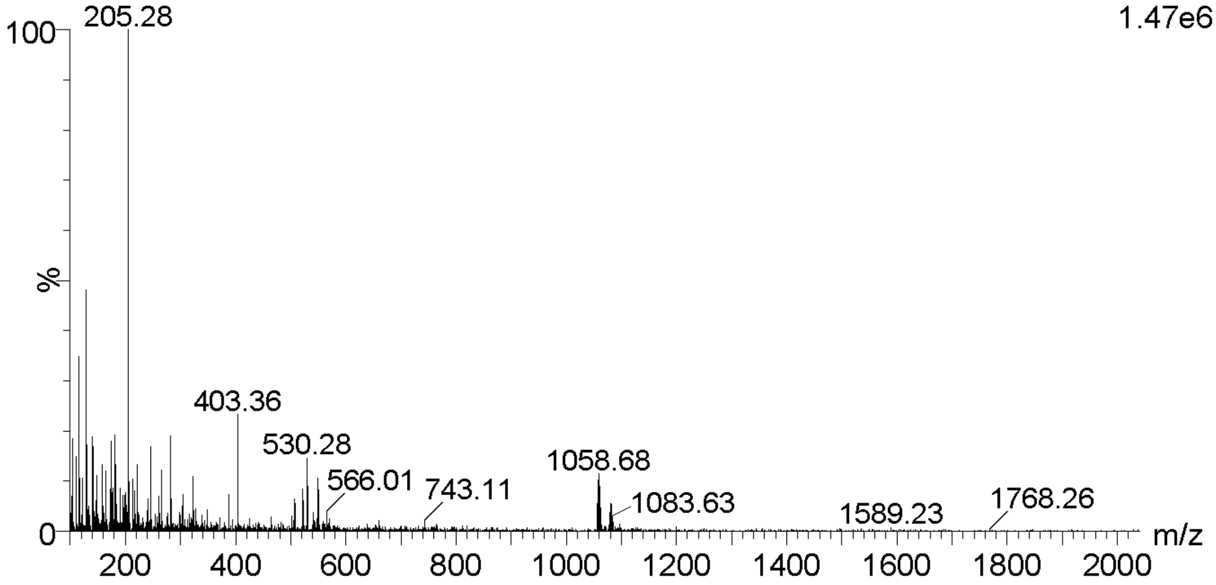

Figure S35: Positive-ion LRMS of H-D-Lys(Gd-DOTA)-D-Trp-D-Trp-NH_2 **(38)**, 1058.68 $[M+H]^+$

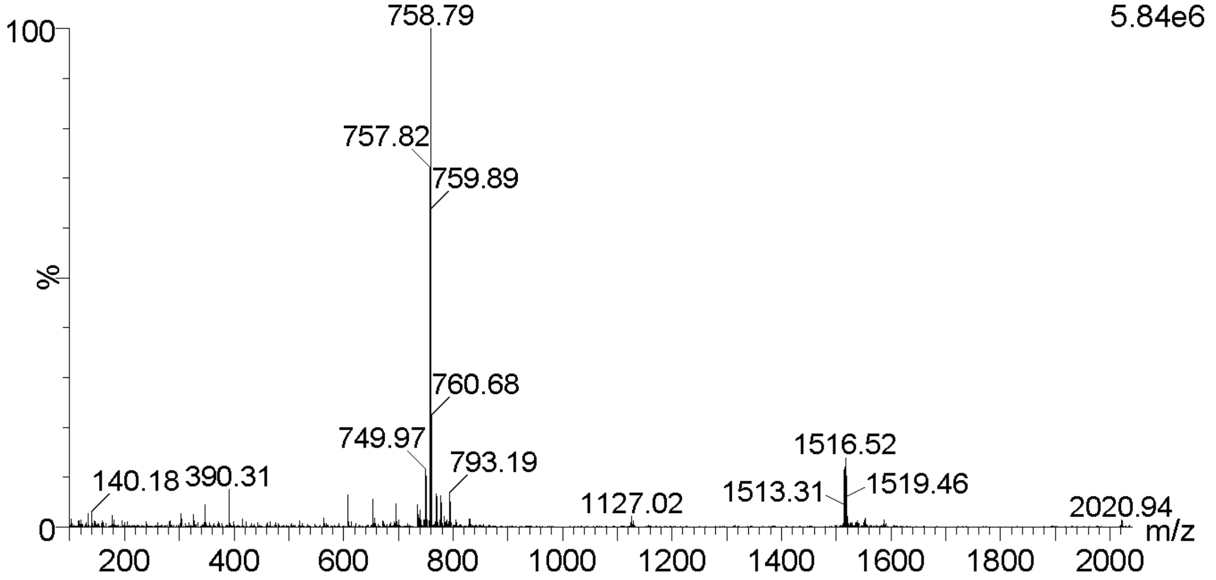

Figure S36a: Positive ion LRMS of DCL-DSS-D-Lys(Gd-DOTA)-D-Trp-D-Trp-NH_2 **(39)**, 1516.52 $[M+H]^+$, 758.79 $([M+2H]/2)^{2+}$

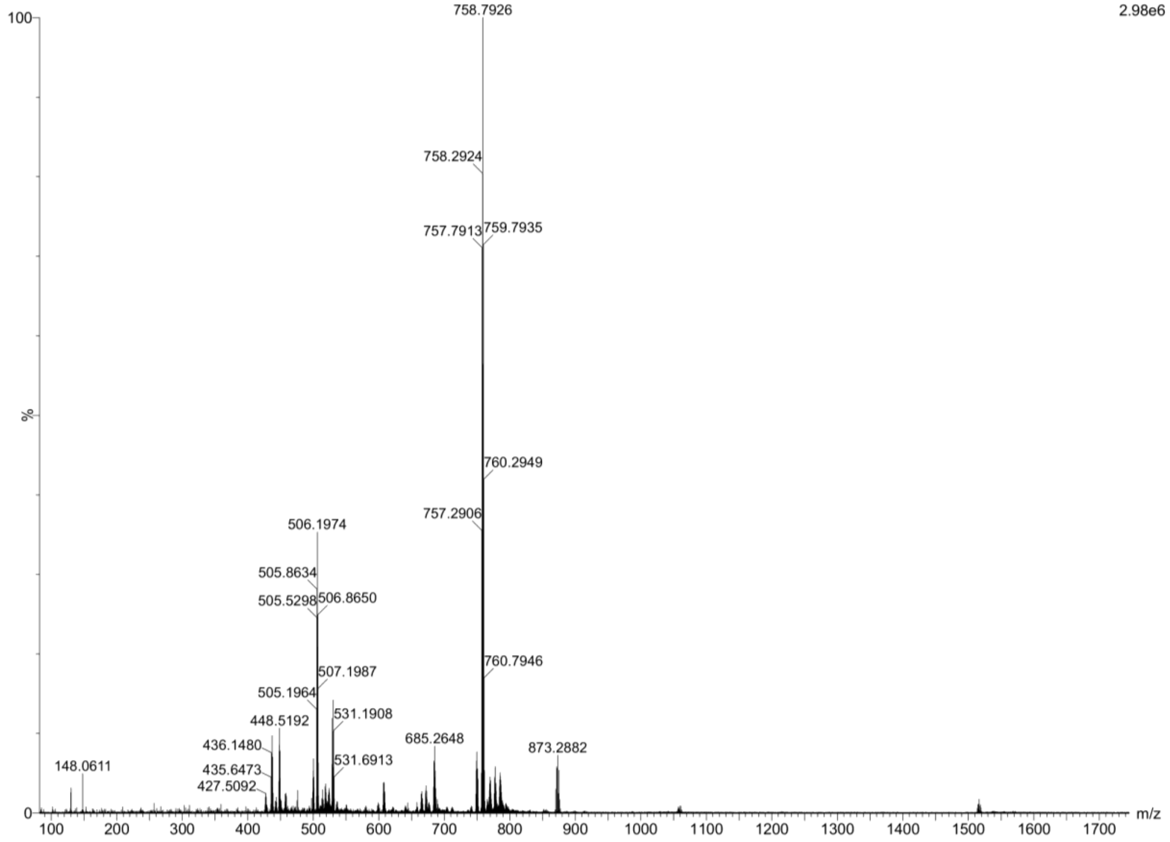

Figure S36b: Positive-ion HRMS of DCL-DSS-D-Lys(Gd-DOTA)-D-Trp-D-Trp-NH$_2$ **(39)**, 758.7926 ([M+2H]/2)$^{2+}$, 506.1974 ([M+3H]/3)$^{3+}$

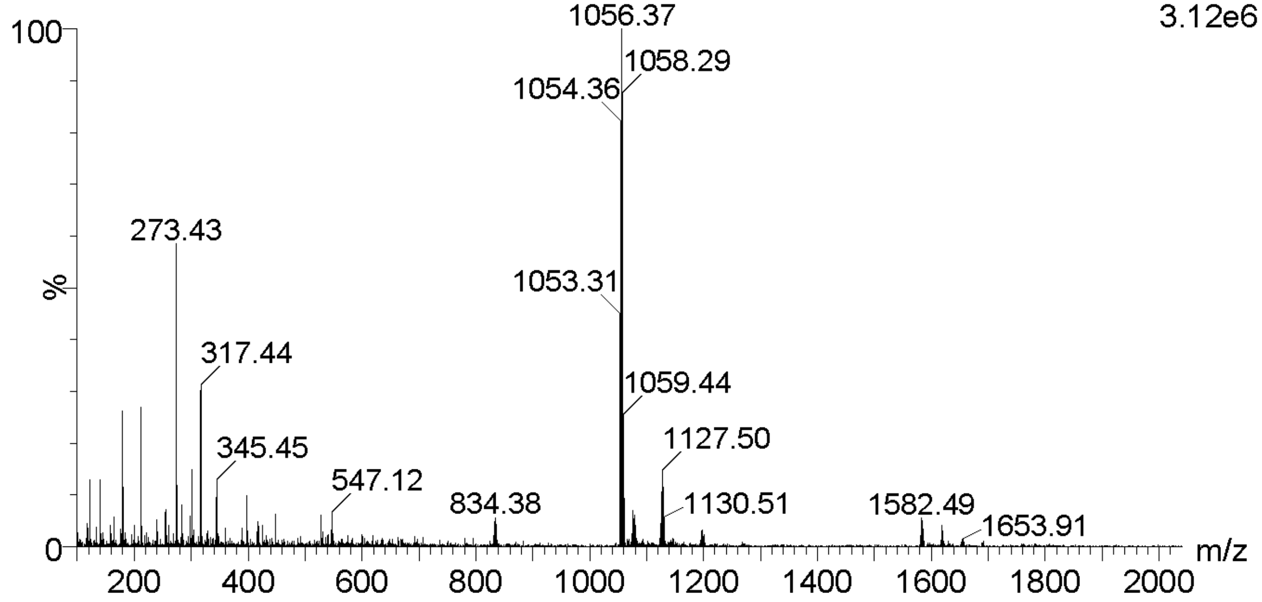

Figure S37a: Positive-ion LRMS of Fmoc-D-Phe-Lys(Gd-DOTA)-NH$_2$ **(40)**, 1056.37 [M+H]$^+$

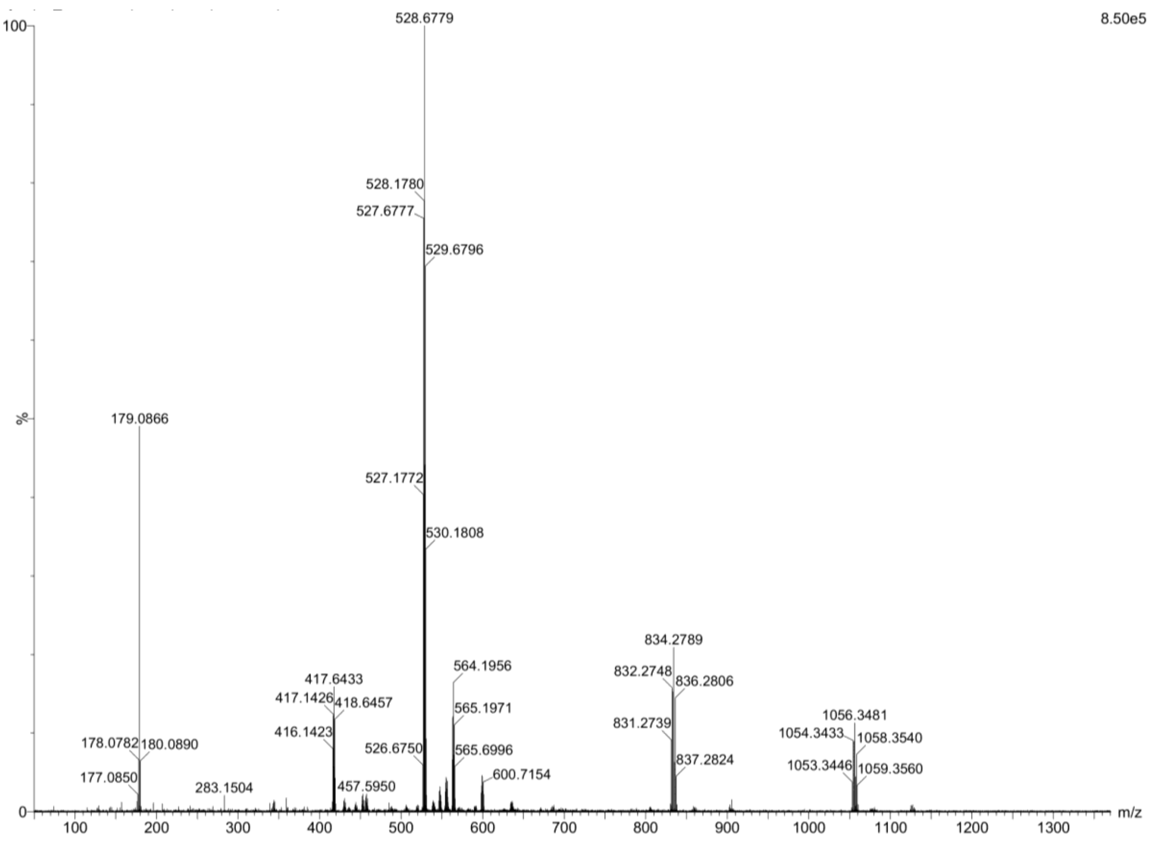

Figure S37b: Positive-ion HRMS of Fmoc-D-Phe-Lys(Gd-DOTA)-NH_2 **(40)**, 1056.3481 $[M+H]^+$, 5228.6779 $([M+2H]/2)^{2+}$

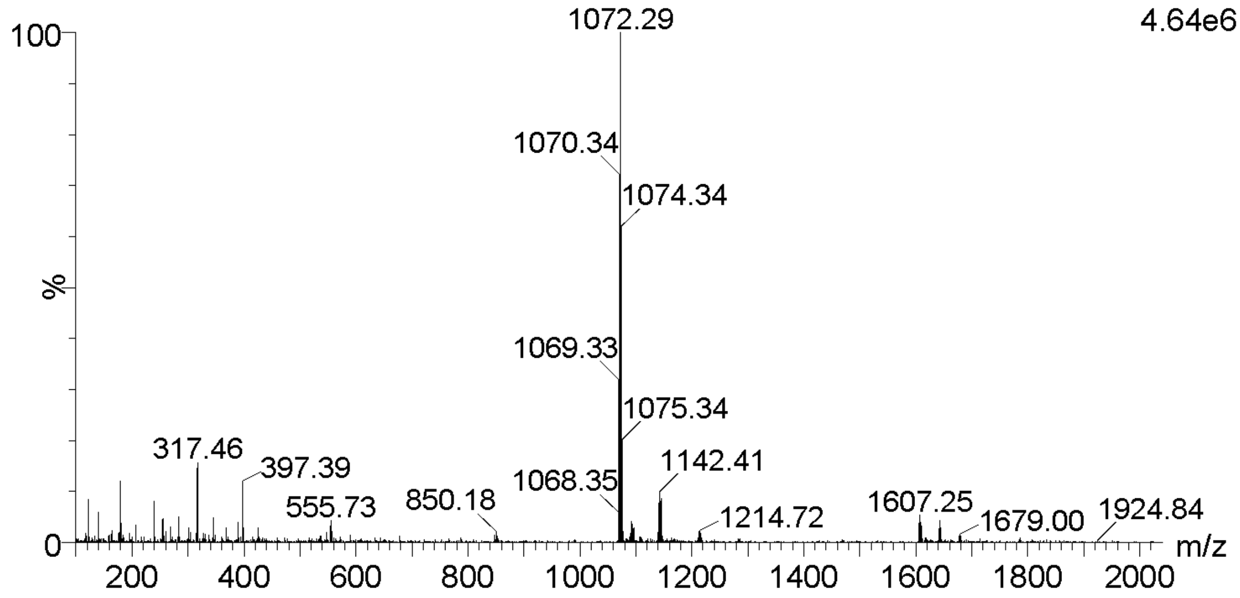

Figure S38a: Positive-ion LRMS of Fmoc-D-Tyr-Lys(Gd-DOTA)-NH_2 **(41)**, 1072.29 $[M+H]^+$

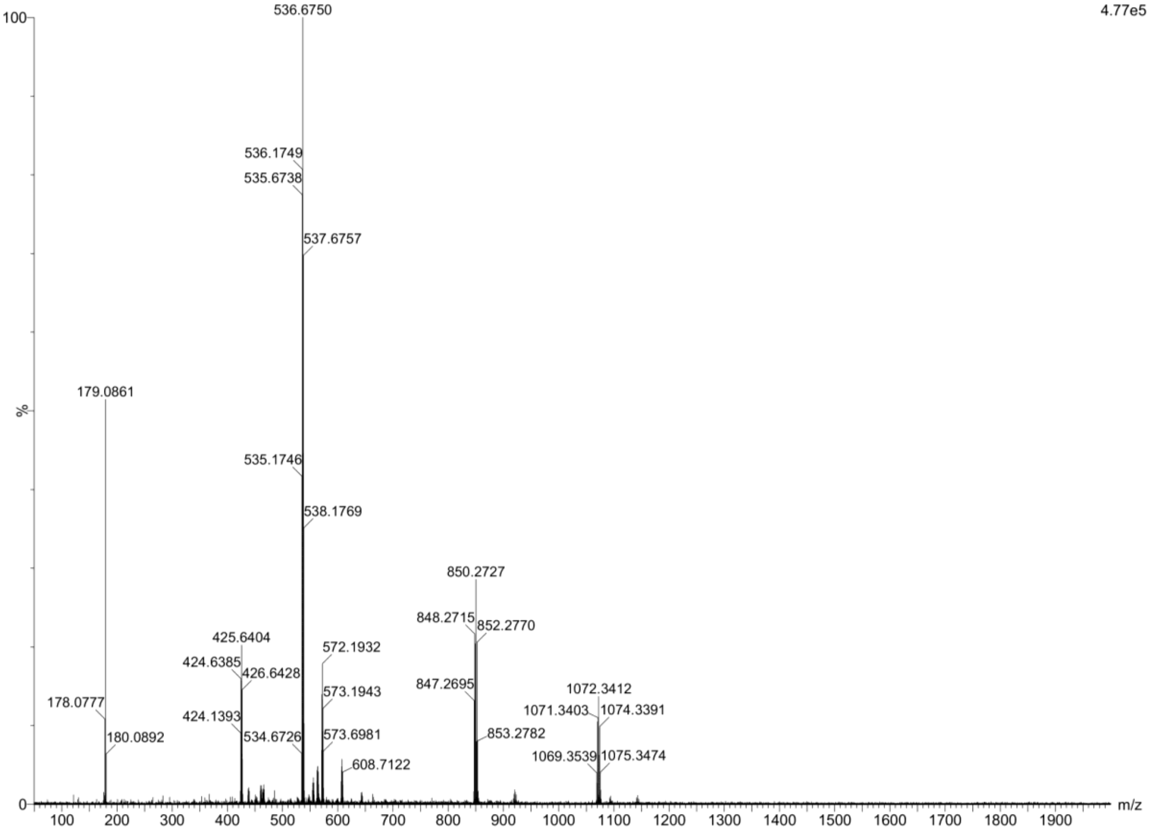

Figure S38b: Positive-ion HRMS of Fmoc-D-Tyr-Lys(Gd-DOTA)-NH$_2$ **(41)**, 1072.3412 [M+H]$^+$, 536.6750 ([M+2H]/2)$^{2+}$

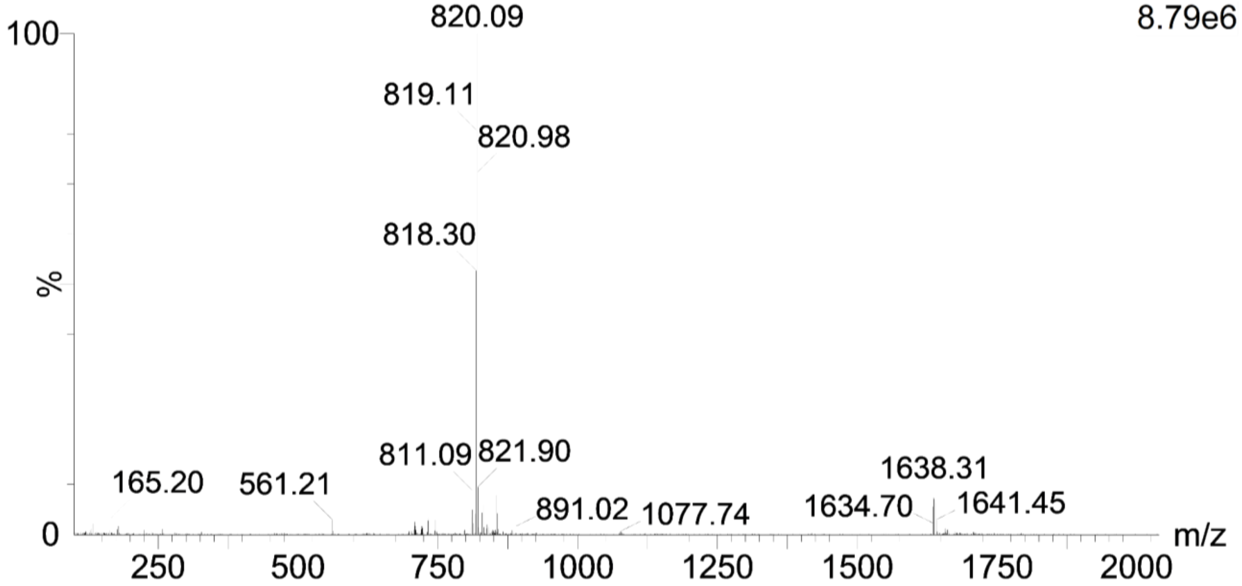

Figure S39a: Positive-ion LRMS of Fmoc-D-Trp-D-Lys(Gd-DOTA)-Dap(DCL-DSS)-NH$_2$ **(42)**, 1638.31 [M+H]$^+$, 820.09 ([M+2H]/2)$^{2+}$

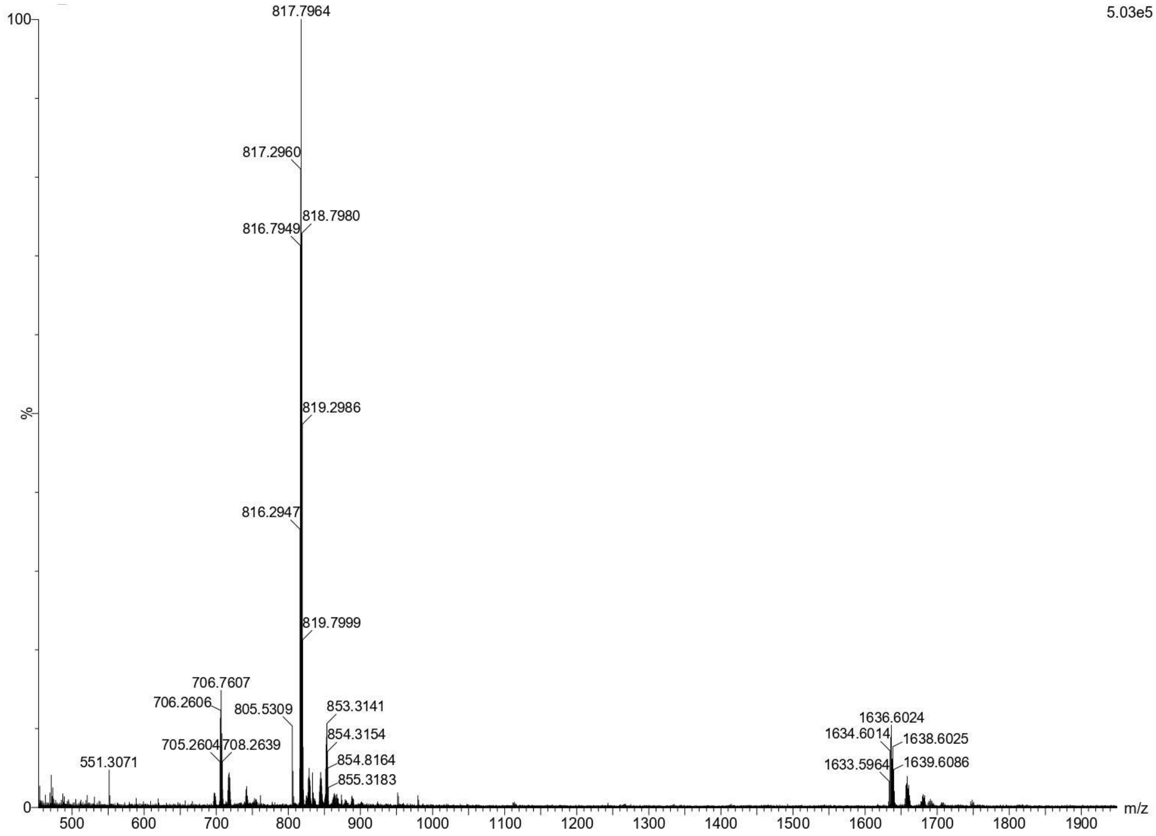

Figure S39b: Negative-ion HRMS of Fmoc-D-Trp-D-Lys(Gd-DOTA)-Dap(DCL-DSS)-NH_2 **(42)**, 1636.6024 $[M-H]^-$, 817.7964 $([M-2H]/2)^{2-}$

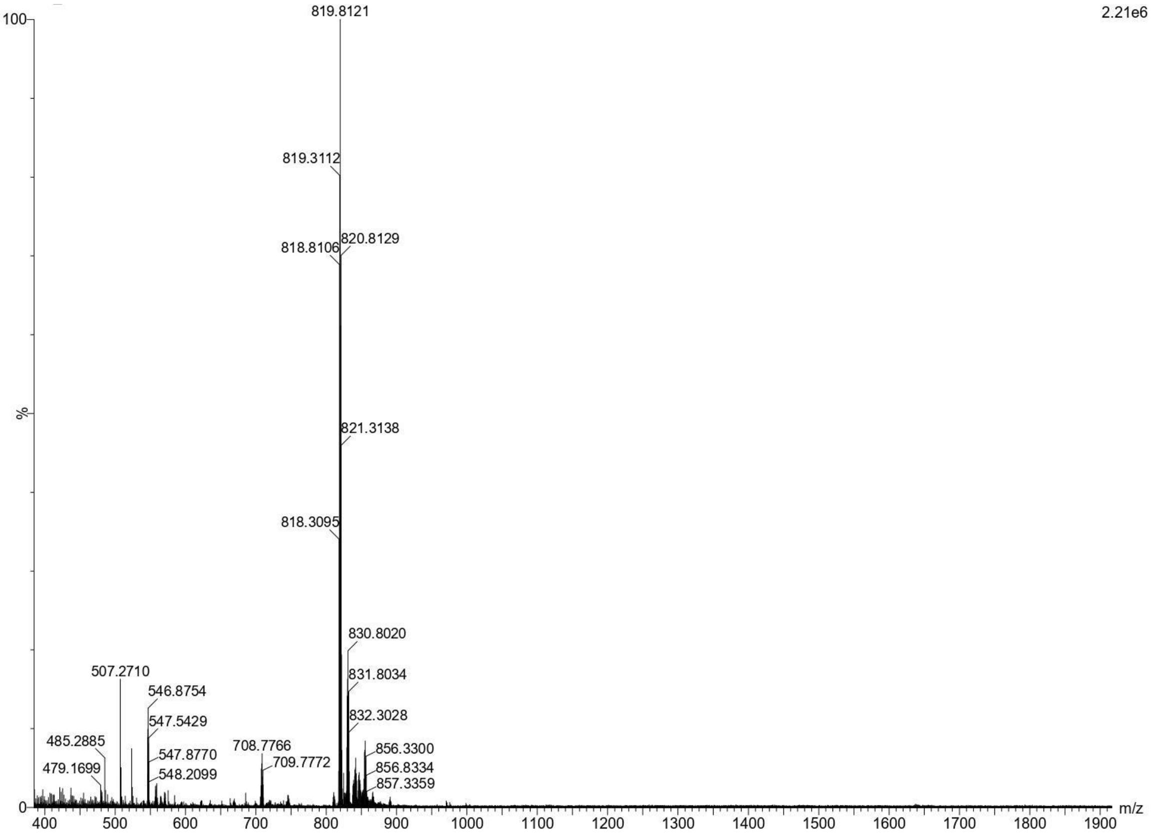

Figure S39c: Positive-ion HRMS of Fmoc-D-Trp-D-Lys(Gd-DOTA)-Dap(DCL-DSS)-NH_2 **(42)**, 819.8121 ($([M+2H]/2)^{2+}$)

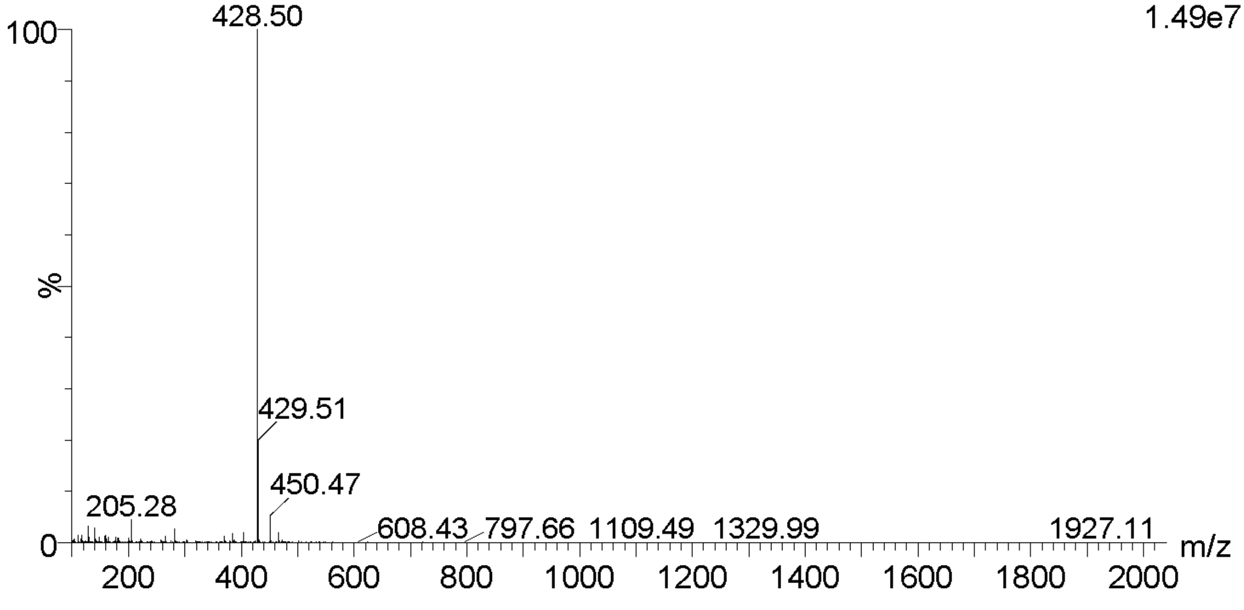

Figure S40: Positive-ion LRMS of H_2N-PEG8-COOH **(43)**, 428.50 $[M+H]^+$

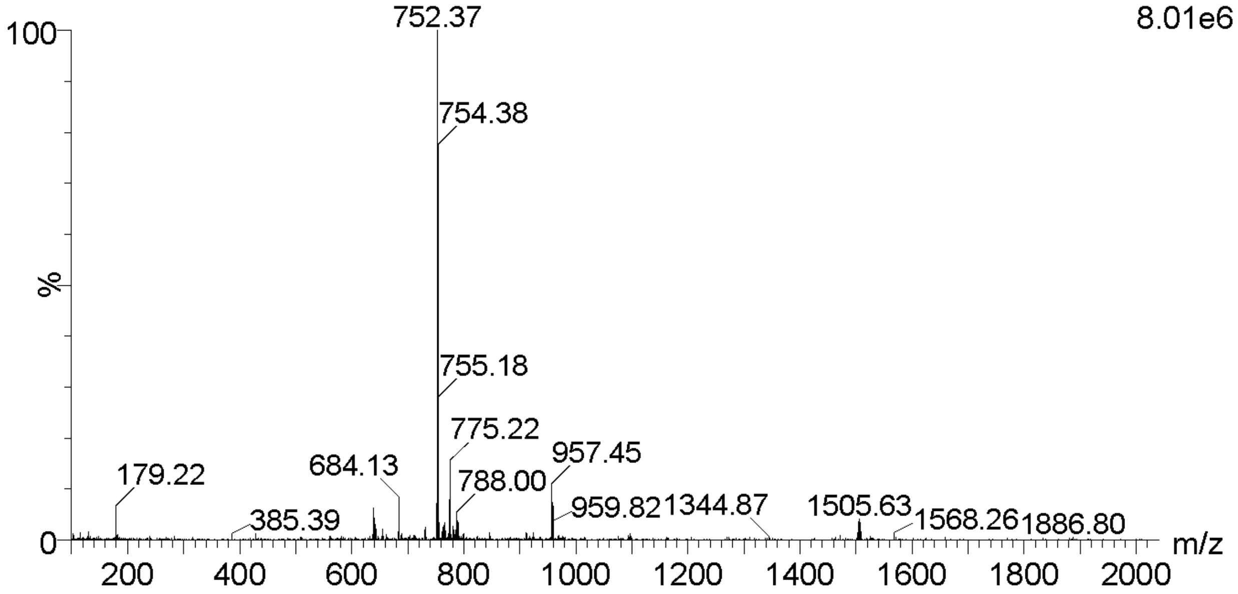

Figure S41: Positive-ion LRMS of Fmoc-D-Trp-D-Lys(Gd-DOTA)-PEG8-COOH **(44)**, 1505.63 [M+H]$^+$, 752.37 ([M+2H]/2)$^{2+}$

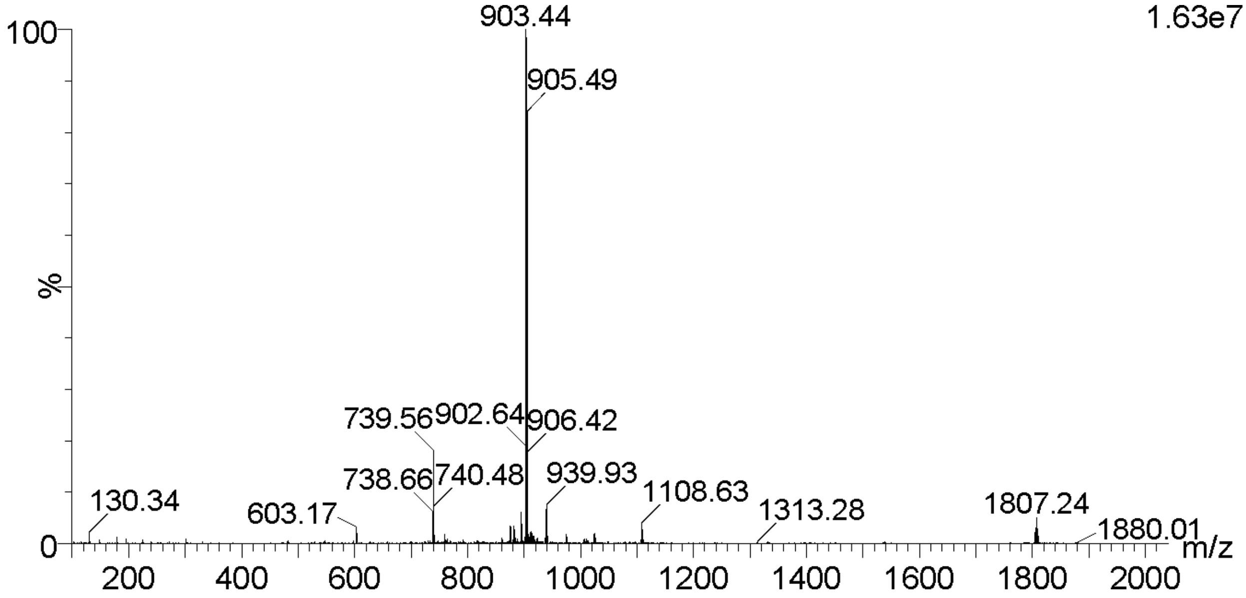

Figure S42a: Positive-ion LRMS of Fmoc-D-Trp-D-Lys(Gd-DOTA)-PEG8-DCL **(46)**, 1807.24 [M+H]$^+$, 903.44 ([M+2H]/2)$^{2+}$

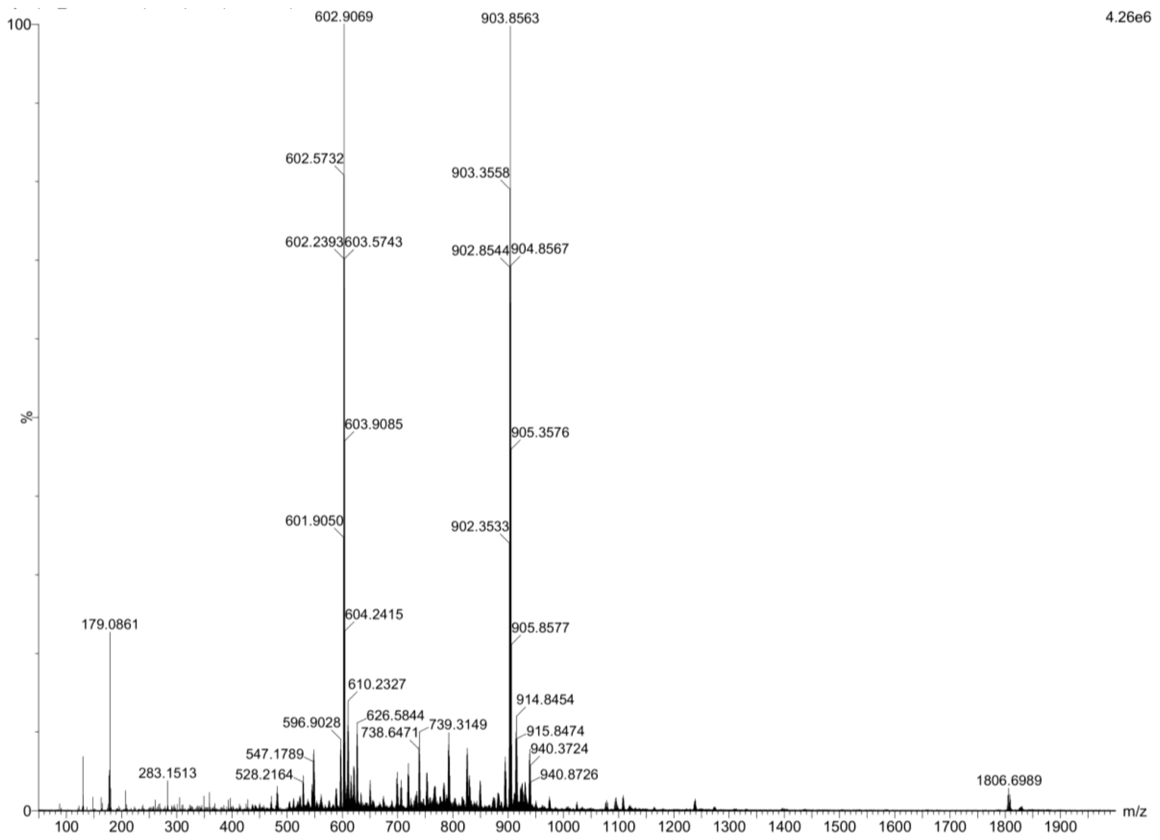

Figure S42b: Positive-ion HRMS of Fmoc-D-Trp-D-Lys(Gd-DOTA)-PEG8-DCL **(46)**, 1806.6989 [M+H]$^{+}$, 903.8563 ([M+2H]/2)$^{2+}$, 602.9069 ([M+3H]/3)$^{3+}$

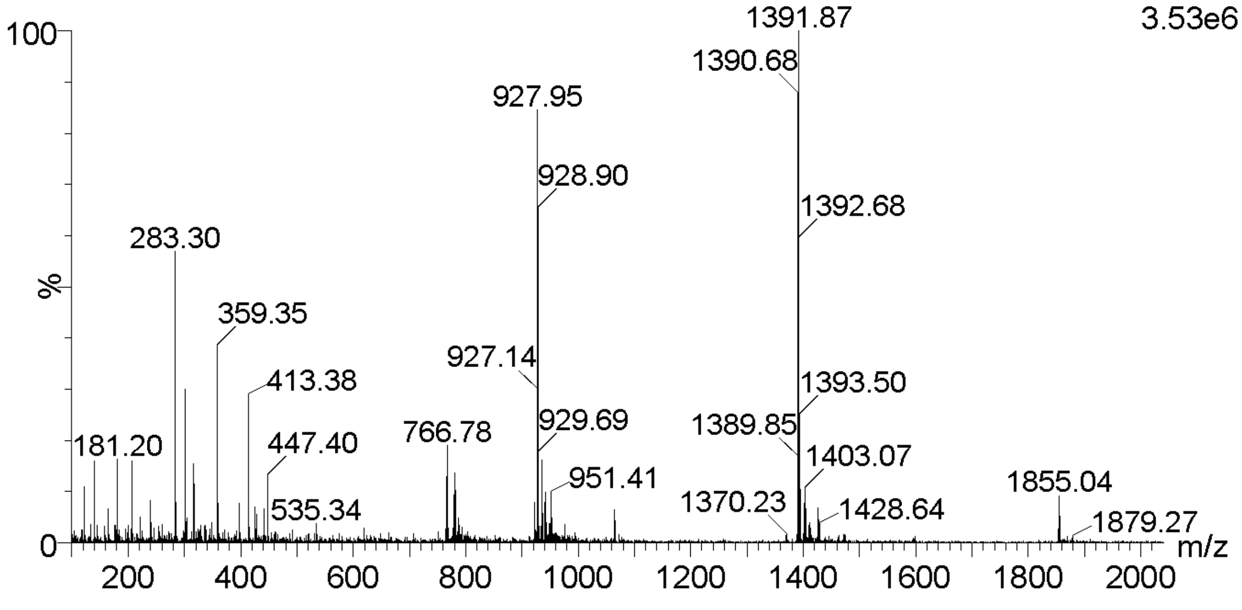

Figure S43a: Positive-ion LRMS of Fmoc-D-Trp-D-Lys(Gd-DOTA)-PEG8-18-4 **(46)**, 1391.87 ([M+2H]/2)$^{2+}$, 927.95 ([M+2H]/3)$^{3+}$

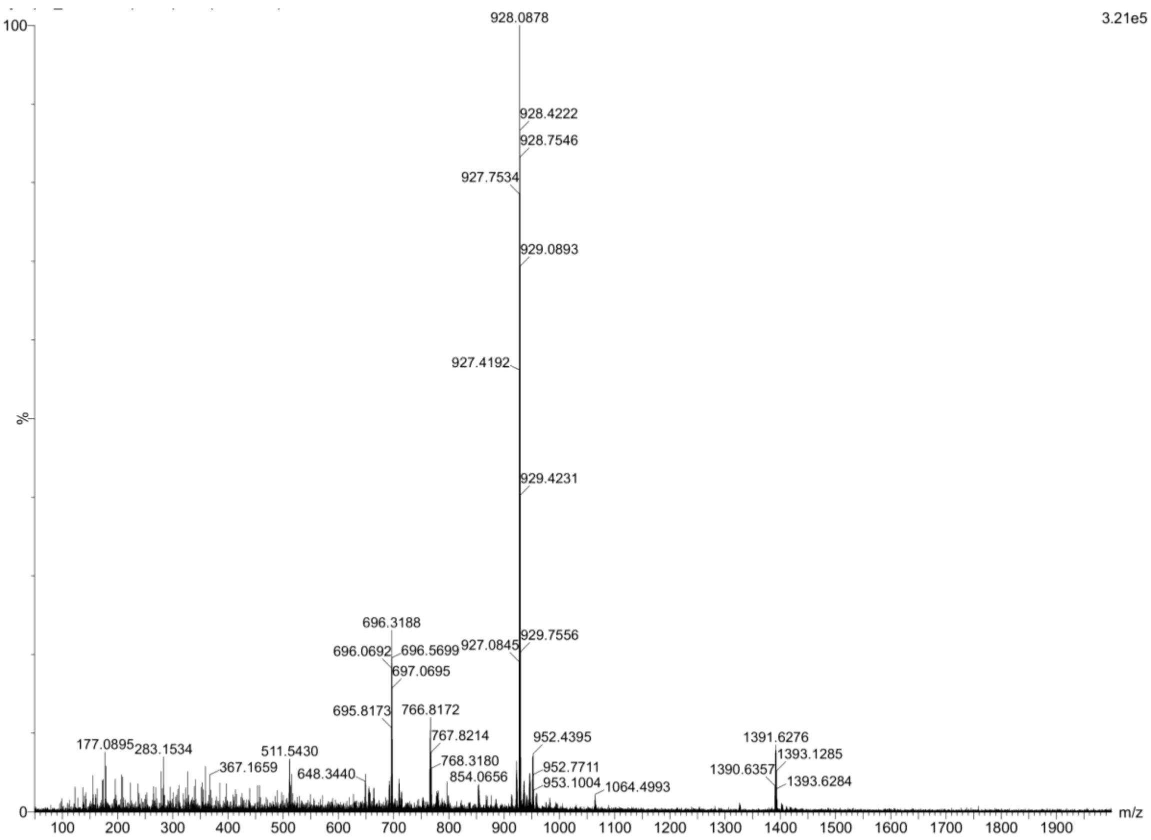

Figure S43b: Positive-ion HRMS of Fmoc-D-Trp-D-Lys(Gd-DOTA)-PEG8-18-4 **(46)**, 1391.6276 ([M+2H]/2)$^{2+}$, 928.0878 ([M+3H]/3)$^{3+}$

Additional 1/T_1 vs. Concentration Graphs

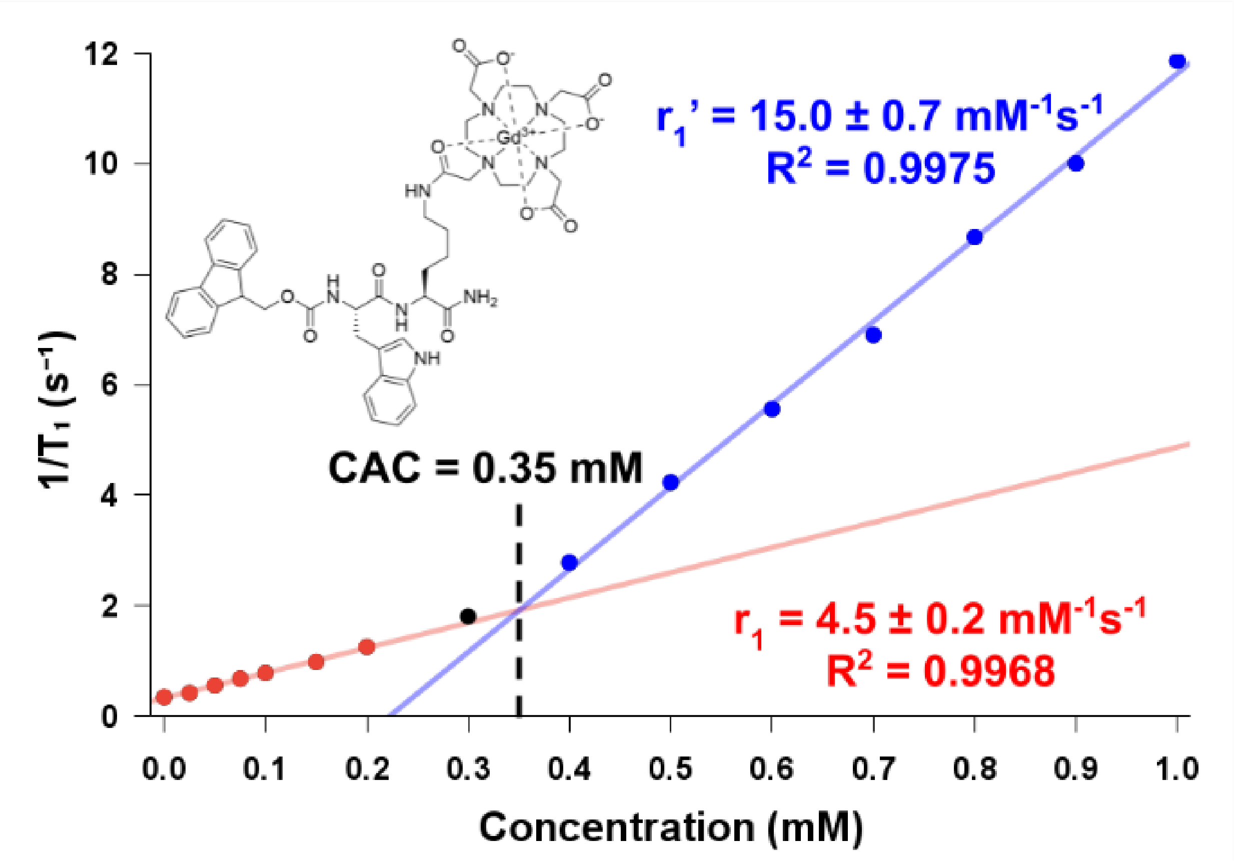

Figure S44: Fmoc-Trp-Lys(Gd-DOTA)-NH_2 **(6)** in PBS

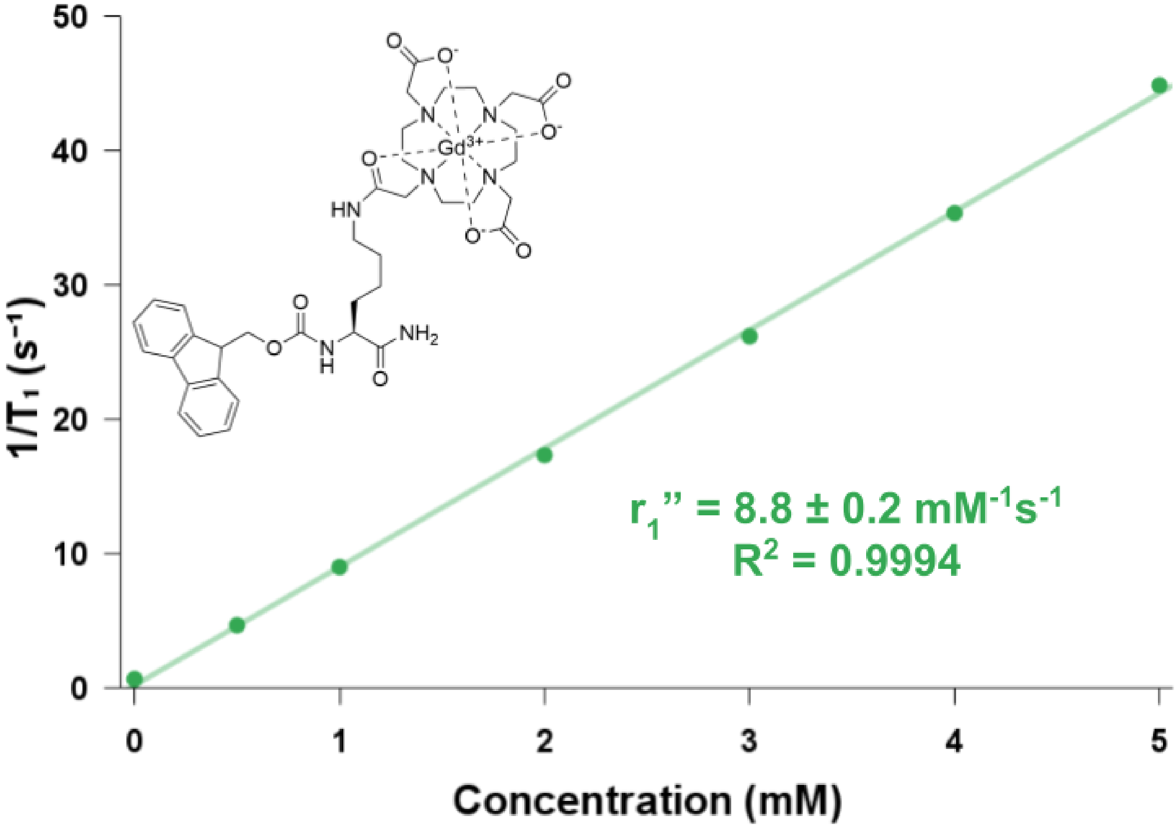

Figure S45: Fmoc-Lys(Gd-DOTA)-NH_2 **(2)** in FBS

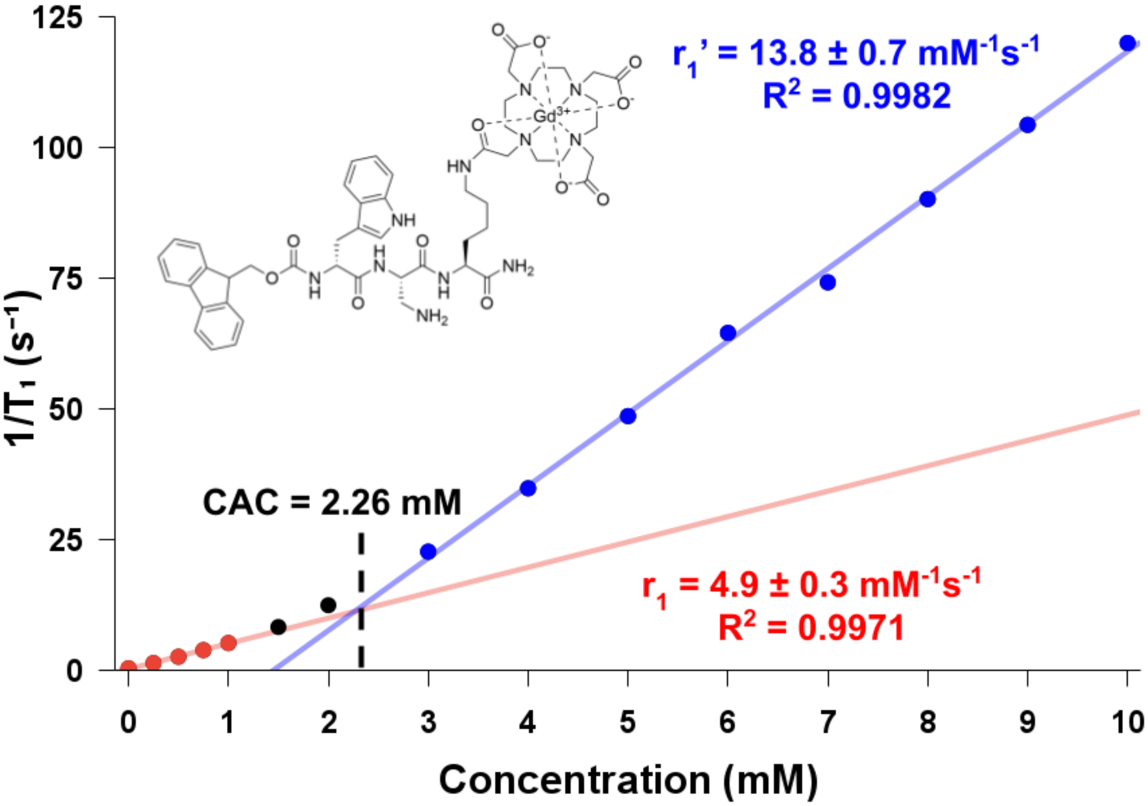

Figure S46: Fmoc-D-Trp-Dap(H)-Lys(Gd-DOTA)-NH_2 **(20)** in H_2O

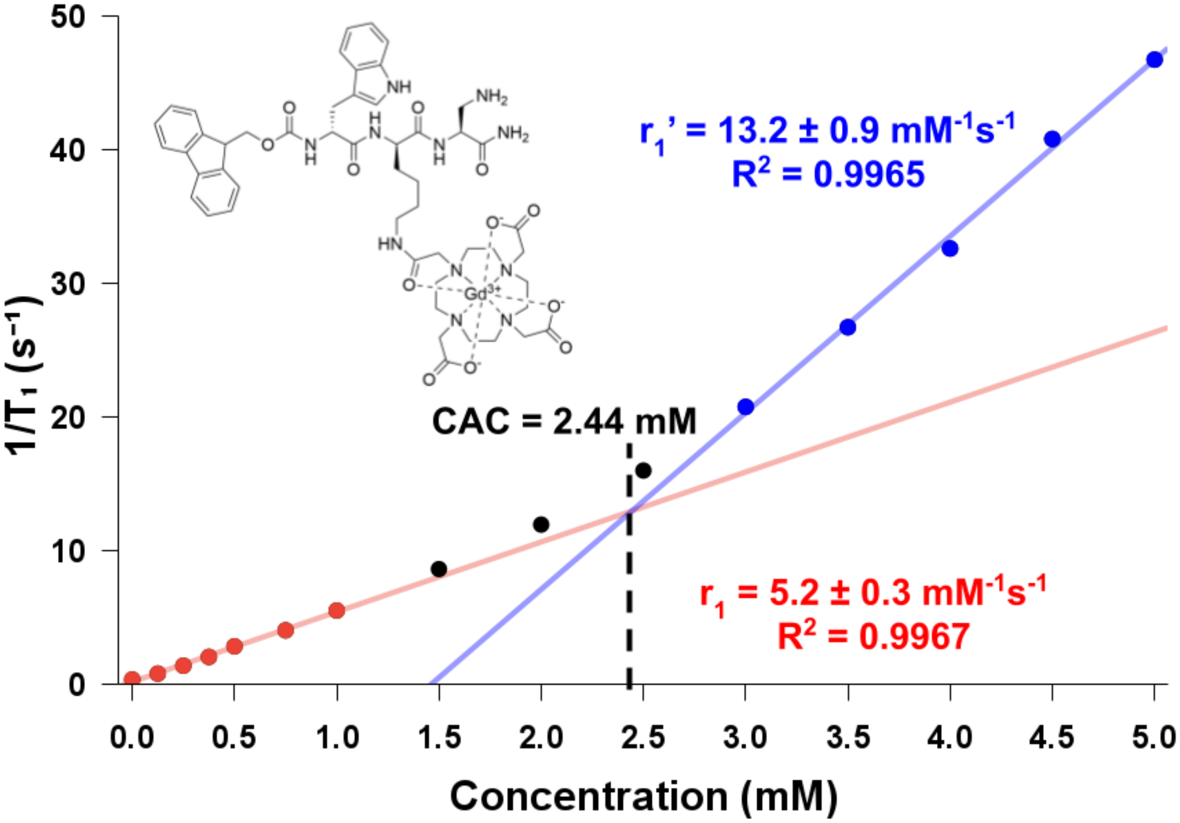

Figure S47: Fmoc-D-Trp-D-Lys(Gd-DOTA)-Dap(H)-NH_2 **(26)** in H_2O

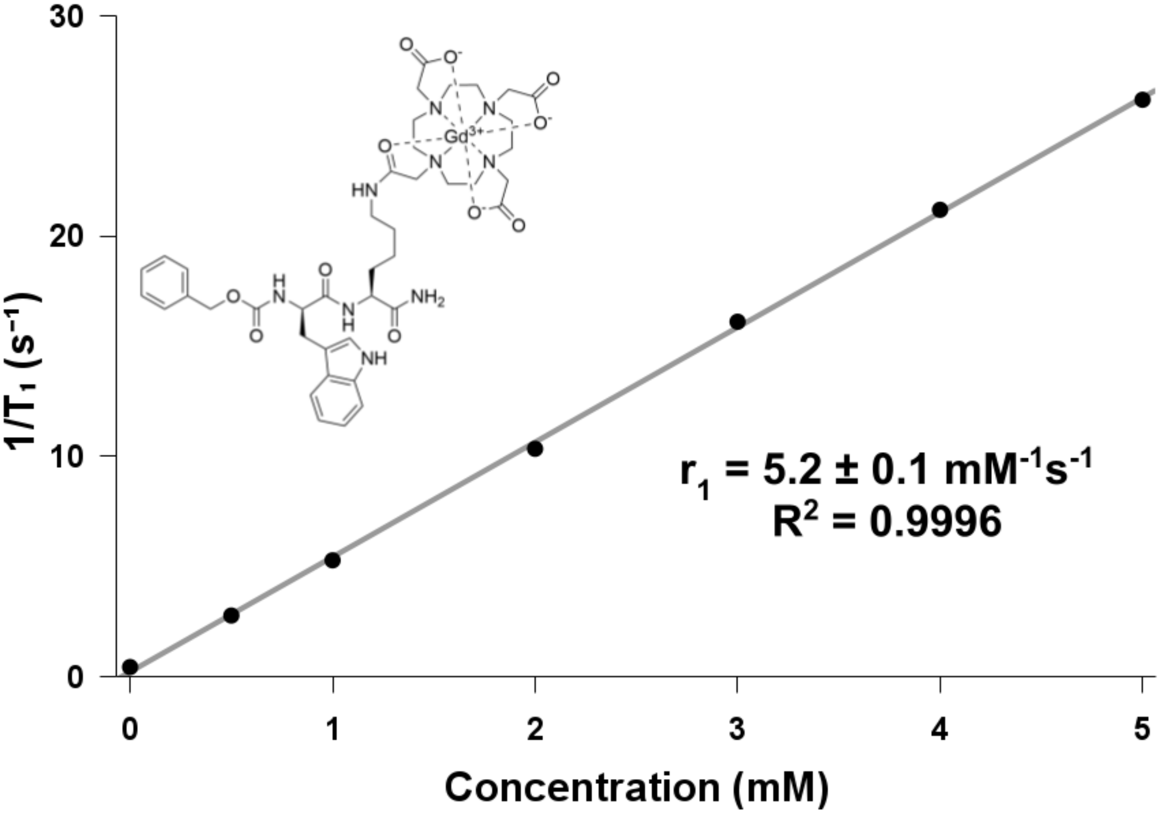

Figure S48: Cbz-D-Trp-Lys(Gd-DOTA)-NH_2 **(27)** in H_2O

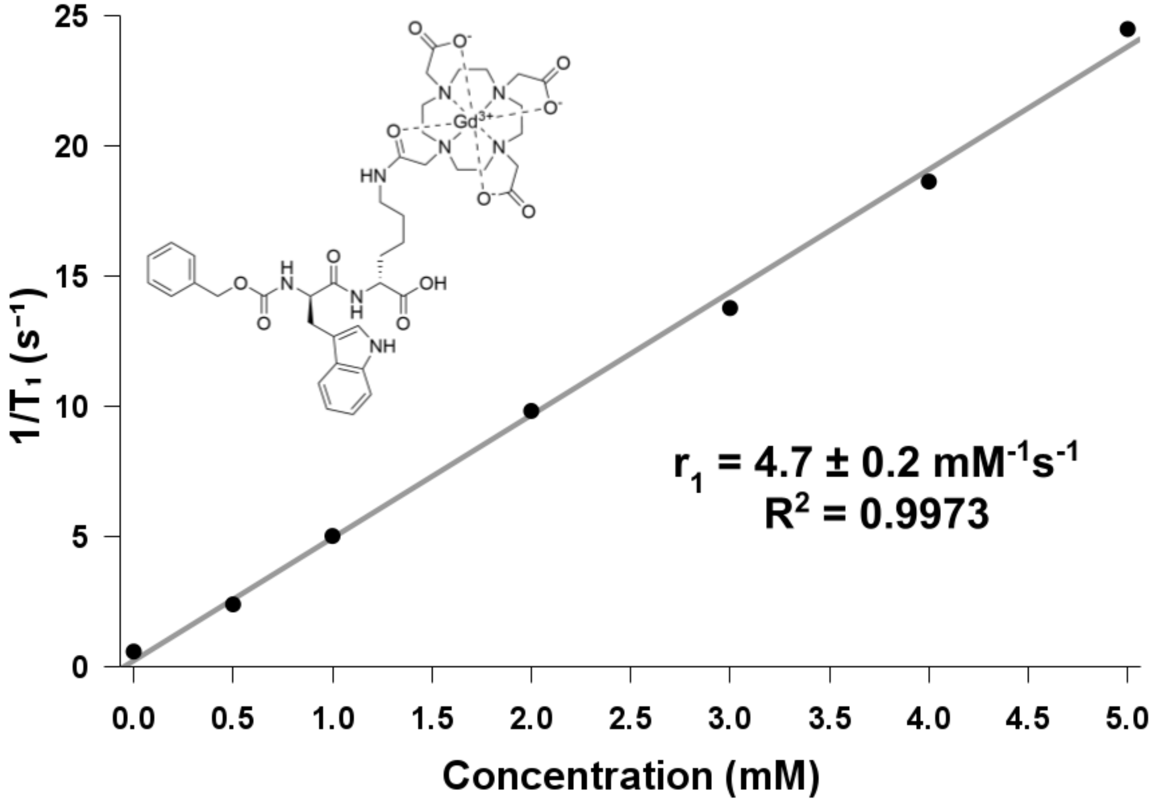

Figure S49: Cbz-D-Trp-D-Lys(Gd-DOTA)-NH_2 **(28)** in H_2O